"Maa"

Heat Transfer and Mixing Studies in a Mechanically Agitated Pilot-scale Bioreactor

by

PANKAJ MOHAN

A thesis submitted to the
faculty of Engineering
of the
University of Birmingham
for the degree of
DOCTOR of PHILOSOPHY (PhD)

SERC Centre for Biochemical Engineering
School of Chemical Engineering
The University of Birmingham
Birmingham, England
July, 1993

ACKNOWLEDGEMENTS

I wish to thank my Supervisors, Mr. A. N. Emery, Professor A.W Nienow, Dr. W. Bujalski and Dr. T. Al. Hassan for their continuous help and encouragement throughout the experimental work. I wish to specially thank Mr A.N. Emery and Dr W. Bujalski for their assistance and advise on preparing this thesis. I also wish to thank Dr. C. R. Thomas and Professor F. Mayinger (Technical University of Munich, Germany) for their continued interest and advice throughout the project.

I am grateful to Dr. A.J. Barker, Dr. J.M. Winterbottom, Dr. C. Kent, Mr. T. Martin, Mr. A. Amanullah, Mr. K. G.Tucker, Ms. H. Jennings, Mr. D. Bowden, Mr. B. Badam, Mr. P. Cox, Mr B. Sharpe and the workshop staff for their help and support.

I wish to acknowledge my gratitude for financial assistance from Overseas Research Studentship Award (ORS), TI group postgraduate scholarship and Hufton postgraduate scholarship.

Finally, it is difficult for me to express in words my gratitude for family support and encouragement.

Abstract

Intensive bioreaction processes are increasingly found to be rate-limited by inadequate heat transfer capability, a situation arising equally from the poor applicability of conventional heat transfer prediction methods in bioreaction environments and from the lack of a body of data covering the appropriate operating regimes. Here the modification of a pilot-scale bioreactor is described to allow heat transfer studies to be conducted in real and simulated bioreaction environments as well as the correlation of the data with relevant operating parameters including vessel and agitator geometry, fluid properties, power input, gas holdup and gas flowrate.

A number of heat flux probes, modified to avoid boundary layer discontinuity effects have been mounted in an 800 litre fermenter equipped also with a range of temperature sensors to enable determination of local temperature gradients as well as both local and global transfer coefficients. The experimental programme has been conceived in three stages using; 1) un-aerated Newtonian (various concentrations of Glucose solutions) and non-Newtonian fluids (various concentration of Carboxymethyl Cellulose), 2) the same fluids aerated, and 3) real multi-phase Penicillin fermentations, fungal broths exhibiting extreme rheological properties, followed by simulation using fibre suspension. Parallel experiments aimed to characterise both the reactor hydrodynamics and the morphology of the solid microbial phases, and these can be related to the heat transfer performance.

Following application of regression smoothing techniques to raw heat flux and temperature data, the measured jacket heat transfer coefficients in unaerated Newtonian fluids agree very well with predictions from the literature. The heat transfer data for both single and dual impeller systems bear a good qualitative relationship with global hydrodynamics. However, in the absence of fundamental understanding of the local hydrodynamics, empirical correlations have been proposed describing the position dependence of heat transfer coefficients in both aerated and unaerated Newtonian and non-Newtonian fluids for this geometry, (using a single impeller). Generally aeration leads to a drop in the heat transfer coefficient for the same impeller tip speed.

Experiments with fermentation broth has shown that significant axial variations of heat transfer coefficient exist. Furthermore, the heat transfer coefficient is influenced not only by aeration rate (at least below the flooding rate), impeller speed and bulk flow but also by the morphology of the solid phase (i.e. the fungal mycelium). The introduction of this third phase adds a new dimension to the engineering challenge. The presence of mycelia modifies the heat transfer in two possible ways: its particulate nature modifies the thermal boundary layer by the brushing action, and on the other hand it also influences the rheology. Both the effects are further examined by simulating the fermentation broth using suspended fibres. The results suggests that the brushing action is position dependent with the maximum boundary layer modification near the impeller plane and that this influence decreases with axial distance away from the impeller. Different morphological states, i.e. filamentous or pelleted, have different effect on both the boundary layer and rheology.

CONTENTS

Page no.

CHAPTER 1

CHAPTER 2

Literature survey

CHAPTER 3

Equipment and methods

CHAPTER 4

Modification of the heat flux probe and validation of the technique

CHAPTER 5

Local heat transfer and mixing studies in unaerated systems

CHAPTER 6

Local heat transfer and mixing studies in two phase systems

CHAPTER 7

Heat transfer and mixing in real and simulated multiphase fermentation systems

CHAPTER 8

CHAPTER 1

Introduction

Origin of this project

The origins of this work lie in a long-term programme in the University of Birmingham on the application of advanced computer-based design methods in Biotechnology. This programme is concerned with the production of an integrated suite of design software specifying the process and mechanical engineering design details based on the processing requirement. This programme, which is a joint collaboration between the Schools of Chemical and Mechanical Engineering (Mr. A.N. Emery and Professor D. Walton), brought to light the fact that, while mass transfer was the subject of extensive literature and, consequently, predictive methods - about the subject of heat transfer there was virtually nothing directly based on bioreactor experience. Not only did the existing correlations for heat transfer in agitated vessels not extend into the flow and thermal regimes particular to bioreactors, but there was no consideration given to the potential modification of heat transfer by the presence of mycelial micro-organism themselves, either in regard to changes in flow properties or to local heat transfer effects in the boundary layer at the heat exchange surface.

Heat transfer in a fermentation is characterised by low temperature driving forces, high sensitivity to temperature (and hence a need for good temperature control) and modification due to the presence of the third phase (especially in mycelial fermentation). There is evidence that with the very high cell concentration that can now be achieved through medium development and the use of genetic engineering techniques, there are increasing instances of heat transfer becoming process limiting. Furthermore, as scale goes up - so the problem of heat transfer gets worse (heat demand increases with volume, D_T^3, whereas heat transfer area increases as D_T^2).

Thus an in-depth understanding of heat transfer is required for better and efficient equipment design. Therefore, the first step was to review the literature, and the first part of this is now published. This suggested that the various heat transfer correlations in the literature are useful only where geometric and process similarities exist and even then the range of scale over which they have been validated is limited. Generally, the heat transfer correlations have the following form:

$$Nu = k\,Re^{a}\;Pr^{b}\;Vi^{c} \qquad (1.1)$$

where the constants k, a ,b and c are experimentally determined.

The major anomaly in such correlations is that the velocity used in the Reynolds number is the impeller tip speed, whereas the heat transfer takes place at the heat transfer surface (boundary layer) which is the vessel wall in the case of jacketed vessels. Therefore an understanding of the local velocity flow field near the vessel wall is of paramount importance in the fundamental explanation of the heat transfer phenomena in such vessels. This also suggests that heat transfer is a local phenomenon and therefore a local study would give a better understanding of the interaction between hydrodynamics and heat transfer.

Thus the aim of this project was to carry out an integrated study of heat transfer at a scale which would lend credibility to the results, particularly in regard to the position-dependence of heat transfer. The geometry of both vessel and agitator were fixed (standard vessel configuration and standard Rushton turbine respectively) and the objectives were therefore to investigate the effects on heat transfer, as measured at various points in the vessel wall, of :

1) Agitator speed, air flow rate and power input.

2) Fluid Rheology ; using simple and complex fluids.

3) Solid phase Morphology ; using real and simulated fermentation broths.

In order to meet the objectives of this programme, the project was divided into three interrelated studies, namely,

a) Heat transfer and mixing in single phase fluids for both Newtonian and non-Newtonian model fluids.

b) Heat transfer and mixing in two phase (gas-liquid) fluids for both Newtonian and non-Newtonian model fluids.

c) Real multi phase fermentations and also simulations using pulp fibres to ascertain the effect of the solid phase on heat transfer coefficients.
This study was related also to other long term programme in the SERC Centre for Biochemical Engineering concerning both the characterisation of mixing and mass transfer performance in bioreactors (Professor A.W. Nienow and Dr. W. Bujalski) and the characterisation of mycelial morphology and its relationship to microbial physiology (Dr. C.R.Thomas and Mr. K.G. Tucker). In the long term the aim must be to be able to predict heat transfer performance in a vessel of given size, geometry, power input and air flow rate for fluids characterised by simply measured parameters.

Layout of the thesis

An extensive literature review is presented in chapter 2 in which the relevant studies in this area are critically examined. The modifications required to the pilot plant (800 l bioreactor) in order to carry out these studies are next reported in chapter 3. For local heat transfer studies a specially designed heat flux probe was conceived in collaboration with Rdf Inc., USA, the details of which are presented in chapter 4. Local heat transfer and mixing studies with unaerated Newtonian and non-Newtonian fluids are described in chapter 5, while the two phase (gas-liquid) system is described in chapter 6. Chapter 7 contains a description of the work on the real multiphase fermentations which is then modelled using fibre suspensions. Finally, the important findings and conclusions of this project, together with suggestions for future work are given in chapter 8.

CHAPTER-2

Literature survey

This chapter is divided into seven main sections. Section 2.1 introduces dimensionless groups used in this study. Section 2.2 and 2.3 follow the historic development of heat transfer studies in mechanically agitated vessels with Newtonian and Non-Newtonian fluids respectively. The various heat transfer correlations for mechanically agitated jacketed vessels available in the literature are summarised in tables. Section 2.4 gives an overview of service side heat transfer in various types of jackets. Concepts in rheology are reviewed in section 2.5 followed by an introduction to hydrodynamics in section 2.6. Finally section 2.7 covers fundamental concepts in real multiphase fermentations.

2.1 Dimensionless groups

Several dimensionless numbers are used in this study and they are defined as follows :

Froude Number, Fr

The Froude number represents the ratio of inertial forces to gravitational and has the form;

$$Fr = N^2 \; D/ g \qquad (2.1)$$

Nusselt Number, Nu

The Nusselt number signifies the ratio of total heat transfer (or more appropriately convective heat transfer) to conductive heat transfer.

$$Nu = h \, D_T \; / \, K_T \qquad (2.2)$$

Power Number, N_p

The power number represents the ratio of pressure differences, which give rise to flow, to the force of inertia. Thus it is equivalent to the drag coefficient on particles though it is usually related to the power input by the impeller for agitated vessels. It is given by,

$$N_p = P / \rho N^3 D^5 \tag{2.3}$$

The power number is sometimes referred to as the Newton number and also as the Euler number.

Prandtl Number, Pr

Prandtl number represents the ratio of momentum diffusivity to thermal diffusivity, which decides how the fluid thermal properties affect heat transfer in forced convection.

$$Pr = c_p \mu / K_T \tag{2.4}$$

Reynolds Number, Re

For Newtonian fluids the Reynolds number for agitation is given by;

$$Re = D^2 N \rho / \mu \tag{2.5}$$

This represents the ratio of inertial to viscous forces which determine whether the flow is laminar, transitional or turbulent.

Viscosity Ratio, Vi

Viscosity ratio accounts for the spatial change in viscosity in the agitated vessel; it is the ratio of viscosity at the bulk to that at the wall.

$$Vi = \mu / \mu_w \tag{2.6}$$

Weber Number, We

The Weber number represents the ratio of inertial force to the surface tension force, and is associated with bubble formation.

$$We = D^3 N^2 \rho / \sigma \tag{2.7}$$

2.2 *Heat transfer to Newtonian Fluids*

The heat transfer correlation for jacketed vessels has most usually been expressed in the form given in equation (1.1) with a subscript "j". There is no physical justification for the form of the functional relationship given in equation (1.1), but it has been widely and successfully used in heat transfer studies and the values of the parameters k_j, a_j, b_j etc. can be readily determined from experimental data.

2.2.1 Single phase heat transfer

Chilton et al [1] made the first significant systematic study of film coefficients in an unbaffled agitated jacketed vessel using flat paddle agitators. This pioneering work laid the foundation for the methods and procedures of heat transfer coefficient determination. Their tests were made under steady state conditions; i.e. the process liquid in the vessel was heated by steam in the jacket while being cooled by water flowing in the coil. The heat loss value was measured for the various steam pressures used (i.e. q_{lost}), and this was subtracted from the heat quantity measured from the steam condensate.

Latent heat of steam condensate = $q = m_s . l$ (2.8)

Effective heat transfer = $Q_h = q - q_{lost}$ (2.9)

The amount of heat transferred was also obtained from the temperature rise and the quantity of cooling water used, and a good agreement was obtained. When the amount of condensate collected per unit time was constant, readings were taken of the bulk liquid temperature (T_b), metal surface temperatures (T_w), steam pressure, steam condensate volume, cooling water temperatures, agitator speed, and height of liquid on the vessel wall. U is then calculated from:

$$Q_h = UA_H (T_w - T_b) \qquad (2.10)$$

and the Q_h value is obtained from equation 2.9 .

Heat transfer coefficients were calculated for the coil and jacket (see table 2.1 equation (1)). Fouling factors were neglected. Chilton et al [1] used graphical methods to obtain the heat transfer correlations. To demonstrate the influence of agitator speed and liquid temperature on the surface heat transfer coefficients, they plotted the impeller Reynolds number against Nusselt number and obtained the exponent "a" as 2/3, and to demonstrate the influence of physical properties of the fluid on the coefficient, they plotted Nusselt number divided by Reynolds number to the exponent 2/3 against the Prandtl number and obtained the exponent "b" as 1/3.

They observed a discrepancy between results for heating and those for cooling in the batch process and this led to the introduction of the Sieder and Tate [2] concept of a viscosity correction ratio, for which they [1] obtained graphically the value of the exponent "c" as 0.14.

A similar correlation was achieved by Kraussold [3] working on a 1m diameter vessel using a paddle agitator [$3\times10^4 < Re < 10^5$, $2 < Pr < 2.5\times10^3$] while Uhl[4], using a geometrically similar system, extended the work of Chilton et al [1], to the viscous range of fluids (Linseed oil and Pennsylvania oil) using a paddle agitator (table 2.1 equation (2)). They also produced correlations for a six (flat) bladed turbine and an anchor agitator (see table 2.1 equations (3) and (4)). Tests were made with both heating and cooling of the process fluids, under batch conditions. According to Uhl the batch method yielded generally consistent results with much simpler equipment than is required for steady state runs. However, Chilton et al [1] felt that it was difficult to obtain consistent results in batch tests given the rapid change of liquid temperatures during the test period. Uhl [4] noted that in the range of Reynolds number from 20 to 200, the introduction of baffles had no effect on the film heat transfer coefficients, and this was confirmed later by Brooks and Su [5].

In Uhl's work, for the first time, "power measurements" were also obtained under isothermal conditions. Besides representing significant complementary information for the agitation system studied, these power data were required for the calculation of the heat transfer results because of the conversion of significant quantities of mechanical energy to heat, especially at the higher impeller speeds. However, this heat evolution was negligible for their vessel size. The power input data were correlated by plotting the Power number versus the Reynolds number. Uhl followed the same method for the correlation of data as that of Chilton et al [1]. The film coefficient was determined from the overall coefficient by a modification of the graphical method proposed by Wilson [6] (described below). The general relation,

$$1/U = 1/h_{oj} + 1/h_j + t_v/K_T + r_d \qquad (2.11)$$

was used in which the terms $1/h_{oj}$, r_d and t_v / K_T were assumed to remain constant. It was also assumed that at a given process fluid temperature;

$$h_j \; \alpha \; N^{2/3} \qquad \text{i.e.} \; h_j \; \alpha \; Re^{2/3} \qquad (2.12)$$

then

$$1/U = 1/h_{oj} + t_v/K_T + r_d + 1/[C \quad N^{2/3}] \qquad (2.13)$$

where C is a constant
and a plot of 1/U versus $1/N^{2/3}$ yields a straight line having an ordinate intercept equal to the term ($1/h_{oj} + t_v/K_T + r_d$). Recently Khartabil et al [7] have reviewed and suggested further improvements in the Wilson method. They [7] have found that the assumption that other resistances are constant may not be universally valid; hence they have given allowance for it in their correlation, which is however only tested for shell and tube heat exchangers.

Cumming and West [8] extended the data of Chilton et al [1] to include film coefficients measured in a larger unbaffled vessel using turbine agitators (see table 2.1 equation (5)). However, instead of independently processing the data, they modified and extended the paddle agitator correlation of Chilton et al [1] to include the turbine agitator data, which resulted in a value of 0.4 for the constant k. In fact, this value is too low for turbines, which generally give a higher heat transfer coefficient [4,5] than those obtained for paddles at constant Reynolds and Prandtl numbers. However, their own data [8] produce a higher value for the constant (k = 0.68) which is acceptable for turbine agitation without baffles [9].

They also carried out tests using retreating (curved) blade turbine impellers, and both straight and 45° pitched blade turbines, under steady state conditions. The pitched blade turbine showed an approximately 10% reduction in film coefficient as compared to the retreating blade turbine, and no significant change in the film coefficient resulted from reversing the pitched blade turbine rotation. Cumming and West reported that the film coefficient would be the same at a given Reynolds number, whether single or multiple impellers are used, but this finding is not consistent with that of Nagata et al [10].

Brooks and Su [5] were the first to report comprehensive data for the effect of baffles on heat transfer coefficients in turbine agitated jacketed systems (see table 2.1 equation (6)). They carried out their experiments under batch conditions and the method of correlation determination was similar to that of Uhl [4]. The value of the constant "k" without baffles was found to be 0.54 which is in agreement with Uhl [4] and Brown et al [11]. The value of the constant "k" with baffles was found to be 0.74, and this was later confirmed by Edwards et al [12], Strek [13], and Holland et al [14]. From this it may be concluded that baffling increases the heat transfer coefficient by 37%, but this difference exists only in the turbulent region [4]. The increase in turbulence when baffles are added tends to decrease the thickness of the liquid film at the vessel wall. The data taken in the laminar and transition ranges however show no difference between baffled and unbaffled conditions.

Chapman et al [14] studied heat transfer in baffled, jacketed, turbine agitated vessels using both standard (see figure 2.1) and non-standard vessel configurations. The exponents in the correlation were obtained using computer based regression which enabled a very large amount of data to be conveniently handled. Furthermore, most of the tedious and imprecise graphical analysis used by previous workers [5,6] was eliminated. They presented a correlation for non-standard geometries in a modified generalised form which also accounts for changes in the liquid level (see table 2.1 equations (7) and (8)). The exponent of the viscosity ratio was 0.24 which agrees with that given by Uhl [4].

Strek [13] studied heat transfer to a jacketed, baffled, turbine agitated vessel under steady state conditions, which were achieved by continuous flow of the process fluid (water). He assumed the values of the exponents on both the Reynolds number and viscosity ratio from Chilton's correlation, and obtained the final correlation graphically (table 2.1 equations (9) and (10)). Strek investigated for the first time the effect of impeller geometry (i.e. influence of the impeller/tank diameter ratio "D/D_T" and the ratio of height of the impeller above the vessel base to the tank diameter "H_A/D_T") on the film heat transfer coefficient. The non-standard geometrical correlation of Chapman et al [14] is not strictly comparable with the generalised equation of Strek [13], as Strek investigated the effect of impeller geometry whereas Chapman et al studied the influence of the variation of liquid height.

Nagata et al [10] present a comprehensive correlation for both turbine and paddle impellers incorporating many geometrical parameters, and in addition also include the effect of multiple impellers, of width "w" each, on heat transfer for jacketed vessel (see table 2.1 equations (11) and (12)). It is assumed that an i-stage multiple impeller is equivalent to a single impeller of width "i x w" located at a height corresponding to the average position (of the "i" positions) on the shaft. This assumption draws it's rationale from the work of Richards [15] according to which the minimum impeller distance at which each impeller, of any type, behaves independently is equivalent to 1.5 times the impeller diameter; so the impeller distance in these experiments was less than 1.5 times the impeller diameter.

Nagata et al [10] recognised that, while the Reynolds number characterises the fluid motion at the impeller tip, the rate of heat transfer to/from the wall is controlled by the boundary layer at the wall, thus suggesting that an equation that would not be affected by the physical dimensions of the equipment could be derived using a Reynolds number corresponding to the velocity adjacent to the wall (V_t).

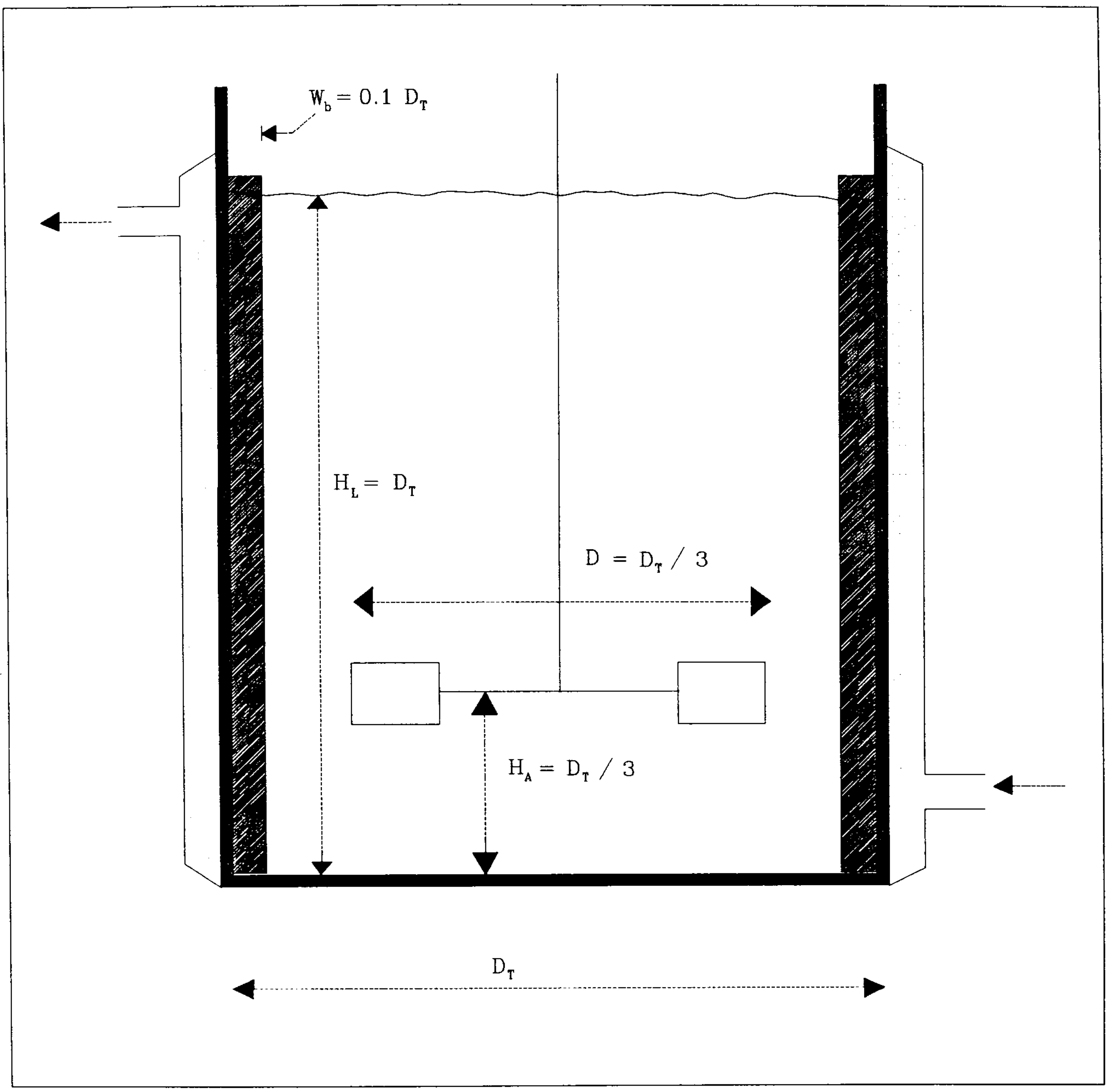

Figure 2.1 : Standard Vessel Configuration

Using Yamamoto's [16] data for unbaffled tanks, the following equation was derived to express the primary mean circulation velocity adjacent to the wall of a vessel as generated by paddle or turbine agitators.

$$V_t = 0.802\, \pi\, N\, D\, (D/D_T)^{0.80}\, (w/D_T)^{0.186}\, (n_p)^{0.162} \qquad (2.14)$$

Zlokarnik [17] studied heat transfer to the jacketed wall of an anchor stirred tank over a wide range of Reynolds number ($1<Re<10^5$). The relationship obtained graphically between Nu, Re and Pr, valid over the whole range of Re values investigated, was described in the form:

$$Nu = 0.274\, (Re\, Pr^{1/3} + 4000)^{2/3}\, Vi^{0.04} \qquad (2.15)$$

This correlation therefore suggests that the influence of Re and Pr on Nu is pronounced only in the region of $Re>10^3$, i.e. when the thermal and hydrodynamic boundary layers are developed. On the other hand, in the region of small Re numbers, the influence of Re on Nu is slight and the influence of Pr is no longer pronounced. Hence it follows that the customary form of presentation [Nu = fn (Re,Pr)] is best applicable in the region of $Re>10^3$.

By contrast Nagata et al [18] separately present a correlation for double helical ribbons, for which they claim that impeller geometry has little effect on heat transfer for $Re>10^3$, (see table 2.1 equations (13) and (14)). These contradictions serve to highlight the limitations of predictive methods that take inadequate account of the hydrodynamic regimes resulting from geometrical and power input variation.

2.2.1.1 Heat Transfer at Low Reynolds Number (Re<1)

Nagata et al [18] attempted a study of heat transfer at low Reynolds numbers (Re<1.0), but a major difficulty was found in determining the bulk fluid temperature, since gross thermal gradients can exist in the vessel. Their [18] results showed that at Re<1 there is only a small change in heat transfer coefficient with impeller speed. Further, they proposed that the critical speed (the speed above which temperature uniformity in the bulk of the liquid is reached) for helical ribbons is 10 rpm regardless of fluid viscosity. This unlikely proposal is opposed by the work of Edwards et al [12] at very low Reynolds numbers (Re<1.0) who indicate (as might be expected) that the critical speed varies markedly with fluid properties.

Author Ref no. & Year	D_T in m.	Type of Impeller	D in m.	Configuration and Details	Process Fluid	Vessel inserts	Re Range	Pr Range	Correlation and Remarks
Chilton Drew and Jebens [1] 1944	0.3	Flat Paddle	0.13	Standard w = 0.02	Water; 92% Glycerol	Coil Un-baffled	Not Given	286 to 258,000	$Nu_j = 0.36\ Re^{0.67}\ Pr^{0.33}\ Vi^{0.14}$ (1)
Uhl [4] 1955	0.6	i. Flat Paddle ii. 6 Flat blade turbine iii. Anchor	i. 0.36 ii. 0.30 iii. 0.59	Standard	Viscous fluids Bodied linseed oil Pennsylv-ania oil	Baffled $n_b = 4$	20 to 300	i. 20-4000 ii. 20-200 iii. 300-4000	$Nu_j = 0.415\ Re^{0.67}\ Pr^{0.33}\ Vi^{0.24}$ (2) $Nu_j = 0.535\ Re^{-.67}\ Pr^{0.33}\ Vi^{0.24}$ (3) $Nu_j = 0.38\ Re^{0.67}\ Pr^{0.33}\ Vi^{0.18}$ (4)
Cumming and West [8] 1950	0.76	Turbine six flat blades	0.31	$D/D_T = 1/2.5$ $H_A/H_L = 1/3$	Water, toulene, isopropa-nol, ethylene glycol, glycerine	Un-baffled coil	$1.53 * 10^3$ to $7.7 * 10^5$	2.0 to $1.2 * 10^3$	$Nu_j = 0.40\ Re^{0.67}\ Pr^{0.33}\ Vi^{0.14}$ (5)
Brooks and Sue [5] 1959	0.52	Turbine six flat blade	0.15	Standard $H_B/H_L = 0.286$ $L/w = 1.20$	Water, Oils:SAE no. 30 no. 50, Corn syrup	Un-baffled and Baffled both	30 to $5 * 10^5$	Not given	$Nu_j = k\ Re^{2/3}\ Pr^{1/3}\ Vi^{0.14}$ k = 0.54 for unbaffled k = 0.74 for baffled (6)

Table 2.1: Process side heat transfer correlations for jacketed vessels - Newtonian fluid

Chapman Holland and Dallenbach [14] 1964	0.30 0.38 0.46 0.69	Turbine six flat blade	$D_T/3$	i. Standard ii. Non standard H_L/D_T varies 1.0 to 0.666 H_A/D_T varies 0.33 to 0.083	Newtonian oils: SAE no. 20/20 lub oil SAE no. 50/50 lub oil Castor oil	Baffled $n_b = 4$	2 * 10 to 4* 10^4	Not given	i. Standard configuration $Nu_i = 0.76\ Re^{0.66} Pr^{0.33}\ Vi^{0.24}$ (7) ii. Non standard configuration $Nu_i = 1.15\ Re^{0.65}\ Pr^{0.33}\ Vi^{0.24}$ $(H_L/D_T)^{-.056}\ (H_A/D_T)^{0.4}$ (8)
Balakrishna and Murthy [20] 1980	0.3	Standard Rushton turbine	0.1	Standard	97%, 70% and 30% Glycerol	Baffled $n_b = 4$	Not given	Not given	i. Heat tr. above the impeller plant $h_1\ L_1/k_T = 0.664\ (UL_1\rho/\mu)^{0.5} Pr^{0.33} Vi^{0.14}$ (20) ii. Heat Tr. below the impeller plane $h_2 L_2/k_T = 0.664\ (UL_2\rho/\mu)^{0.5} Pr^{0.14}$ (21)
Nagate [18] 1972	0.3	Double bladed Helical ribbon	0.28	p/D=1 Clearance between impeller tip and wall = 0.033	Viscous Newtonian (Not specified)	Baffled	i. 1-1000 ii. 10^3-10^5	Not given	i. $Nu_i = 4.2\ Re^{1/2} Pr^{1/3} Vi^{0.14}$ (13) ii. $Nu_i = 0.42\ Re^{2/3}\ Pr^{1/3} Vi^{0.14}$ (14)
Ackley [13] 1960	Not given	i. 3-flat blade turbine ii. Propeller	-	-	-	Baffled	-		i. $Nu_i = 0.33\ Re^{0.67} Pr^{1/3} Vi^{0.14}$ (55) ii. $Nu_i = 0.078\ Re^{0.62} Pr^{1/3} Vi^{0.14}$ (56)
Rao and Murti [37] 1973	0.23 and 0.70	6 flat blade turbine	.075 and .233 resp	Standard	2 phase air-water air-transform oil	Unbaffled coil	Not given	Not given	$Nu_i = 1.35\ (Re^*)^{0.59} Pr^{0.33}\ Vi^{0.14}\ Fr^{-.1}$ where $Re^* = D\rho/\mu(DN+V_s)$ (22)

Table 2.1: Process side heat transfer correlations for jacketed vessel - Newtonian fluid

Nagata, Nishikawa Takimoto Kida and Kayama [10] 1972	0.3 0.2	a. Flat blade paddle b. pitched paddle c. Flat blade turbine d. disk turbine e. Rushton turbine f. pitched blade turbine		Various types and sizes	Water, Glycerin	A. Un-baffled i. with cooling coil ii. without cooling coil B. Baffled	Re > 100	2 to 2000	A) $Nu_i = k\,Re^{2/3} Pr^{1/3} Vi^{0.14} (\Sigma w_i/D_T)^{0.15}$ $(n_p)^{0.15} (\Sigma c_i/iH_L)^{0.15} (\sin\theta)^{0.5}$ (11) i) $k = 0.51$: ii) $k = 0.54$ B) $Nu_i = 1.40\,Re^{2/3} Pr^{1/3} Vi^{0.14} (D/D_T)^{-0.3}$ $(\Sigma w_i/D_T)^{0.45} (n_p)^{0.2} (\Sigma c_i/iH_L)^{0.2}$ $(\sin\theta)^{0.5} (H_L/D_T)^{-0.6}$ (12) Heat transfer coefficient is independent of the presence of a coil.
Strek [13] 1963	0.3	Turbine six flat blade	.050 .075 .100 .125 .150 .175 .200 .225 .250	i) Standard ii) Non-standard	Water	Baffled $n_b = 4$	$5*10^4$ to $8.5*10^5$	Not given	i) Standard Configuration $Nu_i = 0.76\,Re^{0.66} Pr^{0.33} Vi^{0.14}$ (9) ii) Non standard configuration $Nu_i = 1.01\,Re^{0.66} Pr^{0.33} Vi^{0.14}$ (10) $(H_A/D_T)^{0.12} (D/D_T)^{0.13}$

Table 2.1: Process side heat transfer correlations for jacketed vessel - Newtonian fluid

Zlokarnik [21] 1969	0.4	Four geometrically similar anchor	0.40 .392 .377 .374	$D_T/D = 1.0$, 1.02 1.06, 1.07	8 diff. Newtonian liquids Water, Sugar syrup	-	1 to 10^5	Not given	$Nu_i = 0.274\ (Re\ Pr^{1/3} + 4000)^{2/3}\ Vi^{0.04}$ (2.15)
Akse [19] 1967	0.13	3-geometrically similar Rushton turbine	.086 .026 .043	$H_A/D_T = 1/3$ $H_L/D_T = 1$	Water	Baffled $n_b = 4$	10^5 to $7*10^5$	Not given	$Nu_{iav}.\ 0.54\ Re^{0.68}Pr^{0.33}Vi^{0.14}\ (x/D_T)^{0.33}$ (15) $Nu_{iav.}$ is average heat transfer
Man, Edward and Polley [22] 1984	0.3	A) Standard Rushton turbine B) Propeller	0.1	Standard	Electrolyte solution (NaoH)	Baffled $n_b = 4$ Coil	Around 10^4	5.88 to 7.5	A1) For upper portion of impeller plane: x/D_T varies from 0.054 to .67 $Nu_i = 0.4\ Re^{0.68}\ Pr^{0.33}\ (x/D_T)^{-0.33}$ (16) A2) For lower portion of impeller plane: x/D_T varies from 0.06 to 0.28 $Nu_i = 0.76\ Re^{0.667}\ Pr^{0.33}\ (x/D_T)^{-0.06}$ (17) B) x/D_T varies from 0.053 to 1.0 $Nu_i = 0.4\ Re^{0.667}\ Pr^{0.33}\ (x/D_T)^{-0.33}$ (18)
Bourne, Dossenbach and Post [21] 1985	.158	Standard Rushton turbine	.051	$D/D_T = 0.32$ $H_L/D_T = 2.2$	Electrolyte soln. (Pot. feri and ferrocyanide)	Baffled $n_b = 4$	8 to 46,000	6 to 30,000	$Nu_{iav.} = 0.42\ Re^{0.694}\ Pr^{1/3}$ (19)

Table 2.1: Process side heat transfer correlations for jacketed vessel - Newtonian fluid

2.2.1.2 Local Heat Transfer

Heat transfer rates are essentially local phenomena since they are influenced by local hydrodynamics. Akse et al [19] were the first to investigate the concept of "the local heat transfer coefficient" at the wall of a jacketed, baffled, turbine agitated vessel. The coefficient of heat transfer depends on the fluid velocity near the vessel wall and the fluid velocity in an agitated vessel varies from point to point. Therefore the coefficient of heat transfer, and thus the wall temperature, will vary along this wall. Significantly, they used a heat flux meter for the measurement of the local heat transfer coefficient. They tried to incorporate flow pattern studies in order to examine the local variation of heat transfer coefficient. They concluded that the local heat transfer resistances appear to depend upon the vertical distance from the measuring point to the plane in which the agitator is rotating and this was later confirmed and expanded upon by Balakrishna et al [20], Bourne et al [21], and Man et al [22]. Akse et al reported a correlation for average heat transfer at the vessel wall while the term "X/D_T" incorporates the local vertical variations (see table 2.1 equation (15)).

Man et al [22] used an electrochemical technique to measure local variations in mass transfer coefficient to the wall of a vessel agitated by a Rushton turbine. By using the Chilton and Colburn analogy [23] the mass transfer results were converted into heat transfer data (see table 2.1, equations (16) to (18)). The diffusion controlled electrochemical technique has been widely used for the study of mass transfer in liquid phases, and Mizushina [24] has given a thorough review of the method and its applications. The electrochemical system used in the study was the reduction of potassium ferricyanide to potassium ferrocyanide, the application of which has been discussed by Smith [25]. It was observed [22] that the heat transfer coefficients at both the wall and the coil surface change significantly in the axial direction. They are highest in the plane of the impeller and fall away as one moves above and below this plane. The shape of this profile can be explained by the flow pattern. They proposed two correlations; one for the upper portion above the impeller plane, and the other for the lower portion, due to the difference in the flow profile geometry.

Bourne et al [21] also proposed a correlation for the average heat transfer coefficient based on data obtained using the electrochemical method (see table 2.1 equation (19)). Like Akse they confirmed that angular variations in heat transfer rate along the vessel wall seldom exceed 2% of their mean value, this has also been confirmed by a recent study by Fasano et al [26]. On the other hand the vertical variation can be nearly one order of magnitude in deep tanks. Bourne et al [21] studied and measured such vertical profiles for various liquid heights and for one and two Rushton turbines. In the experiment the average mass transfer coefficient, calculated for the whole wall surface, was evaluated and it agreed to within 1% with the measured average heat transfer coefficient. They [21] also observed that by increasing the liquid depth H_L/D_T to 2 from 1 the total heat flux could be increased by about 40% with no rise in turbine power consumption and that the addition of a second turbine nearly doubles the power consumed, whilst raising the heat flux by only about 30%. They also suggested that the use of a dished base compared to a flat base offers a useful contribution to the total heat flux.

Balakrishna and Murthy [20], using Nagata's and Strek's observations, made an attempt to derive a model for heat transfer in a turbine agitated vessel from theoretical principles based on the established flow pattern (see table 2.1 equations (20) and (21)). Nagata [27] had reported that in the case of turbines the liquid is jetted out by the impeller in the radial direction normal to the vessel wall. At the wall this flow is broken up near the stagnation point. One portion joins an eddy flow near the stagnation point, the second portion flows upward along the wall and the third downwards. At the top and bottom of the vessel these streams mix with the bulk of the liquid instantaneously.

Beyond a critical impeller speed for the given scale/geometry examined the bulk temperature is uniform, due to homogeneous mixing [28]. In a heat transfer situation where the wall temperature is constant at T_w and the bulk temperature is T_b the temperature drop T_w-T_b occurs in the layer near the wall. Under these circumstances the average temperature of the fluid flowing inside the boundary layer near the wall T_B would be greater than the bulk temperature T_b at any instant. Therefore, when the fluid flowing in the boundary layers mixes with the bulk at the top and bottom of the vessel, it contributes to the transfer of heat from the wall to the liquid bulk in addition to the transfer occurring across the layer due to convection and conduction. This particular contribution to heat transfer by boundary layer mixing has not been considered so far independently in the prediction of heat transfer coefficients from theory.

Balakrishna and Murthy [20] conducted their experiments under unsteady state conditions for which a heat balance could be written as:

[Rate of heat input into the liquid bulk by
transfer across the layer near the wall]
+
[Rate of heat input into the liquid bulk by transfer
due to mixing of the boundary layer with the bulk]

= [Rate of accumulation of heat in the liquid bulk, $\rho c_p V_L dT_b/dt$] (2.16)

An expression for the rate of heat transfer across the layer is obtained by considering the sections of the wall above and below the stagnation point to be two different flat plates. The flow over these plates is considered to be similar to the flow of a laminar boundary layer over a flat plate with flow at zero incidence. The expression for average heat transfer coefficient in the case of the laminar boundary layer over a parallel plate, given by Schlichting [29], has been used to obtain an expression for two different plates, one above and the other below the impeller plane (h_1 and h_2 respectively). Then the rate of heat transfer across the layer can be written as,

$$h_1 A_1(T_w-T_b)+ h_2 A_2 (T_w-T_b) \qquad (2.17)$$

An expression for the heat transfer due to mixing of the boundary layer with the bulk can be written as,

$$Q_{BL} \rho c_p (T_B-T_b) \qquad (2.18)$$

To obtain an expression for T_B at the top and bottom of the vessel the Blasius' solution for heat transfer across the laminar layer over a flat plate with flow at zero incidence is utilised. The expression for the temperature T_B in the boundary layer is then given by [30],

$$T_B - T_b = 3/8 (T_w - T_b) \qquad (2.19)$$

Substitution in equation (2.16) then gives :

$$\rho c_p V dT_b/dt = (h_1 A_1 + h_2 A_2 + 3/8 Q_{BL} \rho c_p) (T_w - T_b) \qquad (2.20)$$

The term $3/8 Q_{BL} \rho c_p (T_w - T_b)$ represents the contribution to the rate of heat transfer due to mixing of the boundary layer with the bulk. The flow rate of the liquid inside the boundary Q_{BL} would be a fraction of the total discharge flow rate Q_t, given by

$$Q_{BL} = F.Q_t \qquad (2.21)$$

where F is a proportionality constant.

Reviewing the work on local heat transfer it can be concluded that while many [19,20,21 and 22] have observed that heat transfer is affected by the flow pattern, and that the heat transfer coefficient varies only vertically, nonetheless no single correlation emerges due to the uniqueness of the geometries and different experimental methods. Akse et al [19] and Bourne et al [21] propose an average heat transfer coefficient, while Man et al [22] present two different correlations for upper and lower regions above and below the impeller respectively, while Balakrishna and Murthy [20] incorporate the two into one overall correlation, including the boundary layer mixing.

2.2.2 Heat transfer in gassed Newtonian fluids

Many chemical and biochemical processes require the processing of two phase gas-liquid mixtures in agitated vessels. Therefore, a knowledge of the effect of a gas phase on the rate of heat transfer in a jacketed vessel is of importance. Measurements of heat transfer to gas-liquid systems without a mechanically driven stirrer - i.e., bubbling beds, have been made by Kolbel and Siemens [31], Kast [32 and 33], Fair [34], Konsetova [35], and Lehrer [36], but little satisfactory work is available at present on the rate of heat transfer to or from two-phase gas-liquid systems in a mechanically agitated vessel.

Rao and Murti [37] were the first to investigate heat transfer in mechanically agitated gas-liquid systems (see table 2.1 equation (22)). They conducted steady state experiments in a jacketed unbaffled vessel agitated by a six (flat) bladed disk turbine. Heating was provided by condensing steam in the vessel jacket and cooling of the tank fluid was achieved by circulating water in the helical coils. They extended the single-phase heat transfer correlation of Rushton et al [38] to two phase gas-liquid heat transfer, by introducing the Froude number and modifying the Reynolds number.

The results of Rao and Murti's work show that sparging of a gas into an agitated liquid improves the heat transfer coefficient at any impeller speed for any vessel process liquid, mainly because rising bubbles create circulatory currents in the liquid near the transfer surface in addition to those created by the rotating impeller. The intensity of the existing turbulence is thus enhanced by the presence of rising bubbles. To accommodate this Rao and Murti replaced the velocity term in the Reynolds number by "$DN+4V_S$ ", introducing the superficial gas velocity term, V_S. However, the increase in turbulence cannot be in proportion to the gas velocity but depends upon the value of the intensity of turbulence which exists as a result of the rotating impeller.

Thus, at higher impeller speeds, the intensity is already high, and sparging of gas marginally enhances its value; therefore, the improvement in heat transfer coefficient is rather small. It is to be expected that increased velocities tend to increase the heat transfer rate up to a value beyond which the rate should fall because of the gas blanketing of the heat transfer surfaces.

2.2.2.1 Local Heat Transfer

Strek and Karcz [39] studied the local heat transfer using one and two standard Rushton turbine agitated gas liquid systems in a 0.3m diameter baffled vessel. The fluids investigated were distilled water, an aqueous solution of Na_2SO_4 and glycerol with air. The measurements of the local heat transfer coefficients at the wall of the stirred tank were carried out by means of a heat flux meter. The local values of the heat transfer coefficient "h_j" were calculated on the basis of directly measured local values of the heat flux per unit area, Q_f, and the temperature difference, Δt, between the wall and the bulk liquid.

$$h_j = Q_f / \Delta t \qquad (2.22)$$

The graphical result (see figure 2.2) suggests that the greatest values of the heat transfer coefficient, at the vessel wall, occur in the plane of the impellers. This has been demonstrated widely [19,20,21 and 22] for single phase systems, and more recently it has been found to apply to two phase systems as well [39,40]. However for the two phase system the heat transfer and hydrodynamics are more complex [40]. Thus the prediction by Strek and Karcz [39] for two phase systems can only be applied in the hydrodynamically completely dispersed zone, as shown in figure 2.3(c). A significant difference is observed between dispersion in the pure water and that in the salt solution. In the water air system the bubbles tend to coalesce while in the salt water-air system, according to the type and concentration of salts, the coalescence of the primarily produced gas bubbles is more or less hindered, and the local heat transfer is slightly increased with the increase in salt concentration. The result suggests that coalescence bubbles causes a decrease in heat transfer; this is possibly due to the decreased turbulence associated with the reduction in total bubble surface area consequent upon coalescence occurring. The heat transfer coefficient in glycerol is the least.

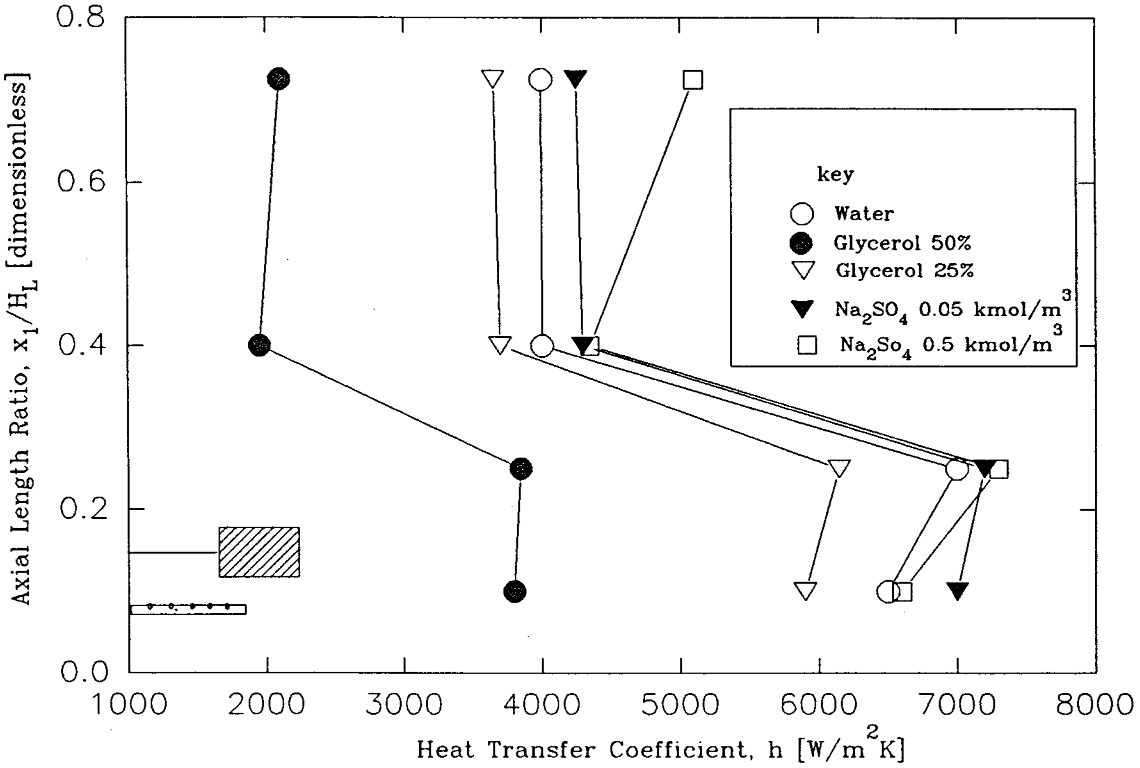

(a) One Disk Turbine

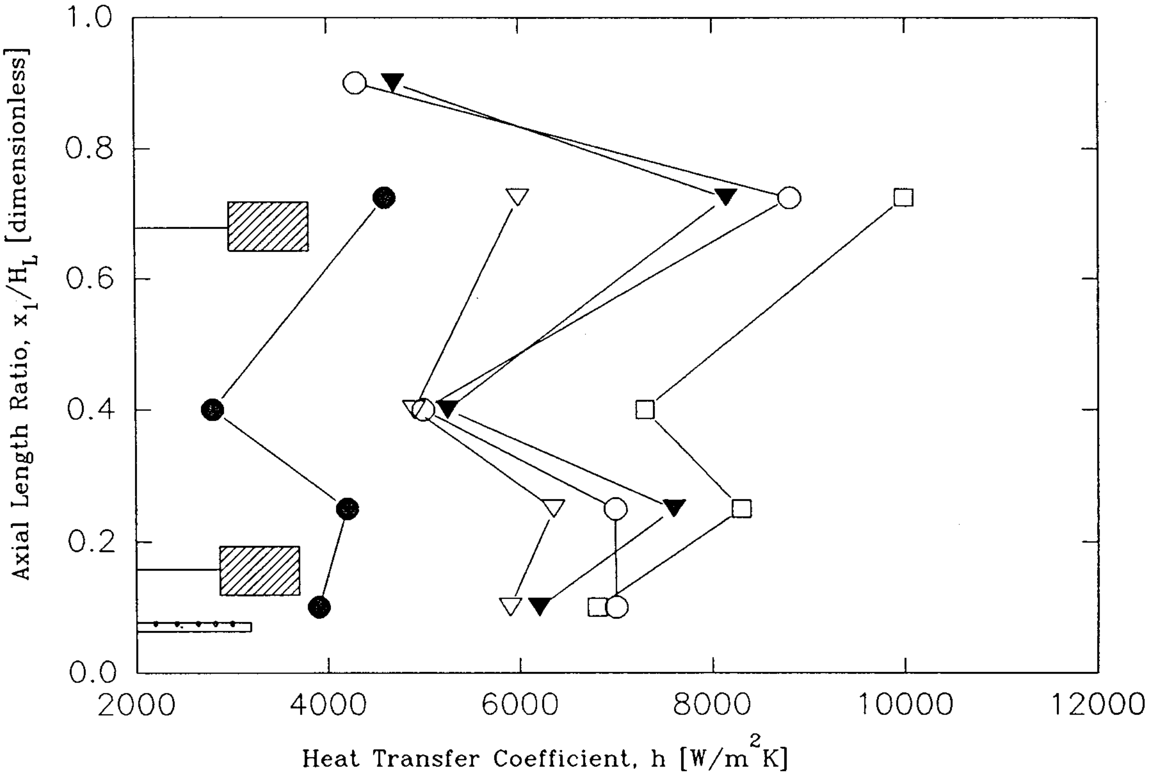

(b) Two Disk Turbine

Figure 2.2 : Local Heat Transfer Coefficient Distribution in Air-Liquid System [39]

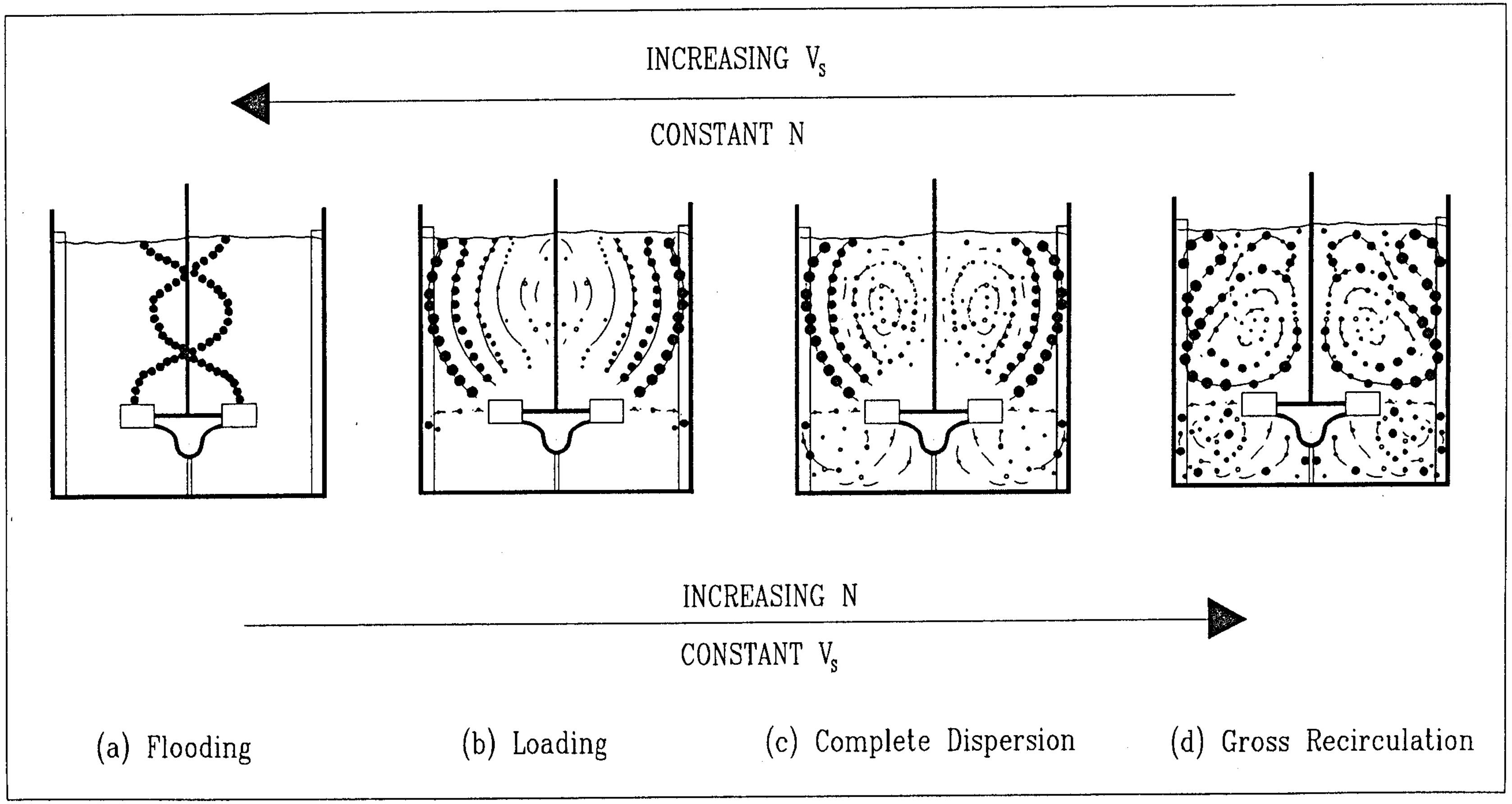

(a) Flooding (b) Loading (c) Complete Dispersion (d) Gross Recirculation

Figure 2.3 : Different Hydrodynamic Zones

Recently Karcz et al [41] extended the above study to two impellers (standard Rushton) in a distilled water - air system ($D/D_T = 0.3$, $H_L = 2D_T$, $H_{A1} = D_T/3$, $H_{A2} = 4D_T/3$) to obtain a new correlation.

$$Nu = 0.76\ Re^{0.67}\ Pr^{0.33}\ Vi^{0.14}\ e^{-40.65\ Fr^{0.5}} \tag{2.23}$$

This correlation is valid in the following range: $0<Fr<9 \times 10^{-6}$ and $5 \times 10^4 <Re<10^5$. Exponents for the Prandtl number and Viscosity ratio were assumed on the base of the literature. The analysis of the equation suggests that the mean heat transfer coefficient for gas-liquid system decreases approximately 12% in comparison with that for the liquid phase. This finding however is in contradiction with that of Rao and Murti [37] and De Maerteleire [42] according to whom, in comparison with a single phase system the value of the local heat transfer coefficient increases in a two phase (dispersed) system.

Man [40] extended the local heat transfer study to aerated conditions for the same system [22]. The experimental data indicated that the profile of local heat transfer coefficient at the vessel wall depends on the gas flow rate and the impeller speed, as illustrated in figure 2.4, and that the heat transfer is significantly different for different hydrodynamic zones.

In the flooding zone, as in shown figure 2.4(a), the gas-liquid system behaves as a partial bubble column. At low impeller speeds (1.67-3.33 rps), below the flooding speed (N_F) at a particular gas flow rate, the profile of the vertical variation of the local heat transfer coefficient in the two phase experiment is very different from that of the single phase, and it was also observed that for the gas-liquid system the local heat transfer coefficient reduces markedly at the impeller plane, and then increases slightly as one moves up to a vertical position of $x/D_T = 0.36$. Above this position and up to the liquid surface a large increase of the local heat transfer is observed except at the lowest gas flow rate. Below the impeller plane the local heat transfer coefficient is almost constant. These phenomena can again be explained in relation to the gas-liquid flow pattern. At the plane of the impeller a gas blanket exists forming a cavern around the impeller causing a reduction in the power drawn. However, above the impeller plane, the ascent of the bubbles displaces the liquid outwards producing a transverse motion aiding turbulence thus causing a larger increase of heat transfer coefficient in this region. In the region below the impeller plane, the more uniform gas distribution results in a constant heat transfer coefficient. This heat transfer coefficient would be lower compared to that at the impeller and above it, because the presence of almost stagnant air will have the effect of reducing the rate of heat transfer. The average heat-transfer coefficients have been calculated from the local values and these results indicated that for the

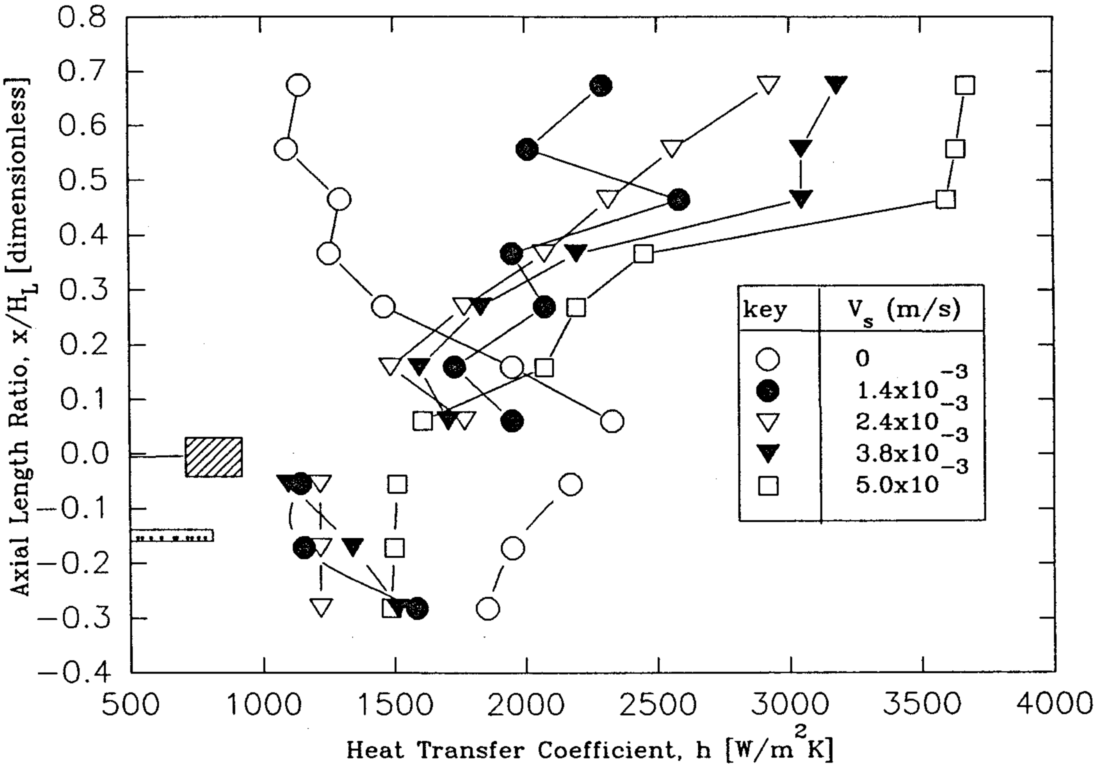

(a) Flooding Zone, N=1.67 s^{-1}

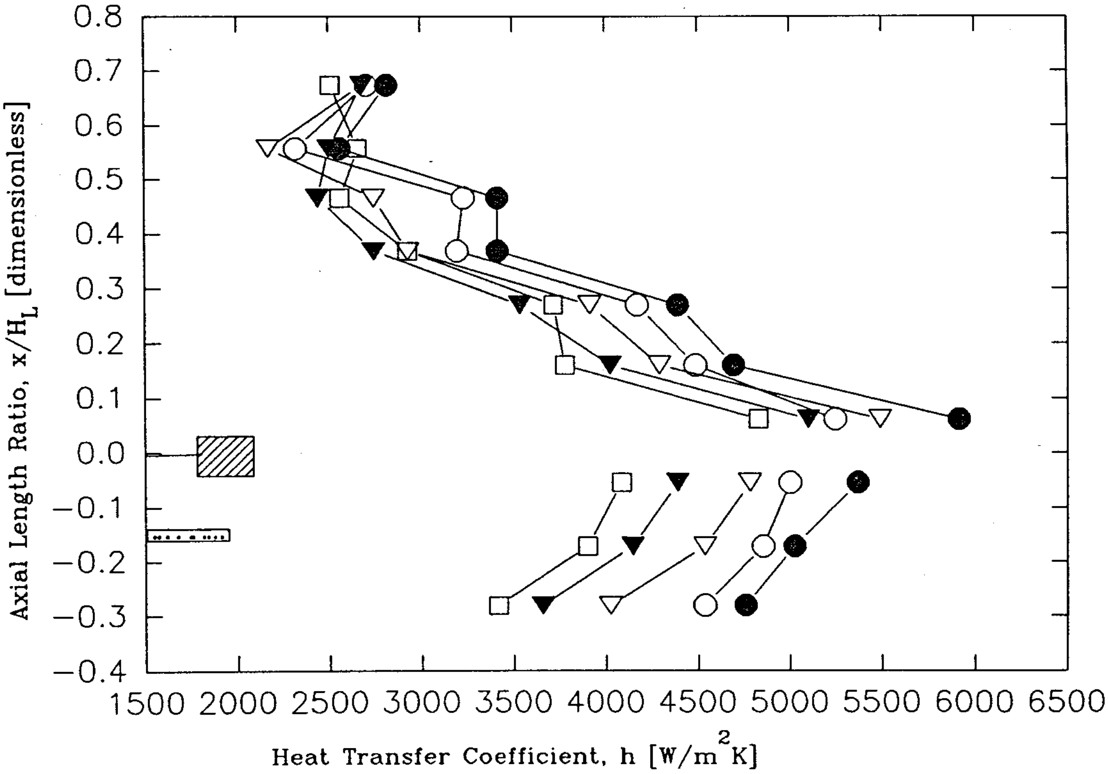

(b) Completely Dispersed Zone, N=6.67 s^{-1}

Figure 2.4 Local Heat Transfer Distribution in Air–Water System [40].

aeration conditions employed (the superficial velocity $V_s = 0.0014\text{-}0.005$ m/s) the heat transfer rates are within ±15% of the values obtained without gas addition. This work could lead to a better understanding of heat transfer and fluid dynamics, but at this stage only experimental results for h_j are presented.

2.2.3 Replacement of the Reynolds Number in Heat Transfer Correlation

Calderbank and Moo-Young [43] were the first to correlate the heat transfer coefficient using the power consumption for mixing per unit volume of liquid for immersed bodies including the coil in a mixing vessel. They proposed the following equation,

$$(h_c / c_p \rho)\, Pr^{2/3} = 0.13\, [\, (P/V_L\,) \mu / \rho^2]^{1/4} \tag{2.24}$$

However the scatter of the date is quite large in their correlation.

Sano et al [44] studied heat transfer at the wall of two geometrically similar vessels (diameter: 0.1 m and 0.19 m). The vessels were heated electrically by means of nichrome wire wound around the outside of the vessel. The experiments were carried out under steady state conditions using a cooling coil to remove the heat. The local heat transfer coefficients along the vertical plane were also studied. The test liquids were water and aqueous solutions of glycerol at various concentrations, for which the viscosity varied from 0.55 - 8.5 mPa s. The impellers used were paddle and turbine.

The mean heat transfer coefficients were correlated by a dimensionless group, $\varepsilon D^4/\nu^3$, obtained by dimensional analysis, which represents flow behaviour; this then replaces the Reynolds number. Assuming that a characteristic velocity "u" in geometrically similar mixing vessels can be expressed in terms of a characteristic length "L_c ", an average value of the power consumption per unit mass of liquid "ε", and the physical properties, viscosity "μ", and density "ρ", then the following equation may be formulated.

$$u = K_c\, L_c\, {}^{a} \rho^{b} \mu^{c} \varepsilon^{d} \tag{2.25}$$

where K is a constant and a, b, c and d are exponents of the corresponding parameters.

According to dimensional analysis, the Reynolds number based on "u" and "l" can be expressed by the following equation:

$$[(u L_c \rho)/\mu] = k_1 [(\varepsilon L_c^4)/\nu^3]^d \qquad (2.26)$$

where k_1 is a constant.

When geometrical similarity of the vessel is not satisfied , k_1 will contain parameters involving the shape of the vessel and type and dimension of the impeller. The diameter, D_T, is adopted as the characteristic length for the correlation of the heat transfer coefficients to the side wall. Then the correlation which results is in the form :

$$Nu = fn\ [(\varepsilon D^4/\nu^3), \text{dimensionless geometrical parameters}]\ Pr^{1/3} \qquad (2.27)$$

The relationship between $\varepsilon D^4/\nu^3$ and the conventional Reynolds number based on the impeller diameter and impeller tip velocity, is

$$\varepsilon D_T^4/\nu^3 = 4/\pi\ (D_T/D)\ (D_T/H_L)\ P\ (D^2 N\rho/\mu)^3 \qquad (2.28)$$

The correlation Sano et al [44] presented is;

$$h_j D_T/K_T = 0.512\ (\varepsilon D^4/\nu^3)^{0.227} Pr^{1/3}\ (D/D_T)^{0.52}\ (w/D_T)^{0.08} \qquad (2.29)$$

They assumed the exponent of the Prandtl number to be "1/3". This correlation is applicable over a wide range of impeller conditions, irrespective of whether the vessel is baffled or not.

2.2.4 Review of the viscosity correction factor

There is some disagreement in the literature on the exact value of the exponent of the viscosity ratio, "c". Uhl [4] gave a range for the viscosity ratio exponent from 0.18 to 0.24 depending on the type of impeller and system geometry, for a wide range of viscosities. He also reanalysed the data of Chilton et al [1] and estimated that a value of 0.21 for the exponent "c" would give a better fit to their data. In the correlation presented by De Maerteleire [42], the exponent on the viscosity ratio is 0.2 . Kraussold [3] found that the heat transfer characteristics for cooling and heating in stirred tanks with blade, bar and disc stirrers can be correlated well with the use of the exponent 0.14. Chapman et al [14] reported the value of the exponent as 0.24. These values are all higher than the commonly reported value of 0.14 as originally obtained by Sieder and Tate [2] for heat transfer in pipe flow. Hrunby [45] conducted for the first time a series of experiments for the determination of the function "c = fn (1/Vi)" within the limits

$0.32 < 1/Vi < 320$, that is, during cooling operation. The results indicate that, generally, the exponent "c" increases when the viscosity ratio decreases. He suggested that the explicit function expressing the relationship between the temperature and the viscosities will be an Arrhenius type equation as suggested by de Guzman and Antrade [46 and 47].

$$\mu = A_t \exp (E/RT) \qquad (2.30)$$

where "E" is the activation energy of the laminar flow according to Eyring [48]. Although this relationship is quite satisfactory within rather narrow temperature limits, for wider temperature limits the activation energy is no longer strictly constant.

2.3 *Heat transfer to non-Newtonian fluids*

2.3.1 Single Phase Heat Transfer

Krishnan and Pandya [49] were the first to study heat transfer to non-Newtonian fluids using a 0.51m diameter jacketed vessel using an anchor agitator under steady state conditions (heating by jacket and cooling by coil). The pseudoplastic fluids used were carboxymethyl cellulose (1%, 2% and 3%), polyvinyl alcohol (8%) and calcium carbonate (15%) suspension in glycerol. They [49] felt that the existing relationships for Newtonian fluids in agitated vessels were not applicable for distinctly non-Newtonian fluids due to the fact that the velocity and the temperature gradients at the wall were different because of different degrees of orientation and collision of molecules and particles as they have completely different rheology and other thermophysical properties. Theoretical considerations on the basis of a power law model [50,51] show that the velocity gradient at the wall of a tube for a non-Newtonian fluid differs from that of a Newtonian fluid by a factor;

$$\delta = 3n+1/4n \qquad (2.31)$$

where n is the flow behaviour index and δ is the ratio of non-Newtonian to Newtonian shear rate which then gives the ratio of non-Newtonian to Newtonian heat transfer rates in a given system.

The result shows that, for a power law fluid, the Nusselt number is a function of "δ" and the generalised forms of Reynolds number, Prandtl number and consistency ratio "K/K_w". On the assumption that "n" is constant with temperature, the viscosity ratio then becomes:

$$Vi = K/K_w \tag{2.32}$$

The study provides for the first time generalised relationships for jacket heat transfer in anchor agitated vessels applicable to Newtonian as well as pseudoplastic non-Newtonian fluids over wide ranges of variables, which also includes a ratio of non-Newtonian to Newtonian shear rates "δ", (see table 2.2 equation (1)).

Heat transfer to non-Newtonian pseudoplastic fluids in jacketed agitated vessels was studied experimentally by Sandall and Patel [52] for two types of impellers, a Rushton turbine and an anchor agitator. The data was correlated based on the use of an apparent viscosity in the expressions for the generalised Reynolds and Prandtl numbers (see Table 2.2 equations (2) and (3)). The apparent viscosity was determined by application of the relationship between impeller speed and the average shear rate existing in the vessel as proposed by previous investigators in correlating power consumption data for the agitation of pseudoplastic fluids [49].

Carreau et al [53] studied heat transfer in 0.76 m diameter baffled jacketed vessel using a 4 blade 45° pitched turbine. They worked with CMC solution (0.67%, 1.00% and 1.5%) and carboxy polymethylene (carbopol 934, 0.2%, 0.3% and 1.5%). The liquid film coefficient h_j was calculated from the overall coefficient U using a modification of Wilson's graphical method.

They correlated the Nusselt number with the generalised Reynolds number. For a generalised Reynolds number range from 100 to 5000 it is possible to predict the heat transfer coefficient for pseudoplastic liquids with an accuracy of 85% or better. For Prandtl number, in order to obtain similarity between present correlations and those found for Newtonian liquids, the exponent of 1/3 was taken for the Prandtl number as a fair value. However the main problem lies in determining the rheological behaviour. Aqueous solutions of CMC and carbopol were assumed to be ideal models of the power law; however the shear diagram shows clearly important deviations. The use of a more appropriate mathematical model (3-parameter model) could probably lead to better correlations.

The equations [53] found are of the same form as those established by previous workers for Newtonian liquids (see table 2.2 equation (4)). However, the values of the constant k (3.41 for heating and 1.43 for cooling) are much higher for pseudoplastic liquids than for Newtonian fluids. This discrepancy arises from the fact that the Reynolds number is not a perfect criterion of agitation for Newtonian fluids and even less so for non-Newtonian. The impeller size and position with regard to the vessel dimensions are of prime importance due to the behaviour of these liquids.

Author Ref no. & Year	D_T in m.	Type of Impeller	D in m.	Configuration and Details	Process Fluid	Vessel inserts	Re Range	Pr Range	Correlation and Remarks
Krishnan and Pandya [49] 1966	0.51	Anchor	0.38	$H_L = 0.25$ m n from 0.66 to 1.0	CMC soln. Polyvinyl alcohol (8%) Calcium carbonate (15%) suspension in gly.	Un-baffled coil	100 to 5.5* 10^5	2.5 to 4950	$Nu_j = 0.63\ Re_g^{0.67}\ Pr_g^{0.3}\ (k/k_w)^{0.18}$ (1)
Heinlein and Sandall [59] 1972	0.18	Anchor	.178 .167	$H_L = 0.184$ m n = 0.211 to 0.542	Aqueous carbopol solution	Un-baffled	12 to 300	868 to 9340	$Nu_j = 0.6\ Re_g^{1/2}\ Pr_g^{1/3}\ (k/k_w)^{0.18}$ (6)
Sandall and Patel [52] 1970	.183 0.3	a) Rushton turbine b) Anchor	a) .064 b) .180	Standard Configuration n = 0.3 to 0.9	Aqueous carbopol -934 soln 0.5%, 0.6% 0.75%, 1%	a) Baffled $n_b = 4$ b) Un-baffled	a) 80 to 93000 b) 320 to 89600	a) 2.1 to 644 b) 2.1 to 644	a) $Nu_j = 0.482\ Re_g^{2/3} Pr_g^{1/3}\ (k/k_w)^{0.12}$ (2) b) $Nu_j = 0.315\ Re_g^{2/3}\ Pr_g^{1/3}\ (k/k_w)^{0.12}$ (3)

Table 2.2: Process side heat transfer correlations for jacketed vessel - non-Newtonian fluid

Carreau Charest and Corneille [53] 1966	0.76	4 blade 45^o pitched turbine	0.46	$D/D_T = 0.6$ $H_L/D_T = 0.83$ $H_A/D_T = 0.32$ $n = 0.343$ to 0.633	CMC: 0.67%, 1%, 1.5% Carbopol: 0.2%, 0.3% 1.5%	Baffled $n_b = 4$	100 to 5000	100 to 800	$Nu_j = 1.474\ Re_g^{0.7}\ Pr_g^{0.33}\ (\mu_d/\mu_{dw})^{0.24/n}$ (4)
Wang and Shengyao [59]	0.3	a) Rushton turbine b) Pfaulder c) MIG impeller d) Plate paddle e) Semi-elliptical impeller f) Anchors	a) .092 b) .092 c) .089 .104 .115 d) .075 .085 .107 e) .142 f) .181 .194 .213	a) Standard b) $w = 0.0184$ m $\theta = 15^o$ c) $i = 2, 3$ $n_p = 2_o$, $\theta = 30^o$ d) $i = 1$ $n_p = 2$ $w = 0.049$ m e) $w = 0.142$ m $i = 1, n = 2,$ $\theta = 45^o$ f) $w = 0.169$ m $i = 1, n_p = 2$	Aqueous CMC $n = 0.49$ to 0.92 $K = 0.02$ to 12	Baffled $n_b = 4$ coil	a) 25 - 6310 b) 25-6310 c) 200-18400 d) 40-18600 e) 40-18600 f) 7-990	50-92000	$Nu_j = k\ (Re_g{}^*)^a\ (Pr_g{}^*)^b\ (k/k_w)^c\ (D/D_T)^d$ $(\Sigma w_i \sin\theta/H_L)^e$ (5) k a b c d e a) 1.19 2/3 1/3 1/6 0 0.74 b) 1.19 2/3 1/3 1/6 0 0.74 c) 0.45 2/3 1/3 1/6 0.3 .387 d) .557 2/3 1/3 1/6 .414 0.2 e) .577 2/3 1/3 1/6 .414 0.2 f) .713 2/3 1/3 1/6 0 0

Table 2.2: Process side heat transfer correlations for jacketed vessel - non-Newtonian fluid

In their work on power requirements for laminar agitation of non-Newtonian liquids, Foresti and Liu [54] suggested that a correction factor be applied to the generalised Reynolds numbers to describe the entire system (agitator and vessel). This geometric factor,

$(H_L/H_A)^n \ [D/(D+D_T)]$

decreases with a decreasing behaviour index and the corrected Reynolds number is lower. However, the application of this correction did not improve the correlation [53].

The use of a Prandtl number with a differential viscosity at high shear rates was apparently justified by the turbulent agitation. However, with pseudoplastic liquids, the differential viscosity increases with distance from the impeller and, close to the wall, the fluids tends to be motionless [55]. By examining the correlations obtained [53], it is believed that the differential viscosity at high shear rates does not represent the true viscosimetric property of all the fluid in the vessel. A first indication that the Prandtl number is not properly evaluated is that most of the data on Carbopol are above the curves while most of data on CMC are below. It was shown on the shear diagram that the CMC behaviour is different from that of Carbopol at low shear rates. Initial work with CMC has shown that the use of differential viscosity values obtained at lower shear rates (5 to 20 sec^{-1}) leads to correlations having a constant k near that of Newtonian liquids. It is possible therefore that the apparent viscosity determined from power curves as proposed by Metzner and Otto [55] would give a better correlation when used in the Prandtl number. Such a Prandtl number would be much larger and the constant k would tend to approach that obtained for Newtonian liquids.

It seems that the clearance between the agitator and the vessel wall could affect greatly the viscosity ratio number. For larger clearances, agitation close to the wall is lower and the laminar sublayer becomes thicker, thus offering a greater resistance to heat transmission. This effect is amplified by the rheological properties of pseudoplastic liquids for which the apparent viscosity is a function of both temperature and shear rate. With these considerations, a generalised viscosity ratio has been included in the final correlation [53] in order to obtain an equation for heating and cooling data. The use of the exponent 0.24 which was found by Uhl [4] for a similar system, divided by the behaviour index "n" gives a correlation with a mean deviation of 19.3%. It is believed that a proper evaluation of velocity profiles will permit a better understanding of this viscosity ratio number and its influence on heat transmission.

Suryanarayanan et al [56] studied the jacket film heat transfer coefficient for water and for dilute aqueous polymer solutions of sodium carboxy-methyl cellulose (SCMC) and sodium alginate (SN) in a turbine agitated vessel for standard and non-standard vessel configurations with agitator diameter, depth of agitation, helix diameter and coiled tube outside diameters as parameters. The results show that the heat transfer coefficient increased with increase in depth of agitation up to a H_A/D_T ratio of 1/2, due to the good mixing conditions and elimination of vortices realised (as the agitator is taken up in the tank from the bottom).

Kai and Shengyao [57] have recently investigated MIG impellers, Rushton turbines, Pfaudler impellers, plate paddles, anchors and a semi-elliptical board impeller. They propose a new shear rate model for determining the apparent viscosity of non-Newtonian fluids (see the following section). This shear rate model can be used to correlate film coefficients in the case of various types of impeller, baffled or unbaffled, for the jacketed vessels. The experiments were carried out under steady state conditions with heating by jacket and cooling by coil.

Heat transfer correlation with Re_g^*

For power law fluids, μ_a is obtained from the new shear rate model by :

$$\mu_a = K\, 0.4^{(n-1)/n}\, N^{[2-\varnothing(2-n)](n-1)/n} \qquad (2.33)$$

The above equation can then be used to define a new generalised Reynolds number Re^* as well as other dimensionless groups:

$$Re_g^* = D^2N\rho/\mu_a = D^2N\rho\,(0.4^{(1-n)/n}\, N^{[(2-\varnothing(2-n)][(1-n)/n]})\,/\,K \qquad (2.34)$$

$$Pr_g^* = c_p\, \mu_a\,/\,K_T = [c_p\, K\, 0.4^{(n-1)/n}\, N^{[2-\varnothing(2-n)](n-1)/n]}\,/\,K_T \qquad (2.35)$$

$$\varepsilon D_T^4/\nu_a^3 = \varepsilon\, D_T^4/(\mu_a/\rho)^3 = (\varepsilon D_T^4/(K/\rho)^3)\, 0.4^{3(1-n)/n}\, N^{3[2-\varnothing(2-n)](1-n)/n} \qquad (2.36)$$

where

$$\varnothing = \text{flow regime coefficient} = e^{(-0.00705D^2N^{2-n}\rho/K)} \qquad (2.37)$$

Then the heat transfer coefficient for non-Newtonian fluids in agitated vessels can be described by either of the following two correlations:

$$Nu = k\ (Re_g^*)^a\ (Pr_g^*)^b\ (K/K_w)^c \qquad (2.38)$$

or

$$Nu = k\ (\varepsilon D_T^4/\nu_a^3)^a\ (Pr_g^*)^b \qquad (2.39)$$

The dimensionless groups D/D_T, $\Sigma w_i \sin\theta/H_L$ and D_T/H_L were introduced in order to take account of the influence of geometrical configuration on the film coefficient [57], where Σw_i is defined as the effective blade width:

$$\Sigma w_i = n_p n_n w \qquad (2.40)$$

The correlation result from regression is presented in table 2.2 equation (5).

Heat transfer correlation with Power

Kai and Shengyao [57] also investigated the relationship between heat transfer and power consumption for non-Newtonian fluids. By applying the dimensionless group $\varepsilon D_T^4/\nu_a^3$, which represents power per unit mass, film coefficients for various agitator systems have been unified to one correlation as follows:

Heat transfer from jacket to fluids;

$$h_j D_T/K_T = 0.456(\varepsilon D_T^4/\nu_a^3)^{2/9} (c_p \mu_a /K_T)^{1/3} (D/D_T)^{0.58} (\Sigma w_i \sin\theta/H_L)^{0.71} (D_T/H_L)^{-1.63} \qquad (2.41)$$

covering the following ranges of values:

$\varepsilon D_T^4/\nu_a^3 = 7.5 \times 10^3 - 3.33 \times 10^{13}$
$c_p \mu_a /K_T = 30 - 37{,}000$
$D/D_T = 0.326 - 0.924$
$w/D_T = 0.067 - 0.735$
$n_p = 2 - 6$; $n_n = 1 - 5$

Irrespective of geometrical configurations, types of impeller,, baffled or unbaffled, all film coefficients can be calculated by using equation (2.41).

The results [66] show that the dimensionless group $\varepsilon D_T^4/\nu_a^3$ is superior to the generalised Reynolds number in correlating heat transfer coefficients. Furthermore, the conventional criterion of comparing the efficiency of equipment has been based on a constant power consumption. Therefore it would be convenient to apply equation 2.41 to design industrial agitated vessels and measure heat transfer efficiency at the same time. However it is of vital importance to understand the limitation of such a correlation, it having been analytically proven [58] that for these correlations there is a strong dependence on the impeller type. This same review [58] analyses the similar correlation of Sano et al [44] for Newtonian fluids and observes that the use of such a correlation results in the same heat transfer coefficient for all the impeller types, based on equal power per unit mass. This highlights the inadequacy in such an approach because plainly it is impossible to maintain the same local hydrodynamic regime with different types of impellers, even at the same power input, and a variation in both local and overall heat transfer coefficients would be expected. Therefore such a correlation should be validated for each impeller type.

2.3.1.1 Heat transfer to non-Newtonian fluids at low Reynolds number

Heinlein and Sandall [59] studied heat transfer at low Reynolds numbers to non-Newtonian time-independent fluids in jacketed vessels. The impellers used in this work were different sized anchor agitators and the fluids used were various concentrations of aqueous carbopol solution. The correlation technique first used by Skelland and Dimmick [60] was used to correlate data obtained at low Reynolds numbers. An attempt was made to fix the exponents on the Reynolds, Prandtl, and viscosity ratio numbers at the values reported by Uhl [4]. Since the variation in the Prandtl and viscosity ratio numbers was not large in this work and also the standard deviation does not increase significantly when the exponents on these numbers are fixed, it was felt that it would be desirable to retain the Newtonian form of the correlation equation, (see Table 2.2 equation (6)).

They also studied the effect of the clearance between the wall and the anchor on the heat transfer coefficient. The rate of heat transfer decreases to a minimum with increasing clearance between the vessel wall and the anchor and then increases with further increase in clearance. This trend is similar to that observed by Uhl and Voznick [61] for anchor agitated Newtonian liquids. An explanation of this phenomenon as proposed by Uhl and Voznick which would appear also to be valid for the case of non-Newtonian fluids, is that at small clearances the rate of heat transfer decreases with increasing clearance because of the increased thickness of the laminar layer adjacent to the wall. Then, as the clearance is increased beyond a critical value, turbulence is developed between the impeller and wall resulting in increased heat transfer rates. The origin of this turbulence would be eddies originating in the wake behind the anchor. From these results it would appear that the optimum design of anchor-agitated heat transfer vessels will have a value of C_L/D_T (where C_L is the clearance between impeller and wall) greater than 0.06 since the power consumption rate increases with decreasing clearance.

Shamlou and Edwards [62], carried out steady state heat transfer experiments in 0.15 and 0.4m diameter vessels using helical ribbon impellers. The fluids used were aqueous solutions of CMC and various grades of chocolates.
The critical impeller speed required to eliminate gross temperature gradients within the bulk of the vessel has been established and has been shown to be influenced critically by agitator geometry and fluid properties.

The largest temperature gradients within the bulk of the fluid are, as observed for Newtonian fluids, in the vertical direction. The effect of fluid viscosity on the vertical temperature profile is very significant and it is seen that as impeller speed increases a sharp critical value is reached when uniformity of temperature is obtained.
Strong dependence of the critical impeller speed (or critical Reynolds number, $Re_c = \rho N_c D_T / \mu$), upon fluid properties (or Prandtl number) and impeller geometry expressed in terms of dimensionless groups, p/D_T, C_L/D_T and n_p were observed. The following equation was found to describe the data generated during the experiment and may be used to predict the onset of gross temperature stratification within the bulk of the vessel.

$$Re_c = 1.9 \times 10^4 \; Pr^{-1.3} \; (p/D_T)^{0.428} \; (C_L/D_T)^{1.26} \; (n_p)^{-1.92} \qquad (2.42)$$

This indicates that the number of impeller blades has a greater influence upon levelling out temperature variations than the impeller pitch. It therefore seems advantageous to use a ribbon having $p/D_T = 1$, $n_p = 2$ rather than $p/D = 0.5$, $n_p = 1$. The power consumption in both cases is almost the same [63] and the fabrication cost for the two impellers is also very similar [64]. This equation is also applicable to non-Newtonian, time-independent, shear thinning fluids, provided that the "average apparent viscosity", μ_a, is used in place of μ.
The results show the influence of impeller geometry on heat transfer characteristics in the laminar region ($Re<1.0$) while its effect on heat transfer in the transitional region ($10<Re<10^3$) is shown to be negligible.

2.3.2 Heat Transfer in gassed non-Newtonian fluids

When an agitated liquid is aerated by a gas via a sparger located beneath a rotating impeller, there is a marked decrease in the power consumed by the impeller. This decrease is very much greater than would be accounted for by the overall decrease in the average density of the gas/liquid mixture as shown by Calderbank [65].

Various researchers have attempted to correlate this power consumption decrease with the volumetric gas flow rate, Q_g, impeller diameter D, and its speed of rotation, N, for both aerated Newtonian and non-Newtonian liquids. The usual approach has been to plot P_g/P versus Q_g/ND^3, where P and P_g are the power inputs for the unaerated and aerated plates at the same impeller rotational speed.

Oyama and Endoh [66] and Calderbank [43] had reasonable success in correlating data for aerated Newtonian liquids using the above approach. However, Michel and Miller [67] found that their data could not be correlated using a simple plot of Q_g/ND^3 versus P_g/P when using Newtonian liquids. Instead these workers proposed the following equation:

$$P_g = C_1 \left\{ \frac{P^2 ND^3}{Q_g^{0.56}} \right\}^{0.45} \qquad (2.43)$$

Where C_1 is a dimensionless constant. A similar approach was used by Nishikawa [68] for the aeration of non-Newtonian pseudoplastic solutions.

Taguchi and Myamoto [69] observed that, when aerating pseudoplastic liquids, P_g/P when correlated with Q_g/ND^3 was shown to depend not only upon the Reynolds number but also upon the rheological properties of the fluid. Poor correlation of the results was achieved in this manner. However, the equation developed by Michel and Miller [67] was found at least to correlate the data in the turbulent region. Blakeborough and Sambamurthy [70], using a non-Newtonian paper pulp suspension, showed that the data could not be correlated as P_g/P versus Q_g when variations in impeller speeds were used.

Bruijn et al [71] using, flow visualisation methods, have shown that the power consumption of a turbine impeller rotating in an aerated vessel is entirely controlled by a gas cavity forming behind the turbine blades. The shape and size of the gas cavity depends upon the gas flow rate to the vessel. These researchers were able to establish a relationship between the size and shape of the cavities with the power consumed by the rotating impeller.
None of the workers however correlated these with the film heat transfer. This problem requires further investigation and the effect of all the independent variables should be carefully examined.

To date, Rao and Murti [42] are the only researchers to present heat transfer data in mechanically agitated aerated systems, (However, their work was only in Newtonian liquids).

2.4 *Service side heat transfer in jackets*

The heat transfer process between the vessel contents and a jacket involves three steps, convective heat transfer between the liquid in the vessel and the heat transfer surface, conduction through the heat transfer surface, and convective heat transfer between the heat transfer surface and the service fluid (fluid inside the heat transfer surfaces). The step having the lowest rate, or the lowest individual heat transfer coefficient limits the overall heat transfer rate. So far we have discussed the process side heat transfer in agitated vessels. Heat transfer is normally expected to be controlled by the process side resistance. This would be the case for the heating of a viscous liquid by the condensation of steam in a jacket when the jacket side resistance would be negligible. However, the jacket side resistance would not be negligible for the case of cooling when the process liquid is of low viscosity. The service side (Jacket) heat transfer resistance is often evaluated by the modified Wilson method, which assumes that the heat transfer coefficient is always proportional to the Reynolds number to the exponent 2/3 (see equation (2.12)), which might not always be true; therefore, it is worth evaluating the service side resistance independently. Jackets have various geometrical arrangements (see figure 2.5) ; i.e. the positions of inlet and outlet branches, presence of baffles etc., and no reliable methods for predicting accurately inside heat transfer coefficient in all geometries exist. However correlations for some standard designs are available in the literature. This section deals with the jacket side resistance.

Jacketing provides the usual method of first choice for heating and cooling process vessels on the basis of control, efficiency and product quality. It is usually adequate for small scale vessels, but it can become inadequate for large ones.

The selection of a jacket design depends on several factors:

a. **Cost.**
b. **Heat transfer requirements.**
c. **The heat transfer medium.**
d. **Pressure limitations.**
e. **Temperature limitations** : High temperatures and large differences between the vessel and jacket fluid temperature require consideration of the thermal expansion differentials between the materials of the vessel and the jacket, and the difference in thickness between the vessel and jacket walls. In some cases, special materials may be required; or the vessel and jacket may have to be made of the same material, or of materials having the same coefficients of thermal expansion, or special closures that can withstand the stresses of expansion are needed at the top and bottom of the jacket.

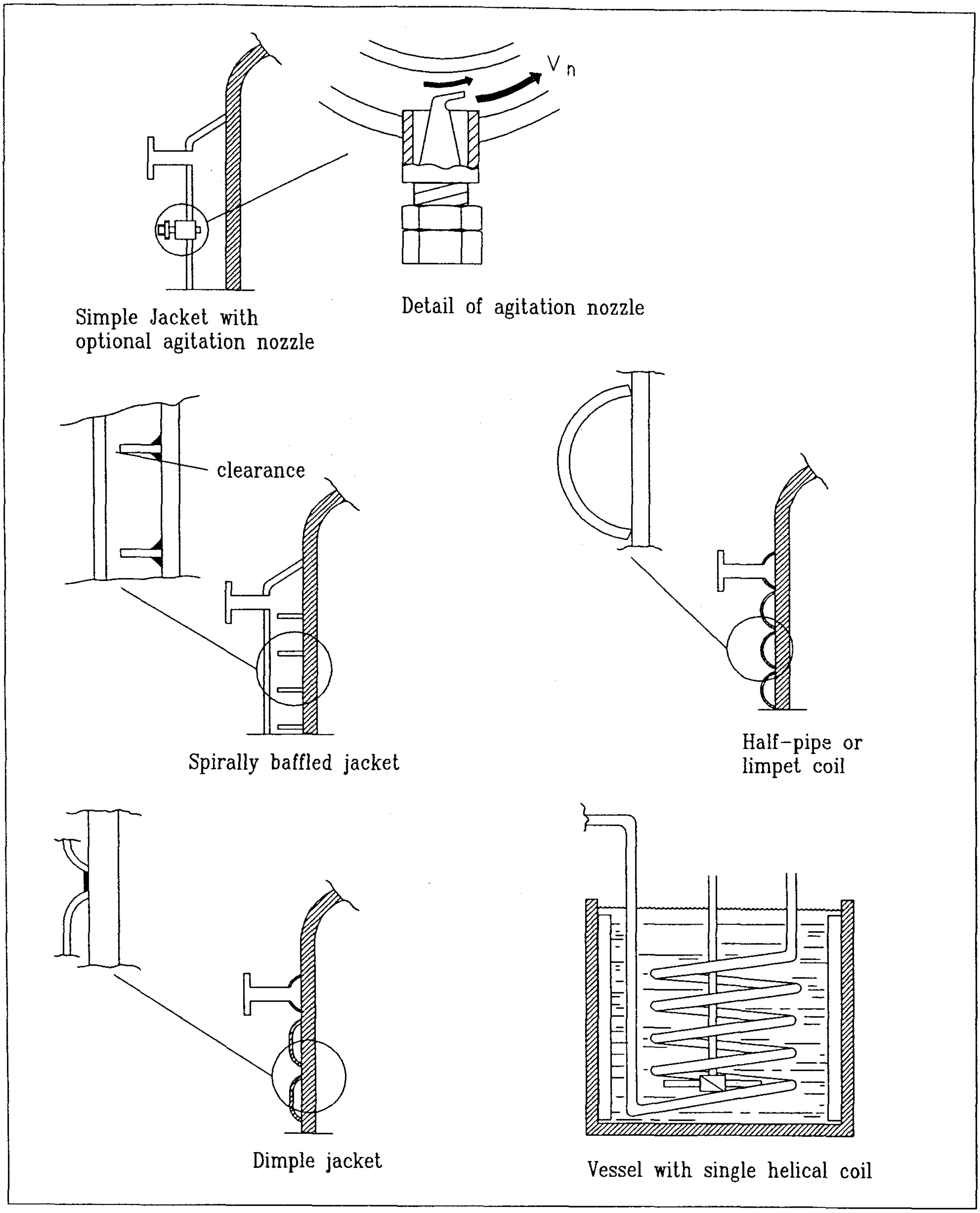

Simple Jacket with optional agitation nozzle

Detail of agitation nozzle

Spirally baffled jacket

Half-pipe or limpet coil

Dimple jacket

Vessel with single helical coil

Figure 2.5 : Types of Jackets and Coil

f. **Suitability** : For example, glass lined vessels can use only agitation nozzles or partial-pipe coils, due to the high thermal resistance of the glass.

g. **Other design considerations** : One such is the need for a high heat transfer fluid flow rate for "hot" reactions, or for rapid heatup or cool down time for batch reactors in proportion to the ratio,

$$\frac{\text{weight x specific heat of batch liquid}}{\text{mass flow rate x specific heat of heat transfer media}}$$

If a high heat transfer fluid flow rate is needed, then a spirally baffled or enlarged partial-pipe coil jacket may be necessary.

There are a number of jacket designs, figure 2.5, and the following sections give details of the heat transfer performance of different types of jacket.

2.4.1 Simple Jacket

Simple jackets [72] have a 0.05 m. to 0.075 m wide annular space, in which flow is low - about 0.03 m/s - and natural convection is the principal mode of heat transfer. Uhl and Gray [73] recommend the following equation for simple jacket heat transfer:

$$h_{oj}/K_T = 0.8k'' \, Pr^{0.33} \, (\rho^2 g\beta(\Delta T)/\mu^2)^{0.33} \qquad (2.44)$$

Equation (2.44) without the "0.8" numerical constant was derived for vertical channels; Uhl and Gray recommend the 0.8 factor for jackets to compensate for the nearly horizontal surfaces at the bottom of a fully-jacketed vessel. To account for variation in the direction of flow inside the jacket they introduced a dimensionless constant k" which has a value of 0.15 for upward flow of a heating fluid or downward flow of a cooling fluid, and a value of 0.128 for flows in the opposite directions. A conventional jacket is likely to be the best choice for small vessels (with capacities less than 2.0m^3).

2.4.2 Jacket with Agitation Nozzles

Nozzles are used to improve jacket heat transfer for glass-lined vessels. Three nozzles, all pointing in the same direction, are recommended. They produce some localised turbulence, but their main effect is to impose a special flow pattern tangential to the jacket wall by momentum exchange between the high velocity stream leaving the nozzle and the jacket fluid. This momentum exchange results in "swirl velocities" in the range of 0.3-1.2 m/s, which are

high enough to cause turbulent flow and to permit the use of conventional (e.g. Sieder-Tate) equations for calculating jacket heat transfer coefficients for forced convection.
Determining such coefficients for jackets having agitation nozzles begins with the calculation of the swirl velocity - which is eventually used as part of the Reynolds number, to obtain h_{oj}. The swirl velocity,V_j, is determined by trial and error solution of the following equation [72]:

$$w_p (V_n-V_j) = (4fL/D_e)(V_j^2)\rho A_f \tag{2.45}$$

Once reasonable agreement has been achieved for Equation (2.45),the jacket heat transfer coefficient can be calculated using one of the following two equations.

$$h_{oj} = 91\,(1 + 0.011\ T_f)\ V_j^{0.8} \ / D_e^{0.2} \tag{2.46}$$

$$h_{oj}D_e/K_T = 0.027\ Re^{0.8}\ \ Pr^{1/3} \tag{2.47}$$

where T_f is the average jacket temperature in ^oF .
Equation (2.46), which is an empirical adaptation by Bolliger [72] of an equation in Perry [74] for heat transfer in circular tubes, is in F.P.S. units and applies only to water. This equation is used in the present study to calculate the jacket side heat transfer coefficient. Equation (2.47) is an adaptation of the Sieder-Tate equation given by Kern [75] which applies to brines and organics. Agitation nozzles result in jacket heat transfer coefficients two or three times higher than those in simple jackets. However, the price paid for this increased jacket heat transfer is in the pumping energy required to overcome nozzle pressure drop.

2.4.3 Spirally Baffled Jackets

A spiral baffle consists of a metal strip spirally wound around a vessel wall from jacket entrance to exit. This strip directs flow in a spiral path to obtain fluid velocities in the range 0.3-1.2 m/s. There is a gap between the baffles and the jacket wall. The gap is a second path for fluid flow from the jacket inlet to outlet, perpendicular to the desired path along the baffle. The fluid that bypasses the spiral baffle, (i.e. the leakage through the gap) does not contribute directly to heat transfer at the vessel wall. The design calculations for a spirally baffled jacket begin with an assumed flow velocity, V, in the range of 0.3-1.2 m/s. This is used to determine the jacket side heat transfer coefficient, using equation (2.46) or (2.47).

In comparison to agitation nozzles, spiral baffles require up to twice the flow, only one-fifth the pressure drop, for equivalent heat transfer rates. Spirally baffled jackets, therefore, require about 40% of the energy needed by jackets with agitation nozzles for a given rating. The flow pattern in spirally baffled jackets approximates plug flow, so the log mean temperature difference should be used in calculating the heat transfer driving force.

The simple jacket, the jacket with agitation nozzles, and the spirally baffled jacket are structurally weak because the jacket pressure is applied over a large area of unsupported metal. For higher jacket fluid pressures, over about 150 psig, one should consider some other design; such as those below.

2.4.4 A Partial Coil Jacket (limpet coil)

A half pipe jacket consists of a half-section of pipe wound around the vessel and welded to it. High heat transfer coefficients can be achieved with a half-pipe jacket because of the high velocity reached by the service fluid. Typical flow rates in a half pipe coil are in the range of 0.6 to 1.5 m/s. Heat transfer coefficients can be calculated by assuming various velocities in this range and using equation (2.45) or (2.46), by selecting the lowest turbulent flow. At the same flow rates, pressure drops for half-pipe coil jackets are less than those for agitation nozzles, but more than those for spirally baffled jackets. Generally, it is not practical to use a half-pipe jacket for vessels with capacities less than 2.0 m^3.

2.4.5 Dimple Jacket

The design of the dimple jacket permits construction from light-gauge metals without sacrificing the strength required to withstand special pressures. Dimple jackets utilise metal sheets with dimples that are welded to the walls of the vessels. They are suitable for use with large vessels, not less than 2.0m^3, although a high pressure drop may be encountered at high service fluid flows. The brewing industry makes extensive use of this design for large fermentation vessels.

2.4.6 Panel Type Coils or Plate Type Coils

These are fabricated from two metal plates. For reactors, one plate is smooth and forms the vessel wall. The outer plate is embossed to form a series of flow paths between the plates. A vessel made with a panel or plate type coil can have a thinner inner wall then a conventional vessel because the jacket pressure does not affect the design of the inner wall. This advantage may be offset by the need to make the outer plate of the same corrosion resistant material as the inner plate. This could occur if the vessel wall were made of stainless steel; if the outer plate were made of less expensive carbon steel, the impurities in the carbon steel could migrate into the stainless and cause corrosion of the inner plate. This situation can also occur in dimple and partial pipe coil jackets where the jacket and vessel wall are in direct contact.

According to Markovitz [76] the basic equation for calculating heat transfer in an annulus is the Stanton equation. This is applicable to conventional, dimple and half-pipe coil jackets:

$$h_{oj} = 0.023\ Re^{-0.2}\ \ Pr^{-2/3}\ c_p\ G\ (\mu_w/\mu)^{0.14} \tag{2.48}$$

The formula varies for each type of jacket in that each has a different equivalent diameter. For a conventional jacket:

$D_{eq} = J/3$

where J - is jacket space in metre

G - is mass velocity in kg/s

For very large heat duties ultimately one must have recourse to external heat exchangers [77] with the liquid being mechanically pumped around the external cooling circuit.

2.5 *Rheology, concepts and definitions*

The rheological properties of a fluid directly affect bulk mixing, heat and mass transfer and can therefore have a profound effect on product yield and the economics of a mixing process.

The theoretical and practical aspects of rheology are covered in depth in a number of standard texts [78,79], so the aim of this section is primarily to review those aspects which are relevant to this study; specifically, the properties referred to in the literature survey and experimental chapters.

2.5.1 Newtonian fluids

The viscosity of a fluid is defined as the ratio of shear stress, (τ), to the velocity gradient, (dv/dy). For a Newtonian fluid, in laminar flow, the shear rate, ($\dot{\gamma}$), is proportional to the velocity gradient and a plot of shear stress against shear rate is linear and passes through the origin,

$$\tau=\mu\dot{\gamma} \tag{2.49}$$

The viscosity of the fluid, (μ), depends on temperature and pressure, but is independent of the rate of shear.

2.5.2 Non-Newtonian fluids

For non-Newtonian fluids, the viscosity is not constant at a given temperature and pressure, but depends on other factors, such as, the rate of shear, the time of shearing and the previous shear history of the sample. An apparent viscosity, μ_a, is defined which is dependant on the value of the shear rate. By analogy with Newtonian fluids,

$$\mu_a=\tau/\dot{\gamma} \tag{2.50}$$

The apparent viscosity is, therefore, given by the ratio of shear stress to shear rate, at a stated value of shear rate.

2.5.2.1 Shear-thinning fluids

Commonly, fermentation broths acquire shear-thinning or pseudoplastic characteristics. In such fluids the apparent viscosity decreases with increasing shear rate. This is thought to be due to the progressive alignment of high molecular weight molecules, or filamentous structures within the fluid. At low shear rates, their alignment is overcome by random motion, resulting in a high resistance to shear and hence high apparent viscosities. At high shear rates, orientation of their major axes with the direction of flow results in a reduction in the apparent viscosity.

In the impeller region of a stirred vessel, shear rates are usually high and apparent viscosity is low. Shear rates decrease rapidly and consequently apparent viscosity increases rapidly with increasing distance from the impeller [80]. The presence or absence of a yield stress, (a minimum shear stress which must be exceeded if the fluid is to flow), may determine whether or not there is any fluid motion outside of the impeller region. Thus, in shear-thinning fluids with a yield stress, Wichterle and Wein [81] and Solomon et al [82] observed the formation of a well mixed cavern region in the immediate vicinity of a disc turbine, outside which the fluid was stagnant or nearly so.

A number of expressions have been used to correlate viscosity data for shear-thinning fluids [78]. None is completely satisfactory for all fluids, nor for the entire range of shear rates for a given fluid. In the region of decreasing viscosity, a logarithmic plot of τ against $\dot{\gamma}$ often reveals linearity over several decades of shear rate. Where this is the case, the power law equation is generally used, although this does not accommodate the Newtonian regions at very high and low shear rates. For a power law fluid,

$$\tau = K\dot{\gamma}^n \qquad 0 < n < 1 \tag{2.51}$$

Where "K", (Ns^nm^{-1}), is the consistency index and "n" is the power law or flow behaviour index. Combining equations 2.50 and 2.51 provides an expression for the apparent viscosity,

$$\mu_a = K\dot{\gamma}^{n-1}$$

The smaller the value of n, the more rapid the decrease in viscosity with increasing shear rate and the more pronounced the effects of pseudoplasticity on flow and other transport phenomena. The consistency index, K, is a measure of the viscosity at a given rate of shear. The larger the value of K, the greater the viscosity at a given rate of shear. It should be noted that values of K and n are generally only valid for a given range of shear rates. Furthermore, K is obtained by extrapolation of viscosity data to "1 s^{-1}" and may not have any real significance at that rate of shear. The dimensions of K are dependant on the value of n making comparisons of experimental results for different values of n difficult.

2.5.2.2 A New Shear Rate Model

Kai and Shengyao [57] proposed a new shear rate model for their heat transfer study. They assumed that the torque offered by the rotating impeller is proportional to the average shear stress, τ_a, exerted on the wall surface of an agitated vessel:

$$M = k_1\, V\, \tau_a \tag{2.52}$$

where k_1 is a proportionality coefficient.
Using equation 2.51 for a power law fluid, equation (2.52) can then be written as:

$$P = 2\pi k_1 V_L K N \dot{\gamma}^n \tag{2.53}$$

They [57] further obtained from a survey of literature the following relation :

$$P/\rho D^5N^3=K_p/\mathrm{Re}_g^f \qquad (2.54)$$

where K_p is a constant and the flow regime coefficient "f" is related to Reynolds number in the transitional regime and equals 0 and 1 in the fully turbulent and laminar regimes respectively. Re_g is the generalised Reynolds number for non-Newtonian fluids (i.e. $D^2N^{2-n}\rho/K$), and by assumption,

$$\varphi=\exp(-m\,\mathrm{Re}_g) \qquad (2.55)$$

where m is the model parameter, and φ defined by equation 2.37.
Substituting of equations (2.52), (2.53) and (2.54) into equation (2.55) and assuming a new constant,

$$k_2=K_p\,\rho D^5\rho/[2\pi k_1V_L\,K(D^2\rho/K)]^{\varphi} \qquad (2.56)$$

one then obtains

$$\dot{\gamma}=k_2^{1/2}N^{[2-f(2-n)]/n} \qquad (2.57)$$

Hence for power law fluids the apparent viscosity could be written as :

$$\mu_a=K\,0.4^{(n-1)/n}N^{[2-\varphi(2-n)](n-1)/n} \qquad (2.58)$$

Their experimental results demonstrated that the model parameters m and k_2 are slightly related to the scale, flow regime, fluid viscosity and impeller type, and have been found through optimisation to be 0.00705 and 0.4 respectively.

2.6 *Concepts in hydrodynamics*

2.6.1 Power Consumption and Power Number

Interest in the accurate measurement of the power consumed during a mixing process arises from economic considerations, since power costs can represent a significant fraction of the operating costs, and from a requirement for reliable design and scale-up data. Power input must be known in order to specify a motor and drive system. Scale-up at constant specific power input is commonly used in vessel design. Interest has also arisen from observations that changes in power consumption are indicative of changes in local impeller and bulk hydrodynamics, and recently attempts have been made to interpret heat transfer in similar terms.

Early studies [83] showed experimentally that the power drawn by an impeller in low viscosity fluids was related to the impeller diameter and rotational speed by the relationship:

$$P \alpha N^3D^5 \qquad (2.59)$$

Dimensional analysis of the relevant variables by Rushton et al [84] showed that the dimensionless Power number was a function of the Reynolds number, the Froude number and geometric ratios, such as D/D_T and H_L/D_T.

$$N_p = \text{fn (Re, Fr, geometric ratios)} \qquad (2.60)$$

The Power number represents the ratio of the forces producing flow to the inertial forces and is analogous to a drag coefficient or friction factor.

$$N_p = P/\rho N^3D^5 \qquad (2.61)$$

For fully baffled vessels, where there is no central vortex formed, the Froude number is generally considered unimportant. Provided that the geometrical simplexes were kept constant, it was found that equation 2.60 could be reduced to the form:

$$N_p = \text{fn (Re)} \qquad (2.62)$$

Application of the Reynolds number is relatively straight forward for Newtonian liquids, since the viscosity is constant and independent of the rate of shear at a given temperature and pressure. For non-Newtonian liquids, the apparent viscosity is a function of the shear rate and may also be a function of time. The question then arises as to what value of viscosity should be used when calculating the Reynolds number. In order to determine the apparent viscosity it is necessary to obtain a value for the shear rate in a mixing vessel which is itself non-uniform, so that it varies with position in the vessel. The method of Metzner and Otto [55] was developed to determine the Reynolds number for pseudoplastic fluids in the laminar flow regime.

Metzner and Otto [55] suggested that the apparent viscosity should be evaluated at an average shear rate, ($\dot{\gamma}_{AV}$). In order to determine these values, they measured the power input for a series of Newtonian and non-Newtonian fluids under the same conditions, (vessels geometry, impeller speed, etc), in the laminar flow regime. It was assumed that the power curves, (Power number plotted against Reynolds number) in this flow regime were identical since viscous forces alone determine power consumption. Thus, by matching the power numbers obtained for the non-Newtonian liquids with those for the Newtonian liquids, equivalent Reynolds numbers were obtained for the former and, from these, values of apparent viscosity at a given impeller speed were determined. By defining the average shear rate as

$$\dot{\gamma}_{AV} = \tau / \mu_a \qquad (2.63)$$

and combining this with data for the relationship between apparent viscosity and shear rate, obtained from rheological measurements, it was shown that the average shear rate was linearly related to the impeller rotational speed:

$$\dot{\gamma}_{AV} = k_s N \qquad (2.64)$$

where k_s is the Metzner-Otto constant.

Measurements of local velocity gradients made by Metzner and Taylor [80] in solutions of sodium carboxymethylcellulose in conventional, baffled, cylindrical vessels, agitated with a single turbine, confirmed that shear rate varied linearly with impeller speed. In addition, shear rate decreased rapidly with increasing distance from the impeller.

For a non-Newtonian fluid, the Reynolds number is given by:

$$Re = \rho \, N \, D^2 / \mu_a \qquad (2.65)$$

For a power law fluid, the relationship between shear stress and shear rate is given by :

$$\tau = K \dot{\gamma}^n \qquad (2.66)$$

and from equations 2.63, 2.64 and 2.66,

$$\mu_a = K \dot{\gamma}^{n-1} = K (k_s N)^{n-1} \qquad (2.67)$$

By substituting for μ_a, the Reynolds number for a power law fluid can be evaluated,

$$Re = \rho \, N^{2-n} D^2 \; / \, K \, k_s \qquad (2.68)$$

Though of doubtful validity, the above equation is often applied for all Reynolds numbers for shear-thinning fluids.

Metzner et al [85] extended the work of Metzner and Otto [55] and determined the values of k_s for various impeller types and non-Newtonian fluids. They found that the relationship applied to the shear-thinning and Bingham plastic fluids tested, but not the dilatants. The values of k_S for different impeller types are shown below.

Impeller type	k_S
Disc turbine	11.5 ± 10%
Pitched blade turbine	13.5 ± 15%
Propellors	10.0 ± 10%

2.6.2 Mixing in single and two phase fluids

The single phase flow around a Rushton turbine is mainly characterised by two roll vortices formed behind the upper and lower edges of the blades. Within these vortices there are very large centrifugal acceleration which result in important underpressures.

When the stirrer is operated in a gas-liquid system the gas is drawn into these vortices and this can lead to the formation of gas filled cavities. At the lowest gassing rate, 6 identical pairs of vortex cavities (one pair above the impeller disk and the other below it) form which is clung only to a small area of the blade, and the gassed power number barely falls. With an increase in the gassing rate the gas cavity envelop whole of the blade and is called 6 clinging cavity which are identical. This leads to a rapid drop in power. Further increasing the gas flow rate causes large cavities to be formed, initially these cavities are unstable and move from blade to blade in response to the random supply of gas rising from the sparger, called 3-3 structure. If this situation exists, only a very small extra amount of gas is needed to pass over the unstable cavities to the configuration with three large stable cavities. Both gas flow rate and stirrer speed have to satisfy certain coupled condition in order to form large cavities. It has been determined experimentally that below a value of the Froude number of 0.045 large cavities cannot be stable [88], however high the gas flow is, as buoyancy forces are so much greater than the centrifugal forces that the gas escapes. When the 3 large cavities have once been formed they have a characteristic size, which is dependent on the stirrer speed. Newly formed cavities at higher speeds are larger than those which are formed at lower speeds. The cavity size, and thus shape and corresponding drag coefficient of the blade cavity combination, therefore corresponds to the particular agitator speed. When the gas flow is increased further the three cavities will grow, the size becomes larger. In the lowest range of stirrer speeds, the next increase of the gas flow rate will lead to the phenomenon termed as flooding; the radial distribution of the bubbles largely disappears and the gas rises directly through the stirrer region to the liquid surface.

Disk turbines are considered to be good for gas dispersion. In the six flat bladed disk turbine (as the one used in the study) the disk forces all the inflowing gas to pass through the high shear impeller region, ensuring efficient break-up of the gas stream into bubbles and effective dispersion of the bubbles throughout the vessel. The effect of gas rate on the capability of an impeller to circulate and impart energy to the dispersion at a constant impeller speed is reflected in the decrease in the ratio P_g / P.

The above representation is for simple Newtonian fluids. For highly viscous shear thinning fluids such as the fermentation broth even a small air input rate leads to the formation of large, stable, equi-sized cavities behind each agitator blade. Increase in aeration rate do not change the cavity size significantly but increase both the rate and, to a lesser extent, the size at which bubbles break away from them. At high aeration rates, the increased breakaway frequency and bubble size at breakaway leads to enhanced coalescence of bubbles, so that bigger and bigger ones break through the top surface. On decreasing aeration rate, cavities commonly remain behind the blades down to zero air rate though they may slowly disperse unless the broth is also significantly viscoelastic.

2.6.3 Mixing in fermentation broth

Fermentation fluids (broths), specially mycelial, are often known to exhibit non-Newtonian properties due to the presence of biomass. The rheological properties of the broth depends on the biomass present and also to some extent on its morphology [87]. Most mycelial fermentation broths are shear thinning because increasing shear rate pulls the intertwined mycelial structures (not the mycelium itself) apart and aligns the hyphae, thereby reducing the broths resistance to flow, i.e. its viscosity. Such a process is reversible, so that as broth moves into the impeller region, its viscosity falls and as it moves away, it rises again. Increases in mycelial concentration (culture dry weight) increase the apparent viscosity and the shear-thinning tendency and towards the end of a fermentation, the broth may develop a yield stress. However, neither Metz et al [85] nor Belmar et al found any significant impact of agitation intensity on rheological properties [86] .

To study such a complex fluid the mixing studies in mycelial fermentations can be broadly divided into two following sets of parameters [86].

1. Physical parameters that are system-independent : A fermentation can be modelled using a suitable model fluids like Carboxymethyl cellulose, fibre suspension etc. to study physical parameters, such as heat transfer, power draw and gas hold-up, which are independent of fermentation conditions but are mostly bioreactor geometric specific. However, it must be noted here that suitable model for a mycelial fermentation is still debatable, because the reproduction of the structure of the broth (which has unique morphology) is not possible with traditional model fluids like carboxymethyl cellulose; in this study the fibre suspension was found to be a better model fluid.

2. Biological parameters that are system-dependent : This comprises of growth and product secretion, damage to micro-organism, morphological changes and oxygen transfer rate. Such mycelial fermentations have complex interrelations between rheological properties, morphology, mixing and transfer processes.

For a comprehensive understanding of such a complex process it is vitally important to have a clear understanding of the system independent parameters and then to integrate with the system specific parameters. This essentially means integrating engineering principles with the biological processes.

2.7 *Fermentation Systems*

Biochemical engineering can be define simply as a design and operation for purposeful utilisation of biological systems. A living cell is a complex chemical reactor in which many independent enzyme catalysed reactions can occur. Still the material and energy balance restrictions and thermodynamic principles apply equally well to biological systems. The total of all chemical reaction activities which occur in the cell is called metabolism, which is organised in metabolic pathways. Before understanding heat transfer on a macro scale it is important to have an understanding of energetics in the micro scale.

In a cell, energy obtained from the environment is typically stored and shuttled in convenient high-energy intermediates such as ATP (Adenosine triphosphate). The cell uses this energy to perform three types of work : Chemical synthesis of large or complex molecules (growth), transport of ionic and neutral substances into or out of the cell or its internal organelles, and in the mechanical work required for cell division and motion. Biosynthesis work is performed with a relatively high efficiency of free-energy utilisation, typically greater than about 20 % . The transport work also involves ATP consumption in a process unique to living systems;

small molecules and ions can be moved through membranes against a concentration gradient. Mechanical work is evident during cell division and bacterial and protozoal movement. Animal muscle activity and sperm swimming also imply ATP participation; the resulting direct conversion of chemical free energy into mechanical work without such intermediates as electricity or heated gases is also unique to life. Losses during chemical energy conversions in cells result in heat generation which must be considered when engineering processes for cell growth. In order to grow and reproduce, cells must ingest the raw materials necessary to manufacture membranes, proteins, walls, chromosomes, and other components. Four major requirements are evident : carbon, nitrogen, sulphur, and phosphorus; hydrogen and oxygen may be obtained from medium components or in some instances from water.
The reaction within the cell have been subdivided into three classes: degradation of nutrients, biosynthesis of small molecules, and biosynthesis of large macromolecules. Each reaction is catalysed by an enzyme.

Enzymatic hydrolysis of ATP to yield ADP and inorganic phosphate has a large negative free energy change.

$$\mathrm{ATP} + \mathrm{H_2O} \Rightarrow \mathrm{ADP} + \mathrm{Pi} \qquad \Delta G^\circ = -7.3\ \mathrm{kcal/mol}$$

where Pi denotes inorganic phosphate.

Thus a substantial amount of free energy may be released by the hydrolysis, and, by reversing the reaction and adding phosphate to ADP, free energy can be stored for later use.

In the above paragraph the role of ATP as a shuttle for phosphate groups bound with rather high energies is reviewed. In this section the connection between oxidation and reduction reactions (conducted biologically) and mechanisms and ATP metabolism is examined. Pair of hydrogen atoms formed during oxidations or required in reduction are carried by nucleotide derivatives, especially nicotinamide adenine dinucleotide (NAD) and its phosphorylated form NADP. When hydrogen atoms are needed ; for example , the nicotinamide group of reduced NAD can contribute them by undergoing the oxidation. This oxidation is readily reversible, so that NAD can also accept electrons (H^+ atoms) when they are made available by oxidation of other compounds. NAD^+ is the oxidised form and NADH is the reduced form. In its role as electron shuttle, NAD serves two major functions:

1. Analogous to ATP : reducing power made available during breakdown of nutrients is carried to biosynthetic reactions. Such a transfer of reducing power is often necessary because the oxidation state of the nutrients to be used for construction of cell components is different from the oxidation state of biosynthesis products.

2. NAD and related pyridine nucleotide compounds carrying hydrogen also participate in ATP formation in aerobic metabolism. In respiration the hydrogen atoms in NADH are combined with oxygen in a cascade of reactions known as the respiratory chain. The energy released in this oxidation is sufficient to form three molecules of ATP and ADP.

2.7.1 The energy fixing process

The breakdown of nutrient to obtain energy is called catabolism. Carbohydrates are by far the most important class of carbonaceous nutrients for fermentations, although some microbial species can also utilise amino acids, hydrocarbons and other compounds. One of the best known pathway for carbon catabolism is Embden-Meyerhof-Parnas pathway (EMP) which involves ten enzyme-catalysed steps which start with glucose and end with pyruvate. Stored chemical energy and reducing power result from the overall pathway. Energy storage accomplished by this or other substrate rearrangement pathways is called substrate-level phosphorylation. Thus, the overall stoichiometry of the EMP pathway is,

$$C_2H_{12}O_6 + 2\,Pi + 2ADP + 2NAD^+ \Rightarrow 2\,C_3H_4\,O_3 + \;2ATP \;+\; 2\,(NADH + H)$$

A free-energy total of 14.6 kcal, or 7.3 kcal for each mole of ATP generated, has been conserved by the pathway as high-energy phosphate compounds. Besides EMP there are two additional reaction sequences for glucose catabolism.

Respiration is an energy-producing process in which organic or reduced inorganic compounds are oxidised by inorganic compounds. In the most common forms of respiration, an organic compound is oxidised using oxygen. In the first, organic compounds are oxidised to CO_2 , and pairs of hydrogen atoms (electrons) are transferred to NAD. Next, the hydrogen atoms (electrons) are passed through a sequence of reactions during which ATP is regenerated from ADP. At the end of their journey the hydrogen atoms are combined with oxygen to give water.

The first phase of this biological oxidation is called the tricarboxylic acid or TCA cycle (also, Krebs cycle or citric acid cycle) whereas the second is named the respiratory chain. The TCA cycle serves a very important function in providing a pool of precursors for biosynthetic reactions. Some of the reducing power derived from the TCA cycle may be needed in biosynthesis reactions; the rest is used to generate ATP.

The second phase is respiration from which aerobic cells derive most of their energy. In its most general form such a reaction could be depicted as,

$$\text{Glucose} + 6\,O_2 \Rightarrow 6\,CO_2 + 6\,H_2O$$

The energy made available form the above reaction is 686 kcal/mol.

It is important for this study to examine how efficiently respiring living systems tap this large source of energy. For comparison with the above reaction, it is presumed here that glucose is completely oxidised to carbon dioxide and water via EMP, TCA and respiratory chain pathways. The overall reaction is [89]

$$C_6H_{12}O_6 + 38\,\text{ADP} + 38\,\text{Pi} \Rightarrow 6\,CO_2 + 38\,\text{ATP} + 44\,H_2O$$

Since ATP hydrolysis has a standard free-energy change of -7.3 kcal/mol, the free energy change of reaction is approximately (-7.3 x 38) -277 kcal/mol glucose.

Therefore the energy capture efficiency = 277 / 686 $\approx$ 40 %.

By carrying out glucose oxidation in many steps, where each has a relatively small free-energy change, the living cell is able to approach reversibility and to maximise efficiency for extraction of energy. Most of the remaining energy is dissipated as heat, which must be removed in some fashion to keep the temperature in the physiologically suitable range. That is why heat transfer is important.

Heat evolution is closely related to the catabolic activity of the cell and is valuable as a measure of the efficiency with which available chemical energy is utilised. Because heat evolution during growth and metabolism is a universal characteristic of living organisms, it can be used to monitor all kinds of microbial systems-whether they are anaerobic or aerobic, in large or small cultures, in defined or complex media, or whether the final product is cell mass or metabolites. This makes heat evolution a particularly interesting parameter of a fermentation. Further, due to the fact that stirred fermentation reactors are usually scaled up with constant power per unit volume it is the heat transfer problem which becomes more and more important as the tank volume gets larger and especially when using non- Newtonian broths. Constant power per unit volume means that constant heat per unit volume is dissipated by the agitator. An increase of the vessel size leads to a reduction of cooling surface per unit volume due to the fact that the volume is proportional to D_T^3, but the cooling surface is only proportional to D_T^2.

2.7.2 Introduction to Penicillin fermentation

Penicillium chrysogenum is the organism used for the experiments described here. The strain used was obtained from SmithKline Beecham Ltd. and is called PC 8. This study concentrates on the heat transfer, power and rheological aspects of the fermentation and at the same time integrates these with morphological studies done by Dr. C. R. Thomas's group (Mr. K. Tucker and Mr. P. Cox).

Pencillia are a widespread family of the Fungi Imperfecti (Eucaryotic cells). The antibiotic effect was first discovered in 1928 by Alexander Fleming. In the early days the antibiotic penicillin was obtained from *Penicilliun notatum*, which was grown as a surface culture. Later (1951) another strain with a higher yield, which was able to grow in a submerged culture was discovered and was named *Penicillium chrysogenum* .

There are three cultivation techniques used in penicillin fermentation. commercially penicillin production is carried out by fed-batch processes; batch and continuous culture techniques are still in use in research. In a batch fermentation (as the one used in this study) a fixed quantity of nutrients is added to the fermenter and the product is withdrawn at the end. Because of the nature of the process, the nutrient concentration changes throughout the process and the cells adapt their physiological state to whatever nutrient limitations occurs during the culture. The efficiency of antibiotic production in the culture begins to decline as early as 20-25 hrs. after the induction of antibiotic production [92]. In the continuous flow process (chemostat type) addition of fresh nutrients and removal of products are carried out continuously. Commercially penicillin production is carried out in a fed-batch mode in large aerated mechanically agitated fermenters typically in the volume range of 40,000 - 200,000 litres in which the nutrients are fed continuously. The process begins with the growth of a starter culture to a suitable biomass concentration in a complex organic medium such as corn-steep liquor or pharmamedia [93].

A typical penicillin fermentation involves various stages. Frozen spores (a standard number) are inoculated on slants or Erlenmayer flasks, and allowed to sporulate, then trasferred to vegetative cultures in shake flasks containing a vegetative medium generally similar to the production medium. This is the inoculum to the seed fermenter, whose volume is of the order of 10% of the main fermenter volume [93], which, after growth, is then asceptically transferred to large production fermenters. There may be more than one seed fermenter depending on the scale of operation. In each fermenter the environment is carefully controlled with respect to temperature, pH, dissolved oxygen and substrate concentration so as to maximise the final antibiotic yield. A commercial fed-batch fermenter is typically run for up to 200 hours or more and several "mini harvests" are taken throughout the run in order to maintain a workable volume.

2.7.3 Inoculum and media for a typical penicillin fermentation

Penicillium grows, as other typical fungi, as a mycelium whose morphology varies from discrete filamentous hyphae to a pelleted form. The inoculum quality and quantity influences irreversible growth, culture morphology, antibiotic productivity and enzyme content of mycelia, as demonstrated by Smith and Calam [94] and is further investigated using image analysis by G.C.Paul [95]. A high spore concentration in the inoculum supports filamentous growth whereas a low concentration leads to pellets; this borderline is roughly in between 10^5 and 10^6 spores/ml.

The primary ingredients for the growth and production phases of penicillin fermentation are sources of carbon, nitrogen, sulphur, and product precursors together with small quantities of vitamins and minerals. In order to optimise a fermentation, a culture medium must be developed which will stimulate the metabolic pathway relevant to growth and product synthesis. The fermentation media could be broadly classified in two types namely ; chemically defined media and Complex media.

2.7.4 Chemically defined media

The use of chemically defined media for submerged penicillin fermentations is restricted to the research laboratory, but is often necessary to simplify experiments. They are formulated from different carbon sources (glucose, lactose, sucrose or a mixture of these, possibly with organic acids), salts (sulphate, ammonium, phosphates) and trace metal salts [96]. The buffering capacity is increased by the addition of $CaCO_3$ or KH_2PO_4 to the medium. However, phosphate can precipitate out because of pH sensitive reactions, which can be prevented by the use of chelating agents such as EDTA [97]. Greatly differing amounts of $(NH_4)_2 SO_4$ and Na_2SO_4 are used in the defined media as nitrogen and sulphur sources, depending on the use of sulphuric acid (supplementing sulphur) and ammonia solution (supplementing nitrogen) for pH control.

2.7.5 Complex media

Production of penicillin by submerged cultivation started with a corn-steep liquor medium using lactose as the carbon source. The corn-steep solids contain mostly a nitrogen source and other complex salts, and phosphates. The use of additional salts depends on the amounts of solids present. The value of this medium was thought to lie in its balance of materials generally favourable for penicillin fermentation. Continuous feeding of glucose has since replaced the use of the more expensive lactose.

Crude carbon sources of lower purity, such as molasses, are commonly used in penicillin fermentation. Animal and vegetable oils [98] have also been used.

2.7.6 Trace elements and side chain precursors

Trace elements such as potassium, calcium, magnesium, zinc, manganese, copper, iron are essential for growth and penicillin biosynthesis. Jarvis and Johnson [99] determined the minimal requirement of S, P, K (0.04 g/l), Mg (0.008 g/l), Fe and Cu (0.0001-0.0005 g/l) for mycelial growth. For penicillin production the requirements for S, P, and Fe are 1.5 (0.1 g/l), 2 (0.2 g/l) and 20 (0.004 g/l) times higher respectively. However, high yielding mutants are susceptible to iron toxicity [100].

It was discovered in 1948 that the addition of the so-called precursor Phenyl Acetic Acid (PAA) initiated the formation of penicillin to penicillin G. Another precursor is Phenoxy Acetic Acid (POA) for the production of penicillin V. These two are the only therapeutically important natural penicillins, and both are similarly active against Gram positive bacteria. They differ in the method of administration, as penicillin G is degraded by stomach acid whilst penicillin V is not. The basic understanding of process kinetics and essential nutritional requirements was established in defined medium studies by Hosler and Johnson [96]. To avoid toxicity of these compounds to the producer micro-organism, and to minimise their hydroxylation, they are added continuously at a later stage of the fermentation.

2.7.7 Engineering variables

Engineering variables, such as temperature, pH, dissolved oxygen concentration, and agitation rate, dissolved oxygen concentration, air flow rate and agitation speed, can be manipulated to change the physical and metabolic states of the culture in order to give optimum yield of penicillin.

The penicillin fermentation has a narrow optimum temperature range which is different for the growth and the production phases [101,102]. It has been reported that mycelial growth was greatest at 30 °C where an enhanced uptake of carbohydrates occurs, while penicillin production was maximal at 24.7 °C [101] . McCann and Calam [102] reported an optimal temperature between 25 and 27 °C for a fed-batch process when a constant temperature was used throughout the fermentation period.

For optimum mycelial growth and penicillin production a pH range of 6.8 to 7.2 has been used [100,103]. However, in recent literature, a range of pH of 6.2-6.8 is mentioned, as high pH values lead to rapid degradation of penicillin [104].

Dissolved oxygen tension is a complex variable because it is intimately associated with many other fermentation variables such as agitation rate, oxygen solubility in the medium, and oxygen uptake rate of the mycelial cells. For the penicillin fermentation a certain minimum supply of oxygen is required to support growth and penicillin production. Varder and Lilly [105] reported that, below 30% saturation of dissolved oxygen, penicillin production decreased sharply and no penicillin was produced below 10% saturation.

Fermentation broths containing suspended mycelia, specially at high biomass concentrations are often non-Newtonian in character; that is their apparent viscosity is a function of the shear produced by agitation. Such behaviour can result in poor mixing and heat transfer, especially in large fermenters where the suspension may be heterogeneous with respect to mass transfer of substrates and products. It would seem that the mixing of the submerged culture should be as intense as possible in particular to promote vigorous oxygen transfer to the mycelium. However, a high degree of agitation may have an adverse effect on productivity [105,106,107] through mechanical damage. An intermediate degree of agitation was found to maximise penicillin yield. There are several possible explanations: the morphology of the mycelium is affected by the applied shear forces, more intense agitation may break up hyphae and as a consequence leakage of constituents may occur from the broken cells [108,109].

The presence of mycelia as a third phase has profound influence on heat transfer. There are only a few serious works on heat transfer to fermentation systems. Amongst them the work of Blakeborough et al [90,91] is worth mentioning even though their study is limited to the air-lift geometry. They used a heat flux probe for a heat transfer study in an air-lift fermenter during laminar pipe flow of *Xanthomonas campestris* and *Aspergillus niger* broths, grown in batch culture. One of their findings that is relevant to this study is the "scraped surface" heat transfer model. The model explains the enhancement of heat transfer with increase in cell concentration suggesting that the boundary layer is scrapped by the mycelial aggregates.

CHAPTER 3

Equipment and methods

This integrated study was carried out in a modern well instrumented LSL-Biolafitte 800 litre pilot plant bioreactor, described in section 3.1, after particular modifications. The modifications given in section 3.2 included installation of micro-foil heat flux probes to study the local axial heat transfer profile, such probes being specially designed in collaboration with RdF Corporation, U.S.A. and supplied by Rhopoint Ltd.. To study the axial local heat transfer profile three probes were placed on the vessel wall at known axial distances from the impeller plane, and three thermocouples in the same planes measured the temperature of the bulk. To complete the heat balance thermocouples were placed in the jacket outlet and inlet and a turbine flow meter was incorporated in the jacket heating/cooling loops. The vessel is equipped with microprocessor-based local controllers (TCS 6000 series units) and a Micro VAX-2 based process management system for supervisory control (using SETCON data management software, SD-Scicon), described in section 3.3, TCS (T 100) interface systems condition the signals from the various sensors for onward transmission to the MicroVAX. The data thus obtained is then processed using SIGMA-PLOT (version 4.1) scientific package on a personal computer. Section 3.4 describes the rheological measurement technique used and section 3.5 describes the model fluids and their preparation technique.

3.1 *The 800 l pilot-scale bioreactor*

The Biochemical Engineering Centre has a very well instrumented 800 l Pilot plant (fabricated in 316L stainless steel) which has 600 l working volume. The details of the pilot plant are given in appendix 1. Figure 3.1 is a photograph of the panel of the pilot plant. The top "section A" is the TCS unit which is an interface between the probes and the Micro-VAX. The "section B" shows the complete process circuit with various switches. In this thesis the heating/cooling circuit will be considered in detail in the following section.

SECTION A - TCS UNIT

SECTION B - PROCESS CIRCUIT
and
SWITCHES

Figure 3.1 : Front Control Panel of 800 L Pilot-Scale Bioreactor

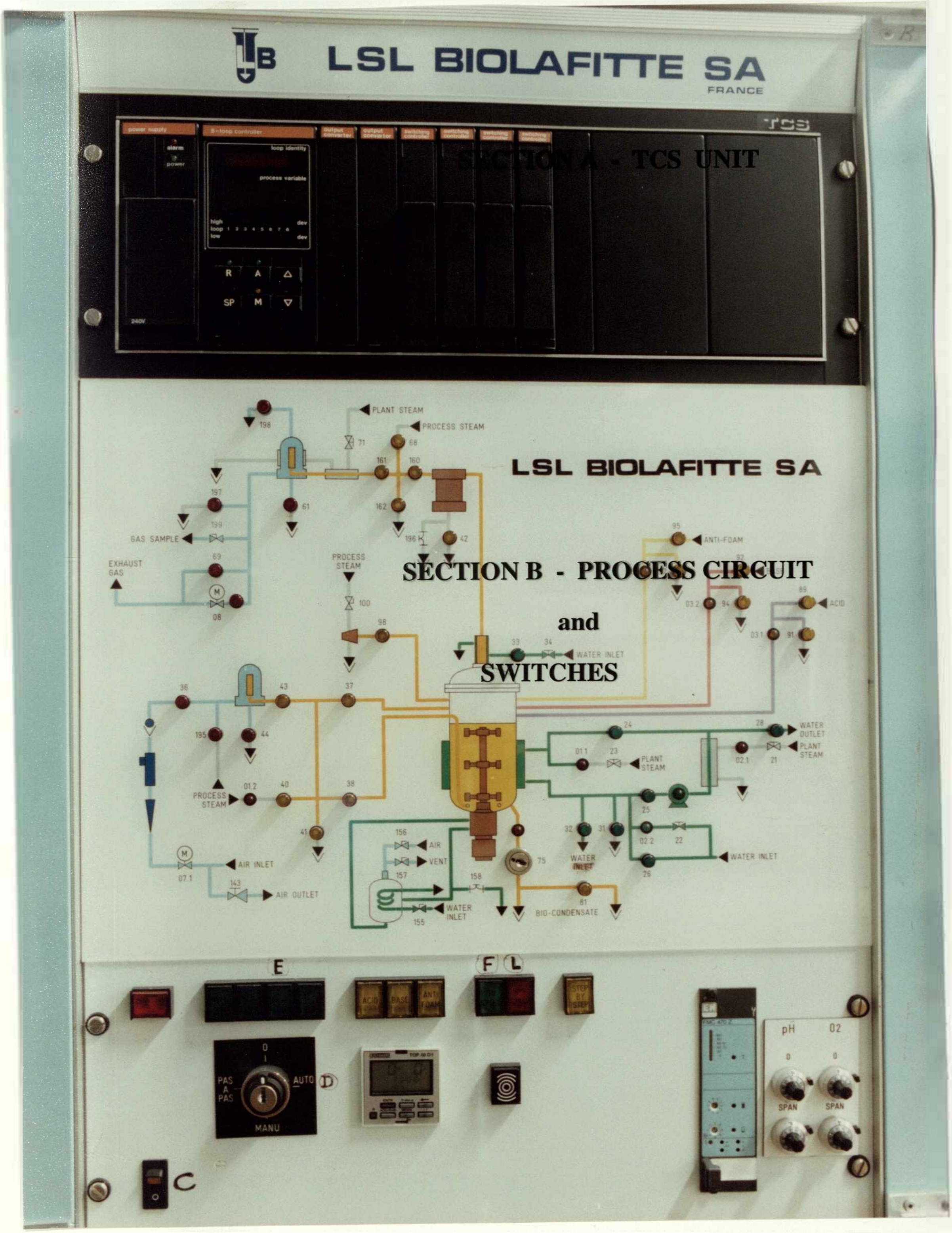

Figure 3.1 : **Front Control Panel of 800 L Pilot-Scale Bioreactor**

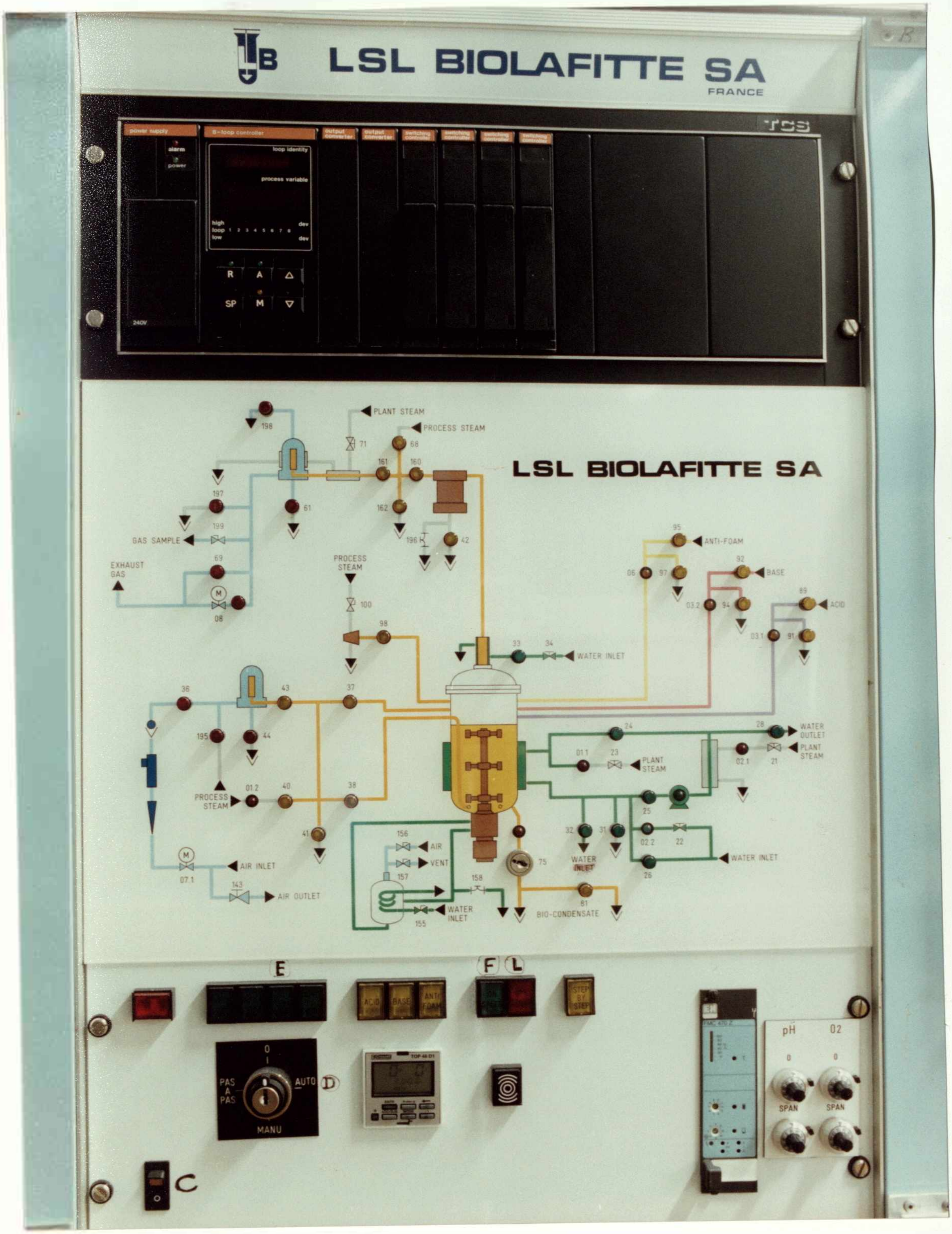
B
LSL BIOLAFITTE SA
FRANCE
TCS
power supply
alarm
power
240V
8-loop controller
loop identity
process variable
high
loop 1 2 3 4 5 6 7 8
low
dev
dev
R
A
SP
M
output converter
output converter
switching controller
switching controller
switching controller
switching controller
LSL BIOLAFITTE SA
PLANT STEAM
PROCESS STEAM
GAS SAMPLE
EXHAUST GAS
PROCESS STEAM
ANTI-FOAM
BASE
ACID
WATER INLET
WATER OUTLET
PLANT STEAM
PLANT STEAM
PROCESS STEAM
AIR INLET
AIR OUTLET
AIR
VENT
WATER INLET
WATER INLET
WATER INLET
BIO-CONDENSATE
E
F
L
ACID
BASE
ANTI FOAM
STEP BY STEP
0
PAS A PAS
AUTO
MANU
D
C
pH
O2
SPAN
SPAN

3.1.1 Heating/Cooling Circuit of the Pilot plant

The temperature on the process side is controlled by the TCS controller under the supervision of the "SETCON" data management system using which the proportional, integral and differential terms assigned on a mimic diagram (see section 3.3). These are set to 2.5, 3.0 and 0.6 respectively to ensure a short heating up period. The control valves then activate the heating or cooling cycles accordingly.

Figure 3.2 shows the cooling circuit of the pilot plant which consists of two loops. One is a recirculation loop that consists of water flowing through the pump to valve -25 into the jacket then to valve -24 and back to the water heater; this recirculation loop is always on when the plant is in operation. Valves 24 and 25 can be manually controlled by their respective switches on the main panel for the pilot plant. The second loop allows direct injection of cold water from the main water supply into the first loop which is activated either by panel mounted valve -26 or by valve -02.2 operating automatically in response to a control signal. The excess water flows into the drain through valve -28. In automatic mode when the temperature of the process fluid exceeds the setpoint then the controller activates valve -02.2 which injects mains water into the recirculation loop bringing the temperature of the process fluid back to the setpoint.

Figure 3.3 shows the heating circuit of the pilot plant. The jacket water is indirectly heated by steam in the water heater, which is a simple pipe heat exchanger with steam on the outer tube. The steam into the water heater is controlled by valve -02.1 which is activated; when the temperature of the process fluid falls below the setpoint, thus allowing live steam onto the outer tube of the water heater increasing the water temperature in the jacket.

The heating and cooling cycles are very efficient and the setpoint is maintained within a range of ±0.5^{o}C.

3.2 Modifications to the pilot plant for heat transfer studies

This pilot plant has been extensively modified for these heat transfer studies. The following equipment has been installed :

Figure 3.2: Cooling Circuits for 800L Vessel

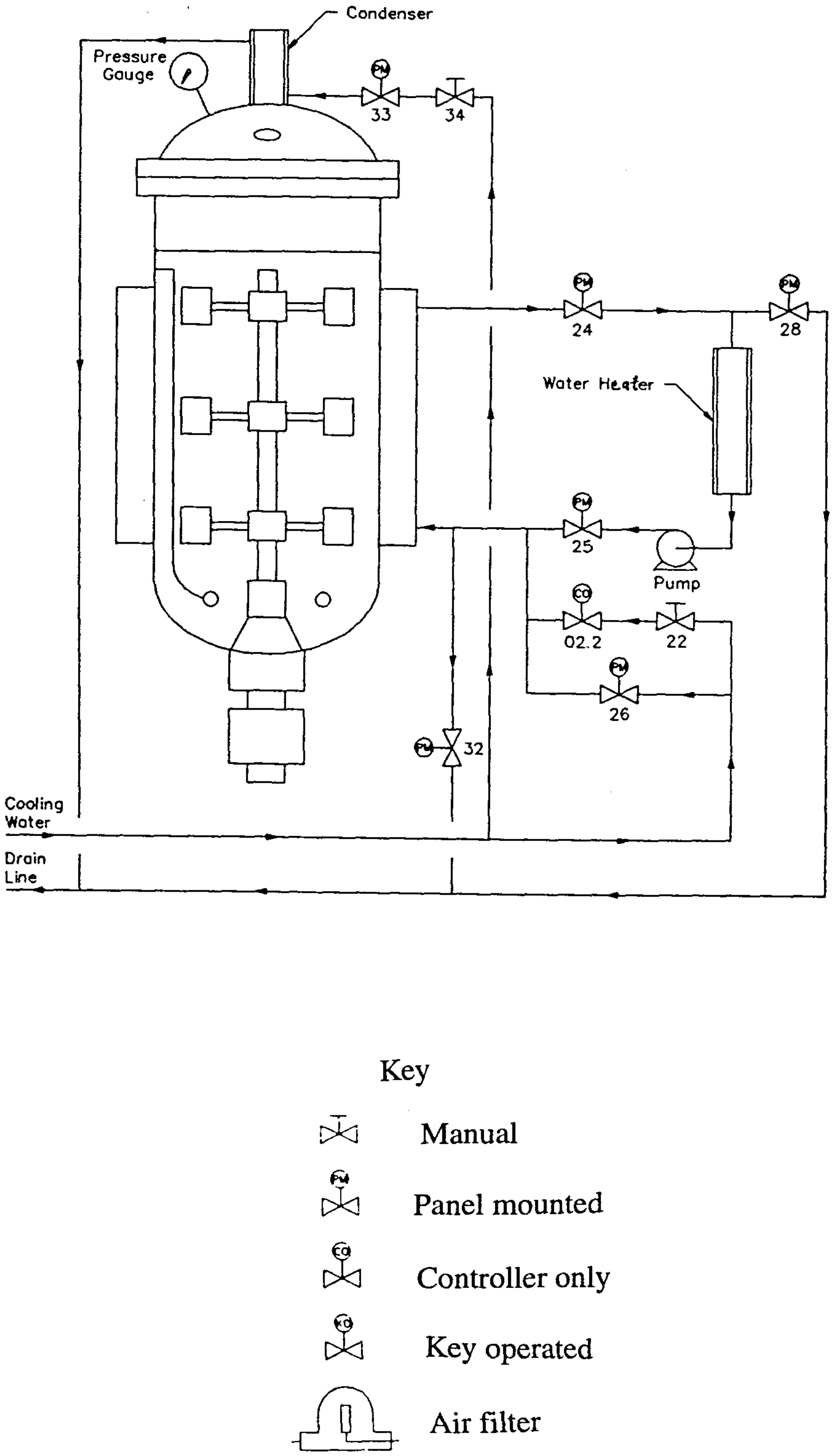

Figure 3.3 : Heating Circuit for 800L Vessel

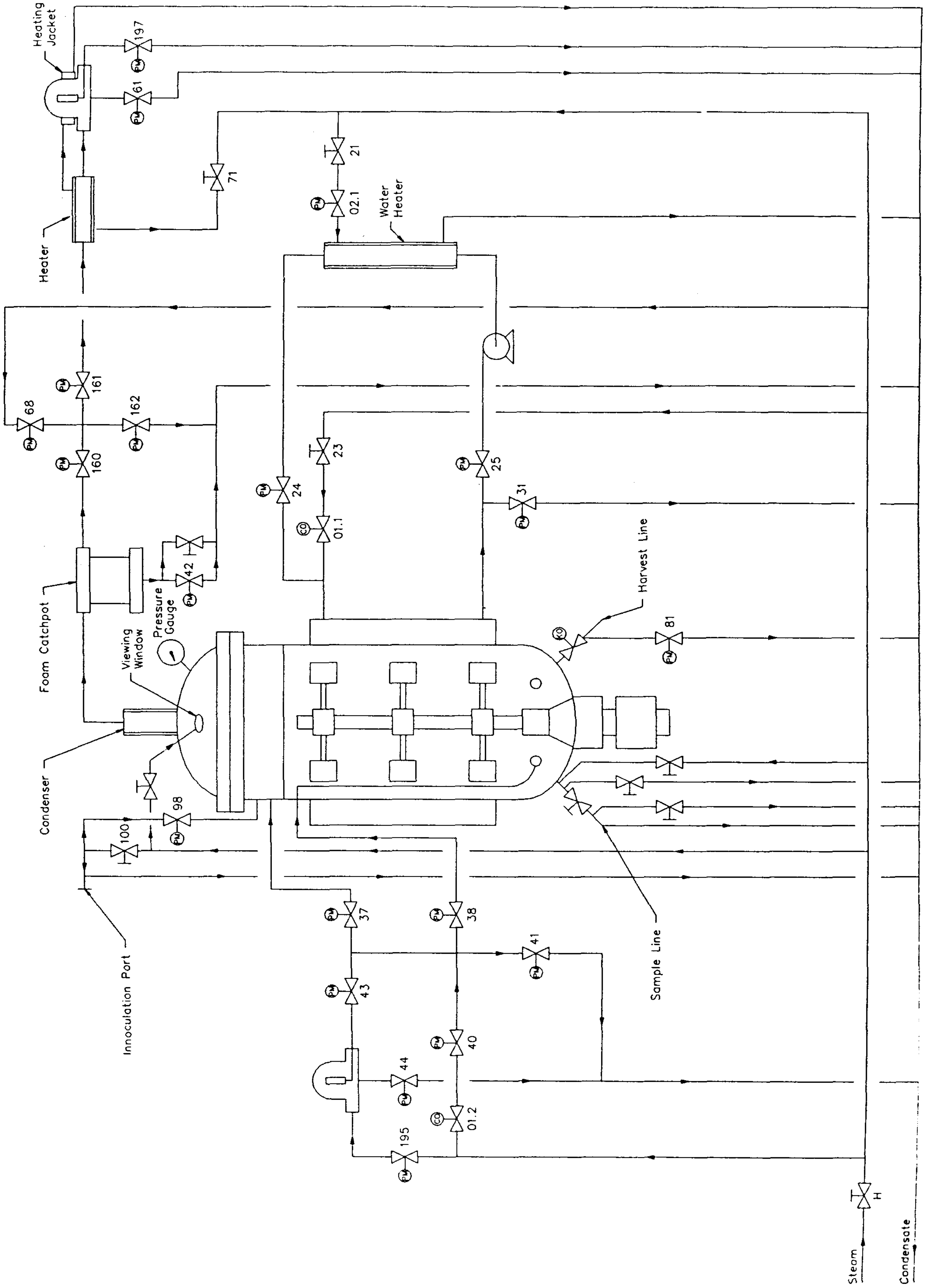

3.2.1 Heat flux and temperature profiling

The heat flux probes manufactured by Rhopoint Ltd., U.S.A., were selected after an extensive review of the literature. The output signal from the sensor is derived when the complete sensor is placed in intimate contact with the inner vessel wall. The heat flux probes are differential thermocouple type sensors consisting of a thin foil thermopile bonded to each side of a known thermal barrier. The difference in temperature across the thermal barrier is proportional to the heat flux through the sensor. Embedding the probe in an extended film allowed the boundary layer to be redeveloped over the sensing element making the probe hydrodynamically non-intrusive. The probe also has a thermocouple in it to measure the temperature of the wall. A simple program was written to process the raw data, compensating for the thermal resistance of the adhesive used in the probe . The next chapter (no. 5) is dedicated to the functioning and improvement of the heat flux probes.

Three heat flux probes were used in the study of axial variation in the heat transfer profile for a single impeller system and an additional probe was installed for a two impeller system. The positions of the various probes are shown in figure 3.4a, and figure 3.4b shows the photograph of the position of various probes placed inside the vessel (as seen from the top).

(a) Position of heat flux probes
Heat flux probe - 1 is placed at a height of 370mm above the bottom of the vessel. This height clearly places the probe on the jacket; also this height is close to the impeller plane.

Heat flux probe - 3 is placed at a height of 655 mm because this would be the probable position of a second impeller.

Heat flux probe - 2 is placed in between the above two probes.
Another heat flux probe is stuck to the outside of the jacket at the same height as the heat flux probe - 3 to monitor the heat lost to the environment.

(b) A support system specially designed to hold three movable thermocouples was placed on the baffles to allow measurement of the process fluid temperature at various heights.
(c) Two resistance temperature detectors (RTD) were stuck to the wall. These RTD were also modified following the same flow criterion as that for the heat flux probe.
RTD - 1 is placed at a height of 262mm above the bottom, this is at the height of the impeller plane for the standard vessel configuration.
RTD - 2 is placed at a height of 780mm, this is at level of the liquid for the standard vessel configuration. For two impeller system an additional heat flux probe was installed at this position (heat flux probe-4).

Figure 3.4 a: 800L Vessel dimension with probe positions

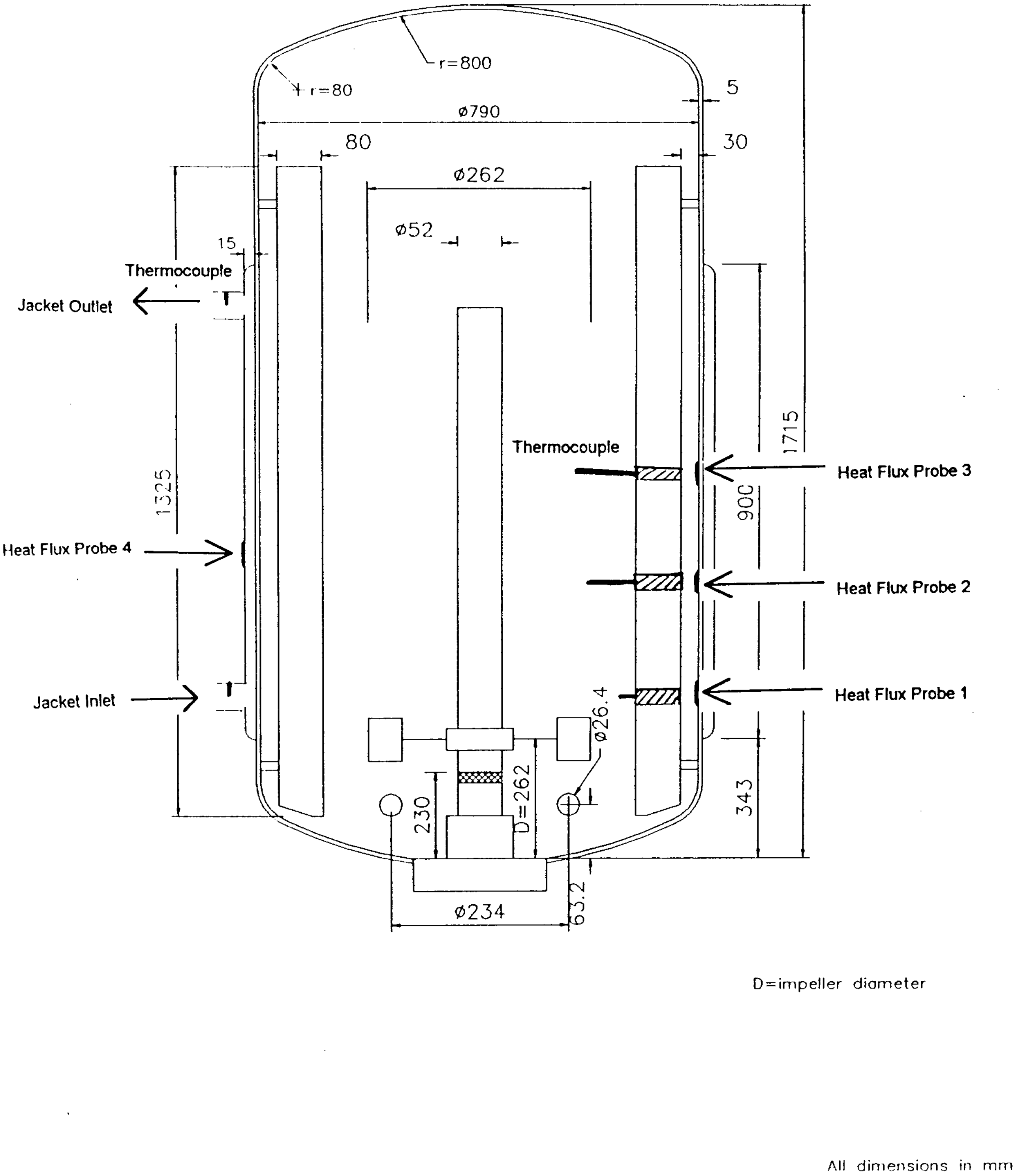

RTD-2 and HEAT FLUX PROBE-3

HEAT FLUX PROBE-2

HEAT FLUX PROBE-1

RTD 1

THERMOCOUPLES

Figure 3.4 b: 800 L Pilot-Scale Bioreactor Modification

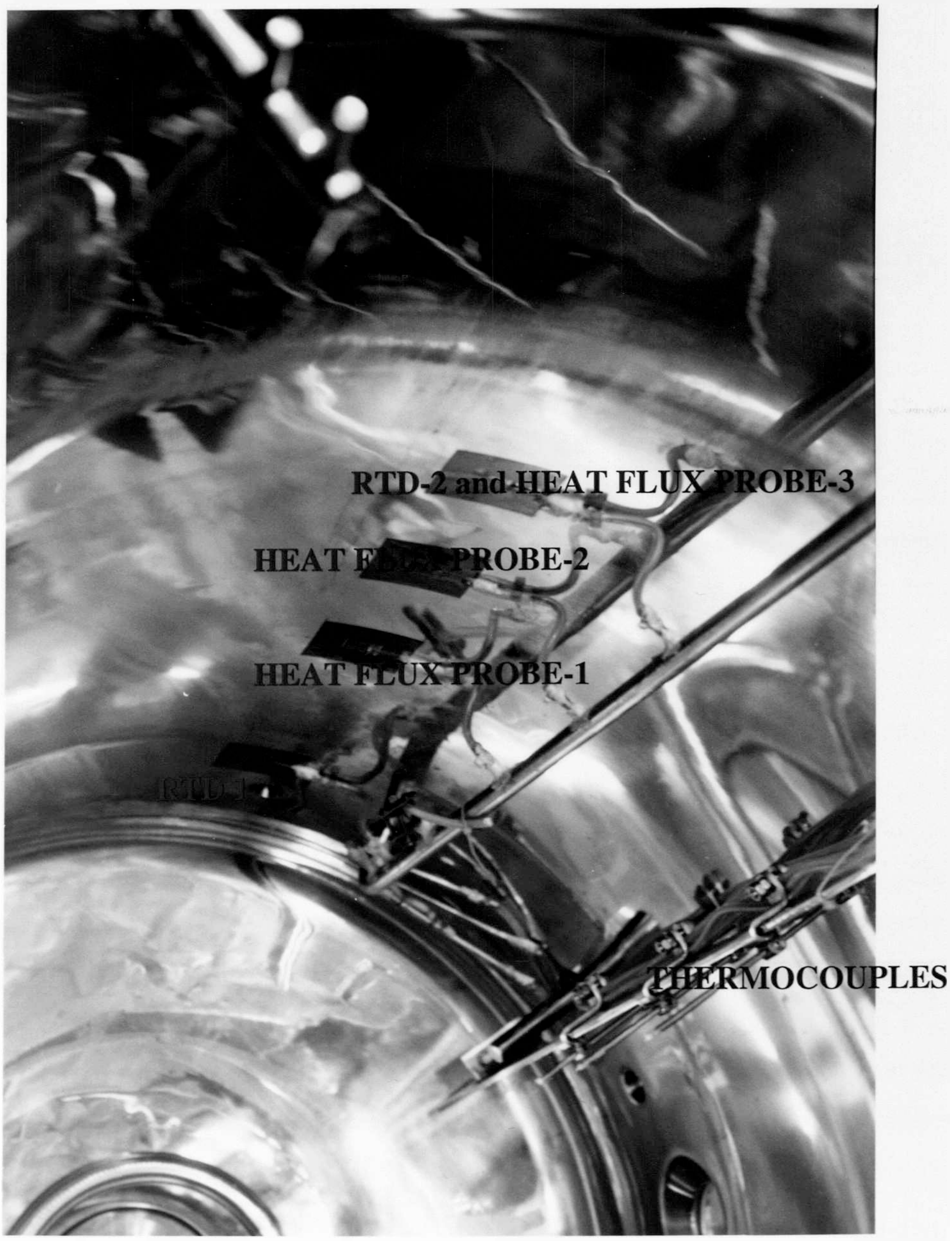

Figure 3.4 b: 800 L Pilot-Scale Bioreactor Modification

(d) Two thermocouples in thermowells were placed one each at the jacket inlet and outlet to measure the corresponding temperatures of the jacket fluid (water).

3.2.2 Turbine flow meter

One turbine flowmeter was installed in the jacket loop for the on-line measurement of water flow rate. The turbine flowmeter was supplied by Platon instrumentation, U.K. . The turbine flowmeter consists of a helically cut turbine rotor supported in two plain bush bearings, the rotor being machined from solid ferritic stainless steel of a grade compatible with the metered fluid (water), all contained within a housing of non-magnetic stainless steel. A pick off coil having a permanent magnet core is mounted in the housing adjacent to the rotor blade tips such that a magnetic circuit is set up via the rotor blades, figure 3.5 . Rotation of the rotor varies the reluctance of this magnetic circuit, and the flux changes induce a small voltage in the coil, the frequency of which is directly proportional to the volumetric flowrate. The pulses per unit volume are almost constant over a wide range of flowrates (as claimed by the manufacturer) and it is thus possible to establish a meter factor of pulses per unit of volume by which the output pulses must be divided in order to register real flow units on the associated electronic integrator. The flowmeter was linked to the SETCON by using a T 130 (T 100, TCS interface) frequency input interface module. However the length of the output lead from the turbine flowmeter to the T 130 exceeded the maximum recommended length of 3 meters and this then required a pre-amplifier which was then incorporated in the circuit. The complete arrangement is shown in the block diagram, figure 3.6 .

The flowmeter was installed with ten diameters of a straight pipe (of the same internal diameter as the flowmeter) upstream and five diameters downstream for flow straightening. The pressure drop in the flowmeter for the flow range used is around 0.2 kg/cm^2. The calibration supplied by the company was checked, after installation by simple flow measurement experiments, and was found to be applicable. The calibration factor was,

$$\text{Volumetric flow rate for 1 kHz} = 2.71 \times 10^{-3} \text{ m}^3/\text{s}$$

The output from the flowmeter is in kHz which is then processed by a simple programme to give values in mass per unit time (kg/s).

Figure 3.5 : Turbine flowmeter

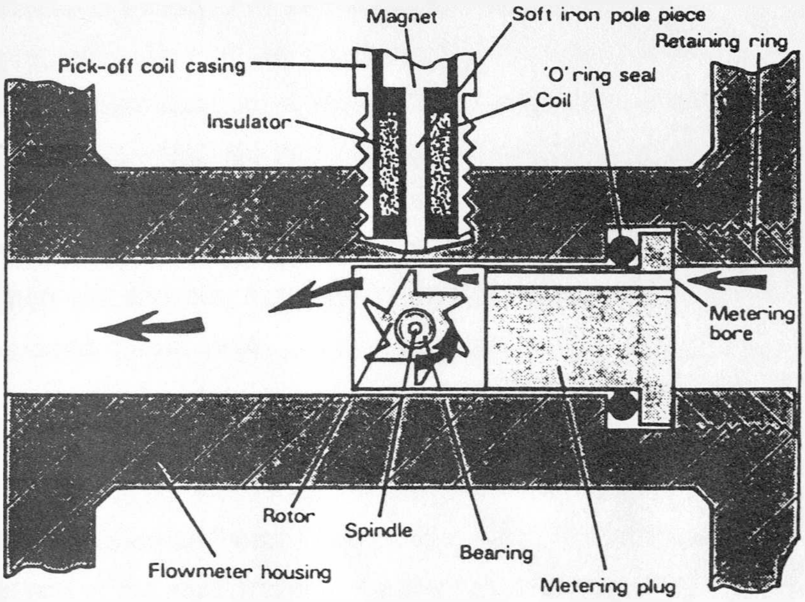

Figure 3.6 : Flowmeter Setup

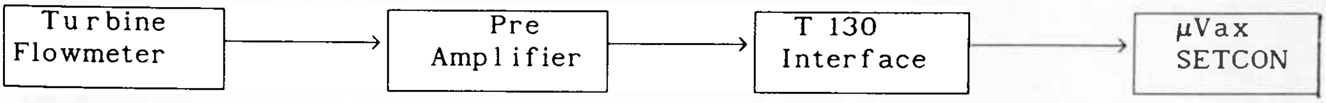

3.2.3 Strain gauge

A specially designed straingauge (fabricated in the departmental workshop) was incorporated inside the hollow shaft for power measurement. A strain gauge is a passive transducer, in which small quantities of mechanical strain are detected by passing an electrical current through an electrical resistor. Because the resistance of an electrical wire is proportional to it's length therefore any change in the length, introduced due to the twist or strain, changes the resistance of the wire. Due to the small strain levels the electrical resistance and the signal are very small and thus accurate amplification is required for good strain measurement. A load cell is designed in which the strain gauge is inserted in a complementary circuit to form a Wheatstone bridge. This load cell is then placed inside the hollow shaft and is pegged at the ends, so that the strain in the shaft is transmitted to the load cell. Any deformation by the strain in the shaft will result in a change of the strain gauge resistance; this will unbalance the previously balanced circuit (with a reference resistor) which will result in a signal which is proportional to the applied torque and hence the applied power. The signal from the strain gauges is picked up and amplified by the Telemetry placed at the bottom of the shaft. The output from the telemetry was linked to the chart recorder. For, calibration the shaft was removed form the vessel and was clamped to a specially designed equipment in a horizontal position. The end of the shaft close to the telemetry was tightly clamped while the other end having an impeller attached to it rested on a ball bearing. Known weight were then applied at the impeller end and corresponding value of signal in mV was noted, which resulted in a linear calibration curve. This then gives the sensitivity of the gauge, a typical value for this vessel was 0.014 Nm/mV. The torque M in Nm was calculated by the following equation:

$$M = 9.8 * L_S * (D/2) \tag{3.1}$$

where L_S is the load in kg.

In real operation, the reading from the chart recorder which is in milli Volts is recorded which is then multiplied by the respective slope to give the output in Newton meter (Torque). The Power is then calculated by the following equation:

$$P = 2\,\pi\,N\,M \tag{3.2}$$

A simple computer programme is written to process the raw data from the computer following the above method.

3.2.4 Ultrasonic echo gauge

An ultrasonic echo gauge was installed in the head plate of the vessel for gas hold up measurements. This was a continuous non-contact level measurement Nivosonic FMU 2780 (Endress+Hauser Ltd.) sensor which was mounted on the top of the vessel. The sensor emits ultrasonic pulses at a frequency of approximately 46 kHz. The inaudible sound waves are reflected by the liquid surface and are received by the sensor. The roundtrip time (i.e. the time elapsed between transmitting and receiving the echo) is measured electronically in the FMU 2780 and appears as an output signal proportional to the level. The built-in temperature probe in the ultra sonic sensor automatically compensates round-trip time errors which are caused by the temperature coefficient of the speed of sound in air. The signal is outputted to a chart recorder.

3.2.5 Experimental Setup

The experiment was setup for a standard vessel configuration (SVC) with a single impeller. The details of the SVC are shown in figure 2.1 . The impeller used was a Rushton turbine the details of which are given in appendix-1B

However the setup has the drawback from the heat transfer point of view, that when used in this pilot plant, the height of the process fluid covers only half of the jacket. This effect makes it difficult to establish the heat balance between the process side heat transfer, measured by the heat flux probe, and the jacket side heat transfer, measured by two thermocouples in the jacket inlet and outlet respectively.

For the two impeller system the liquid height was 1.5 D_T and the spacing between the two impellers was 1.5 D.

3.3 <u>Data management system</u>

The Biocentre uses "SETCON" data management software package (supplied by SD-Scicon) installed on the DEC MicroVAX computer running with the VMS operating system. T.C.S. interface systems are used to transfer and condition signals to the MicroVax.

3.3.1 New T-100, TCS Interface

A new T.C.S. unit model T-100, type 6438, has been installed to interface the installed equipment for heat transfer studies and the strain gauge to the MicroVax. The T-100 intelligent I/O system is a powerful multichannel instrument, capable of conditioning analogue and digital plant signals and providing analogue and digital outputs from the supervisory system. It has the same communications protocol and database structure as the other TCS intelligent instruments, making it fully compatible with the controllers and supervisory computer systems in the Network 6000 range. T-100 consists of a base unit comprising of a backplane, processor, indicators and switches, communications ports and a power supply; and a series of individual I/O modules, each comprising 1, 2 or 8 channels of analogue or digital I/O, which fit into the backplane. The I/O modules fit into the 16 sites in the backplane completely interchangeably, and the plant lines are taken directly into the front of the module. Figure 3.7 shows schematically the layout of the T-100 base unit, with external communications to a supervisory computer and to the configuration tool - a TCS 8263 hand-held terminal. The internal data bus is shown with the interaction of the processor, memory, I/O modules and external communication. The isolation between the I/O modules is also illustrated.

The T- 100 was configured manually allocating appropriate protocol, addresses ranges etc. for each piece of heat transfer equipment using an 8263 hand held terminal. The following modules were used :

i) Two T-111 - RTD input conditioners were used to interface the output from RTD-1 and 2.

ii) Two T-112 - Eight channel thermocouple input interfaces were used for all the heat flux probes and all the thermocouples.

iii) One T-120 - High level analogue input interface for the strain gauge.

iv) One T-130 - Frequency input interface for the turbine flowmeter.

The main operator interface was provided by a Graphic Console System (GCS) which generated mimic diagrams for individual fermenters on IBM compatible PCs. These were connected via a serial link to the μVAX.

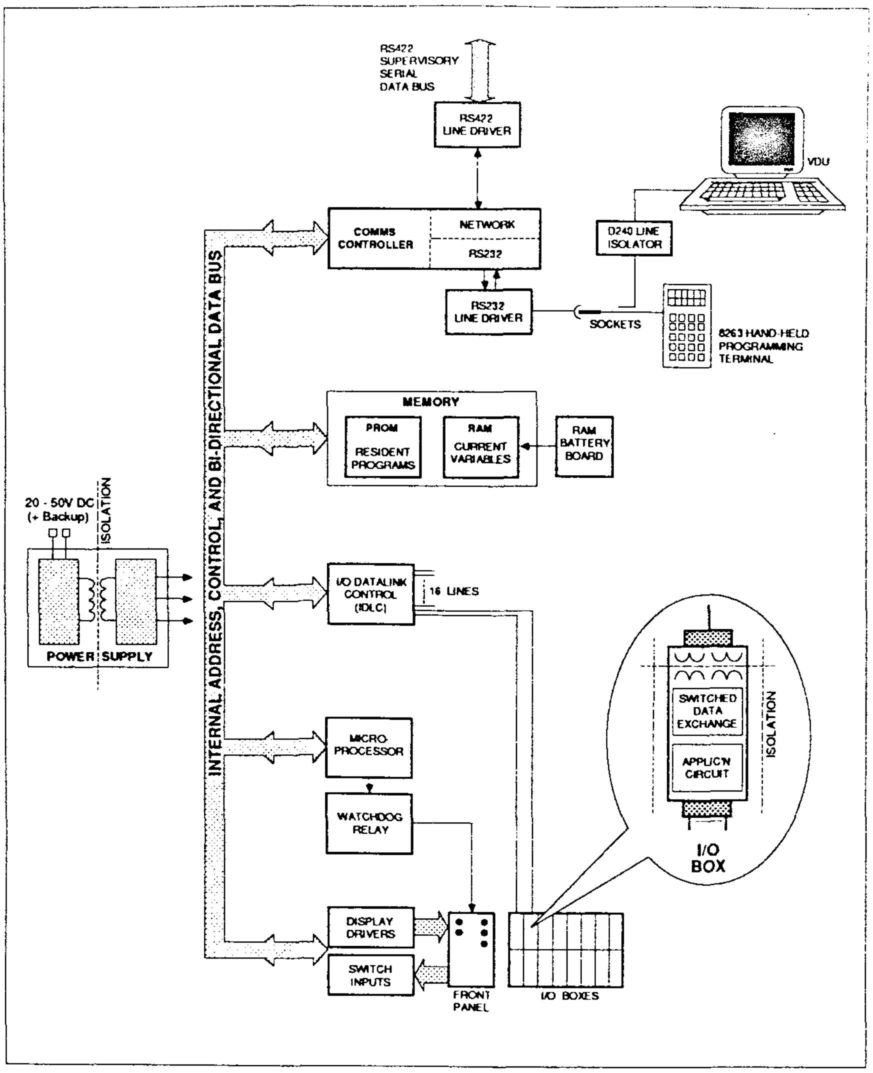

Figure 3.7 : Layout of the T100 Base Unit

T100 BASE UNIT FRONT PANEL

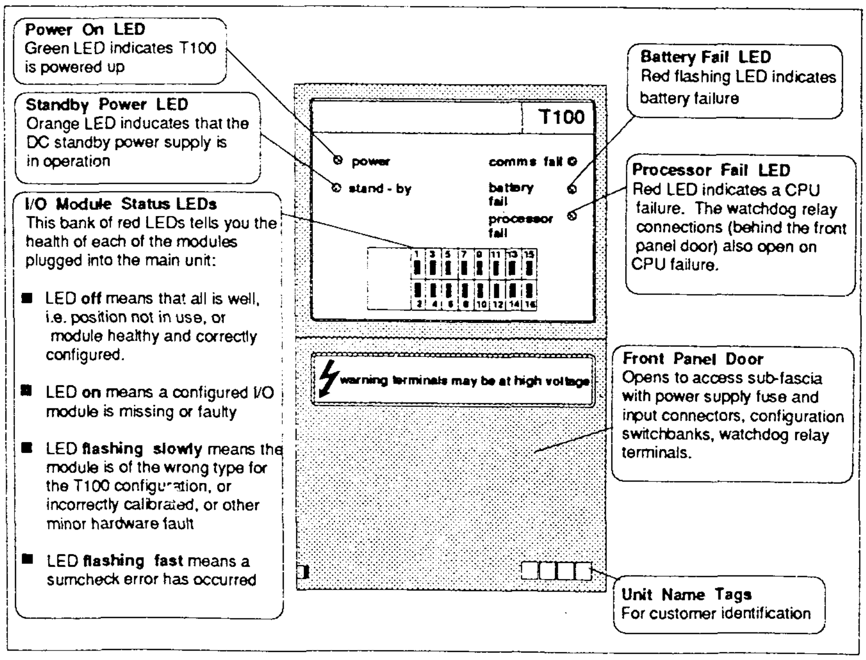

Power On LED
Green LED indicates T100 is powered up

Standby Power LED
Orange LED inducates that the DC standby power supply is in operation

I/O Module Status LEDs
This bank of red LEDs tells you the health of each of the modules plugged into the main unit:

- LED **off** means that all is well, i.e. position not in use, or module healthy and correctly configured.
- LED **on** means a configured I/O module is missing or faulty
- LED **flashing slowly** means the module is of the wrong type for the T100 configuration, or incorrectly calibrated, or other minor hardware fault
- LED **flashing fast** means a sumcheck error has occurred

Battery Fail LED
Red flashing LED indicates battery failure

Processor Fail LED
Red LED indicates a CPU failure. The watchdog relay connections (behind the front panel door) also open on CPU failure.

Front Panel Door
Opens to access sub-fascia with power supply fuse and input connectors, configuration switchbanks, watchdog relay terminals.

Unit Name Tags
For customer identification

3.3.2 Description of SETCON

All process measurements and definitions were stored in the SETCON database which was located on the hard disk of the μVAX. Process variables and digital variables for control input and output were termed PV's and DV's and were used to provide a logical link to a particular vessel or function. A typical tag name used is :

03SP1IPV

"SP1" indicates the measurement of speed of the impeller in rpm and "IPV" was used to indicate an input process variable.

Other tag names used for data gathering for heat transfer studies in the 800 l pilot plant are:

03HF1IPV : Measurement of heat flux probe-1
03HT1IPV : Measurement of wall temperature on heat flux probe-1
03HF2IPV : Measurement of heat flux probe-2
03HT2IPV : Measurement of wall temperature on heat flux probe-2
03HF3IPV : Measurement of heat flux probe-3
03HT3IPV : Measurement of wall temperature on heat flux probe-3
03EF1IPV : Measurement of heat flux lost to the environment
03EW1IPV : Measurement of wall temperature on the outside Jacket wall
03EN1IPV : Measurement of room temperature outside the vessel
03RT1IPV : Measurement of temperature of the wall inside the vessel
03RT2IPV : Measurement of temperature of the wall inside the vessel
03TK1IPV : Measurement of bulk temperature of the process fluid
03TK2IPV : Measurement of bulk temperature of the process fluid
03TK3IPV : Measurement of bulk temperature of the process fluid
03TKBIPV : Measurement of bulk temperature of the process fluid
03ST1IPV : Measurement of the strain gauge
03JT1IPV : Measurement of jacket inlet temperature
03JT2IPV : Measurement of jacket outlet temperature
03JFLIPV : Measurement of jacket flow rate
03AR1IPV : Measurement of air flow rate

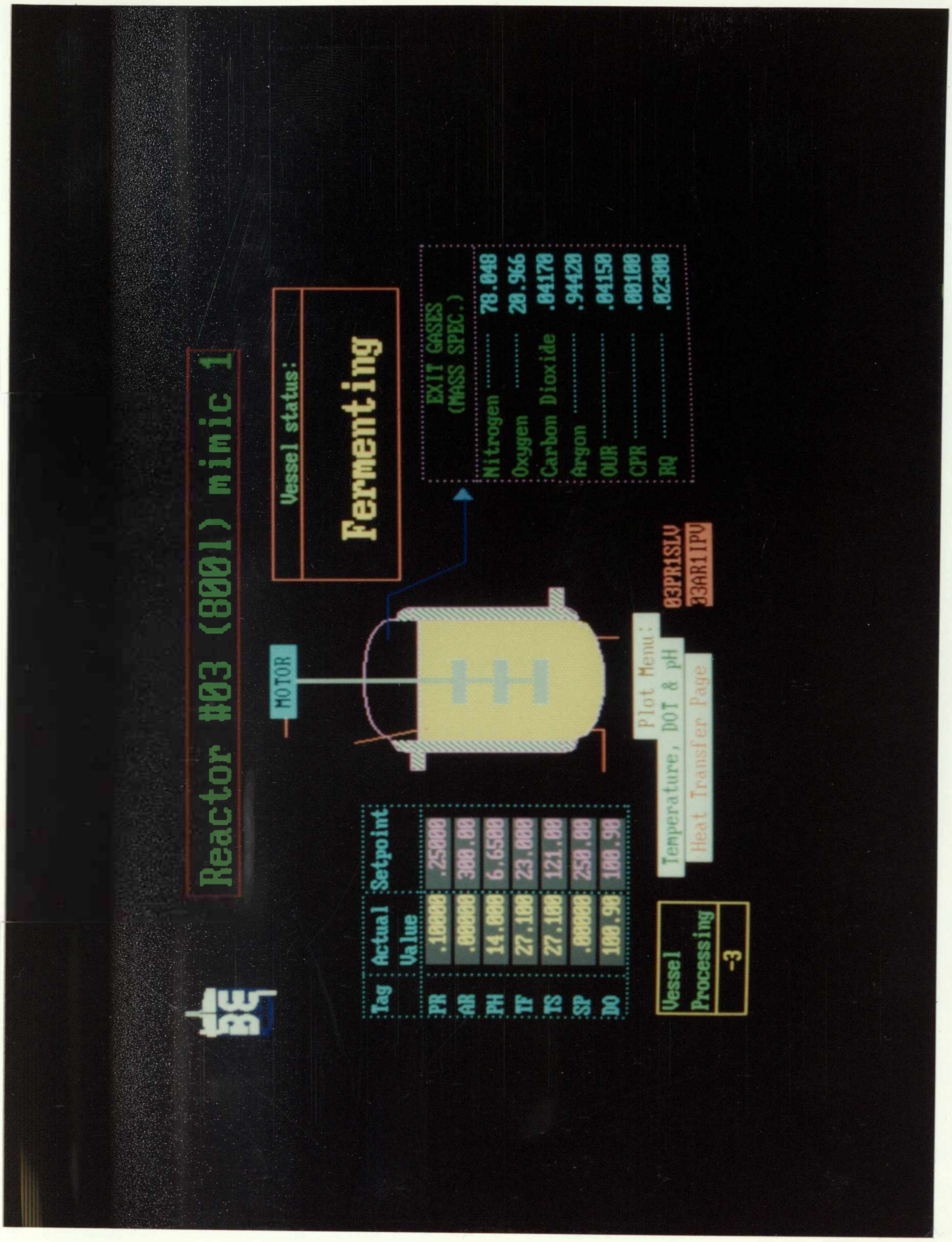

Vessel status:

Fermenting

EXIT GASES
(MASS SPEC.)

Nitrogen 78.048
Oxygen 20.966
Carbon Dioxide .04170
Argon .... .94420
OUR .... .04150
CPR .... .00100
RQ .... .02300

Tag	Actual Value	Setpoint
PR	.10000	.25000
AR	.00000	300.00
PH	14.000	6.6500
TF	27.100	23.000
TS	27.100	121.00
SP	.00000	250.00
DO	100.90	100.90

Figure 3.8 : Setcon Main Mimic Drawing for 800 L Pilot-Scale Bioreactor

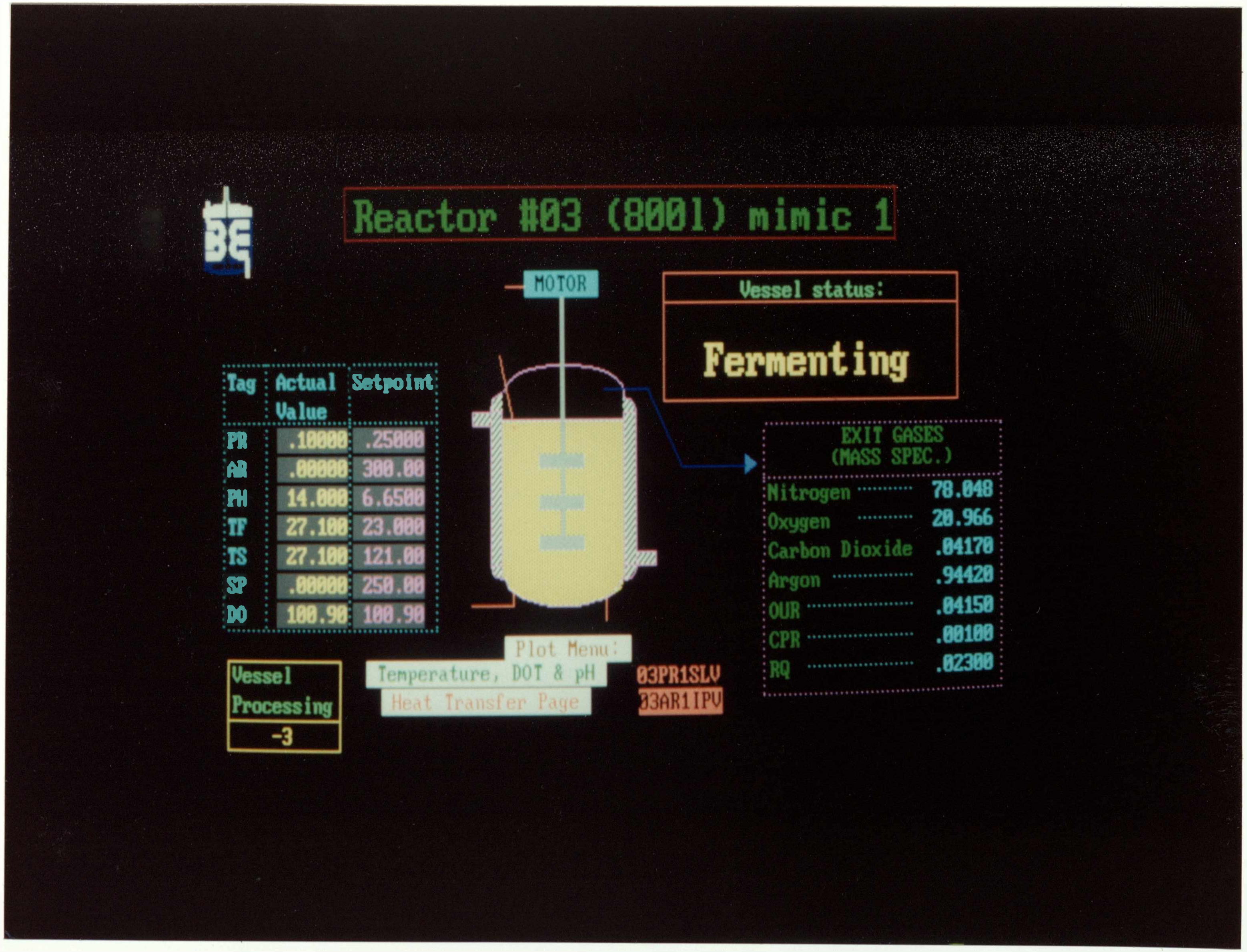

Reactor #03 (8001) mimic 1

Tag	Actual Value	Setpoint
PR	.10000	.25000
AR	.00000	300.00
PH	14.000	6.6500
TF	27.100	23.000
TS	27.100	121.00
SP	.00000	250.00
DO	100.90	100.90

Vessel status:

Fermenting

EXIT GASES
(MASS SPEC.)

Nitrogen	78.048
Oxygen	20.966
Carbon Dioxide	.04170
Argon	.94420
OUR	.04150
CPR	.00100
RQ	.02300

Vessel Processing

-3

The GCS program displayed the mimic diagrams on the PC and communicated between the PC and SETCON on the μVAX to retrieve process data. The mimic diagram represented a bioreactor and included a display of all current probe measurements. The main mimic drawing of the vessel is shown in figure 3.8. The Analogue inputs from the probes are received by the TCS under unique "addresses" which are transferred and stored in the respective tags after initial processing. Scanning is the term used in SETCON to indicate when an "AI" is requesting or receiving data. Scanning time could be entered in the group information and this set the time interval (3 seconds) at which the TCS unit associated with a particular AI.

A special mimic was drawn for this heat transfer study as shown in figure 3.9; this mimic drawing also shows a section of the vessel showing the approximate position of the various probes. Trending is the term used for the storage of historical data by SETCON. Data is stored every minute in a circular buffer for up to 14 days. The data was stored using either the Batchdat, for 60 seconds storage or above, or Faststore , for 3 sec to 60 sec storage, facility.

3.4 Rheological Measurements

3.4.1 Model fluids

A Contraves rheometer (Rheomat 30, Contraves Industrial Products Ltd, Ruislip, Middlesex, U.K.) was used for rheological measurements. Details of the operating principles and theory of a concentric cylinder rheometer are given by Whorlow [79]. The test fluid in the gap between a rotating inner bob and a stationary outer cylinder is subjected to a pre-programmed, reversible, shear cycle. The torque-rotational speed data of the bob is interpreted to yield the shear stress. Measuring system "A" of the Contraves was used, over a shear rate range of 8.99 to 660 s^{-1} . The average shear rate in the vessel was estimated as, 19 - 87.0 s^{-1} , using equation (2.64), ($N = 100 - 450$ rpm, $k_s = 11.5$). The cylinder containing the test fluid was immersed in a constant temperature water bath to reach a steady state temperature. Viscosity is temperature sensitive and care was taken to ensure that a steady state was reached before the measurement. In more viscous model fluids cylinders B and C were used.

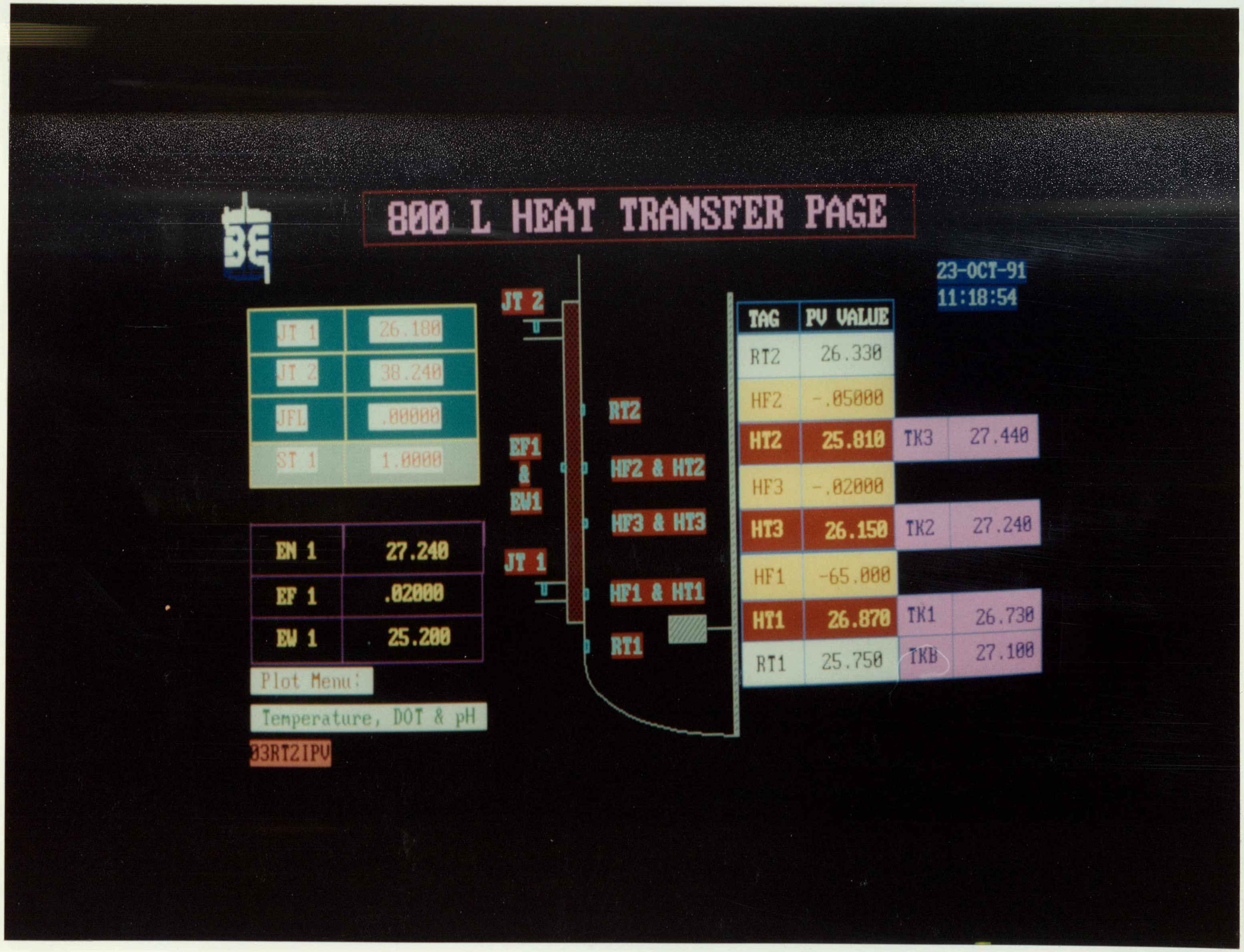

800 L HEAT TRANSFER PAGE

23-OCT-91
11:18:54

JT 1	26.180
JT 2	38.240
JFL	.00000
ST 1	1.0000

EN 1	27.240
EF 1	.02000
EW 1	25.200

TAG	PV VALUE		
RT2	26.330		
HF2	-.05000		
HT2	25.810	TK3	27.440
HF3	-.02000		
HT3	26.150	TK2	27.240
HF1	-65.000		
HT1	26.870	TK1	26.730
RT1	25.750	TKB	27.100

Figure 3.9 : Setcon Mimic Drawing for Heat Transfer Study in 800 L Pilot-Scale Bioreactor

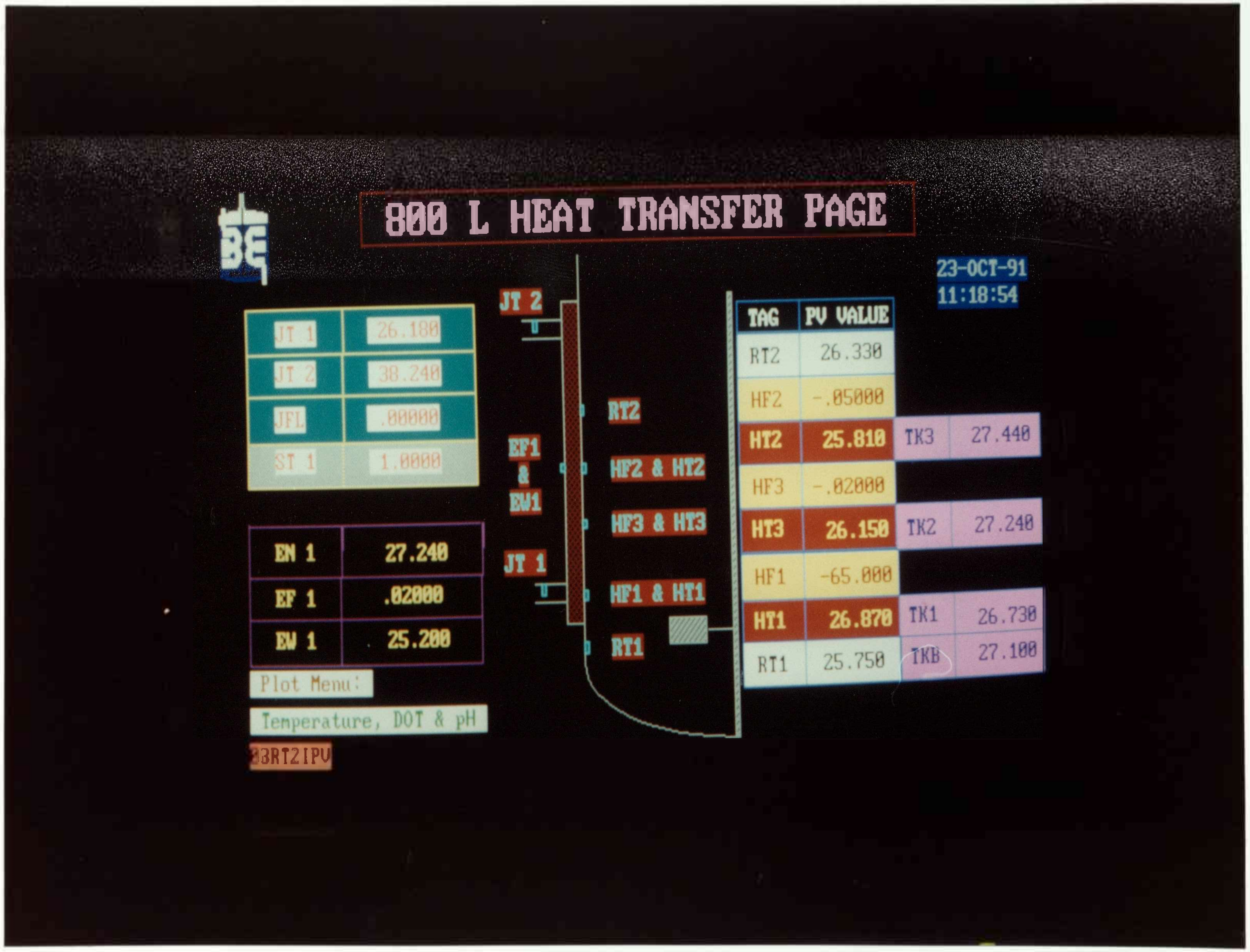

800 L HEAT TRANSFER PAGE

23-OCT-91
11:18:54

JT 1	26.180
JT 2	38.240
JFL	.00000
ST 1	1.0000

EN 1	27.240
EF 1	.02000
EW 1	25.200

Plot Menu:

Temperature, DOT & pH

3RT2IPV

TAG	PV VALUE		
RT2	26.330		
HF2	-.05000		
HT2	25.810	TK3	27.440
HF3	-.02000		
HT3	26.150	TK2	27.240
HF1	-65.000		
HT1	26.870	TK1	26.730
RT1	25.750	TKB	27.100

3.4.2 Mycelial broths and solid suspension

The particulate nature of mycelial suspensions poses particular problems to the use of conventional viscometers e.g. concentric cylinder, cone and plate and tube viscometers [110,111]. Problems arise because of the close clearances in concentric cylinder viscometers since the particle size can often be of a similar order of magnitude as the gap. This effect, combined with settling of the solid phase, leads to phase separation [112].

Bogenaar et al [113] developed a less fundamental but more reproducible method of characterising the rheology of mycelial suspensions. The technique overcomes the problems stated above by mixing the sample at the same time that the measurements are being made. A standard Rushton disc turbine replaces the bob of a concentric cylinder device rotating in a beaker containing the sample. It is then possible to relate the torque on the impeller to the apparent viscosity and the shear rate can be inferred from the impeller speed ($Re \leq 10$).

When a disc turbine rotates in a suspension or solution the power draw by the impeller is a function of the Reynolds and Froude numbers, which could be written as,

$$N_p \propto Re^a Fr^b \qquad (3.3)$$

Under laminar condition the Froude number could be neglected as no vortices are formed. The relationship then simplifies [114] to

$$N_p = c/Re \qquad (3.4)$$

where c is a constant.

Substitution of equations 2.3 and 2.5 in the above equation and rearranging gives,

$$P = c\, N^2 D^3 \mu \qquad (3.5)$$

thus, if the power draw at a given impeller speed is known, the viscosity can be found. It is however more convenient to measure the torque (M) on the shaft,

$$P = 2\,\pi\, N\, M \qquad (3.6)$$

Substituting in equation (3.5) and rearranging gives,

$$\mu = 2\,\pi\, M/\, c\, D^3 N \qquad (3.7)$$

the viscosity can now be directly calculated. For shear thinning broths the apparent viscosity could be correlated using the power law model, i.e.,

$$\mu_a = K\,(k_s N)^{n-1} \tag{3.8}$$

However before this technique is used the values of two calibration constant (c and k_s) must be obtained. The value of c is calibrated using a known Newtonian solution. It is then possible to construct a graph of power number against Reynolds number (log-log plot). The intercept would give the value of c.

For shear thinning fluids the value of k_s needs to be calibrated. Substituting equation (3.8) in equation (3.5) gives,

$$P = c\,D^3\,K\,k_s^{\,n-1}\,N^{\,n+1} \tag{3.9}$$

or

$$P = A\,N^{n+1} \tag{3.10}$$

where $A = c\,D^3\,K\,k_s^{\,n-1}$

Thus a plot of power against impeller speed for a pseudoplastic fluid on logarithmic co-ordinates will be a straight line of slope n+1 and the intercept (N=1) will give A. From this value, k_s could be calculated. The Rushton impeller used was of diameter 53 mm and the calculated values of k_s and c were 12.544 and 80.88 respectively.

3.5 Model fluids and their preparation

3.5.1 Glucose solutions

The sugar solution used for this study was supplied by Tunnel refineries limited, under the brand name glucose-140. It was a mixture of simple and complex sugars (19% Dextrose, 14% Maltose, 11% Maltotriose and 56% Higher sugars) and the true solid content was 80%. The company provided data for thermal conductivity, specific heat and viscosity for various concentration of solids (see appendix 2) Three concentrations of what is hereafter referred to as glucose were used in this study. Glucose 1 was the most viscous containing 56-57% solids, Glucose 2 contained 54-55% solids whereas Glucose 3 had 46-48% solids.

The original solution supplied by the company (viscosity=65,000 cP) was mixed with water to give a solids concentration of 56-57%. This was the maximum concentration used in the

400 litre configuration. A preservative (Kathon) was also added. After 2 days of experiments additional amount of water was added to make 54-55% solution of glucose (glucose-2). After the experiments using this concentration then an additional amount of water was added to make a total of 600 litres solution (glucose-3) which was used with the two impeller system at a 1.5:1 aspect ratio. After this the volume in the vessel was brought down to 400 litre (same concentration, 46-48% solids) and then experiments were conducted using a single Rushton impeller.

3.5.2 Pulp solutions

The paper pulp fibre was supplied by I.C.I plc (courtesy Mr. M. Cooke) and was a raw (unprocessed) eucalyptus fibre in a form of sheets. These fibre sheets were suspended in a small volume of glucose-3 solution (outside the vessel) using a homogeniser, which was then transferred to the vessel. Four concentrations of pulp namely, 1 g/l, 2.5 g/l, 5.0 g/l and 10 g/l were suspended successively in a similar manner in the glucose-3 solution.

3.5.3 Carboxymethyl Cellulose

Sodium Carboxymethyl cellulose, (CMC), type 7H4, (Hercules Ltd, London, U.K.) is an anionic water soluble polymer. The cellulose ether is produced by reacting alkali cellulose with sodium monochloractate. CMC has numerous commercial applications, acting as a thickening, suspending, binding, stabilising or film-forming agent in, example, the food, pharmaceutical and adhesive industries.

CMC powder is hygroscopic (i.e. it absorbs moisture from the air) and therefore it was stored in a tightly sealed container. The rheological properties of the solution vary, depending on concentration and method of preparation.

The percentage of moisture content was taken to be 7.7% w/w [115]. Solutions (0.1% and 0.28%), were prepared in the pilot plant using the following calculation to obtain the required weight of undried polymer:

$$X = \frac{W * Z}{100 - M - Z}$$

where

X = weight of undried polymer (kg)
M = moisture content (% w/w)

W = weight of water to which polymer is added (kg)
Z = required final polymer concentration (% w/w)

The solution was madeup in tap water and no preservative (anti-bacterial/fungal agent) was added. It was confirmed experimentally that the solution of CMC could be used safely for 48 hours without significant bio-degradation.

The powder was added carefully to the surface of the water via a long plastic tube to allow an even distribution. The impeller speed was gradually increased but was maintained at a value just below that required for surface aeration throughout the preparation stages. The solution was mixed for a period of 6 hours and left overnight to allow complete hydration of the polymer and the escape of small bubbles from solutions.

CHAPTER-4

Modification of the heat flux probe and validation of the technique

In this chapter the local heat flux probe ,which is at the heart of the study, is described in detail in section 4.1. The shortcomings of the probe were soon realised and, based on boundary layer principles, a suitable modification of the probe is described in section 4.2 . Also examined in this section is the improvement of the robustness and reliability of the probe. Then the principles behind the signal processing of the probe are described in section 4.3. Lastly, but most important, the results obtained from these probes are validated using a comprehensive correlation available in the literature (section 4.4).

4.1 *Working principle of the probe*

The heat flux probe manufactured by Rdf Inc., U.S.A., (see figure 4.1) was selected after an extensive review of the literature . Factors that affected this selection were the method of measurement, calibration, accuracy, robustness, cost, prior knowledge, sensitivity and response time.

The heat flux sensor is a differential thermocouple type sensor which utilises a thin foil type thermopile bonded to both sides of a known thermal barrier as shown in figure 4.1. The difference in temperature across the thermal barrier is proportional to the heat flux through the sensor. Thermoelectric junctions are formed from the materials "Chromel" and "Alumel" on the upper surface of the barrier. In series with these are corresponding junctions mirror imaged on the lower surface. This construction results in an equal number of junctions on the upper and lower surfaces.

Figure 4.1

MODIFIED HEAT FLUX PROBE

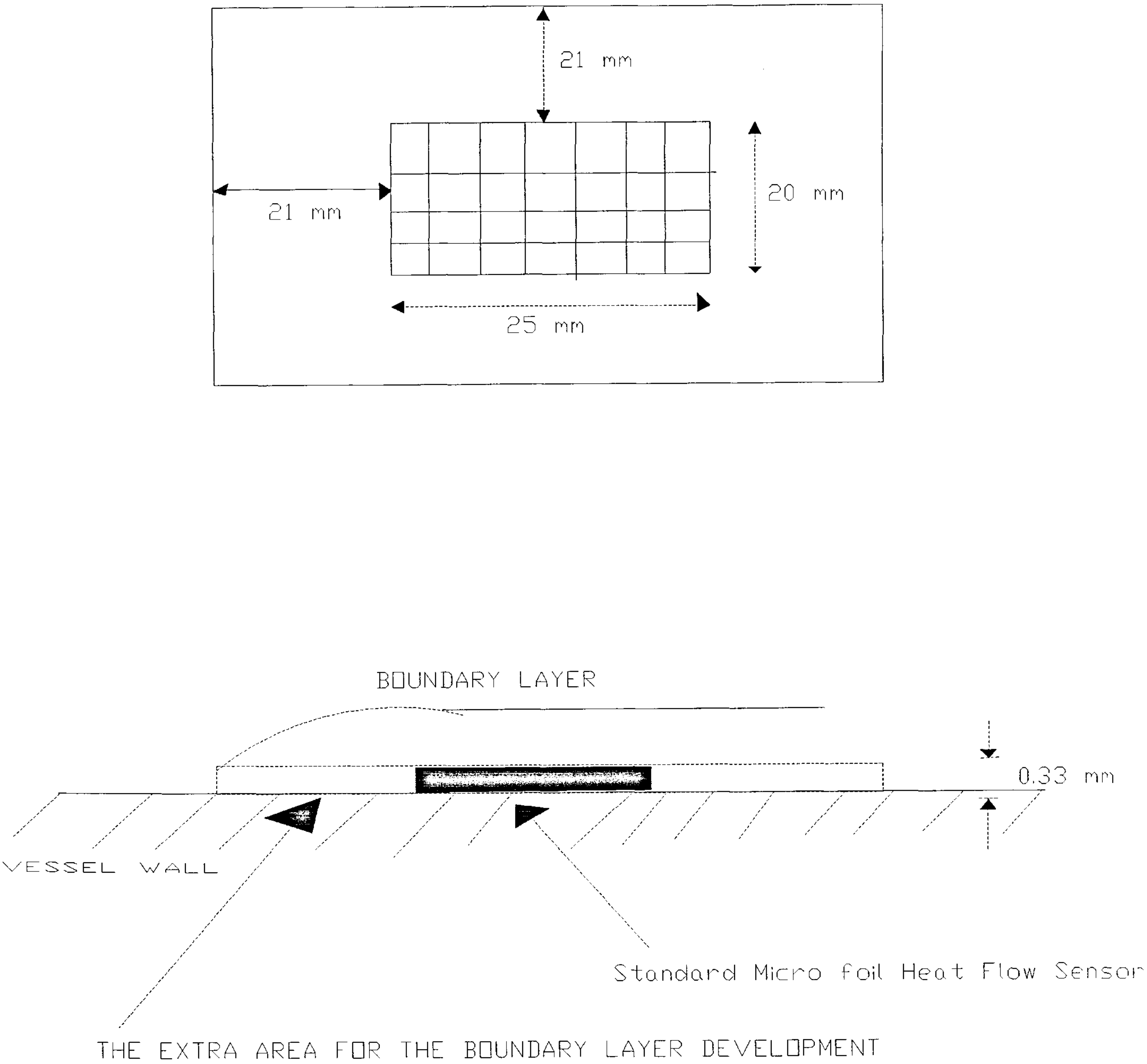

The output signal from the sensor is derived when the complete sensor is placed in intimate contact with the inner vessel wall. The same energy must pass through the sensor as passes through the wall, assuming no heat losses normal to this flow. As a result of the thermal energy passing through this thermal barrier a temperature gradient (ΔT) is generated. This gradient is directly proportional to the magnitude of the heat transfer rate. The factors which affect the magnitude of (ΔT) are the heat transfer rate, the thickness of the barrier, and the thermal conductivity of the barrier material. The relationship between these factors is (for one dimensional heat transport):

$$\Delta T = Q\, S / K \tag{4.1}$$

where:

Q = heat transfer rate , Watts

S = thickness of the thermal barrier in the heat flux probe , m

K = thermal conductivity of the barrier in the heat flux probe , W/m K

4.2 Modification to the heat flux probe

4.2.1 Boundary layer modification

The prime consideration in film heat transfer measurement is that the boundary layer at the vessel wall should be maintained. It is of course unavoidable that some disturbance must take place when a physical probe such as that in this case needs to be installed so, instead, allowance must be given for the boundary layer to become fully developed again over the probe measuring surface so as to make the probe hydrodynamically and thermally non-intrusive. In the following section the fundamentals of the boundary layer are described on the basis of which the improvement in the probe design was carried out, for the first time specifically for this study, to make the probe hydrodynamically and thermally non-intrusive.

4.2.2 Boundary-layer fundamentals

The concept of a boundary layer was introduced by Prandtl in 1904. There are two types of boundary layer; the hydrodynamic and the thermal boundary layer.

The concept could be physically explained as follows. For a fluid flow along a flat plate (for a vessel of diameter 0.79 m used in the study the small area where the probe is stuck on the wall can be assumed to be a flat plate), irrespective of whether the flow is laminar or turbulent, the fluid elements are slowed down by virtue of viscous forces. Due to friction the fluid elements adjacent to the surface stick to it and have zero velocity relative to the boundary. Other fluid elements attempting to slide over them are retarded as a result of an interaction between faster and slower fluid, a phenomenon which gives rise to shearing forces. In laminar flow the interaction, called viscous shear, takes place between molecules on a submicroscopic scale. In turbulent flow an interaction between lumps of fluid on a macroscopic scale, called turbulent shear, is superimposed on the viscous shear. The effect of the viscous forces originating at the boundary extends into the body of the fluid, but a short distance from the surface the velocity of the fluid particles approaches that of the undisturbed free stream. The fluid contained in the region of substantial velocity change is called the hydrodynamic boundary layer. The thickness of the boundary layer has been defined as the distance from the surface at which the local velocity reaches 99% of the external (main stream) velocity u_∞ . By means of the boundary layer concept, the equations of motion (Navier-Strokes equation) can be reduced to a form in which they can be solved; the effects of viscosity on the flow can be determined and the frictional drag can be calculated. The velocity profiles near the leading edge (in this case the heat flux probe) are representative of laminar boundary layers. However, the flow within the boundary layer remains laminar only for a certain distance from the leading edge and then becomes turbulent. As the laminar boundary layer thickens, the ratio of viscous forces to inertia forces decreases, and eventually a point is reached at which disturbances will no longer decay, but will grow with time. Then the boundary layer becomes unstable and the transition from laminar to turbulent flow begins. Eddies and vortexes form and destroy the laminar regularity of the boundary layer motion. Quasi-laminar motion persists only in a thin layer in the immediate vicinity of the surface. This portion of a generally turbulent boundary layer is called the laminar sublayer. The region between the laminar sublayer and the completely turbulent portion of the boundary layer is called the buffer layer. The distance from the leading edge at which the boundary layer becomes turbulent is called the critical length x_C . This distance is usually specified in terms of a dimensionless quantity called the local critical Reynolds number,

$$Re_C = u_\infty \rho \, x_C / \mu \tag{4.2}$$

which is an indication of the ratio of the inertia to viscous forces at which disturbances begin to grow. The point of transition has been shown [116] to depend on the surface contour, the surface roughness, the disturbance level, and even on the heat transfer. When the flow is calm and no disturbances occur, laminar flow can persist in the boundary layer at Reynolds numbers as high as 5×10^6 . If the surface is rough, or disturbances are intentionally introduced into the flow, as for example by means of baffles, the flow may become turbulent at Reynolds numbers as low as 8×10^4 . Under average conditions, the flow over a flat plate becomes turbulent at a distance from the leading edge x_C and local velocity u_l, where the local Reynolds number

$$Re_l = u_l \rho x_C / \mu \qquad (4.3)$$

is approximately equal to 5×10^5

Just as a velocity boundary layer develops when there is fluid flow over a surface, a thermal boundary layer must also develop if the fluid freestream and surface temperature differ. Consider flow over an isothermal plate in the immediate vicinity of the wall; heat can only flow by conduction because the fluid elements are stationary here relative to the boundary. One would naturally expect a large temperature drop in this layer. As one moves further away from the wall, the movement of the fluid aids in the energy transport and the temperature gradient will be less steep, eventually levelling out in the main stream. When a fluid flow is laminar, heat is transferred only by molecular conduction within the fluid as well as at the interface between the fluid and the surface. There exist no turbulent mixing currents or eddies by which energy stored in fluid elements is transported across streamlines. Heat is transferred between fluid layers by molecular motion on a submicroscopic scale. On the other hand, in turbulent flow the conduction mechanism is modified and aided by innumerable eddies which carry lumps of fluid across the streamlines. These fluid elements act as carriers of energy and transfer energy by mixing with other elements of the fluid. An increase in the rate of mixing (or turbulence) will therefore also increase the rate of heat flow by convection. The fluid may be set in motion as a result of density differences due to a temperature variation in the fluid; this mechanism is called free, or natural convection. When the motion is caused by some external energy, such as an impeller or gas flow, it is termed forced convection.

The thermal boundary-layer thickness δ_t is defined as the distance from the surface at which the temperature difference between the wall and the fluid reaches 99 percent of the free-stream value. According to Pohlhausen's calculations [116], the relationship between the thermal and hydrodynamic boundary layer is approximately ,

$$\delta_t = \delta / Pr^{1/3} \qquad (4.4)$$

Therefore, for liquids ($Pr > 1$), the thermal boundary layer is smaller than the hydrodynamic boundary layer.

Furthermore, the thermal boundary layer thickness can be predicted using a simple model by assuming a hypothetical layer of fluid of thickness δ_t' which, if completely stagnant, offers the same thermal resistance as the actual boundary layer. In this stagnant layer, heat can flow only by conduction which can be equated with Newton's law of cooling,

$$Q/A = K (T_w - T_\infty) / \delta_t' = h (T_w - T_\infty) \qquad (4.5)$$

therefore

$$\delta_t' = K / h \tag{4.6}$$

This is an oversimplification [116], but the results will be within acceptable error limits .

For laminar boundary flow over a flat plate, Hansen [117] define the hydrodynamic boundary-layer thickness as ,

$$\delta_L = 5\, x / (Re_x)^{0.5} \tag{4.7}$$

and for the turbulent case the boundary layer thickness is ,

$$\delta_T = 0.376\, x / (Re_x)^{0.2} \tag{4.8}$$

where, $Re_x = u_\infty \rho\, x / \mu$ and x is the distance from the leading edge.

It can be seen from equations 4.7 and 4.8 that, at any given value of x, a turbulent boundary layer thickness increases at a faster rate than a laminar boundary layer. Despite its greater thickness, the turbulent boundary layer offers less resistance to heat flow than a laminar layer because the turbulent eddies produce continuous mixing between warmer and cooler fluids on a macroscopic scale. These eddies diminish in intensity in the buffer layer and hardly penetrate the laminar sublayer. Unless the Prandtl number is unity, the relative magnitudes of the eddy conductivity and the molecular conductivity in the vicinity of the surface have a pronounced effect on the heat-transfer coefficient.

von Karman [118] divided the turbulent flow field into three zones: a laminar sublayer adjacent to the surface in which the eddy diffusivity is zero and heat flows only by conduction; next to it, a buffer layer in which both conduction and convection contribute to the heat transfer mechanism; and finally, a turbulent region in which conduction is negligible compared to convection. He used experimental data for the velocity distribution and the shear stress. He assumed that the physical properties of the fluid are independent of the temperature and predicted theoritically the thermal resistance in each of the three zones:

Thermal resistance of laminar sublayer,

$$R_{sub} = 5\, Pr / [\, c_p\, (\rho\, \tau_s)^{0.5}\,] \tag{4.9}$$

Thermal resistance of buffer layer,

$$R_{buf} = 5 \ln (5Pr + 1) / [\, c_p\, (\rho\, \tau_s)^{0.5}\,] \tag{4.10}$$

Thermal resistance of turbulent layer,

$$R_{tur} = 5\,(1 + \ln 6) + [\,u_\infty / (\tau_s / \rho)^{0.5}\,] / [\,c_p\,(\rho\,\tau_s)^{0.5}\,] \qquad (4.11)$$

The three-distinct-layer concept is somewhat of an oversimplification of the real situation but is satisfactory for Prandtl number less than 25 or 30. For larger Prandtl numbers it is preferable to assume turbulent boundary layers and continuous damping of these eddies as they approach the wall.

4.2.3 Modification of the physical structure of the probe

The previous section clearly points out the significance of the boundary layer in any heat flux measurement. The rule of the thumb should be that the boundary layer must be fully formed over the sensing element, otherwise the measurement would not reflect the characteristic film heat transfer coefficient of the system.

In order to achieve this a modification of the heat flux sensor area was made; around the main foil an extended area of the same material was made so that the boundary layer could be formed again over the sensor (see figure 4.1 and 4.2).

Combining equations 4.4, 4.6 and 4.7 ,for the laminar thermal boundary layer, gives the following equation for the calculation of the entrance length, x_i ,

$$x_i = \rho\ u_\infty\ K^2\,Pr^{2/3} / (\,25\,\mu\,h^2\,) \qquad (4.12)$$

using this equation one can approximately calculate the entrance length after which the thermal boundary layer will be fully developed .

The velocity at the wall of the vessel (u_∞) can be calculated using Yamamoto's equation [16] for an unbaffled turbine agitated vessel using Newtonian fluid,

$$u_\infty = 0.802\,\pi\,N\,D\,(D/T)^{0.80}\,(w/T)\,(n_p)^{0.162} \qquad (4.13)$$

Using the dimensions of the 800 L vessel the above equation reduces to

$$u_\infty = 0.84\,N\,D \qquad (4.14)$$

The above equation should only be used for calculation at or near the impeller plane. However, it would be clear from the discussion in chapter 5, section 5.1, that till date there is no comprehensive correlation to predict the local velocity flow field near the vessel wall.

From equation 4.6 it is clear that the lower the heat transfer coefficient the larger the thermal boundary layer and hence the longer is the entrance length (equation 4.12). For this study the entrance length is based on a calculation using the most viscous Newtonian fluid used, i.e Glucose-1 (a 56-58 % glucose solution). The lowest heat transfer coefficient for Glucose-1 at 100 rpm at the location of the first probe (which is closest to the impeller plane) is 535 W/m^2 K; the Prandtl number is 128. The viscosity, the thermal conductivity and the density are given in the appendix 2. Based on this data the entrance length works out to be 14 mm. The allowance actually given for the entrance length is 21 mm, see figure 4.1.

In the case of shear thinning fluids such as, CMC, pulp solution and fermentation broth, it is not possible to ascertain the velocity at the wall and, even though the heat transfer coefficient is much lower (of the order of 100 W/m^2 K), it is highly probable that the velocity u_∞ would be much lower than that predicted by equation 4.14. However to account for fluids such as these an extra allowance of 35% is made in the sensor area.

Photographs of the modified heat flux probe and a similarly modified RTD are shown in figures 4.2.and 4.3 respectively. Similar but unmodified heat flux probes have been used recently by Fasano et al [26] and Murray et al [119].

4.2.4 Increasing the robustness and reliability of the probe

During the initial phase of this work a serious problem of probe failure (within one to two month of successful operation) was encountered. This problem was then closely examined into with the help of the company and it was discovered that there was moisture ingress which was short circuiting the thermopile. It was then decided that a very thin layer of teflon (FEP) should be included as an effective moisture and chemical barrier. Furthermore, in biotechnical applications the heat flux to be measured is low and therefore it was important to have probes with high sensitivities. Efforts were therefore made to increase the sensitivity of the probes throughout this work.

The basic construction of the heat flux probe can be set out in the manner shown in the table below, with the process fluid side toward the top of the page and the heat transfer surface towards the bottom. The FEP is an industrial grade teflon which is used along with Kapton to envelope the thermal barrier against moisture and chemical ingress. The adhesive is used to stick the probe to the wall. Extreme care is taken while sticking the probe to the vessel wall to avoid trapping any air bubbles in the adhesive layer as this will interfere seriously with the working of the probe. An additional resistance called the contact resistance is not taken into

Extra Skirt Area (Modification)

Thermopile

Thermocouple

FIGURE 4.2 : MODIFIED HEAT FLUX PROBE

Extra Skirt Area (Modification)

FIGURE 4.3 : MODIFIED RESISTANCE TEMPERATURE DETECTOR (RTD)

FIGURE 4.2 : MODIFIED HEAT FLUX PROBE

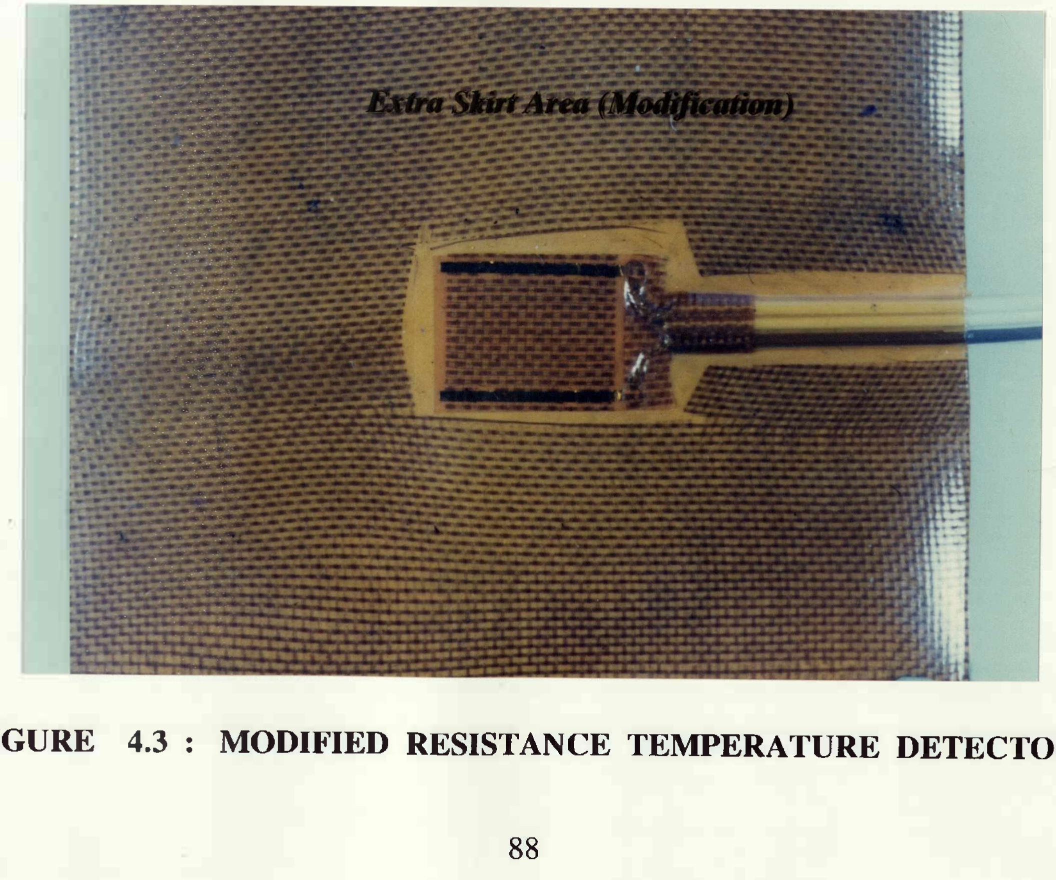

FIGURE 4.3 : MODIFIED RESISTANCE TEMPERATURE DETECTOR (RTD)

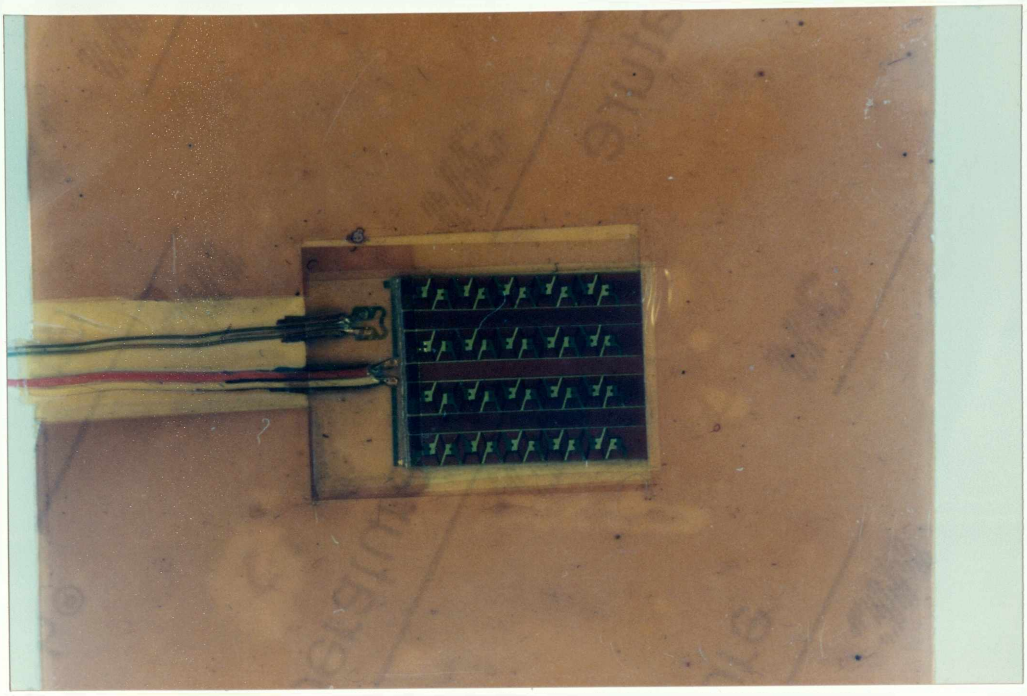

account because the vessel wall has a smooth and polished surface.

Material	Thickness m	Thermal Conductivity W / m K	Thermal Resistance m^2 K/ W
FEP	1.27×10^{-5}	0.1442	$R_f = 8.81 \times 10^{-5}$
KAPTON	2.54×10^{-5}	0.155	$R_{k2} = 16.4 \times 10^{-5}$
	Thermocouple and Thermopile (Thermal barrier)		
KAPTON	1.27×10^{-5}	0.155	$R_{k1} = 16.4 \times 10^{-5}$
ADHESIVE	5.08×10^{-5}	0.2423	$R_a = 21 \times 10^{-5}$

The resistances to heat transfer can be represented as a simple impedence diagram as follows,

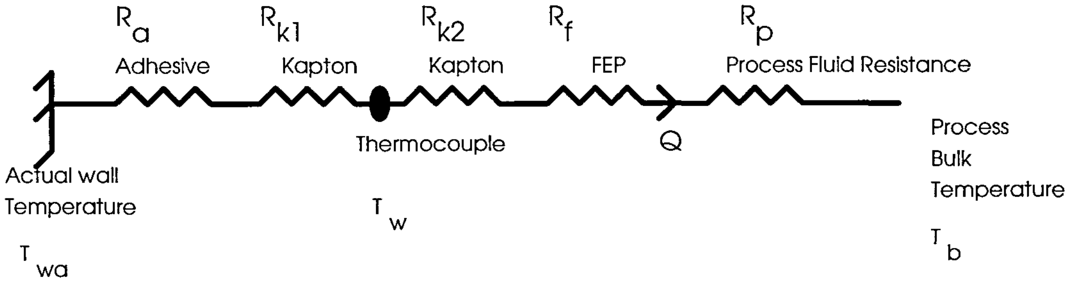

The dominant resistance is the Acrylic Adhesive (0.00021 m^2 K/ W). The accuracy of the probe would be much better when the process side heat transfer coefficient is less than or equal to 1/0.00021 or 4800 W/m^2K (approx.). Practically speaking, for better accuracy, the process side conductance should be less than the overall probe conductance which is "1/0.000544=1838 W/m^2K". This limits the applicability of the probe for heat transfer measurement in low viscosity fluids such as water in which the typical heat transfer coefficient is in the range 6000-8000 W/m^2K. The overall impedence calculation should also include that offered by the jacket (service) side heat transfer (typically heat transfer coefficient of 3500 W/m^2K) and also that due to the vessel wall (typical coefficient 4000 W/m^2K), which are nearly of the same order. Therefore the probe resistance becomes the limiting factor. Thus, in the experimental set-up used in this study the probe could not be properly validated using water. The main effect in that condition is then that the probe acts as an insulator thus altering the measuring temperature and the thermal boundary layer is also modified thus altering the measured heat flux.

If, of course, the process fluid is viscous enough to produce a process side heat transfer coefficient "h" less than about 2000 W/m^2K (the measurement could be within acceptable error limits till about 3500 W/m^2K) , this is not a serious limitation. It was found that the heat flux probes work well in Glucose solutions and other viscous non Newtonian fluids, where this is the case. However, use of these probes in fermentations add another problem namely Biofouling, i.e. the deposition of the biomass over the probe surface, to minimise this the probe surface (FEP) was highly polished.

Considering again the one dimensional analysis of the resistances in series model:

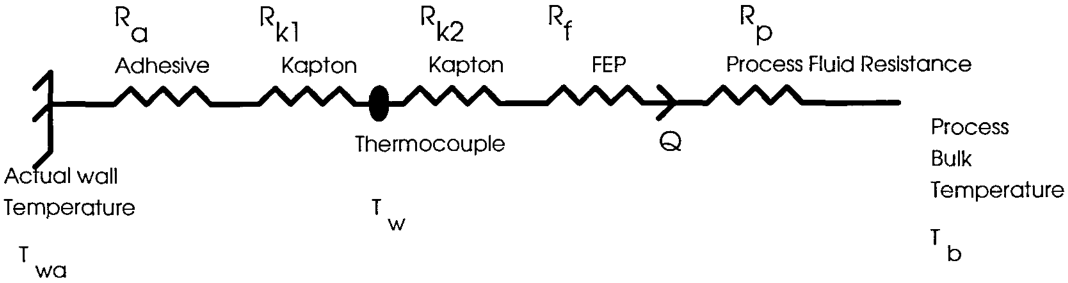

It this is compared to the real situation (i.e. without the probe):

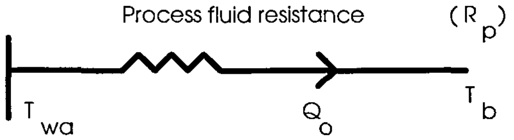

Therefore for the heat fluxes in each case,

$T_{wa} - T_b = Q_o R_p$ (for the real situation)

$T_{wa} - T_b = Q(R_a + R_{k1} + R_{k2} + R_f + R_p)$ (with the heat flux probe)

Hence, $Q_o R_p = Q(R_a + R_{k1} + R_{k2} + R_f + R_p)$ and

$$Q_o = Q + (Q/R_p)(R_a + R_{k1} + R_{k2} + R_f)$$

The factor $(Q/R_p)(R_a + R_{k1} + R_{k2} + R_f)$ can be reduced to reasonable proportions only if;

a) Q is low ; b) R_p is high and c) the sum of the resistances is very low.
The thermocouple temperature needs a correction factor given by:

$T_{wa} = T_w + Q(R_a + R_{k1})$

Where T_{wa} is the true wall temperature and T_w is the temperature read by the thermocouple.

4.2.5 Calibration of the probe

One of the most important aspects of probe operation is the calibration of the probe. The calibration carried out by the company is performed in two stages. First, since there are no official laboratories prepared to furnish a certified heat flux calibration, it is necessary to establish a known heat flux traceable to certifiable measurements. This is done by RdF by an adiabatic calorimeter process where time, temperature, mass, specific heat, area and voltage are verifiable parameters. In this way a one master sensor is calibrated which is then used to calibrate the production sensors. The calibration is done under steady state conditions; therefore when such a probe is used for quasi-steady or unsteady state process studies (as in this case) it is vitally important to have precise information about the construction of the probes, and then using the above approach, the corrections to the temperature and the heat flux must be applied.

4.3 Signal Processing

The output from the probe is in millivolts as it is in an analog form. This signal is conditioned using signal processor (a TCS unit, T-100) and converted into digital form which is transmitted onwards to the µ-Vax 2, which has a data management package called Setcon. The data is then displayed on the corresponding mimic diagram on a personal computer. This data is then stored and latter on processed and plotted using Sigma-plot 4.1 software. This is explained in detail in section 3.3. The company provides a calibration factor for each probe which is used to convert the millivolt signal into engineering units. The calibration of the probe would change with the temperature, because of corresponding change in the thermal conductivity of the thermal barrier; to take this into account the company supplies with correction factor for temperature. A simple program is written in Sigma-plot 4.1 to process the data and to produce a graphical output (see appendix 4).

The raw data obtained from the heat flux probes (see figure 4.4c) shows fluctuations resulting from the effects of the following factors: a) The local heat transfer coefficient is influenced by flow patterns and local hydrodynamics; this has been recently confirmed, using a similar probe, by Fasano et al [26]. Thus, these fluctuations in the heat flux signal

Fig 4.4 : Signal processing

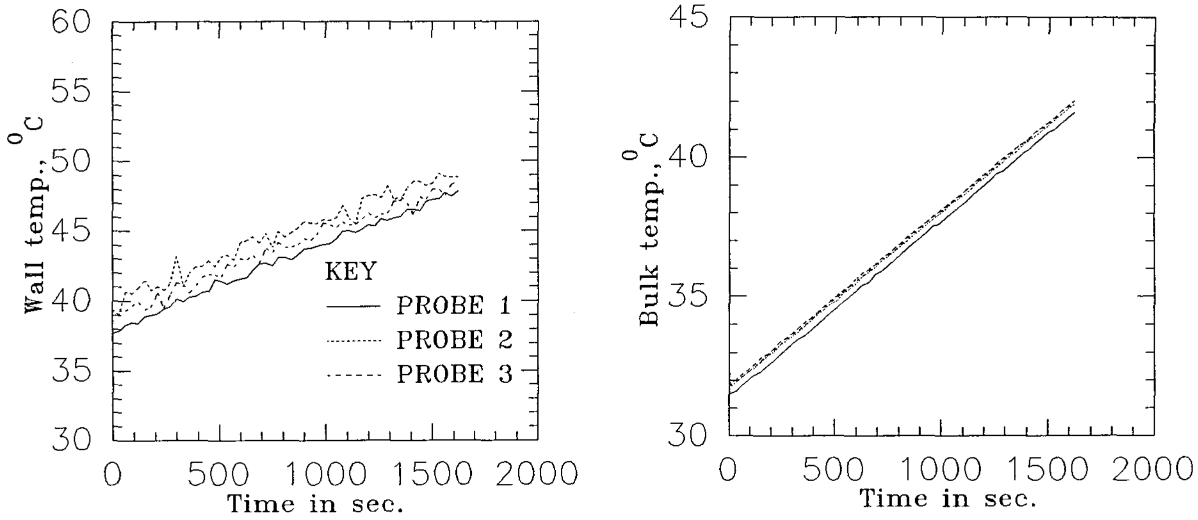

Fig 4.4a: Wall temperature

Fig 4.4b: Bulk temperature

Fig 4.4c: Signal from the heat flux probes

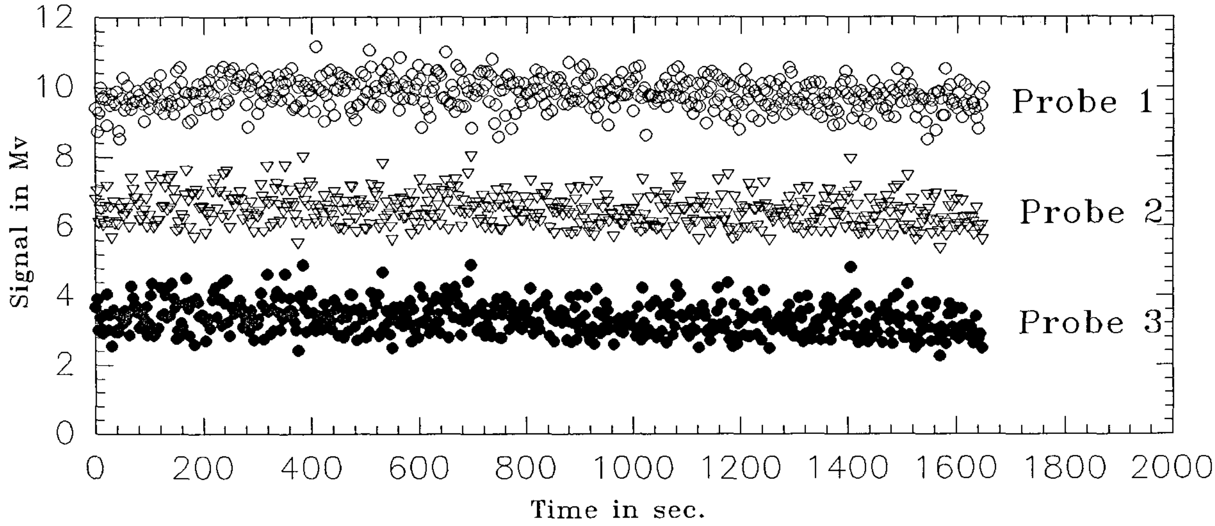

Fig 4.4d: Processed local heat transfer coefficients

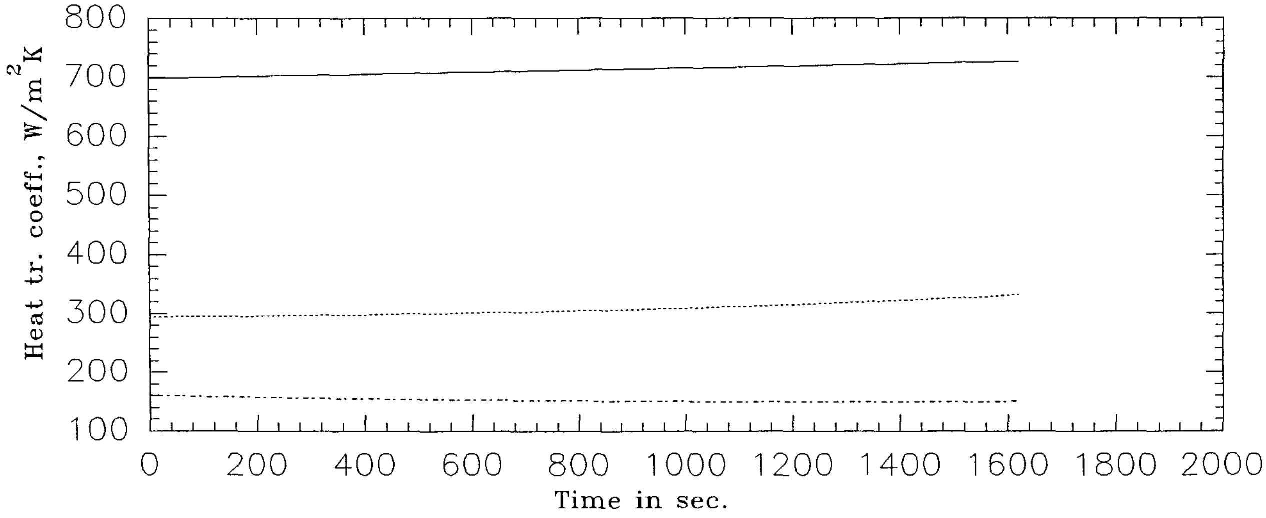

are mainly due to hydrodynamic fluctuations inside the vessel. Also, due to the 3 sec. sampling interval, these fluctuations are randomly picked up by the probes; b) there are temporal fluctuations in heat transfer, specially noticeable near the jacket inlet, because the inlet temperature is changing with time, and c) the signal from the heat flux probe is small and the circuit is susceptible to pick up of electrical noise from other equipment. Figures 4.4a and b show the unprocessed wall temperature and bulk temperature profile respectively. The heat flux signal is regressed and converted into engineering units, and is then divided by the regressed driving force (temperature at the wall - temperature in the bulk) to yield the local heat transfer coefficient (figure 4.4d). A one dimensional quasi-steady state model within each 3 sec. interval is assumed on the basis that the wall is nearly isothermal and the change in temperature is very gradual.

4.4 *Validation of the technique*

All the local heat transfer experimental results for unaerated Newtonian fluids (Glucose-1,56-58%, Glucose-2, 53-55% and Glucose-3, 46-48%) for a range of impeller speeds (100, 200, 300 and 400) are shown in figures 4.5 to 4.7 (all the data is taken at a constant bulk temperature of 25 ± 2^0C). Also shown on the same plots are the values obtained using the predictive method of Man et al [22]. This method is chosen as the comparator, it being the more detailed of only two previous studies presenting methods for the prediction of local heat transfer.

The results for the three Glucose solutions match closely (within ±5%) with the local heat transfer coefficients predicted using the Man et.al. correlation (see Figure 4.5 to 4.7). The local heat transfer coefficient shows distinct axial variation, with the maximum value near the impeller plane. Ideally such a profile should be explained in terms of local velocity flow fields; however in the absence of such information the local heat transfer phenomenon has to be explained empirically. Man et al used an empirical local factor $(X/T)^{-0.33}$ in their correlation shown in Equation 4.15 (valid for turbulent region):

$$Nu=0.4\ Re^{0.67}\ Pr^{0.33}\ (X/T)^{-0.33} \qquad (4.15)$$

This validates the probe and the technique used in this study.

Fig 4.5: Comparison of unaerated experimental and predicted data for glucose -1 solution

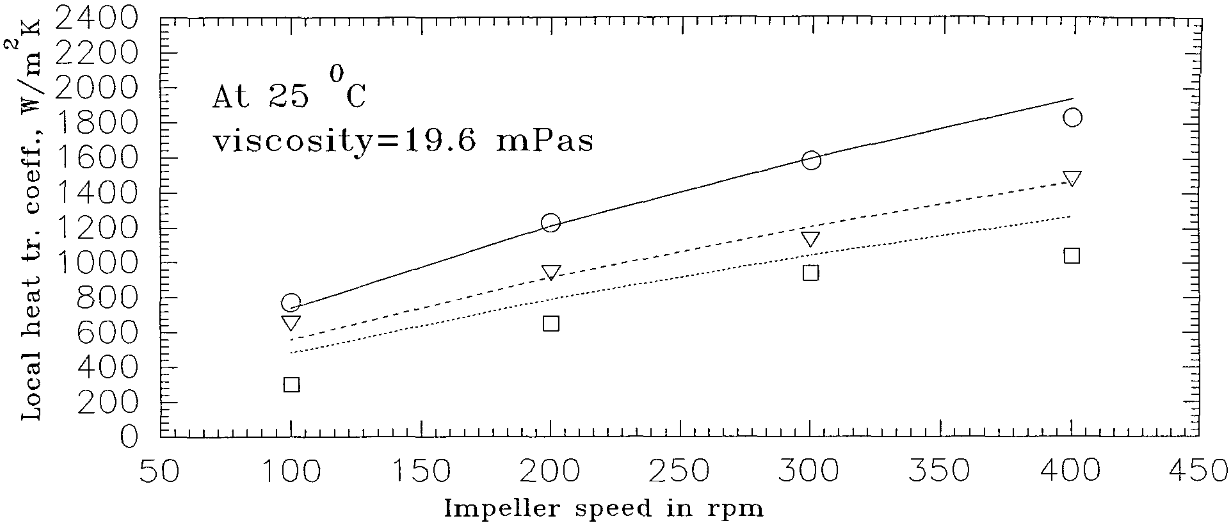

Key:	*Experimental values*	*Predicted values*
Probe 1	○	———
Probe 2	▽	- - - - -
Probe 3	□	···········

Fig 4.6 : Comparison of unaerated experimental and predicted data for glucose-2 solution

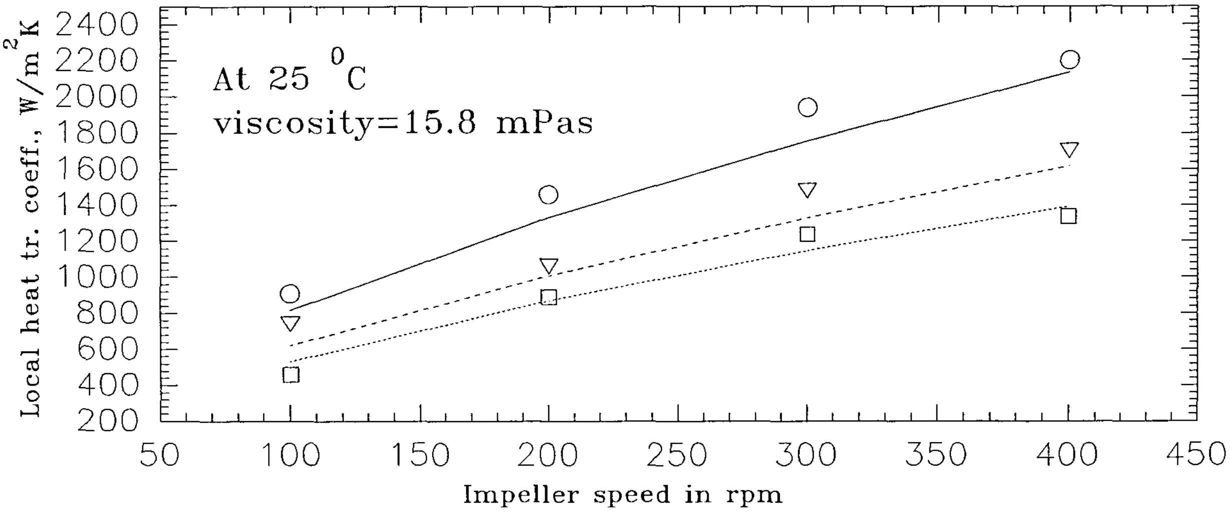

Fig 4.7: Comparison of unaerated experimental and predicted data for glucose-3 solution

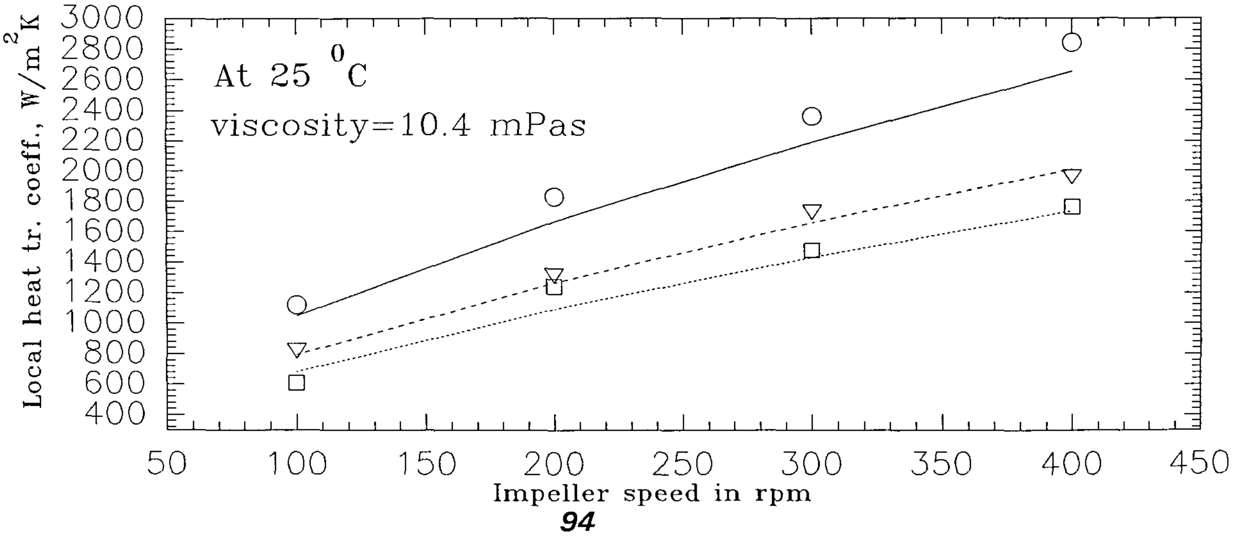

CHAPTER 5

Local heat transfer and mixing studies in unaerated systems

The first stage of the project was to study unaerated systems using simple Newtonian fluids and single Rushton impeller (see section 5.1), since there is a body of data and correlations available in literature for comparison . This is then followed by a similar study using non-Newtonian model fluids (for modelling the broth) as reported in section 5.2 .

Since most industrial application of mechanically agitated vessels use multiple impellers, therefore the next step was to study dual Rushton impeller system with Newtonian fluid (see section 5.3), followed by non-Newtonian fluids (see section 5.4).

5.1 Unaerated Newtonian fluid - one impeller system

For this first step three Newtonian fluids of increasing viscosity were prepared using glucose as the solute. The details of their composition and preparation technique are given in chapter 3 (section 3.5.1). The viscosities and their variation with temperature is shown in appendix 2. The experimental values for the local heat transfer coefficient reported in this chapter are each determined at 25 °C during the cooling process, as this assured a nearly isothermal wall temperature with only a gradual change in the driving force, thus fulfilling the criterion for quasi-steady state operation. The details of the placement of the probes are given in chapter 3, section 3.2.5.

Unaerated heat transfer data for the three Glucose solutions 1, 2 and 3, are shown with the corresponding power and power numbers in figures 5.1 to 5.3 together with aerated power data. The comprehensive form of the data is compiled in appendix 5. The unaerated local heat transfer coefficient shows distinct axial variation, in all cases, the maximum value being

Fig 5.1: Local unaerated heat transfer coefficient, power draw and power number profile for glucose-1 solution

a) Local unaerated heat transfer profile

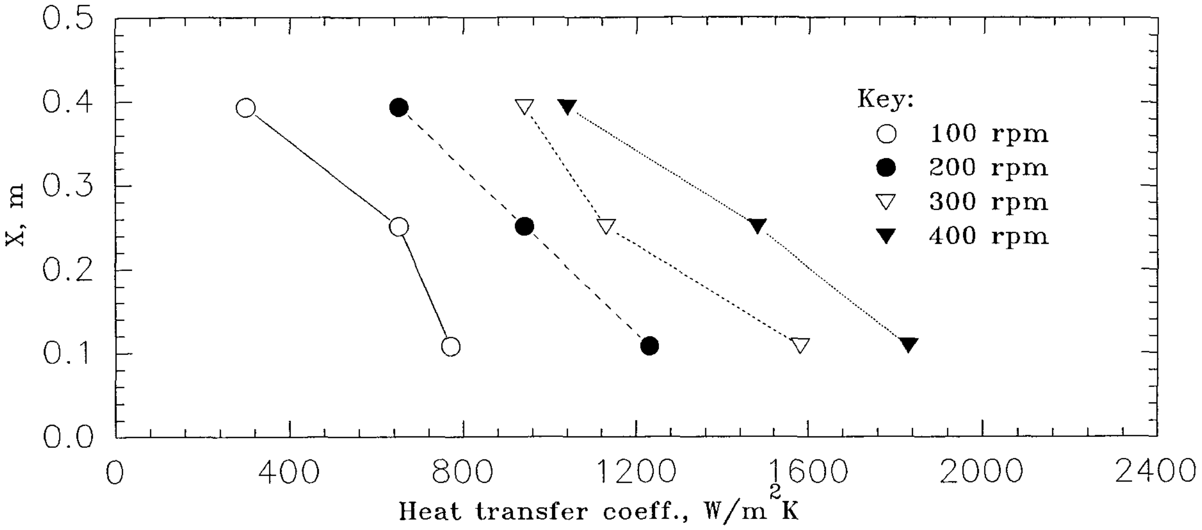

b) Power draw profile

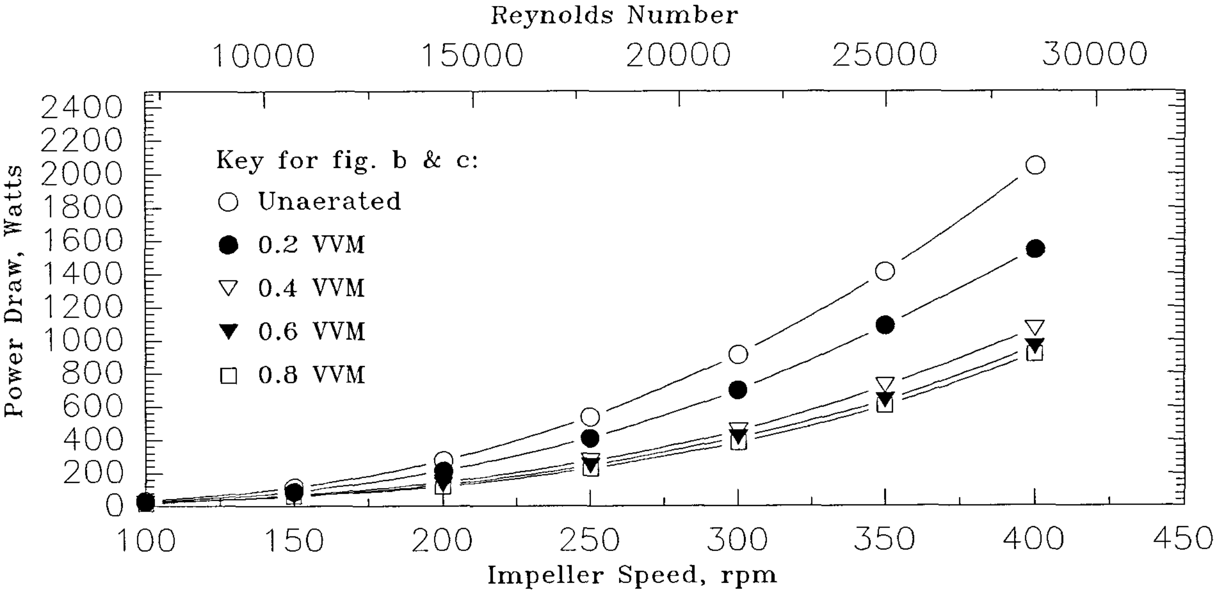

c) Power number profile

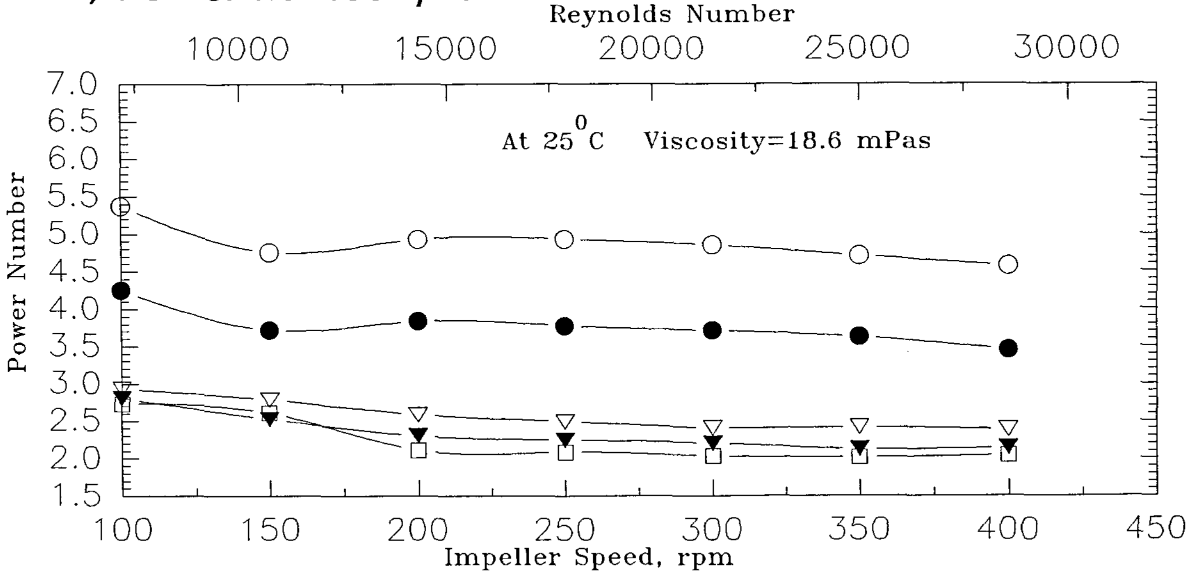

Fig 5.2: Local unaerated heat transfer coefficient, power draw and power number profile for glucose-2 solution

a) Local unaerated heat transfer profile

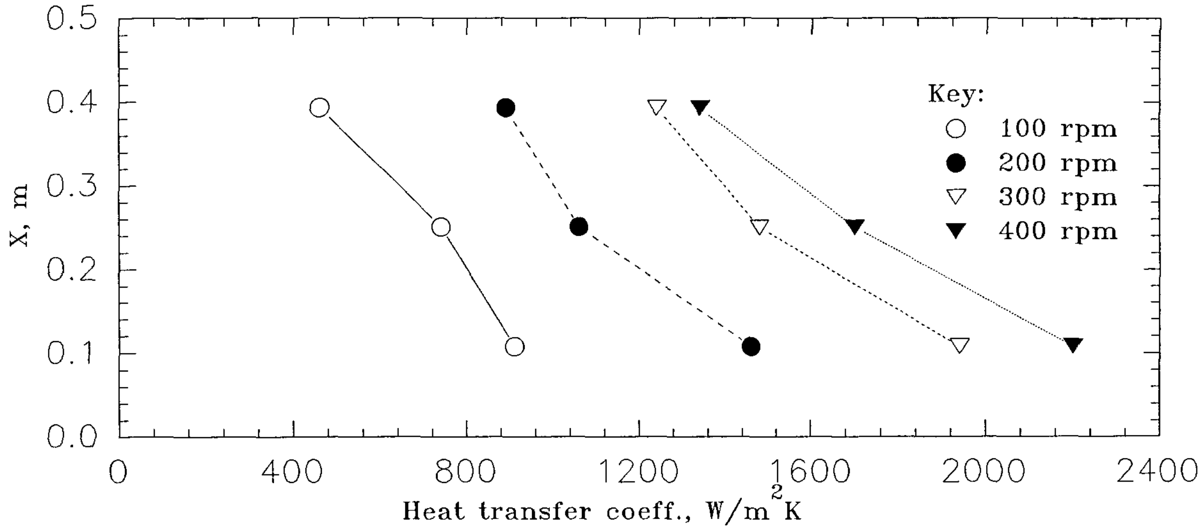

b) Power draw profile

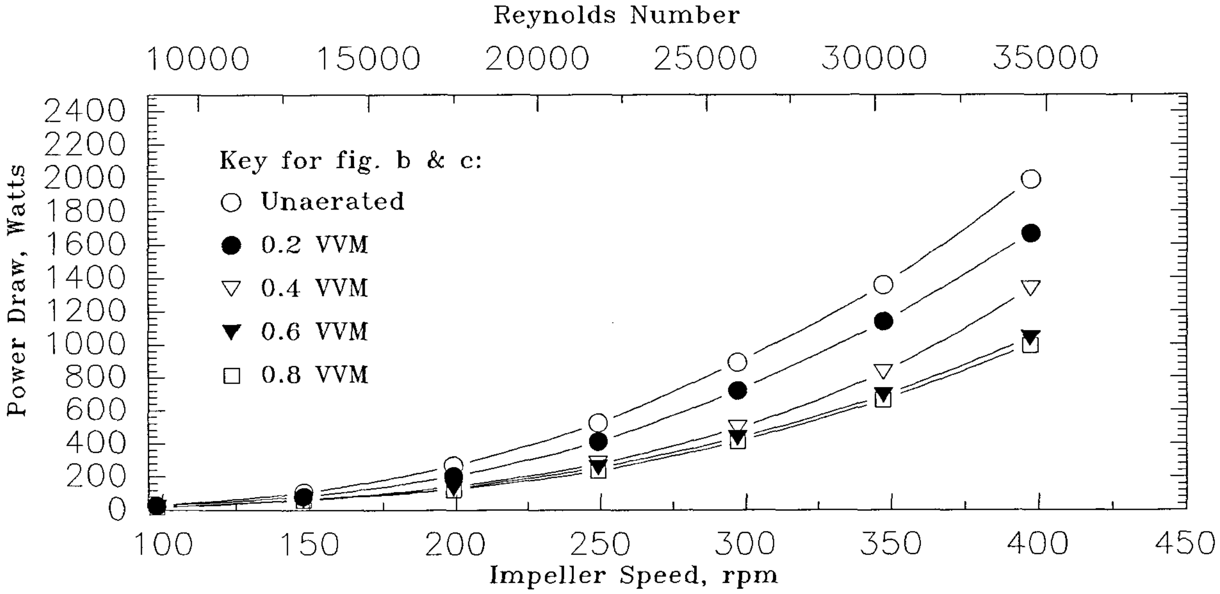

c) Power number profile

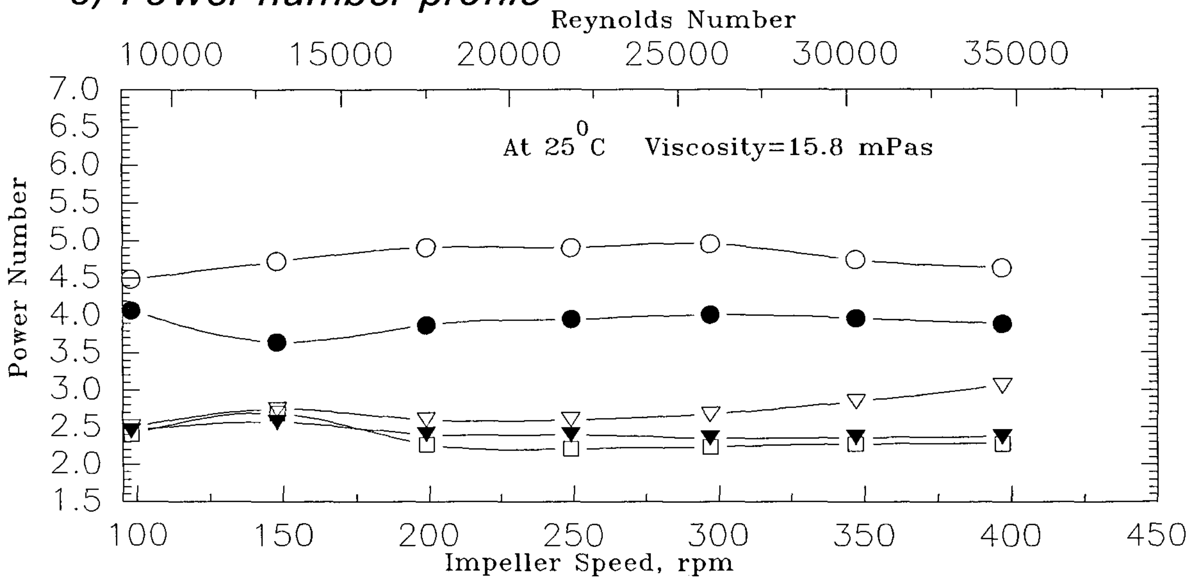

Fig 5.3: Local unaerated heat transfer coefficient, power draw and power number profile for glucose-3 solution

a) Local unaerated heat transfer coefficient profile

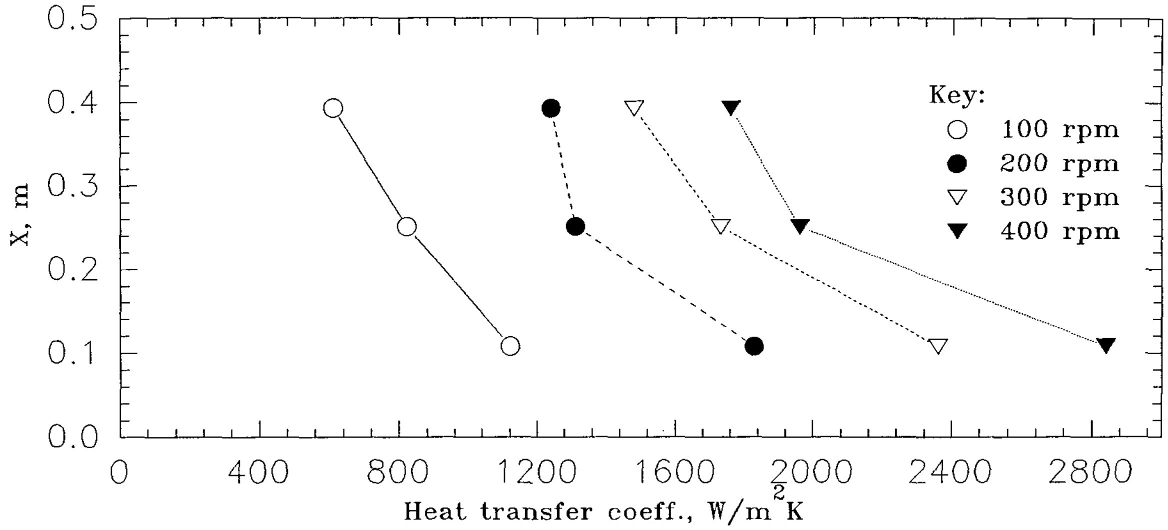

b) Power draw profile

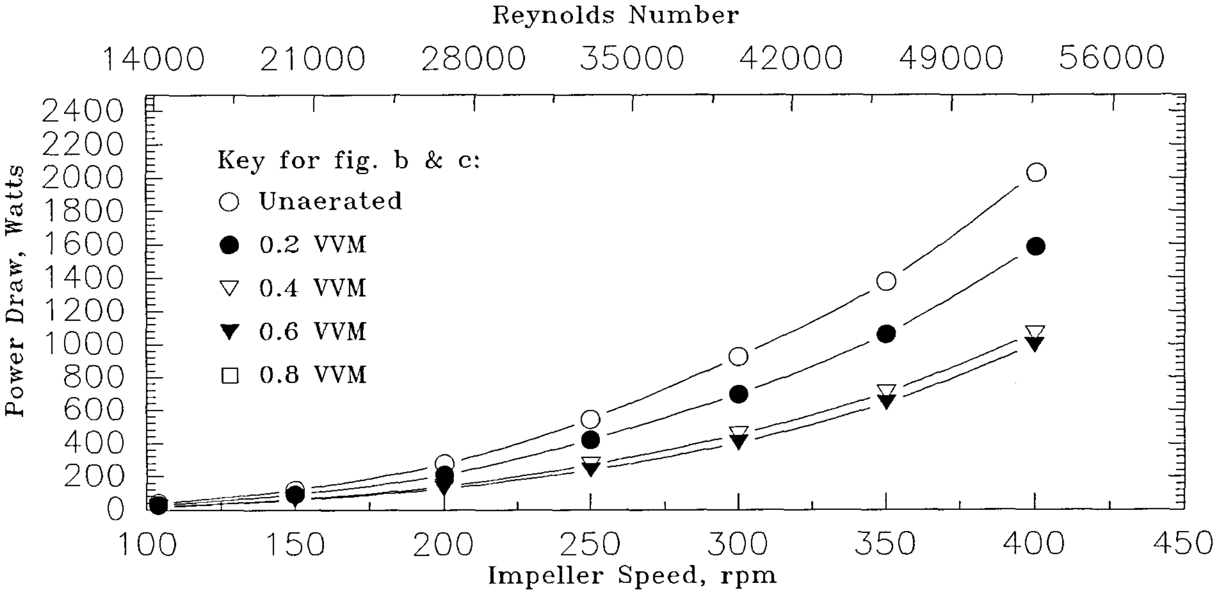

c) Power number profile

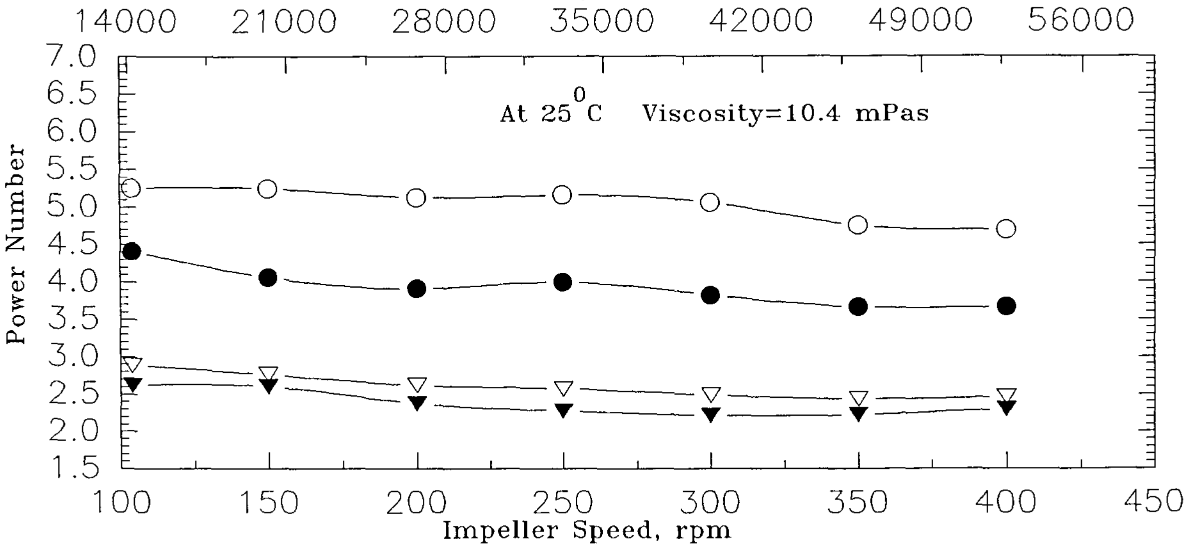

close to the impeller with a progressive decrease away from it. Furthermore, as would be expected, the heat transfer coefficient increases with impeller speed at each position.

The crucial determinant of film heat transfer is the velocity flow field near the vessel wall; if this could be quantified then a fundamental approach to the prediction of the film heat transfer coefficients could be made. Qualitatively one expects the impeller tip speed to determine the velocity flow field near the heat transfer surface (vessel wall), and the higher the tip speed, so the higher is the velocity and hence the heat transfer coefficient. Further, given the axial velocity profile for a typical Rushton turbine one would expect the velocity component to be at a maximum near the impeller plane and to decrease progressively with axial distance above (or below) the impeller.

The critical question is however whether local velocity flow field can be predicted in practice in the light of recent related work in hydrodynamics. Is it possible, knowing global parameters such as impeller tip speed or power input, to predict the local hydrodynamics near the vessel wall ?

Van der Molen and Van Maanen [120], who used vessels from 0.12 to 0.9 m diameter, found that, in the turbulent region, the mean radial velocity just off the tip of the blade and on its centre line was a constant ratio (0.85) of the impeller tip speed V_{tip} ($V_{tip} = \pi ND$), and decayed as it moved out along the radius, r, such that:

$$V_r / V_{tip} = 0.85 (r / R)^{-7/6} \tag{5.1}$$

where R is the impeller radius.

The above work has recently been extended at the University of Birmingham by Dyster et al [121] using LDA (Laser Doppler Anemometry) to study the radial discharge flow from a Rushton impeller. The agitated vessel used in the experiment had a diameter of 0.15 m and a flat base. It was equipped with 4 baffles (D_T /10) and the liquid height was equal to the diameter of the vessel ($H=D_T$) . Agitation was by a Rushton turbine impeller, diameter $D= D_T/3$ or $D_T/4$ with six blades with their centreline at the mid-height of the liquid. The fluids studied were water, glycerol, glucose and polyethylene glycol. Their data lead to the following correlation,

$$V_r / V_{tip} = 0.73 (r / R)^{-0.94} \tag{5.2}$$

The agreement with Van der Molen and Van Maanen [120] is good except close to the impeller [121]. Furthermore, both the correlations have an exponent close to -1 as would be suggested by conservation of momentum.

The corresponding root-mean square centre-line velocity ratio (V_r'/V_{tip}) profile shows that the dimensionless fluctuating radial velocity (which includes a random fluctuating element and the velocity changes due to passage of the impeller blade) decreases almost linearly with increase in radial distance from the impeller tip. The correlation suggested from this work [121] is,

$$V_r'/V_{tip} = 0.454 - 0.128\,(r / R) \qquad (5.3)$$

There was an increase in the value of V_r'/V_{tip} near the baffles mainly due to local enhancement of the turbulence. Also with increase in the viscosity, the fluctuating component of the velocity decreased. It is interesting to note that in this work it was generally observed that the fluctuations in the heat flux signal (referred to in chapter 4, section 4.3) was greater in low viscosity fluids compared with that in high viscosities.

The axial profiles for various radial positions were also measured and reported [121]. The axial profile varied with radial position for a range of Newtonian fluids; this was especially reflected in a marked reduction in V_r / V_{tip} with increasing radial distance from the impeller, up to a radial position of R/2 from the impeller axis. The axial profile varied significantly with Reynolds number, impeller speed and viscosity. For water the velocity profile had a maximum gradient between the axial positions of the impeller plane and the farthest position measured (14 mm above the impeller plane); but at low Reynolds number (for 100% glucose, 248 mPas) the shape of the profile became flatter with a lower maximum gradient. The root mean square velocity also is significantly reduced in the lower transitional and laminar regions.

The effect of viscosity on the axial profile was further demonstrated with 100% glycerol (1.16 Pas), for which there was an even a greater difference in the gradients at different Reynolds numbers. Parallels can be drawn with these effects by comparing the local heat transfer results for Glucose-1 (viscosity=18.6 mPas) and Glucose-3 (viscosity=10.4 mPas). The low viscosity glucose-3 solution exhibits a sharper heat transfer coefficient gradient at probe 1 and 2 as compared to glucose-1 data (see figure 5.1 and 5.3), and glucose 2 data (figure 5.2) supports this trend by having intermediate values. Viscosity clearly has a direct effect especially in the impeller discharge stream (but note that probe-1 is not exactly in the impeller plane).

The change in viscosity also affects the mean centre line velocity [121]. In the turbulent region the change in Reynolds number does not significantly alter the V_r / V_{tip} ratio. However, in the transitional region (especially in the lower transitional region around Re=100), the Vr/Vtip ratio increases with the impeller speed and at around a Reynolds number value of 300 the profile becomes similar to that suggested by equation 5.2. For a highly viscous fluid in the laminar region V_r / V_{tip} is very low. As the laminar region is entered (Re<20) V_r / V_{tip} falls to about 1/5 of the value in the turbulent region.

An interesting feature Dyster et al [121] reported for Newtonian fluids, that for r/R greater than or equal to 1.7 the mean radial velocity tends towards zero. At similar Reynolds numbers in high viscosity non-Newtonian fluids, such a rapid reduction in velocity has been observed using bulk flow visualisation [122], and has been ascribed to the enhancement of viscosity associated with reducing velocity and therefore shear rate. However, since there is no change in the viscosity of Newtonian fluid with shear rate, such a sudden reduction in the mean radial velocity can only be due to the viscous drag associated with the proximity of the baffle and vessel wall.

Such wall shear effects must play an important role in characterising fluid flow near the vessel wall especially so in the lower transitional and laminar regions. Quantitatively , the flow near the walls can be characterised by the distribution of the shear stress or through its dimensionless representation as, a friction coefficient [123]. Although there has been considerable research on the phenomena occurring at the vessel walls, no representative set of shear data is available. Therefore, since the viscous drag at the vessel wall plays a significant role in shaping the axial velocity flow field, it would be difficult to extrapolate the data from Dyster et al [121] work to arrive at a prediction of the axial velocity profile actually at the vessel wall. So, in summary, while contemporary studies are making progress in defining bulk flow fields one is still faced with little better than qualitative inference when it comes to dealing with events close to the vessel wall.

5.1.1 Empirical correlations

The alternative then is to correlate the data empirically using the Reynolds number or a dimensionless power number as a global hydrodynamic descriptor. The challenge then is to find an empirical factor which can relate the global determinants to the local phenomena. Man et al [22] used a factor X/D_T which seems to fit very well with the unaerated glucose data as shown in chapter 4. However, in their correlation the viscosity ratio was not taken into account. The first step then was to include a viscosity ratio, an exponent of 0.14 being assumed as this is a standard value reported in the literature (see chapter 2, section 2.2.4). The Prandtl number exponent was likewise given a value of 1/3 as the standard value from literature. Correlation is accomplished for each probe after which a general local heat transfer correlation is achieved. Two approaches adopted to arrive at a standard correlation. Firstly, a best fit was found for the constant k, exponent of the Reynolds number and the exponent of (X/D_T) for the experimental value of $Nu/(Pr^{1/3}\ Vi^{0.14})$, using the statistical package in a standard scientific software namely Sigmaplot-4. Then another correlation was attempted by forcing the exponent on the Reynolds number or power factor to a standard value accepted in literature (2/3 or 2/9 respectively), these two correlations were then statistically compared, using a relevant statistical technique (see appendix 7). If there was no significant difference between the two then the standard form was accepted as a correlation for this particular geometry.

5.1.1.1 Correlation using Reynolds number as a global hydrodynamic determinant

Reynolds number is predominantly used in almost all heat transfer correlations available in the literature. Figure 5.4 shows the heat transfer correlation for unaerated glucose (all concentrations). The solid line is the experimental data whereas the correlated value, as shown by the symbols circle and triangle, represent the two approaches to correlation, the former shows the best fit while the latter is obtained by forcing the Reynolds number exponent to universally accepted value of "2/3". Figure 5.4 a and d shows that the two approaches closely matches and satisfies the statistical test (within 95% confidence limit). Thus the local heat transfer correlation for each probe is,

For probe-1

$$Nu=2.4\ Re^{2/3}\ Pr^{1/3}\ Vi^{0.14} \tag{5.4}$$

For probe-2

$$Nu=1.8\ Re^{2/3}\ Pr^{1/3}\ Vi^{0.14} \tag{5.5}$$

For probe-3

$$Nu=1.5\ Re^{2/3}\ Pr^{1/3}\ Vi^{0.14} \tag{5.6}$$

The above correlation clearly shows a decreasing trend in heat transfer coefficient (Nusselt number) from probe-1 to 3, as manifested in the constant k. Further, the discussion in the previous section points out that this change is fundamentally due to change in the local velocity flow field (near the heat transfer surface), however due to the inability to quantify

Fig 5.4 Heat transfer correlation for unaerated Newtonian solutions with Reynolds number using single Rushton impeller

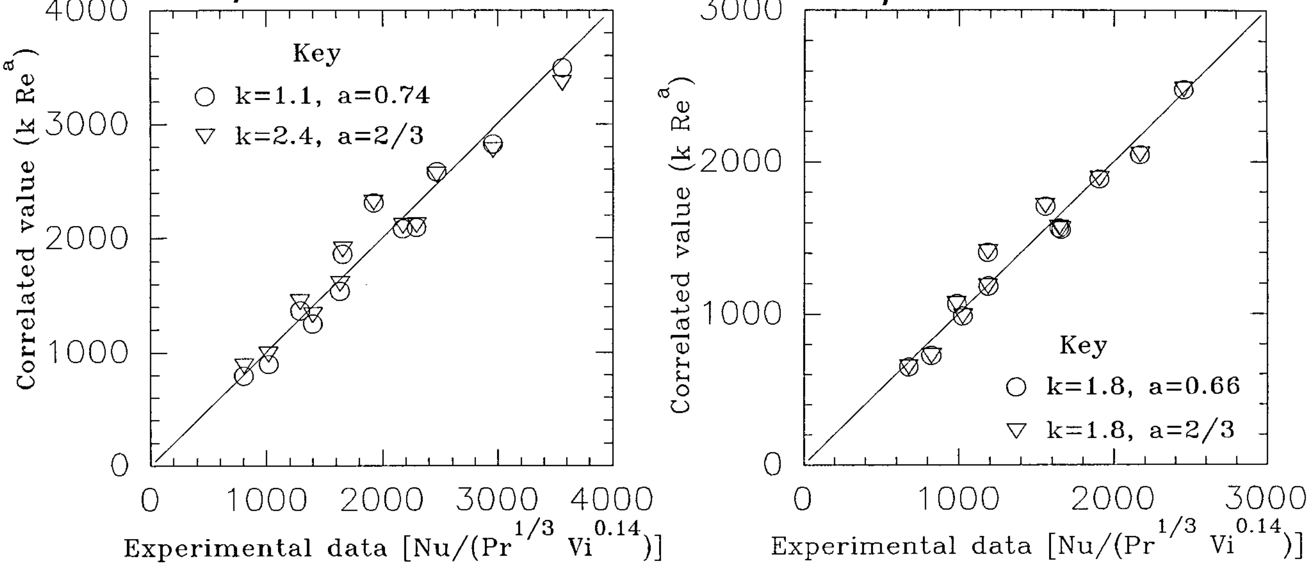

a) Local correlation for probe -1

b) Local correlation for probe -2

c) Local correlation for probe -3

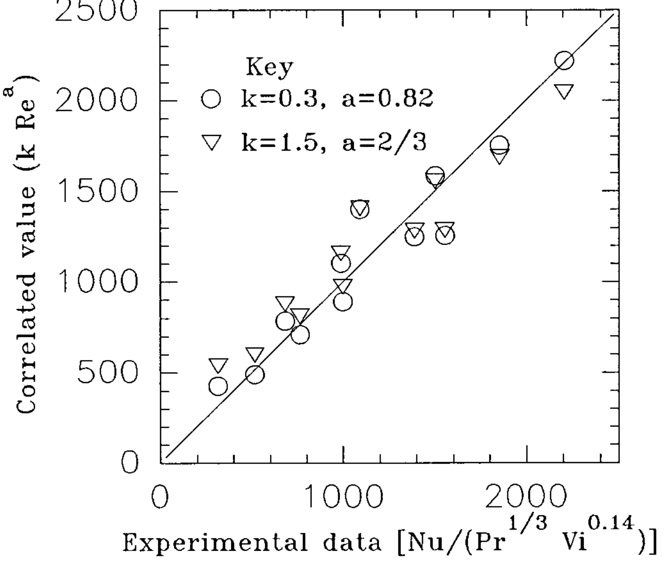

d) Overall local heat transfer coefficient correlation

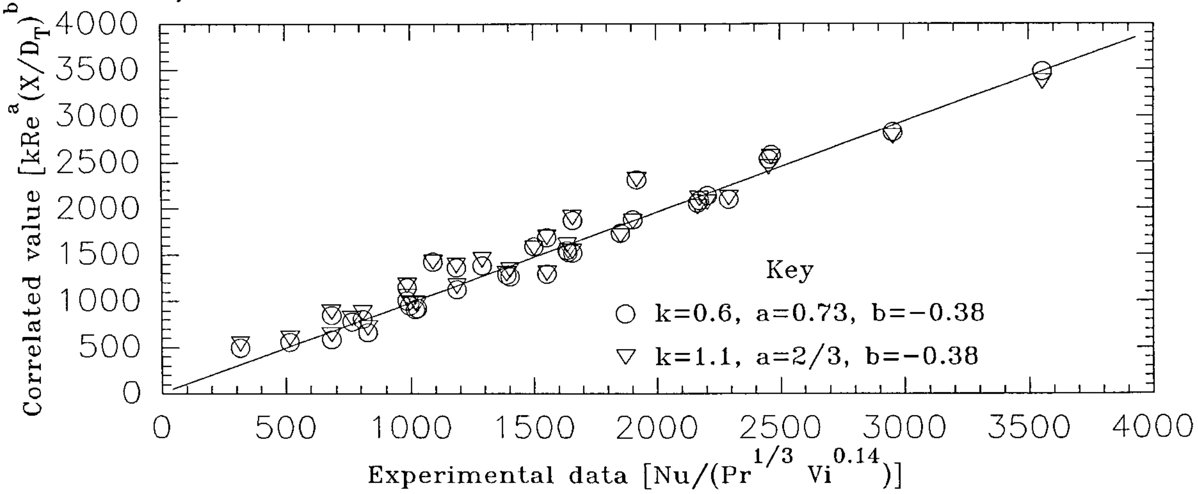

such a change in the velocity, one can use an empirical approach as shown above. However, such a correlation is highly geometric specific.

The changes in the constant k could be quantified independently by incorporating an axial variation term, as used by Man et al [22] and Akse et al [19], namely X/D_T. Figure 5.4d shows an overall local heat transfer correlation for all probe positions incorporating the axial variation term. The two approaches to the correlation closely matches the statistical test (95% confidence limit), thus producing the following standard form of the correlation,

$$Nu=1.1\ Re^{2/3}\ Pr^{1/3}\ Vi^{0.14}\ (X/D_T)^{-0.38} \qquad (5.7)$$

Comparing the above correlation with that by Man et al [22] (see table 2.1, equation 16) one can observe differences in both the value of the constant (k=0.4 from Man et al) and the exponent on the term X/D_T (-0.33 from Man et al). Generally in literature (see chapter 2), for global heat transfer using a standard Rushton turbine, a constant value of 0.76 is quoted (for overall global correlations). For local heat transfer, given the three points in the vessel one could expect a higher value of the constant. Further the impeller used is strictly not a standard Rushton impeller (refer appendix 1B) as the blade thickness is smaller, this leads to a higher power number and could be reflected in higher value of the constant "k". Differences in the geometry and also in the measurement technique (Man et al used electrochemical technique) between this work and that of Man et al could result in different correlations. Also the incorporation of the viscosity ratio in the above correlation makes the difference even more prominent. However, as shown in chapter 4 (section 4.4) the Man et al correlation is still valid for the experimental data, though the correlations reported above give a much better fit for the data.

5.1.1.2 Correlation using power factor as a global hydrodynamic determinant

The use of correlations including a dimensionless power factor ($\varepsilon D_T^4/\nu^3$) dates back to 1959 (see chapter 2 section 2.2.3) but, despite its distinct advantage over Reynolds number (especially for aerated fluids), it has been rarely used as its replacement. Sano et al [44] and most recently Strek and Karcz [124] have used this factor in their correlations. Sano et al proposed the exponent of the power factor to be 0.227 whereas Strek and Karcz [124] propose an exponent of 2/9.

Fig 5.5: Heat transfer correlation for unaerated Newtonian solutions with power factor using single Rushton impeller

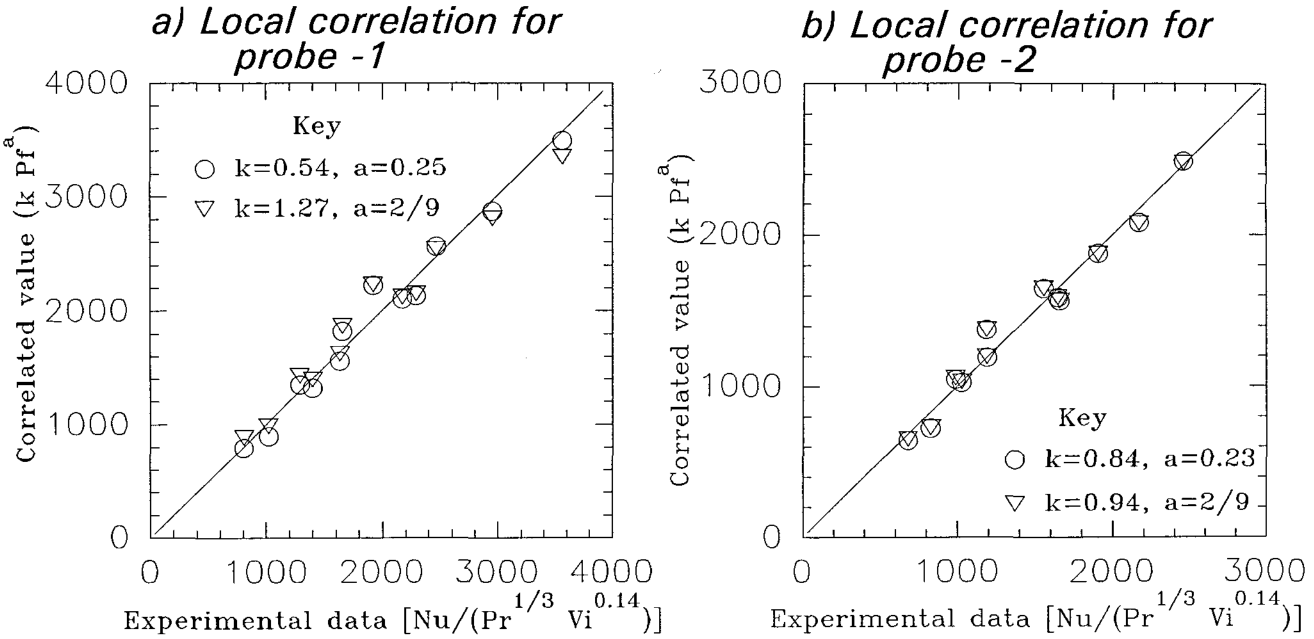
a) Local correlation for probe -1

b) Local correlation for probe -2

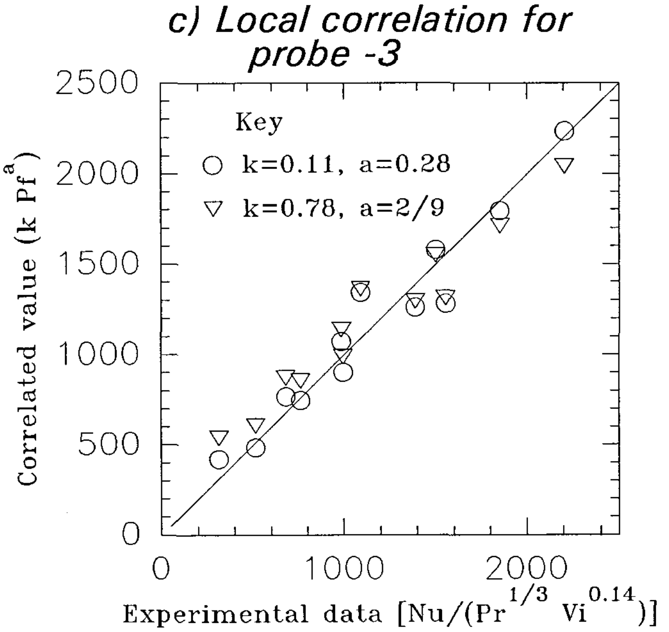
c) Local correlation for probe -3

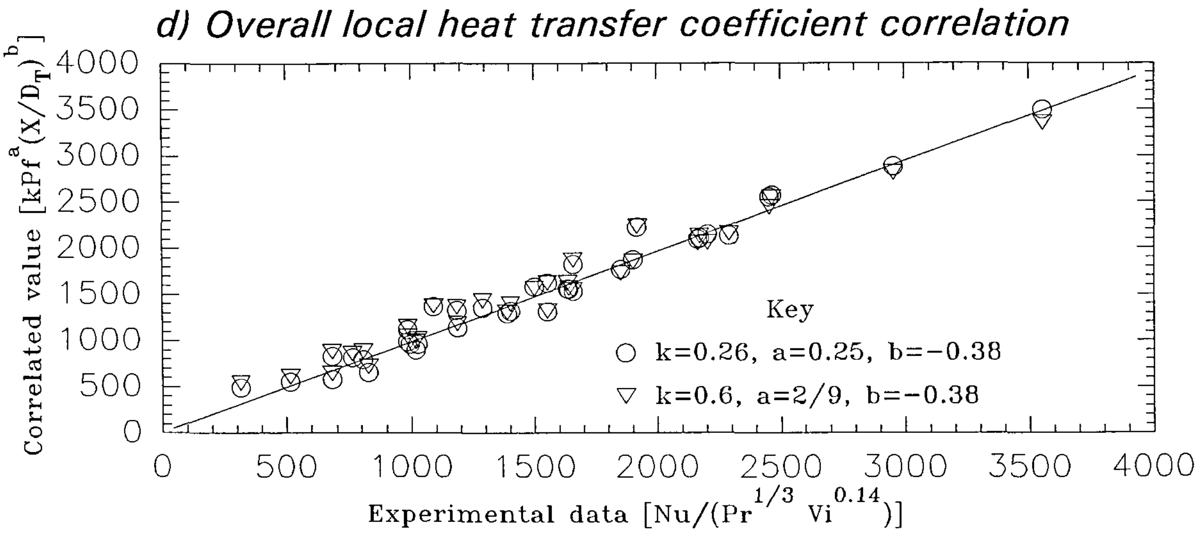
d) Overall local heat transfer coefficient correlation

Figure 5.5 shows heat transfer correlation using power factor. The local correlation for each probe satisfies the statistical condition and the standard local correlations thus achieved were,

For probe-1,

$$Nu = 1.27\, Pf^{2/9}\, Pr^{1/3}\, Vi^{0.14} \qquad (5.8)$$

For probe-2,

$$Nu = 0.94\, Pf^{2/9}\, Pr^{1/3}\, Vi^{0.14} \qquad (5.9)$$

and for probe-3

$$Nu = 0.78\, Pf^{2/9}\, Pr^{1/3}\, Vi^{0.14} \qquad (5.10)$$

A similar trend in the value of the constant, as in the case of Reynolds number correlation, is observed. For the unaerated fluid the heat transfer coefficient value from both Reynolds number correlation and power factor yield similar value. This is mainly because the power number does not vary significantly (only between 4.8-5.4) in the turbulent region. The advantage of using heat transfer correlation with power factor is that it gives a better representation of the velocity flow field (local hydrodynamics) as compared with the Reynolds number, which relies on the impeller tip speed. This difference, though subtle in the case of unaerated fluids, becomes highly significant when the same fluid is aerated (see chapter 6).

Again the local axial profile could be incorporated in the correlation yielding the following standard form of the correlation.

$$Nu = 0.6\, Pf^{2/9}\, Pr^{1/3}\, Vi^{0.14}\, (X/D_T)^{-0.38} \qquad (5.10)$$

The exponent on the axial variation term is exactly similar to that observed in the case of Reynolds number correlation (see equation 5.7), which again reinforces the above argument.

5.2 Unaerated Non-Newtonian fluid - one impeller system

Figures 5.6-5.8 show the unaerated heat transfer and power data for 0.28% carboxymethyl cellulose (CMC) , 0.8% CMC and 1.4% CMC respectively. There is (with the exceptions discussed below) a distinct axial variation in the heat transfer coefficient especially noticeable at low viscosity. Qualitatively, comparing the trend with the Newtonian fluids, one can observe a distinct difference because of the rheology, which adds another dimension to the engineering challenge. CMC is a shear thinning fluid that is to say that the rheology changes with shear (see section on Rheology, chapter 2, section 2.5), so the higher the shear rate the lower the apparent viscosity. The rheology will also change within the vessel depending on the energy dissipation. In the impeller discharge region (or near to the impeller plane) there is high shear which reduces in proportion away (axial distance) from the impeller plane. For apparent viscosity calculations for Rushton turbine an average shear rate calculated as 11.5N is assumed; however, it has been suggested in literature [125] that the shear rate could be as high as 90N in the vortices behind the impeller blade. This is most evident in the case of 1.4% CMC, which was the most viscous (K=21.5) and highly shear thinning (n=0.34), where there was a dramatic difference between the heat transfer coefficients measured by probes 1 and 2, except at the lowest impeller speed (100 rpm) (see figure 5.8a). A similar effect is also observed for 0.8% CMC, though, as might be expected, the effect is less pronounced, and it is even less so for 0.28% CMC (see figures 5.6a and 5.7a respectively).

The heat transfer data for 1.4% CMC is in the laminar and lower transitional regions and, except near to the impeller plane, the heat transfer profile shown by probes 2 and 3 is almost independent of the impeller speed (see figure 5.8a). This suggests that there is little or no fluid motion at the probe positions 2 and 3 due to the highly shear thinning nature of the fluid. It seems likely that in such cases the heat transfer is predominantly due to free convection, (such data are excluded for the purpose of correlation for forced convection). The situation improves with 0.8% CMC and even more with 0.28% CMC (see figure 5.6a and 5.7a respectively).

It is again important from this projects point of view to explore possible links with related work in hydrodynamics, although it is clear from the above discussion that the rheological characteristics make it even more challenging as compared with Newtonian fluid.

Work with a range of non-Newtonian fluids which was complementary to Dyster et al's [121] work was carried by Koutsakos et al [126]. They [126] reported a flattening of the axial velocity flow field (this observation is not near the vessel wall) and a reduction in the fluctuating radial velocity component with increase in the pseudoplasticity and viscosity of the fluids. The flow field inside the vessel could be related to the power curve. In the laminar region Power number is inversely proportional to the Reynolds number. It is evident that measurable deviations from this inverse linearity occur at Re>~ 60, which marks the beginning of the transition region after which the power curve becomes relatively flat; thus large increases in Reynolds number causes only small change in the Power number. Therefore this value of Reynolds number, within the transition region, should also represent an important transition point for the velocity distribution[126]. The slight curvature of the

Fig 5.6: Local unaerated heat transfer coefficient, power draw and power number profile for 0.28% CMC solution

a) Local unaerated heat transfer coefficient profile

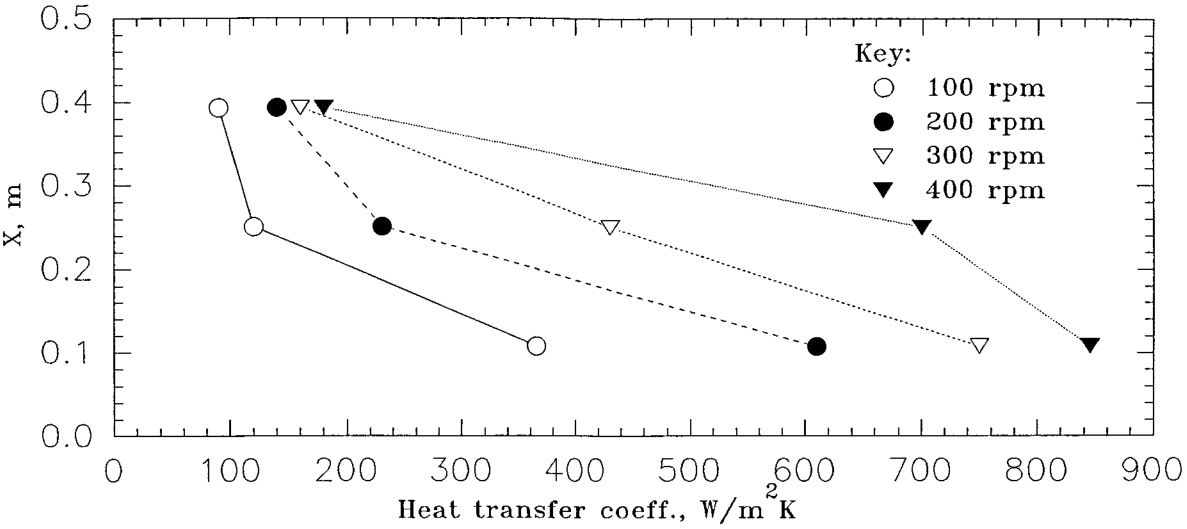

b) Power draw profile

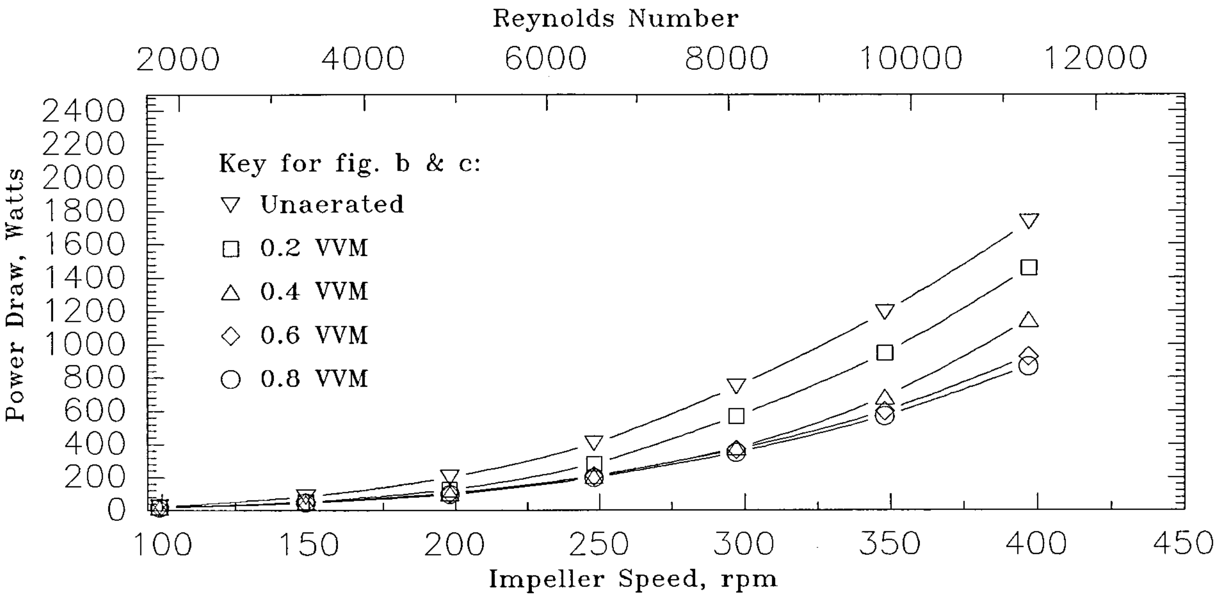

c) Power number profile

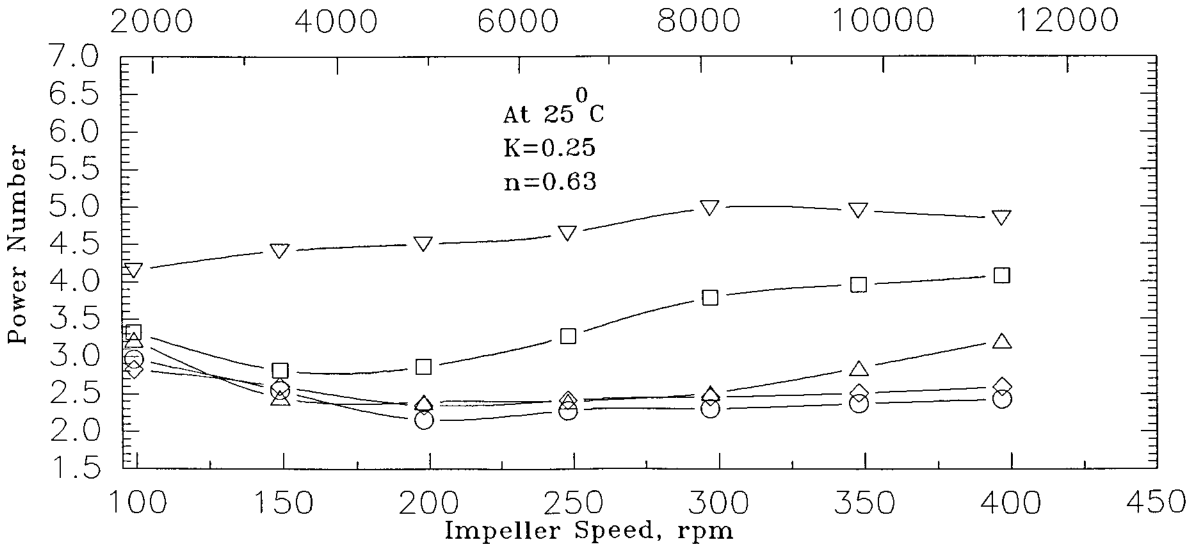

Fig 5.7: Local unaerated heat transfer coefficient, power draw and power number profile for 0.8% CMC solution

a) Local unaerated heat transfer coefficient profile

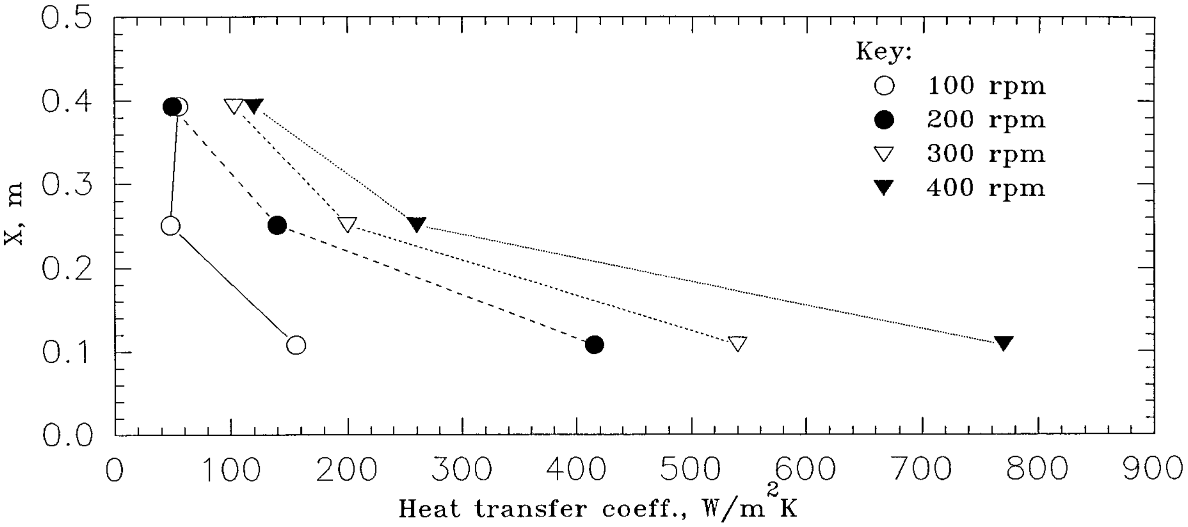

b) Power draw profile

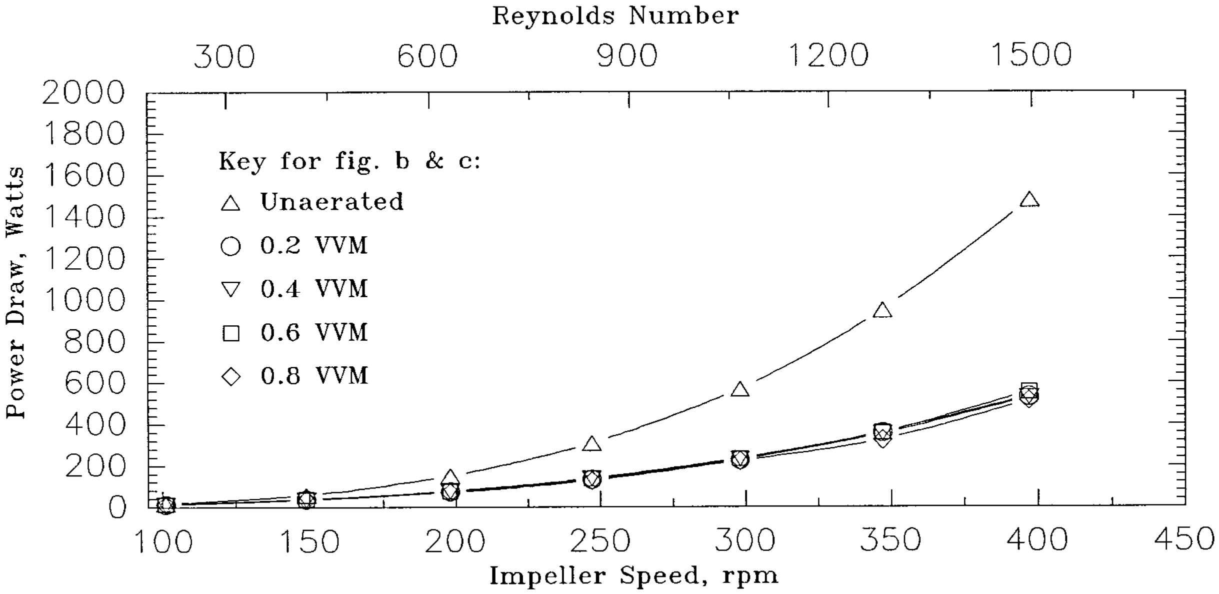

c) Power number profile

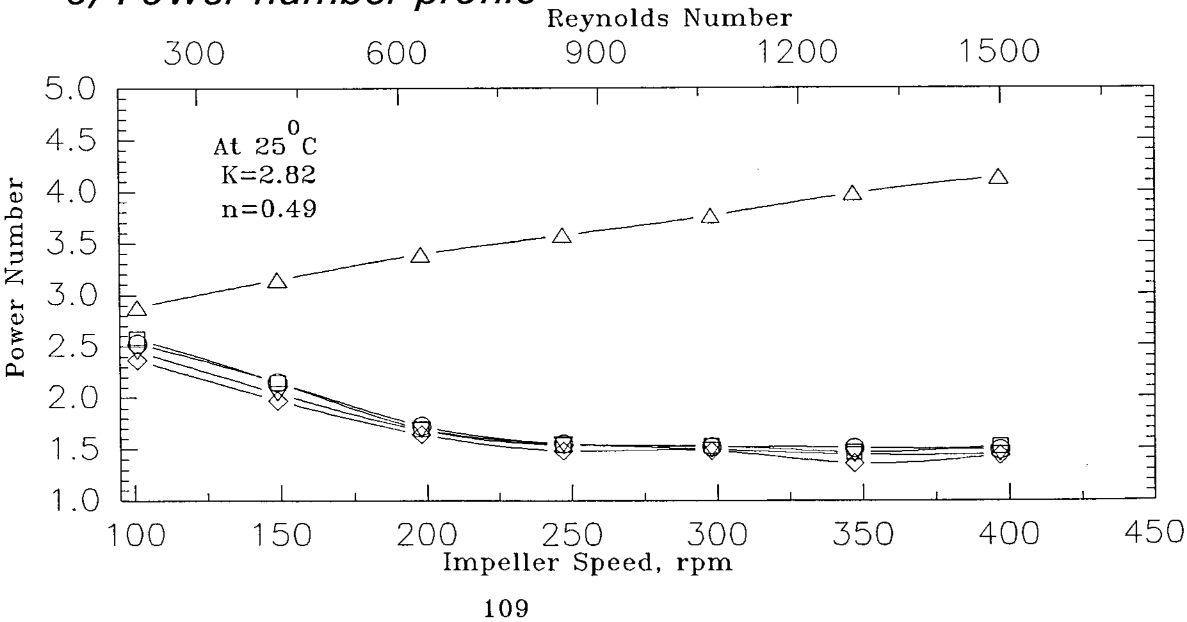

Fig 5.8: Local unaerated heat transfer coefficient, power draw and power number profile for 1.4% CMC solution

a) Local unaerated heat transfer coefficient profile

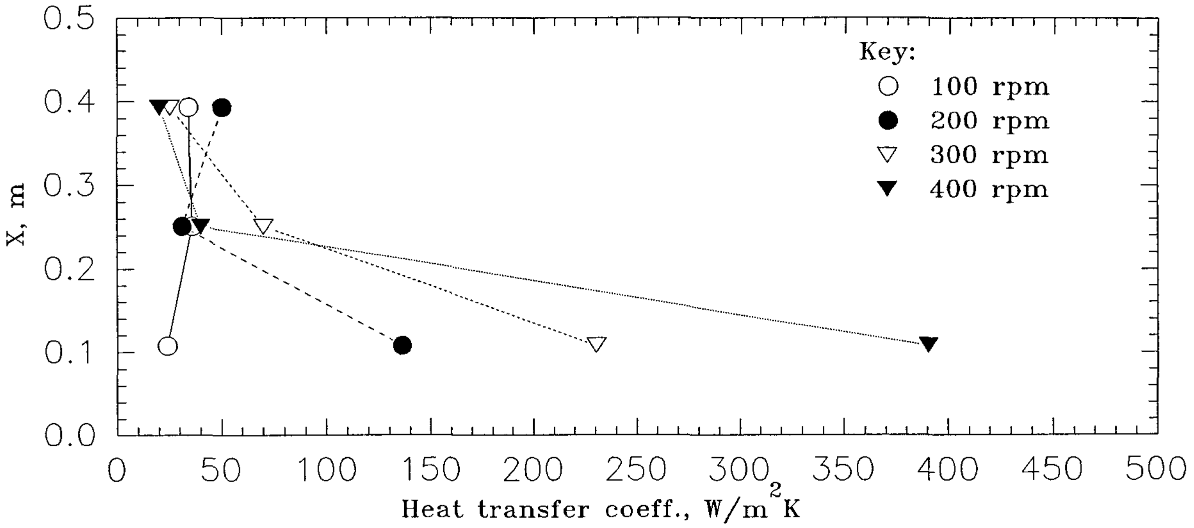

b) Power draw profile

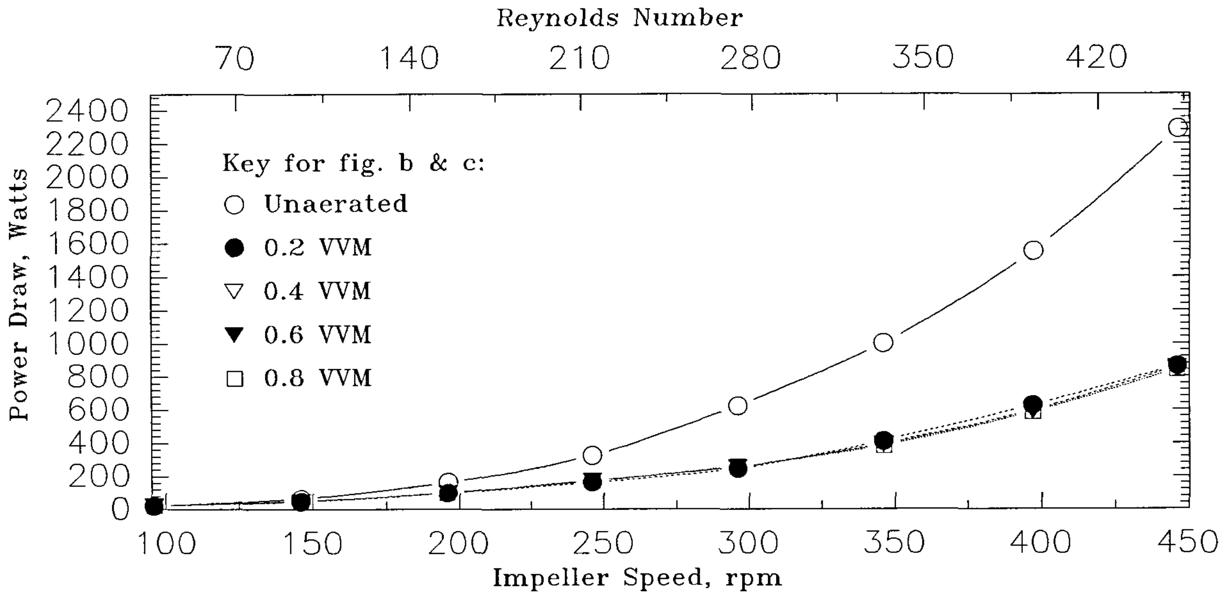

c) Power number profile

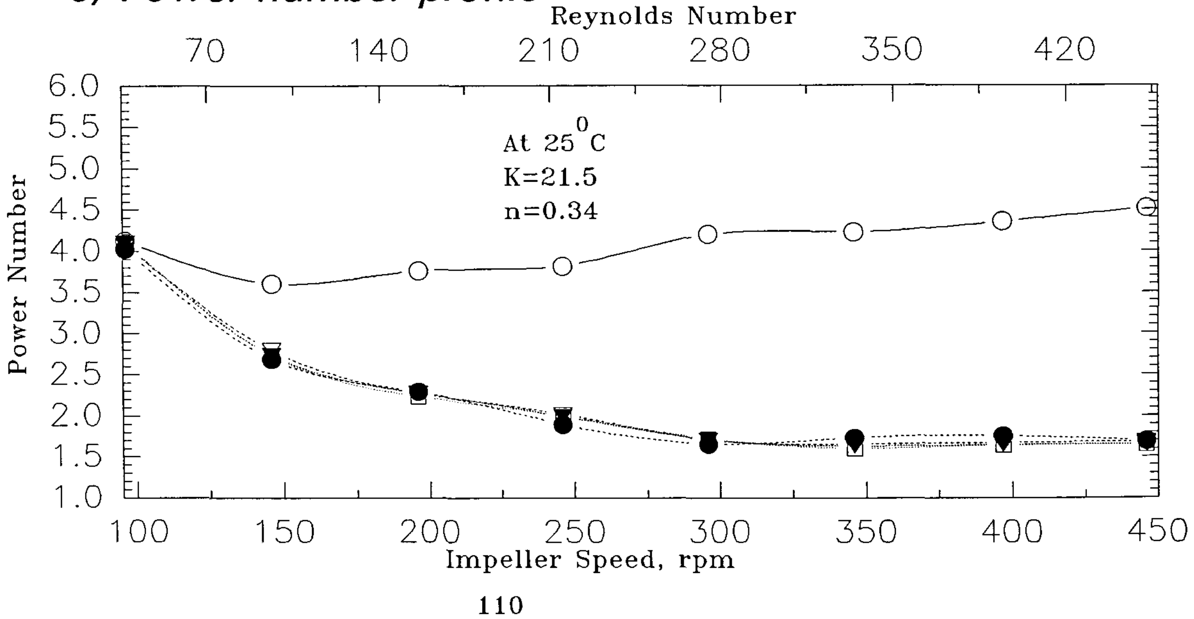

power curve observed for $100<Re<1000$, was considered by Nienow et al [127] to be related to the change in the angle of discharge from the impeller blade. A study on non-Newtonian fluids as early as 1960 by Metzner and Taylor [128] reported a change in the flow fields as one moves from the laminar into the early transition range defined by the power curve. The value of Fl (i.e. the pumping capacity of stirrer) increases relatively steeply with reduction in apparent viscosity until $Re\cong60$. Further reduction of apparent viscosity (i.e. by increasing impeller speed) results in relatively smaller increases in the value of Fl. Thus, the change at $Re\cong60$ between the flat and sloped part of the power curve has a definite effect on the velocity distribution around the rotating impeller. However, this discussion fails to deliver any quantitative relationship between power draw and the local velocity flow field, paving the way once again for empirical correlation.

5.2.1 Empirical correlations

A similar attempt, to that used for unaerated Newtonian fluid, was made to correlate the data for the non-Newtonian fluids. The correlation with the Reynolds number is shown in figure 5.9. The two correlation approach matches very well with the statistical test (95% confidence limit) . The standard form of which for the three probes are,

For probe-1,

$$Nu=0.95\,Re^{2/3}\,Pr^{1/3}\,Vi^{0.14} \tag{5.11}$$

For probe-2

$$Nu=0.59\,Re^{2/3}\,Pr^{1/3}\,Vi^{0.14} \tag{5.12}$$

and for probe-3

$$Nu=0.2\,Re^{2/3}\,Pr^{1/3}\,Vi^{0.14} \tag{5.13}$$

The trend for the constant value k shows a decrease (as might be expected) with increase in the distance above the impeller plane. However, it is interesting to note that, the constant value is significantly lower for each probe position as compared with the respective correlations with Newtonian fluids. Further, the differences in the constant value increases as one moves away from the impeller, i.e. the difference is least for probe-1 and maximum for probe-3. This is due to the shear thinning nature of the fluid which further complicates the empirical correlation. Due to this shear thinning nature of the fluid the local velocity away from the impeller decreases, depending on the power law index, more rapidly as compared

Fig 5.9: Heat transfer correlation for unaerated non-Newtonian solutions with Reynolds number using single Rushton impeller

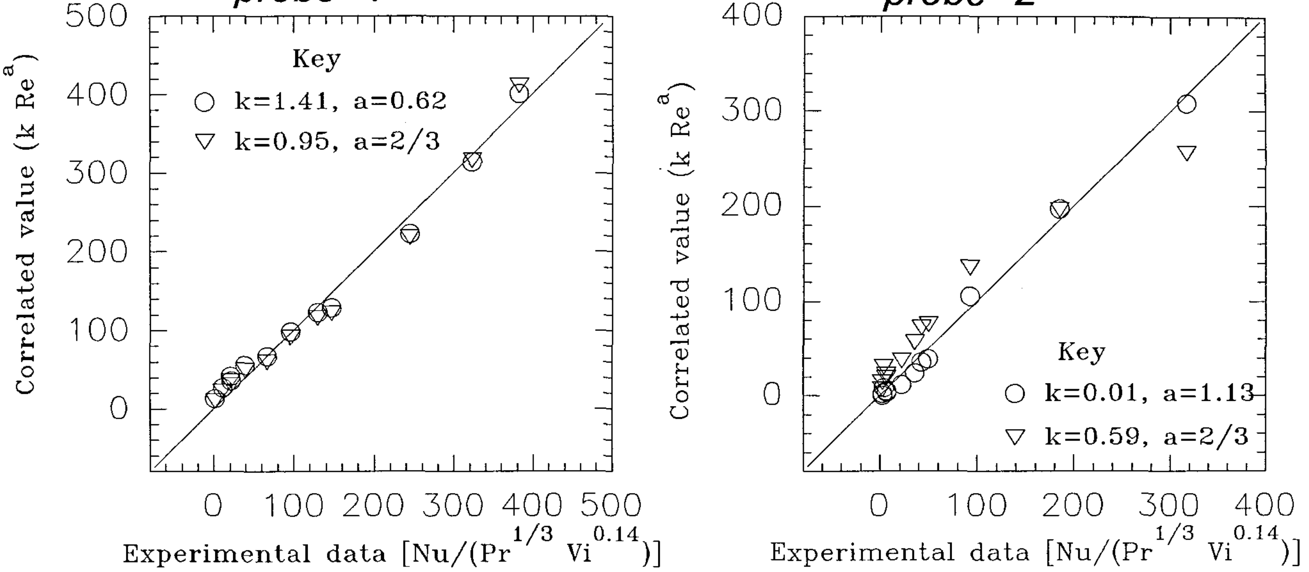
a) Local correlation for probe -1

b) Local correlation for probe -2

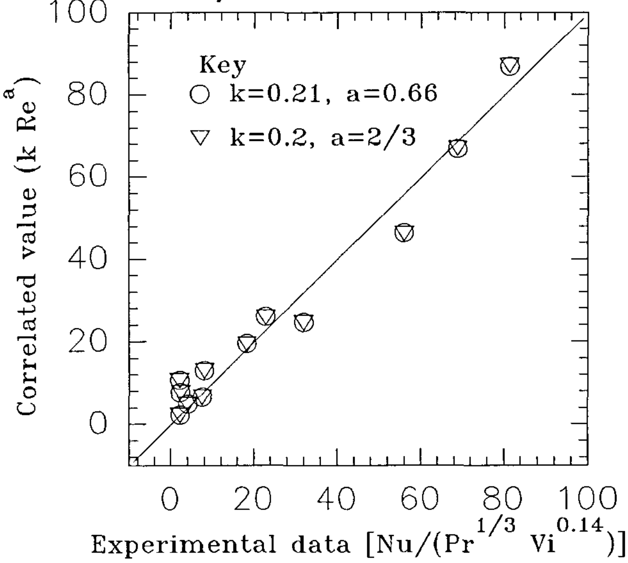
c) Local correlation for probe -3

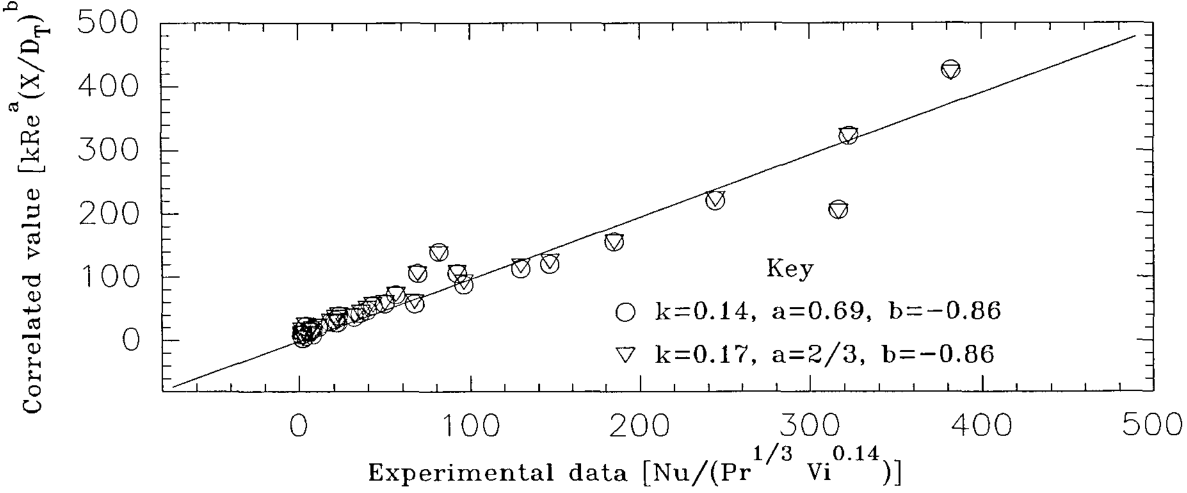
d) Overall local heat transfer coefficient correlation

with the Newtonian fluid. This effect is better quantified in the standard heat transfer coefficient incorporating the local axial profile term, which is,

$$Nu=0.17\,Re^{2/3}\,Vi^{0.14}\,Pr^{1/3}\,(X/D_T)^{-0.86} \qquad (5.14)$$

In the above correlation the exponent on the local axial profile is significantly higher (quantitatively) than that in the case of Newtonian fluid, which reinforces the argument that the shear thinning behaviour plays a significant role in heat transfer. However, this value will depend on the shear thinning nature of the fluid and for such a fluid the apparent viscosity will be a function of local shear. But, for all rheological calculations an average shear of 11.5N is assumed (refer chapter 2). Therefore to attempt a better understanding of heat transfer phenomenon in such fluids, a local distribution of shear (near the heat transfer surface) must be understood. However, there is no such data available in the literature and one has to be satisfied with the above correlation.

Figure 5.10 shows the correlation of the heat transfer data using the dimensionless power factor, which matches the statistical test for 95% confidence limit (see appendix 7). The standard local correlations achieved were,

For probe-1,

$$Nu = 0.50\,Pf^{2/9}\,Pr^{1/3}\,Vi^{0.14} \qquad (5.15)$$

For probe-2

$$Nu = 0.32\,Pf^{2/9}\,Pr^{1/3}\,Vi^{0.14} \qquad (5.16)$$

and for probe-3

$$Nu = 0.11\,Pf^{2/9}\,Pr^{1/3}\,Vi^{0.14} \qquad (5.17)$$

The standard overall local correlation incorporating the local axial variation factor is,

$$Nu = 0.09\,Pf^{2/9}\,Pr^{1/3}\,Vi^{0.14}\,(X/D_T)^{-0.86} \qquad (5.18)$$

The profile from the above correlations show similar trend as observed with the Reynolds number correlations.

Fig 5.10: Heat transfer correlation for unaerated non-Newtonian solutions with power factor using single Rushton impeller

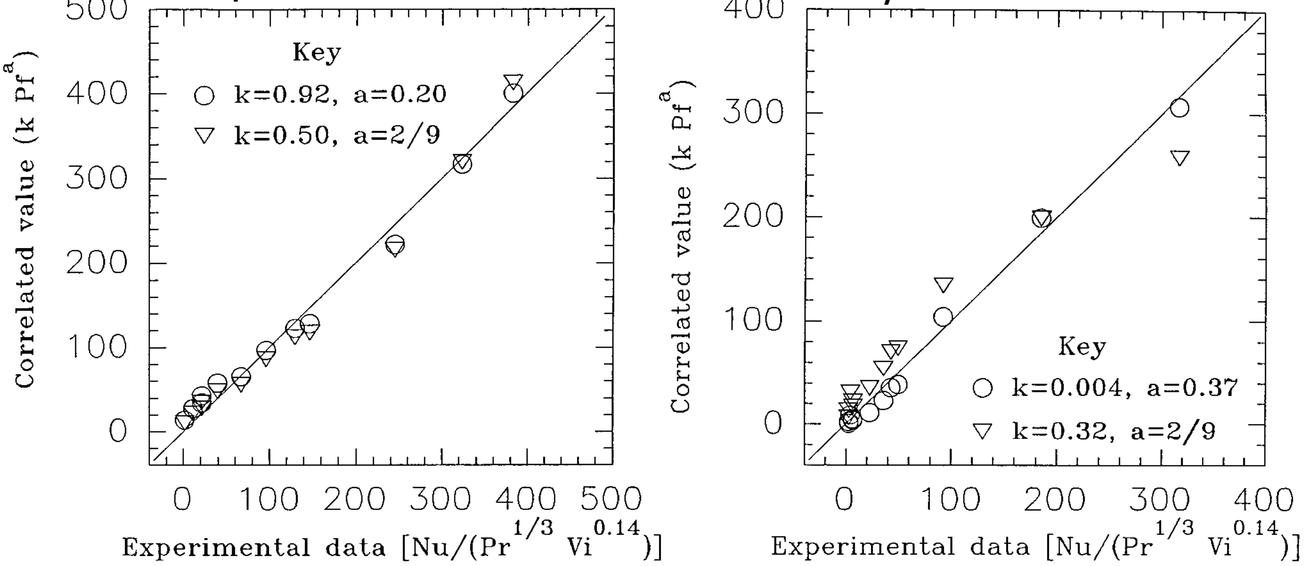

a) Local correlation for probe -1

b) Local correlation for probe -2

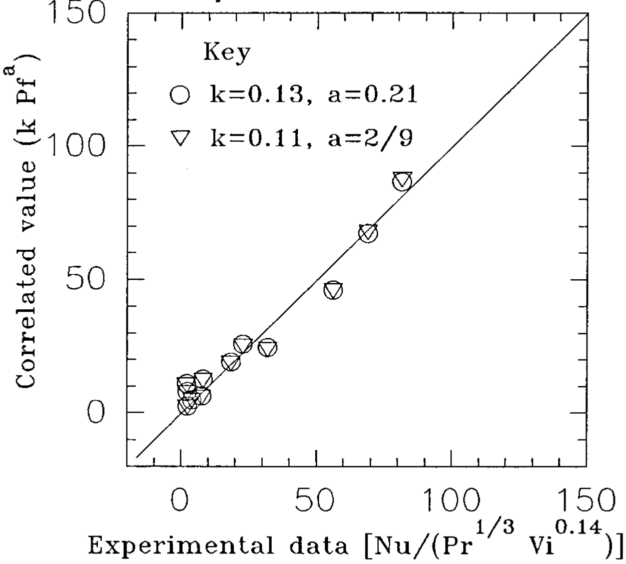

c) Local correlation for probe -3

d) Overall local heat transfer coefficient correlation

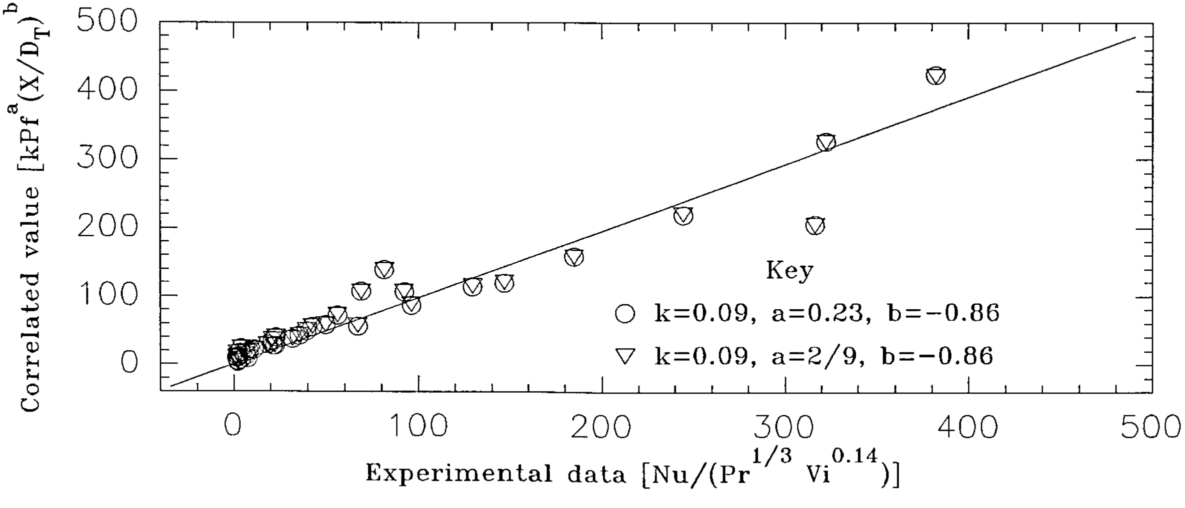

5.3 Unaerated Newtonian fluids- two impeller system

In a bioreactor there is generally the need for more than one impeller therefore the next phase of the project was to introduce a dual impeller system. For this dual impeller system additional heat flux probe was installed. The position of the probes and configuration of the vessel is given in chapter 3.

It has often been reported that in unaerated systems, the total power draw is the sum of the powers drawn by each impeller when acting alone [129] provided the impeller spacing is equal to or greater than the impeller diameter [130]. For a typical single Rushton turbine the unaerated power number in the turbulent region is about 5; therefore, for the dual impeller system, the total unaerated power number would be 10. However, Kuboi and Nienow [131] reported a total measured power number of 7.5 (instead of 10) using a standard dual impeller system and an impeller clearance of D. They [131] conclude that each impeller assists the other and that the summation rule in this case is conservative. The flow pattern in a dual impeller system strongly depends on the impeller spacing. When the impellers are touching, and both impellers operate as a single one of twice the blade height then an increase in power draw is about 30% [132] as compared with that of a single impeller. If the impeller spacing is in the range 0.5D to 1.5D, one circulation loop per impeller is found, though these loops have independent existence, there is actual interaction in the region between the two impellers by secondary loops. The total power draw for 0.5D and D clearance was about 55% more than that for a single turbine. Whereas for a clearance of 1.5D the total power draw was slightly less (5% less) than twice that of a single impeller. For spacing greater than 2D each impeller develops the characteristic radial discharge found with a single turbine and the power draw approximates twice that of a single impeller, with the lower impeller drawing slightly more (which is true for all the case). Thus the above discussion suggests that for an impeller spacing of 1.5D or greater there is a hydrodynamic compartmentalisation between the two impellers, which means that there is little or no interaction between the flow fields of the two impeller. It would be interesting to examine the heat transfer behaviour in such a typical hydrodynamic case in dual impeller system.

The impeller spacing for this project was 1.5D. The comparison of the unaerated power number data for single and dual impeller (see figure 5.3 and 5.11 and appendix 5) suggests that the latter is twice (approximately) the former, and following from the above argument one can assume that the two impellers nearly act independently. The data (see figure 5.11) for the dual impeller Newtonian system (Glucose-3) shows that for probe 1 the heat transfer coefficient value is almost similar (within ±20%) to that for the single impeller. Which suggests that though the power draw has doubled with the addition of another impeller the

Fig 5.11: Local unaerated heat transfer coefficient, power draw and power number profile for glucose-3 solution using dual Rushton impeller

a) Local unaerated heat transfer coefficient profile

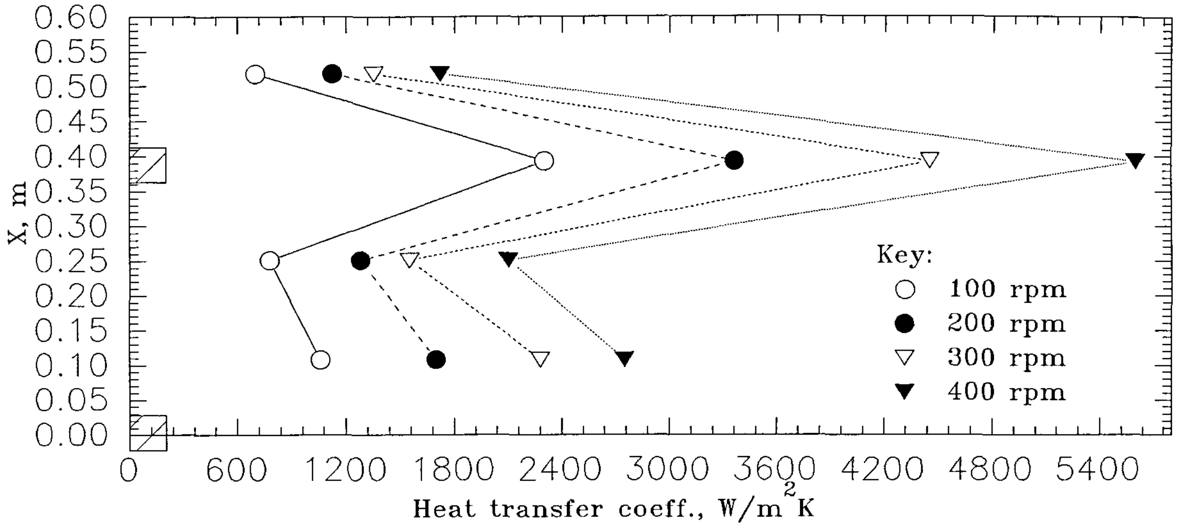

b) Power draw profile

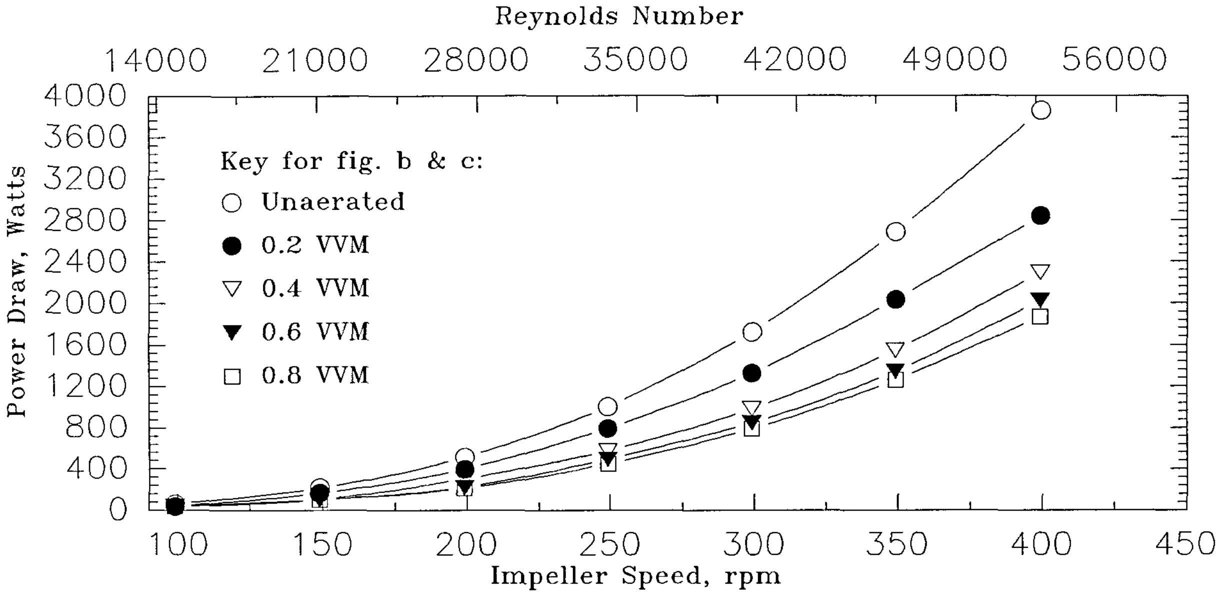

c) Power number profile

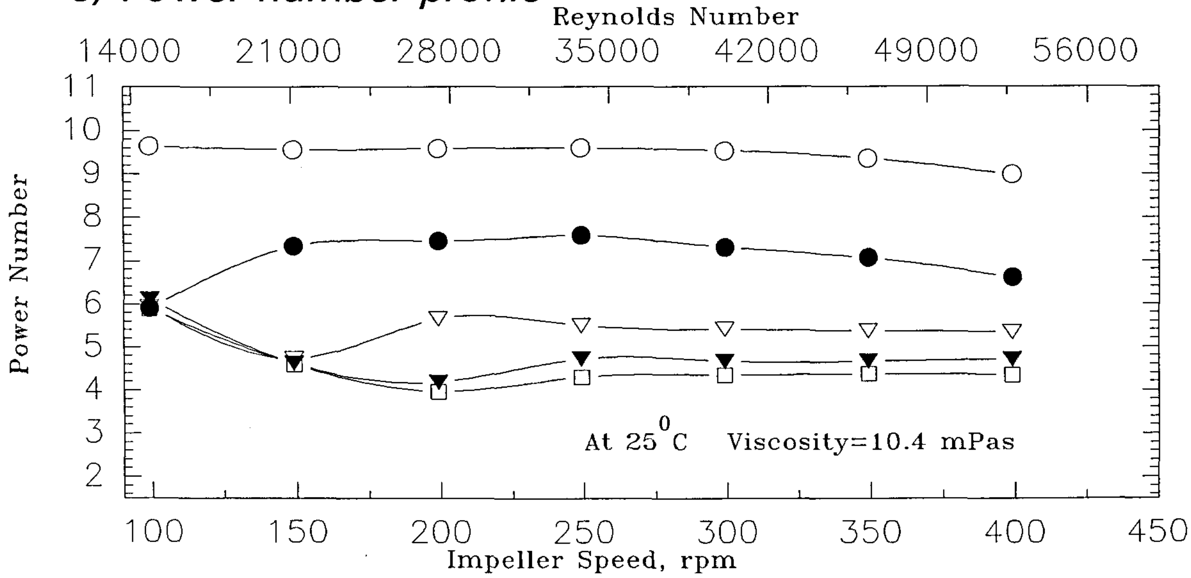

local heat transfer coefficient remains the same at probe position 1, therefore the second impeller has no influence on the probe position 1 at all impeller speed. The similarity of the single and dual impeller data for probe position 1 also supports the reproducibility of the probe and the technique.

For probe position 2 the unaerated single and dual impeller data (see appendix 5, table A5.3 and A5.4) shows similarity at low impeller speeds (impeller speed of 100 and 200 rpm), however at high impeller speed of 400 rpm the dual impeller system shows a significant increase in the heat transfer coefficient. This suggests that though at low impeller speed a compartmentalisation (independent primary loop) does exist but at higher speed there is certainly some interaction (secondary loop) between the impeller flow fields, so as to enhance the heat transfer coefficient. It should be noted here that the probe position 2 is closer to the second impeller (and is not in the middle of the two impellers). A comparison between probe positions 2 and 4 for the dual impeller system (see figure 5.11 a, also appendix 5, table A5.4) suggests that though probe 4 is closer (0.125 m) to the second impeller than probe 2 (0.143 from second impeller and 0.25 from the first impeller) the value of the heat transfer is greater for the latter and that this difference increases with the impeller speed. This observation further reinforces the concept that there is an interaction between the two impellers at high impeller speed.

It is clear from the above discussion that without any fundamental development in the hydrodynamic knowledge of dual impeller system there is unlikely to be a significant development in the understanding of heat transfer in such a system. However, at low and moderate impeller speeds compartmentalisation could be safely assumed, in which case the correlations derived for single impeller systems would be valid for dual impeller systems as well. Further, for the region between the two impellers, it is difficult to draw a strict compartment boundary, for practical purposes the midpoint between the two impellers seems to be a reasonable assumption.

Another interesting observation is that, Probe 3 which is in the impeller discharge stream registers a considerably higher value of heat transfer coefficient than the other probes, and that this difference increases with impeller speed. This suggests that there is drastic difference in the velocity flow field in the impeller plane and away from it. Therefore it may be more suitable to have an independent correlation for the impeller discharge stream. Such a correlation derived for dual impeller system would be valid for single impeller system as well, at all impeller speed, because in the case of dual impeller system the influence of the other impeller would be negligible in the impeller discharge stream of the former. However, due to small number of data points (only 4) it was not possible to comprehensively correlate.

Fig 5.12: Local unaerated heat transfer coefficient, power draw and power number profile for 0.28% CMC solution using dual Rushton impeller.

a) Local unaerated heat transfer coefficient profile

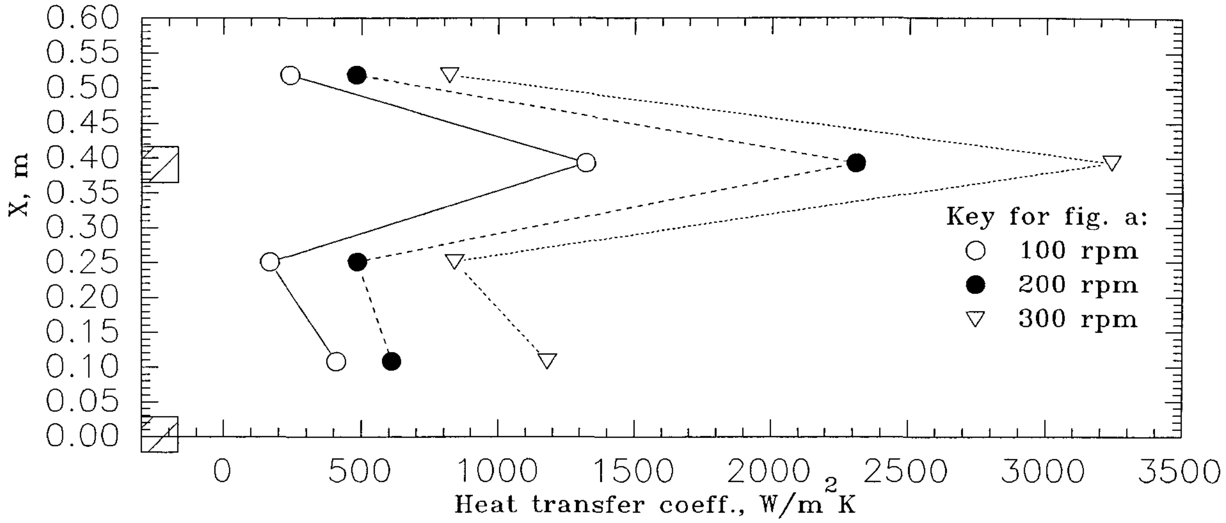

b) Power draw profile

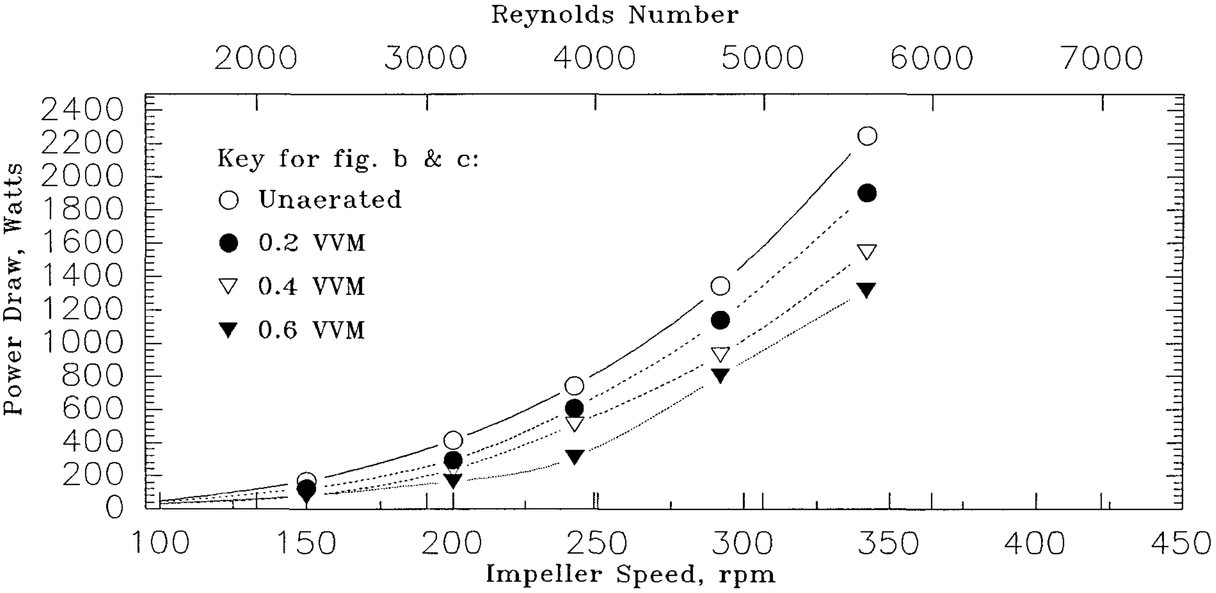

c) Power number profile

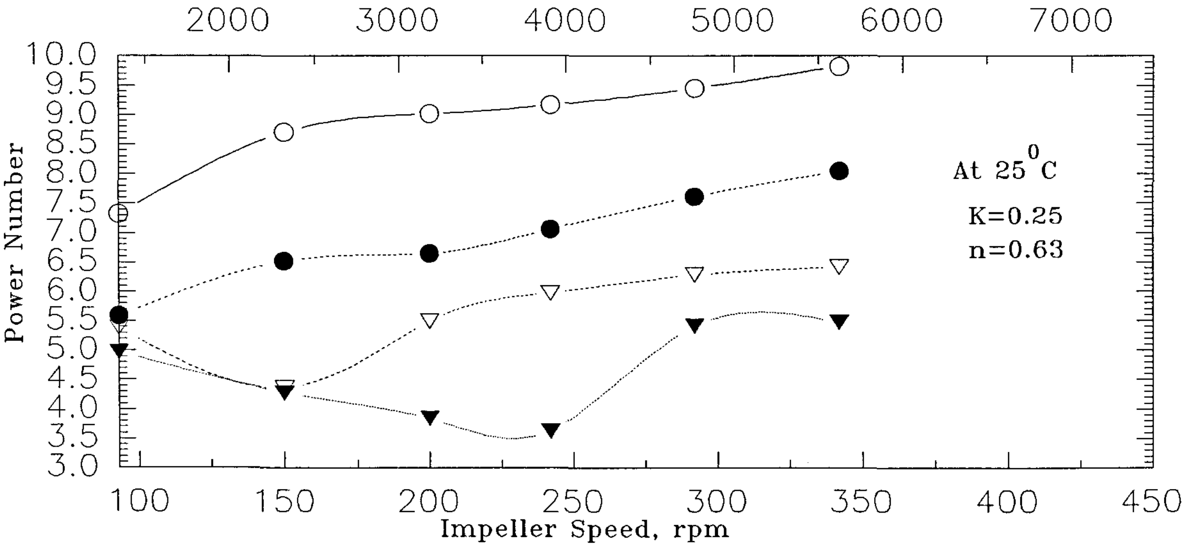

Fig 5.13: Local unaerated heat transfer coefficient, power draw and power number profile for 0.8% CMC solution using dual Rushton impeller.

a) Local unaerated heat transfer coefficient profile

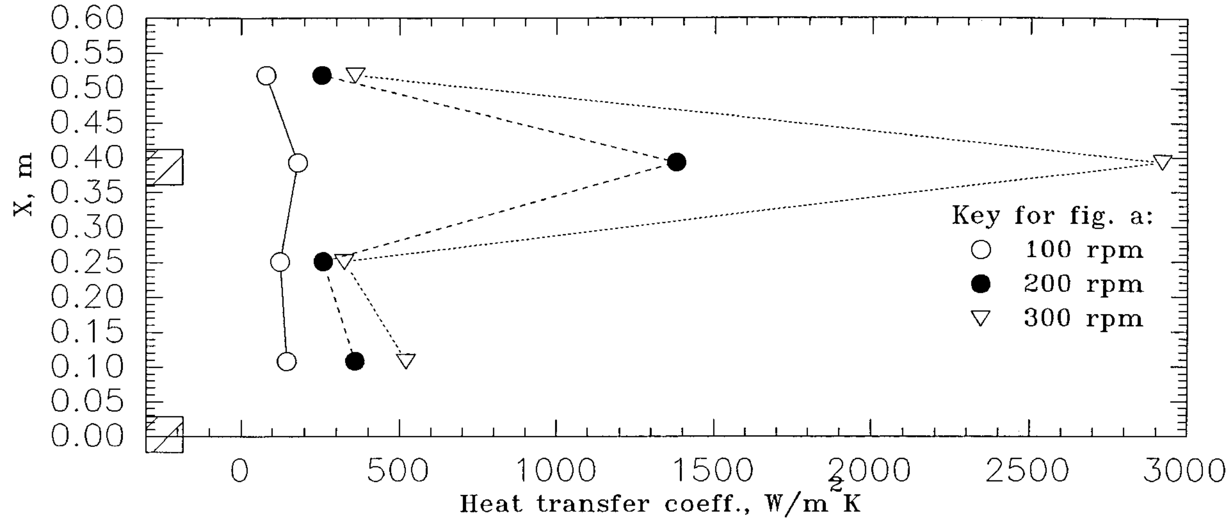

b) Power draw profile

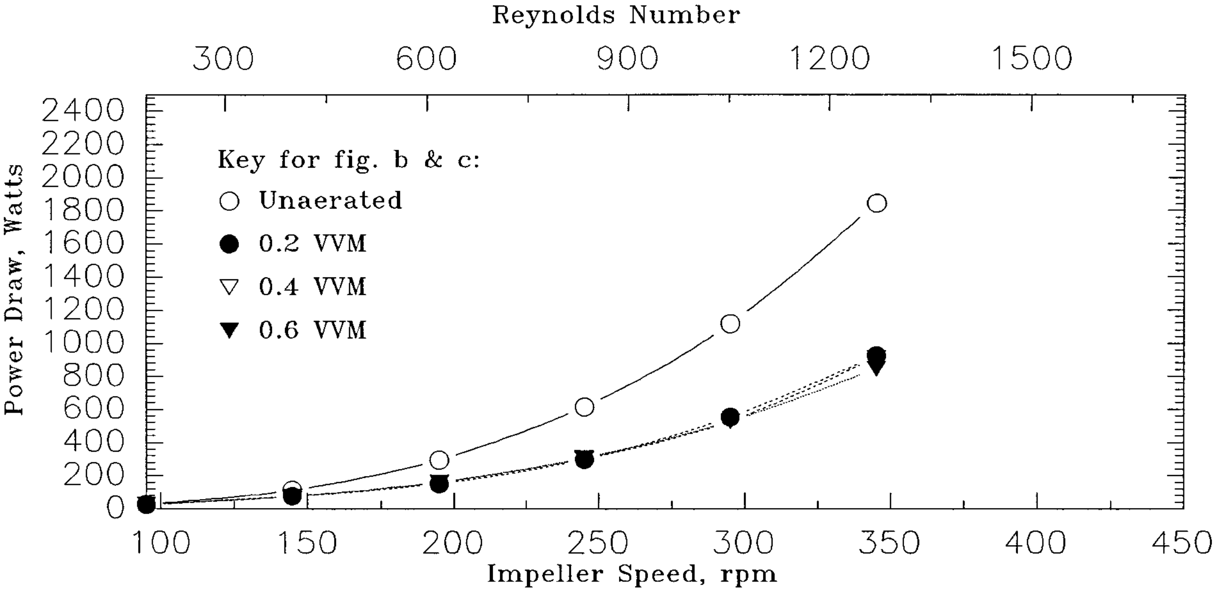

c) Power number profile

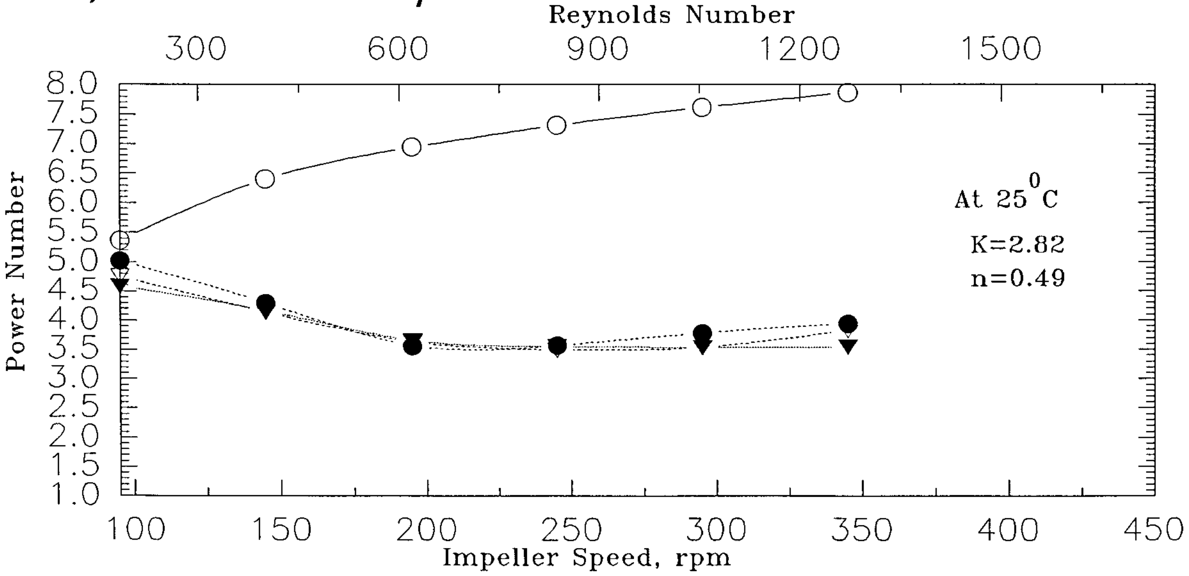

Fig 5.14: Local unaerated heat transfer coefficient, power draw and power number profile for 1.4% CMC solution using dual Rushton impeller.

a) Local unaerated heat transfer coefficient profile

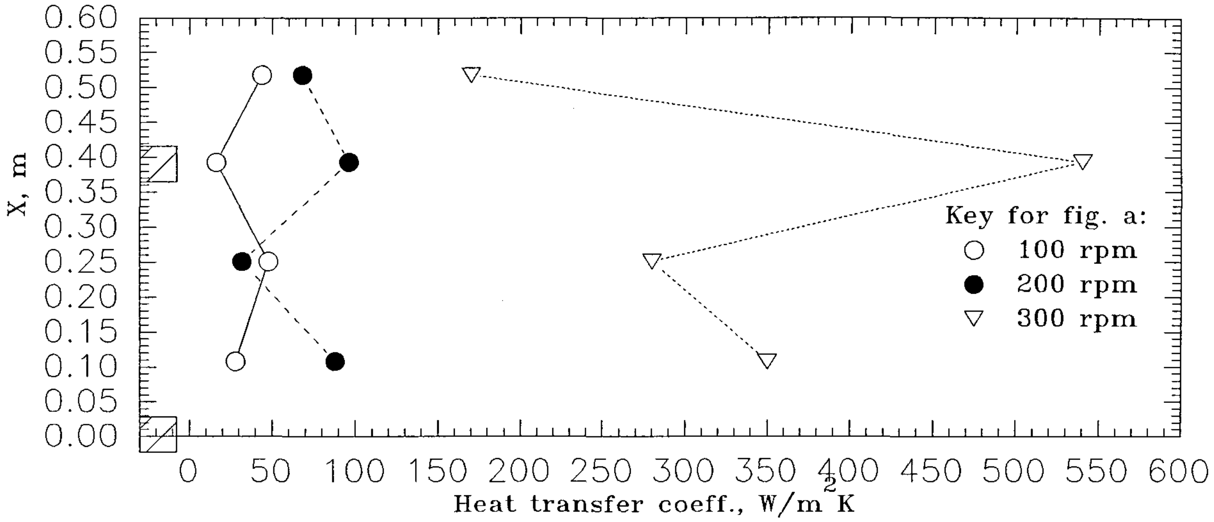

b) Power draw profile

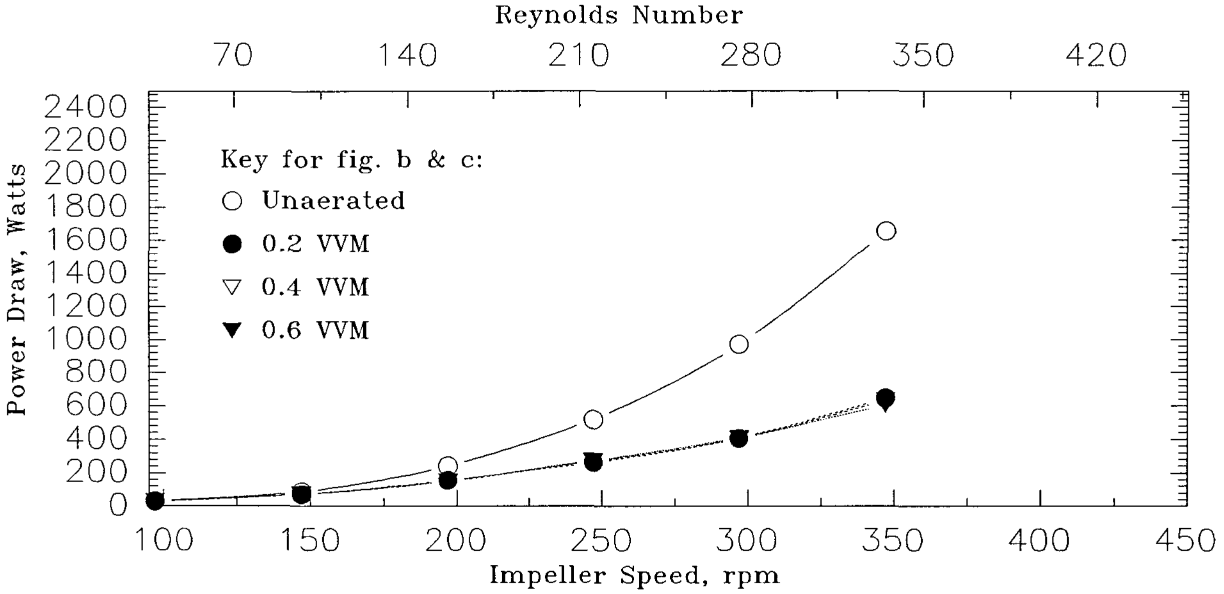

c) Power number profile

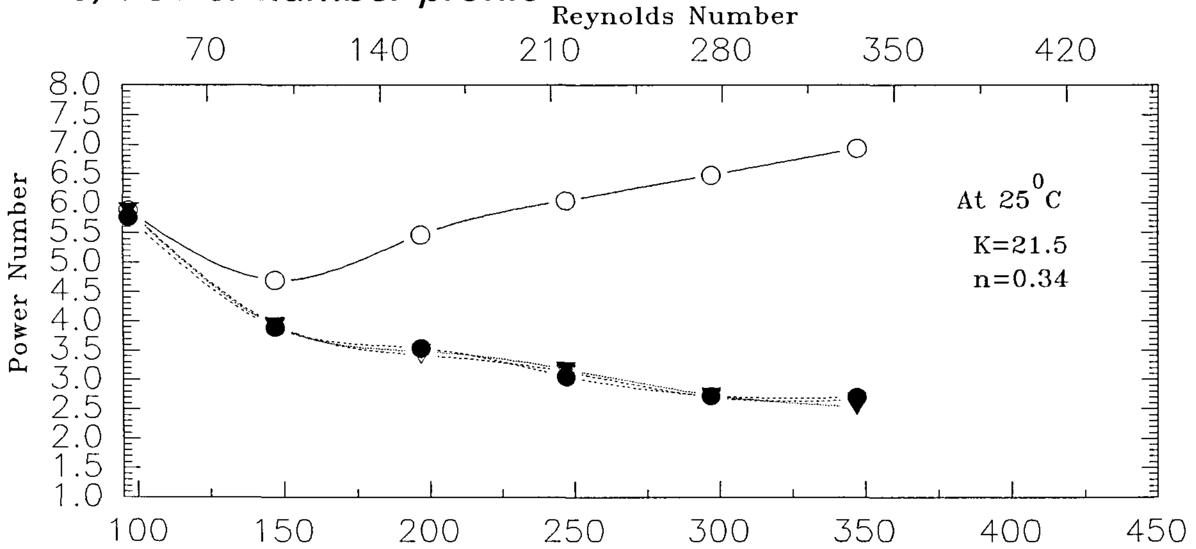

5.4 Unaerated non-Newtonin fluids- two impeller system

Figures 5.12 to 5.14 shows the local heat transfer and power data for 0.28%, 0.8% and 1.4 % CMC respectively. The rheological properties of the shear thinning solutions adds another dimension to the already complex problem.

The values of heat transfer coefficient at the probe position 1 for dual impeller and single impeller system (see appendix 6) does not show a clear trend. However, the majority of values suggests that there is a similarity between the values of single and dual impeller system at this probe position.

The value of the heat transfer at probe position 3 (which is in the impeller discharge stream) shows a considerably higher value than the other probe, this difference, in general, is higher than the Newtonian fluids. This suggests that there is very high shear rate at the impeller discharge stream, which markedly reduces the fluid viscosity thus causing an enhancement of the heat transfer coefficient.

Unlike the Newtonian fluids, the heat transfer coefficient values for the probe position 2 for dual and single impeller systems are significantly different. The value for dual impeller system being higher, further this difference increased with the impeller speed. It seems likely that for shear thinning fluid the interaction between the impeller system is more prominent than the Newtonian fluids. Probably there is only one secondary loop instead of two clearly defined primary loops. The data for probe position 1 (see appendix 5) which is very close to lower impeller shows a general increase (with a few exceptions) in the heat transfer coefficient value as compared to the corresponding single impeller data. This is unlike the Newtonian case, where for probe position 1, for the same impeller tip speed the single and dual impeller system gave similar results. This reinforces the thought that for non-Newtonian fluids one secondary loop exists and the concept of compartmentalisation is no longer valid. Thus, the correlation for single impeller system cannot be extended for the dual impeller system in non-Newtonian case.

The characteristic of secondary loop will vary with the shear thinning nature of the fluid, it seems unlikely that much progress could be made in understanding of heat transfer in dual impeller system without a better knowledge of local hydrodynamics and local shear.

CHAPTER 6

Local heat transfer and mixing studies in two phase systems

Introduction of air into a mechanically agitated vessel significantly changes the hydrodynamics inside the vessel. When the Rushton impeller is operated in a gas liquid system the gas is drawn into the vortices behind each impeller blade and this leads to the formation of gas filled cavities, whose size and shape characteristically changes with impeller speed and gas flow rate. The hydrodynamic characterisation of aerated Rushton turbine systems is described in detail in chapter 2 (section 2.6). In this chapter the effect of aeration on heat transfer (as in section 6.1) and its correlation with the global power draw is discussed. This study aims to relate the heat transfer to the aerated power, thus incorporating the effect of the two phase global hydrodynamics (albeit empirically) on heat transfer. This investigation is for both Newtonian (see section 6.2) and non-Newtonian fluid (see section 6.3) using single Rushton impeller, and also for dual impeller system using same fluids (see sections 6.4 and 6.5 respectively).

6.1 The affect of aeration on local heat transfer

Edney and Edwards [132] have reported that aeration had no effect upon heat transfer to a submerged coil for a six blade turbine agitated in a 1.22 m diameter vessel. It was suggested that this was because the extra momentum imparted to the liquid due to gas sparging, which should result in increased heat transfer, was offset by the reduction in fluid density and hence thermal convection and conduction due to the presence of the dispersed gas bubbles. De Martelaere [133] found a small effect of gas flow rate at low impeller speed, in what was probably a gas dominated regime when the momentum of the gas is most noticeable, whereas at higher speeds there was only negligible effect.

Shah et al [134] reviewed the impact of the gas on the energy input in a bubble column. They showed for a bubble column that, by using Kolmogoroff's approach, the energy dissipation rate could be calculated from the pressure drop experienced by the gas flow. The energy input P' is then approximately given by;

$$P' = V_s \; \rho \; g H \qquad (6.1)$$

Therefore, the energy dissipation rate ε_g (W/kg) can be calculated as

$$\varepsilon_g = V_s \, g \qquad (6.2)$$

The data in tables in the appendix 5 quantitatively compares the power dissipated by the gas (in Watts) and that by the impeller for a range of fluids used in this project. This comparison highlights the fact that at low impeller speed the power dissipated by the gas is comparable to the impeller power draw, but at high impeller speeds the contribution of the energy imparted by the gas becomes negligible. The former is then the gas dominated regime while the latter is impeller dominated. It is thus important to incorporate the power dissipated by the gas in power calculations (especially for correlations), so that the total power includes both impeller power and power dissipated by the gas.

Thus the introdution of gas has two opposing effects: a) the formation of gas filled cavities behind the impeller blade leading to a drop in impeller power draw and b) power input in the system as defined by equation 6.2 . In the following sections the effect of these factors on heat transfer would be examined.

6.2 Aerated Newtonian fluid - one impeller system

The understanding of hydrodynamics is of paramount importance in understanding of heat transfer. The hydrodynamics strongly depends on the gas cavity (structure) behind the impeller blade which is a function of impeller speed, gas flow rate and the type of fluid. Figures 5.1c, 5.2c and 5.3c show the drop in power number on aeration as compared with the unaerated power number. The drop in power depends on the type and size of the cavity structure (see chapter, section 2.6) and further, it was not possible to carry out any flow visualisation in this experimental setup therefore inferences were drawn from the ratio of aerated to unaerated power number, which reflects the affect of cavity structure on the global hydrodynamics. Figures 6.1d, 6.2d and 6.3d show the ratio of aerated to the unaerated power number which is clearly dependent on all the above stated factors. It then becomes interesting to explore the interaction between hydrodynamics and heat transfer.

At low gas flow rate of 0.2 vvm the impeller is able to disperse the gas even at the lowest impeller speed of 100 rpm (see figures 6.1a, 6.2a and 6.3a). This is an impeller dominated region ($N_F < 100$ rpm for this gas flow rate) and hence there is distinct axial profile with the

Fig 6.1: Local aerated heat transfer and mixing results for glucose-1 solution

a) 0.2 vvm *b) 0.4 vvm*

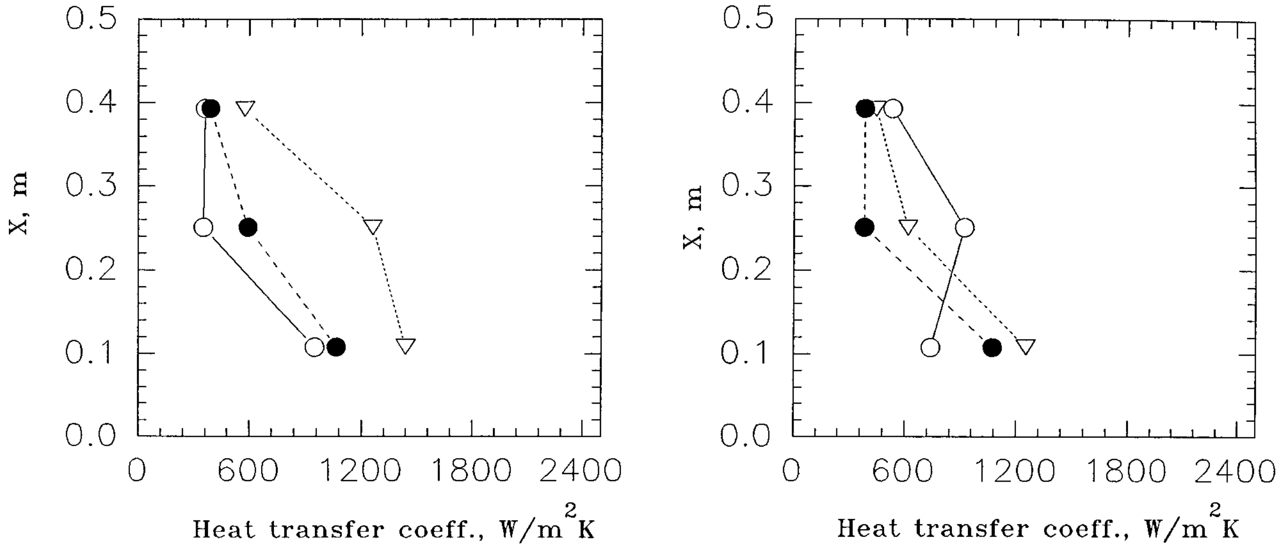

c) 0.6 vvm

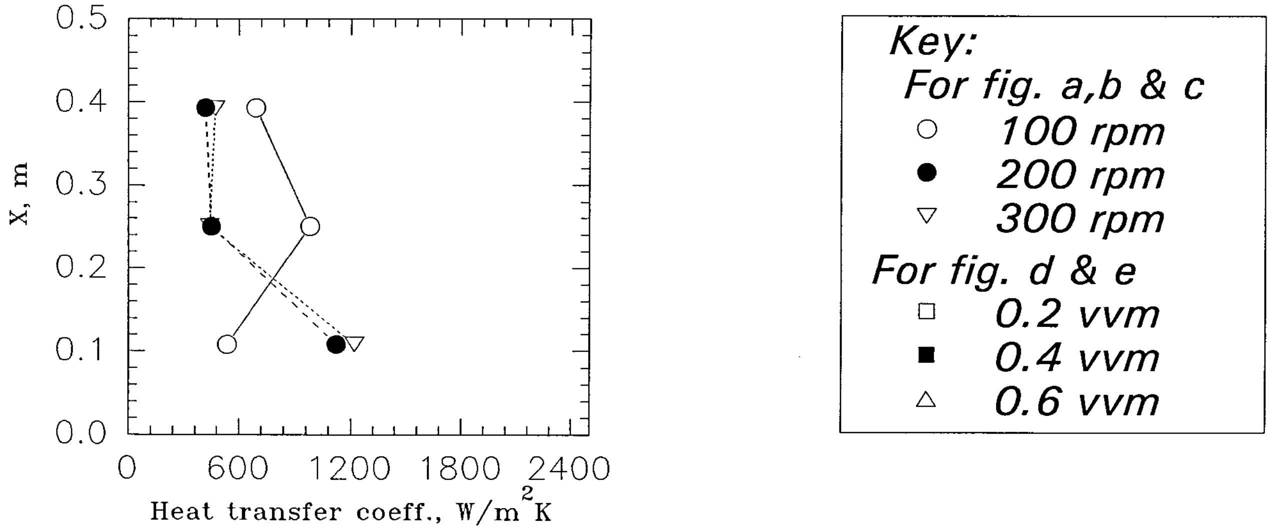

d) Power curve *e) Gas holdup profile*

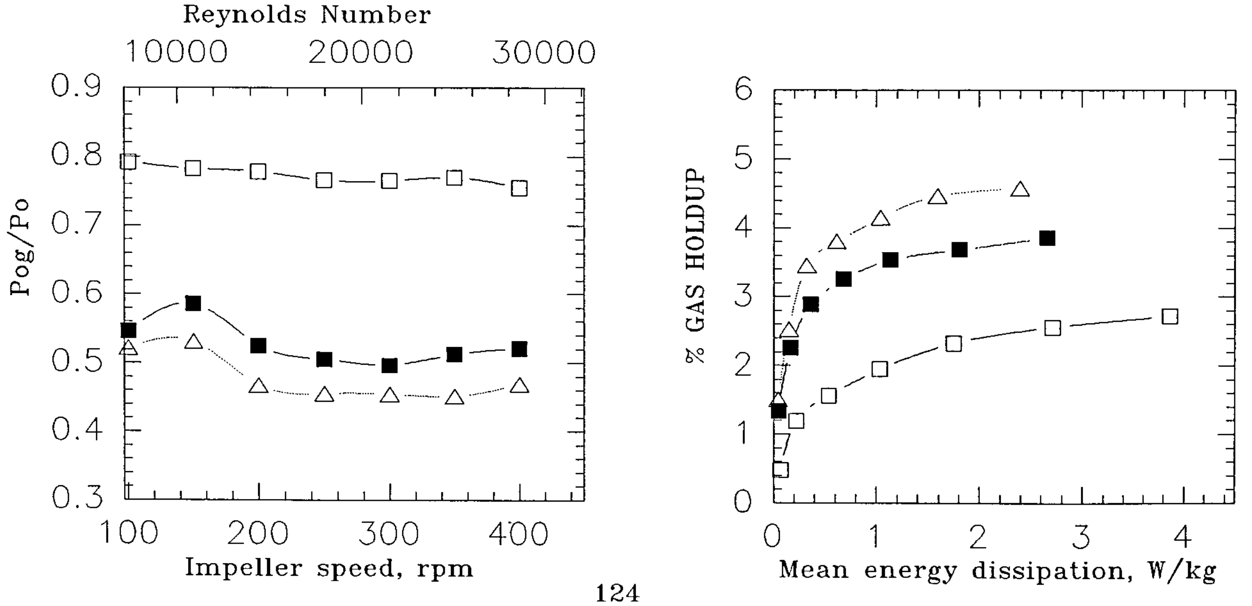

Fig 6.2: Local aerated heat transfer and mixing results for glucose-2 solution

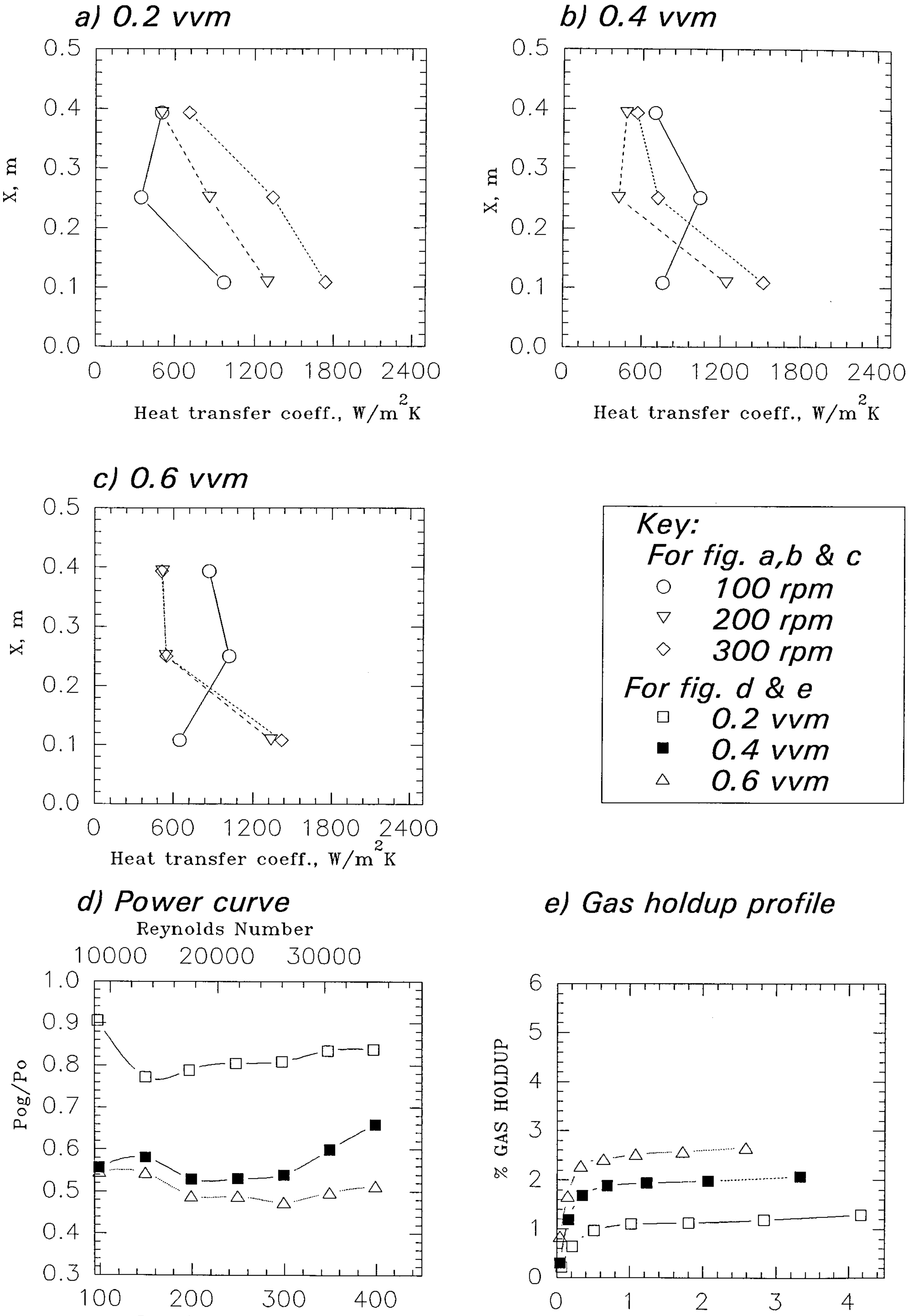

Fig 6.3: Local aerated heat transfer and mixing results for glucose-3 solution

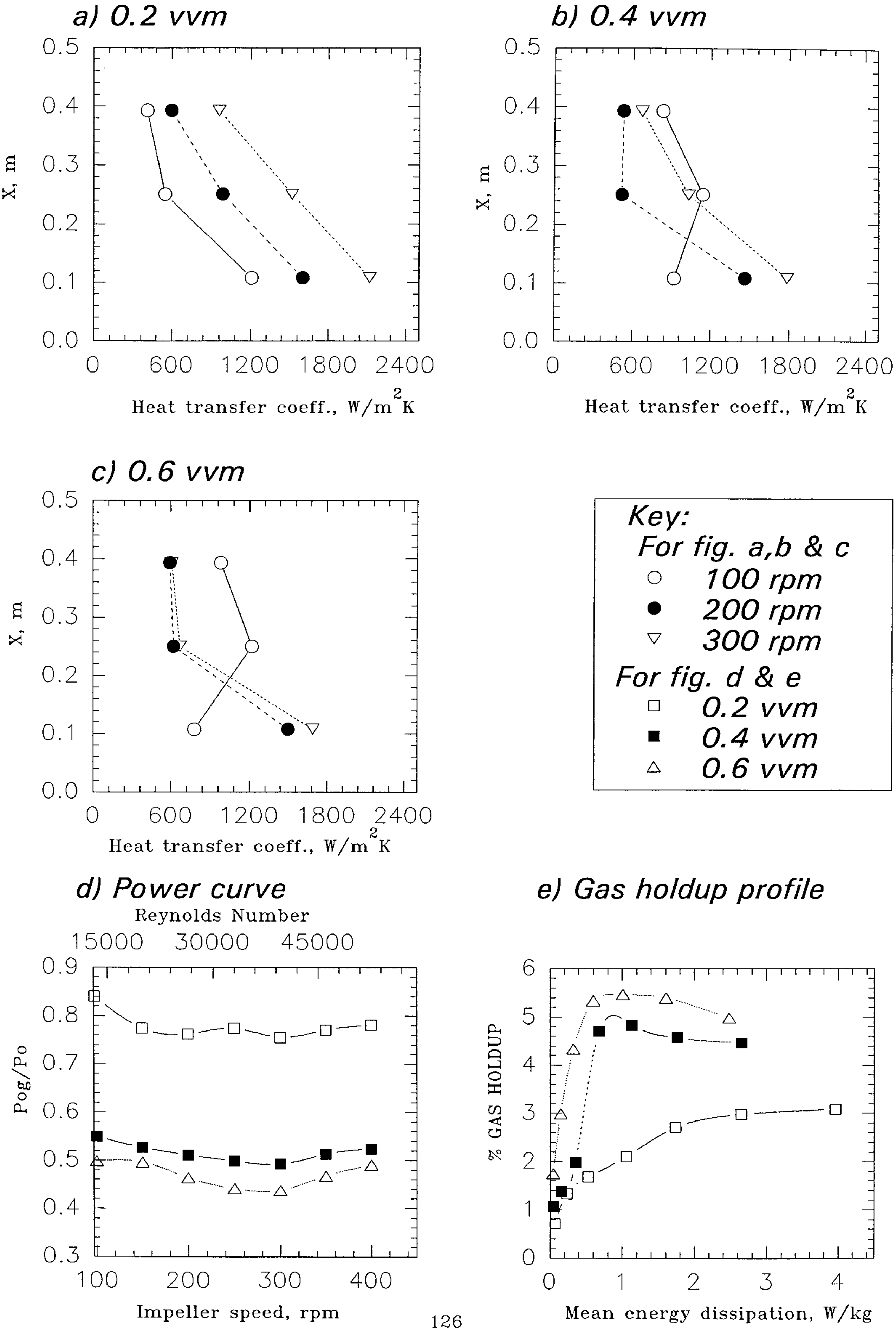

maximum value of heat transfer coefficient near the impeller plane. Further increase in impeller speed (and hence the power draw) leads to an increase in the heat transfer coefficient too. Therefore there is a qualitative relationship between heat transfer coefficient and power draw, which will be quantitatively discussed in the following section. Further, comparing the results of the three concentration of glucose (see figure 6.1a, 6.2a and 6.3a) it becomes clear that rheology plays a significant role also in aerated fluids. The high viscosity fluid (Glucose-1) shows a lower heat transfer coefficient than the low viscosity fluid (Glucose-3) at all impeller speeds (in complete dispersed conditions).

At high gas flow rate of 0.4 and 0.6 vvm, the low impeller speed of 100 rpm is below N_F and the impeller is engulfed in gas which it is unable to disperse. It is known that in such conditions the cavity structure formed behind the impeller blade is ragged and this hydrodynamic condition is referred to as flooding (refer chapter 2, section 2.6). Since, impeller has very little influence on the velocity flow field and that the hydrodynamics is dominated by the gas flow, therefore the heat transfer coefficient value near the impeller plane shows a marked reduction and no distinct axial profile emerges (see figures 6.1- 6.3 a and b). However, clearly the increased gas flow rates have significant influence on the heat transfer coefficients registered by the top two probes (probe 2 and probe 3) as compared to their values at 100 rpm and 0.2 vvm in all the fluids used. With the increase in the impeller speed the size and the shape of the cavities behind the impeller blade changes. These changes could not be seen but it can be inferred from the changes in the power ratio that they followed the general trend of moving from ragged ($N<N_F$) to large "3-3" structure for ($N_F< N< N_{cd}$) and clinging for $N \geq N_{cd}$ where N_{cd} is the impeller speed necessary for complete dispersion. Certainly the impeller speed of 200 rpm and above were higher than N_F for this configuration and this was reflected in the heat transfer measurement, i.e there was a distinct axial variation in heat transfer coefficient (see figures 6.1-6.3 c).

Comparing the aerated data with unaerated heat transfer data from the previous chapter, the general trend is that there is a reduction in local heat transfer coefficients under aeration. The reduction is certainly attributed to the reduction in the global power draw by the impeller caused by the formation of gas cavities behind the impeller blade which leads to the drop in the power number (see chapter-2, section 2.6). However, the comparison must be done using the total aerated power. At the lowest gas flow rate of 0.2 vvm and at 100 rpm (see figures 6.1 a, 6.2 a and 6.3 a) there is actually an increase in the local heat transfer coefficient near the impeller plane (probe 1) as compared with the corresponding unaerated data (see chapter 5, figure 5.1 to 5.3) even though there is a reduction in the impeller power draw. This is due to the effect of the energy input by the gas which is comparable (13.1 Watts) to that by the impeller (25.5 Watts) thus the total power at 38.6 Watts (see Appendix 5) is greater than the corresponding unaerated power (32 Watts). Similar influences are noted at high gas flow rates where the power dissipated by the gas becomes more significant. Therefore in aerated systems the total power dissipated must be taken into account specially when interpreting the heat transfer results.

Figures 6.1e, 6.2e and 6.3e shows the gas holdup data as measured by the ultrasonic gauge (see chapter 3, section 3.2.5), which shows an increase with increase in both gas flow rate and impeller speed. The use of gas holdup data, in this project, is to give the indication about the actual presence of the gas in the system which then gives a clear idea about the reduction in fluid density and potential thermal convection and conduction, caused by the presence of the dispersed gas bubbles. Since the gas holdup is low, one can safely assume the physical properties to be close to that of the continuous medium (glucose).

6.2.1 Empirical correlation

It became clear in chapter 5 that the description of the velocity flow field in an impeller agitated system is not yet adequate to explain heat transfer effects on a mechanistic basis even for an unaerated system. This is even more true for aerated system. Therefore, recourse has again to be taken to empirical correlation of the data using global parameters such as Reynolds and Power numbers. The correlation with Reynolds number for aerated fluids is however meaningless as the conventional form does not include the effect of gas phase on hydrodynamics and hence on the heat transfer. Hence the only alternative left is to correlate the data using the dimensionless power factor. Figure 6.4 shows the correlation of the data for the dispersed regime (impeller dominated) a similar approach to correlation is adopted as in the unaerated case (see chapter 5, section 5.1.1). The solid line represents the experimental data whereas the symbols (circle and triangle) represent the two approaches to the correlation. The former approach to correlation yields the best fit for the data whereas the latter one forces the correlation by assuming a standard exponent (2/9) to the power factor. The correlated value shows a significant scatter about the experimental data line, and the statistical tolerance limit was not completely satisfied specially in the case of the probe-2 data (see figure 6.4 b). This suggests that in the aerated systems it becomes even more difficult to correlate the local heat transfer coefficient, because aeration introduces another level of complexity. However, the standard form of the correlation, which satisfies the statistical 80% tolerance limit, is,

for probe-1,

$$Nu = 1.18\, Pf^{2/9}\, Pr^{1/3}\, Vi^{0.14} \qquad (6.3)$$

Fig 6.4: Heat transfer correlation for aerated Newtonian solutions with power factor using single Rushton impeller

a) Local correlation for probe -1

b) Local correlation for probe -2

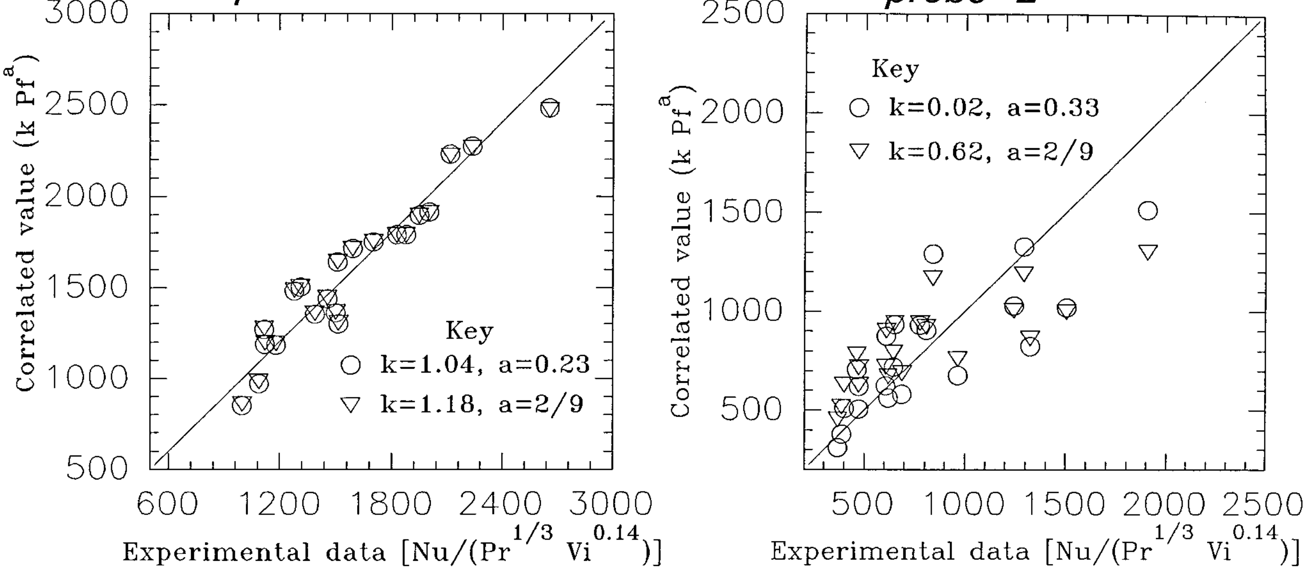

a) Local correlation for probe -3

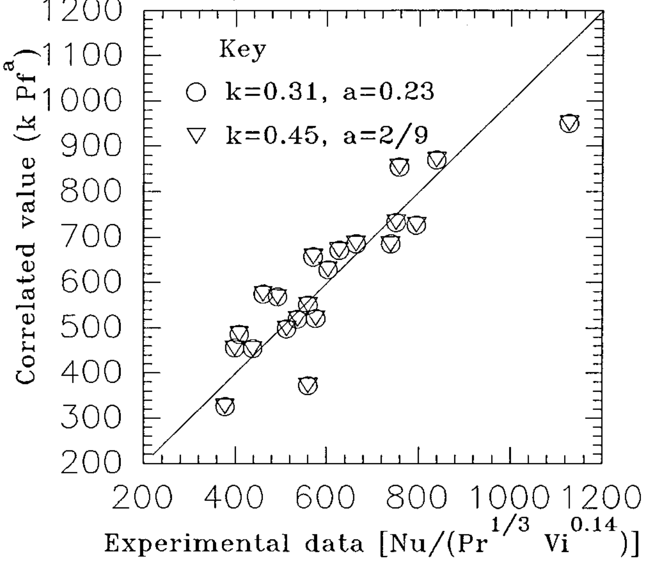

d) Overall local heat transfer coefficient correlation

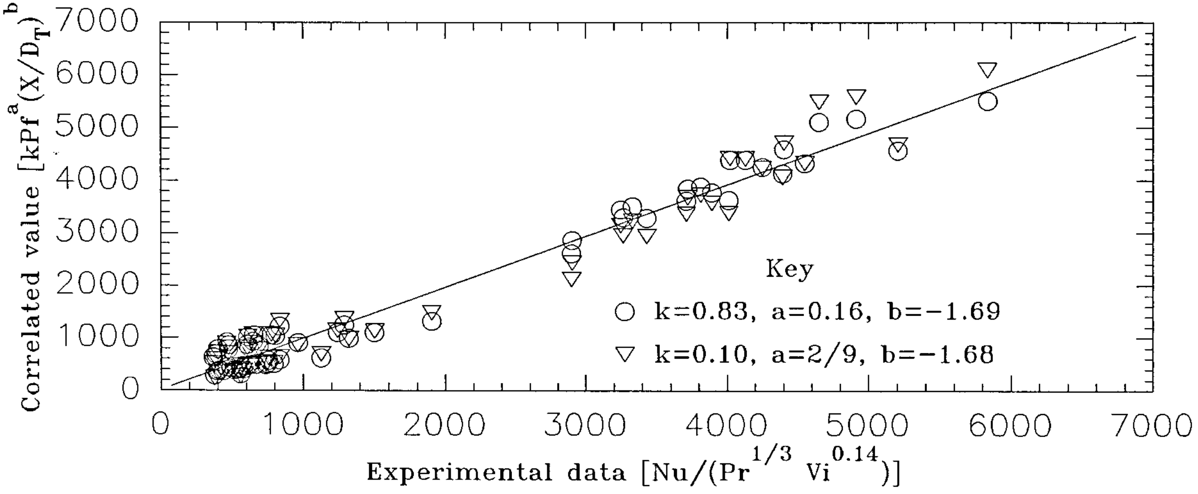

for probe-2,
$Nu = 0.62\ Pf^{2/9}\ Pr^{1/3}\ Vi^{0.14}$ (6.4)

and for probe-3,
$Nu = 0.45\ Pf^{2/9}\ Pr^{1/3}\ Vi^{0.14}$ (6.5)

Like the unaerated case, the above correlations clearly show a decreasing trend in heat transfer coefficient (Nusselt number) form probe-1 to 3, as manifested in the constant k. However, this trend is only for the impeller dominated regime (above flooding-loading transition). Comparing with the corresponding unaerated correlation one can clearly observe a decrease in the value of the constant k for the aerated case. This denotes a general trend that aeration essentially leads to a drop in heat transfer coefficient (the only exception is at low impeller speed, as discussed above) due to a drop in the aerated power draw as compared with the unaerated case at the same impeller speed.

In order to produce an overall local heat transfer correlation the axial variation term, (X/D_T) was incorporated, and the standard form of correlation which matches closely with the best fit as shown in figure 6.4 d, is,

$$Nu = 0.10\ Pf^{2/9}\ Pr^{1/3}\ Vi^{0.14}\ (X/D_T)^{-1.68} \qquad (6.6)$$

The exponent on X/D_T (-1.68) for aerated case is significantly different than the unaerated exponent (-0.38). This suggests that the local velocity flow field (specially near the heat transfer surface) is significantly different for aerated case as compared with the unaerated one. There is a sharper decrease in the local heat transfer coefficient value (as compared to the unaerated case) as one moves away from the impeller plane. This may suggests that for an aerated cases there is a well mixed region around the impeller and beyond which it starts to behave as a bubble column specially near the liquid surface.

6.3 <u>*Aerated non-Newtonian fluids - one impeller system*</u>

Figures 6.5 to 6.7 shows the local aerated heat transfer and mixing (global) results for 0.28%, 0.8% and 1.4% CMC. For 0.28% CMC, which is less shear thinning (n=0.63) the aerated to the unaerated power ratio (see figure 6.6 e) shows a profile similar to that for Newtonian fluids (presumably because the cavity structure is still similar). At low gas flow rates the impeller is able to disperse the gas at all impeller speeds and therefore flooding does not occur

Fig 6.5: Local aerated heat transfer and mixing results for 0.28 % CMC solution

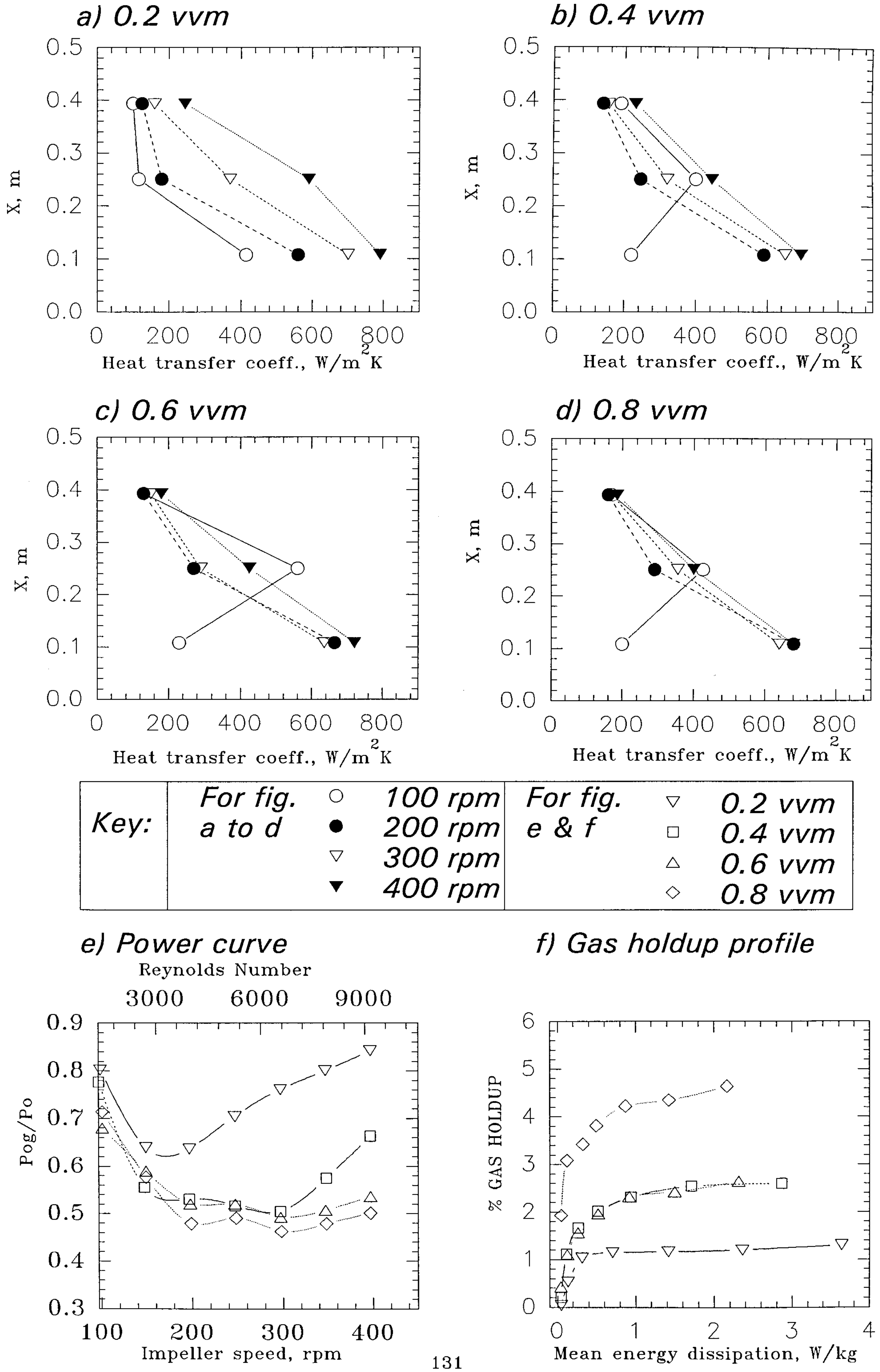

Fig 6.6: Local aerated heat transfer and mixing results for 0.8 % CMC solution

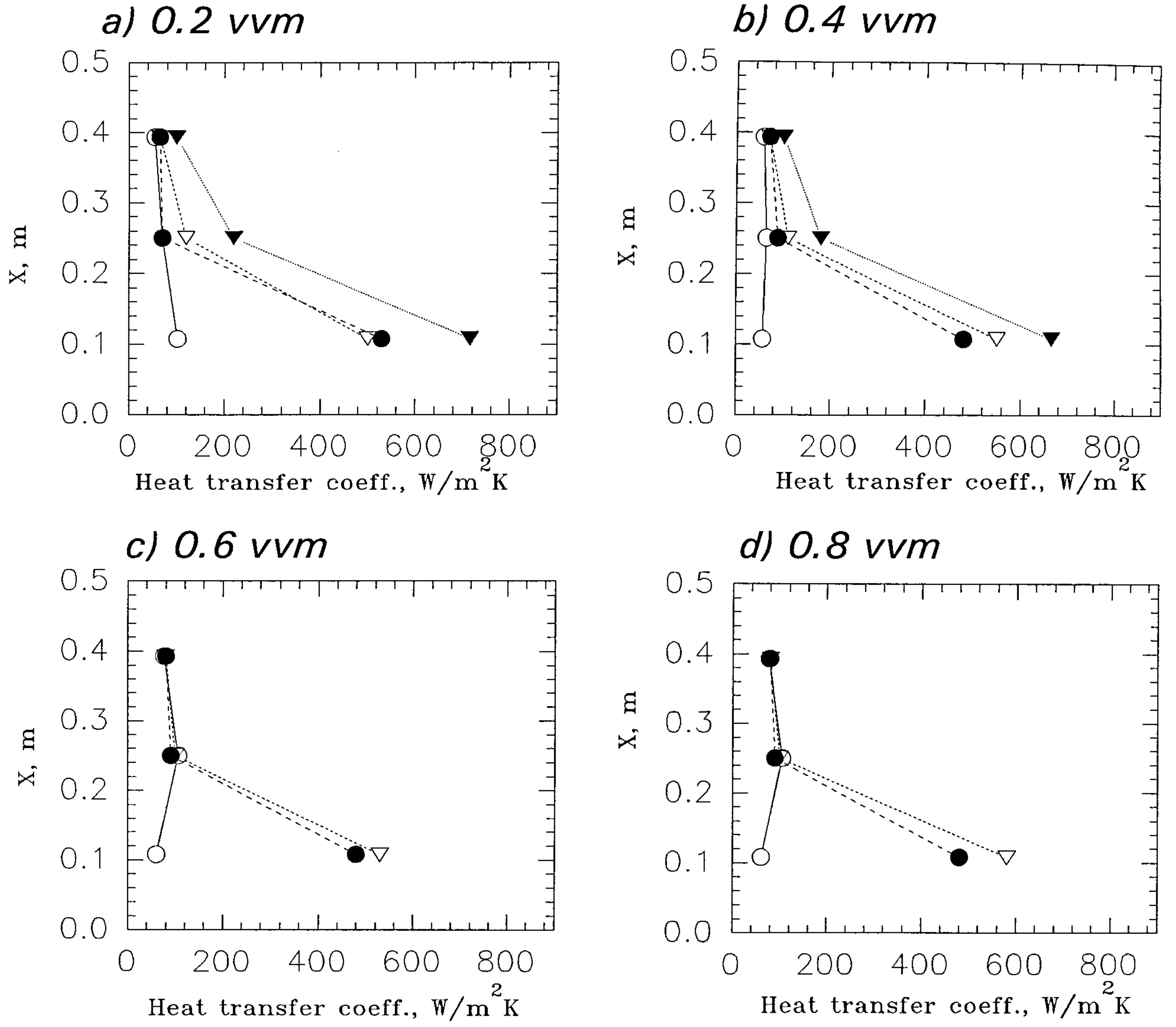
a) 0.2 vvm

b) 0.4 vvm

c) 0.6 vvm

d) 0.8 vvm

Key:	For fig. a to d			For fig. e & f		
		○	100 rpm		□	0.2 vvm
		●	200 rpm		■	0.4 vvm
		▽	300 rpm		△	0.6 vvm
		▼	400 rpm		▲	0.8 vvm

e) Power curve

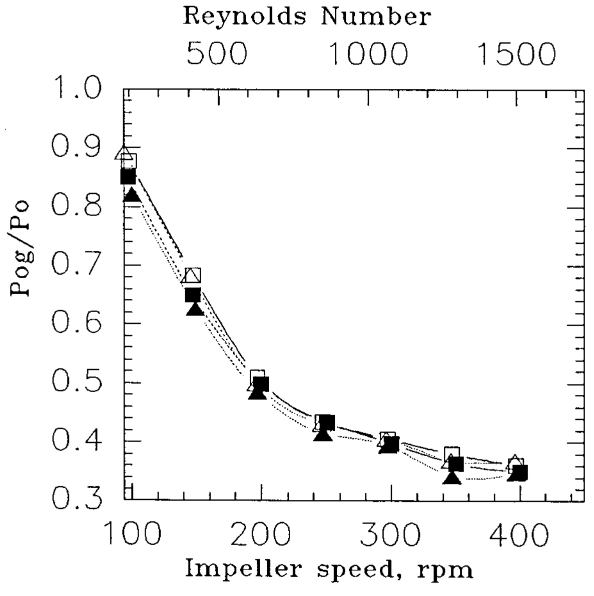

f) Gas holdup profile

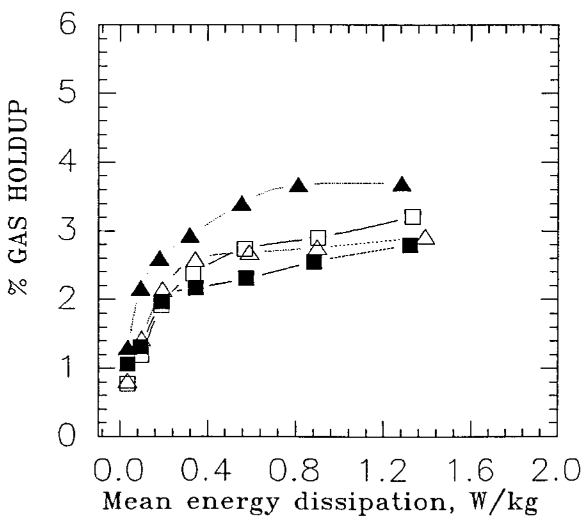

Fig 6.7: Local aerated heat transfer and mixing results for 1.4 % CMC solution

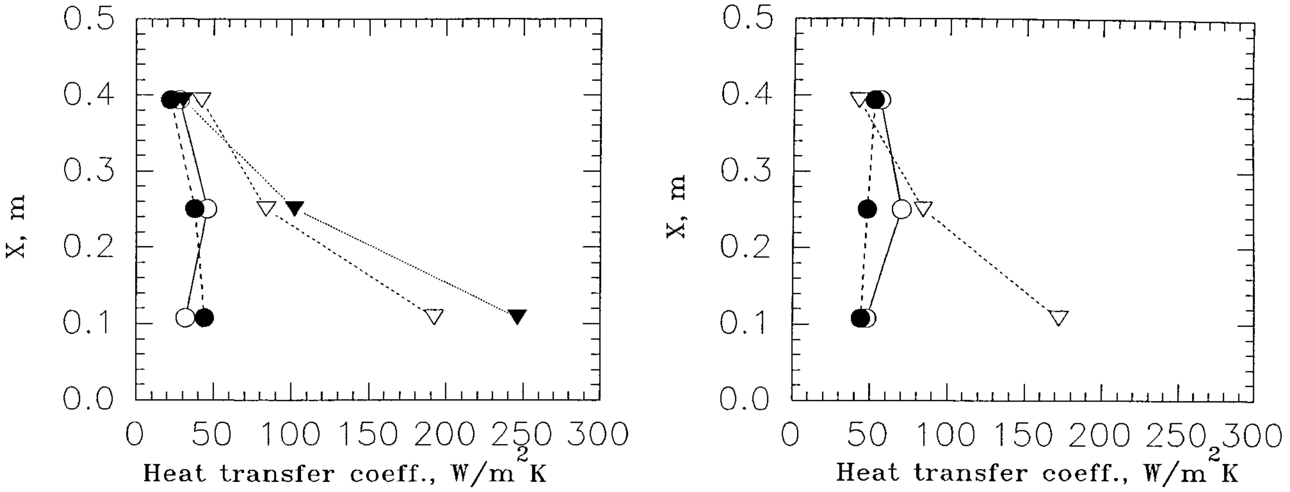

a) 0.2 vvm

b) 0.4 vvm

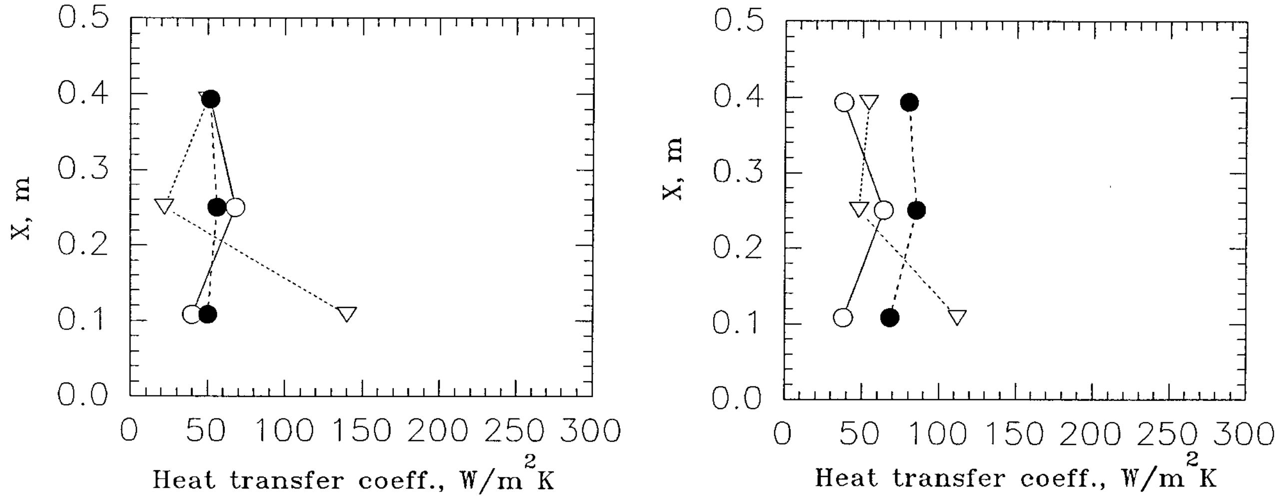

c) 0.6 vvm

d) 0.8 vvm

Key:	For fig. a to d			For fig. e & f		
		○	100 rpm		□	0.2 vvm
		●	200 rpm		■	0.4 vvm
		▽	300 rpm		△	0.6 vvm
		▼	400 rpm		▲	0.8 vvm

e) Power curve

f) Gas holdup profile

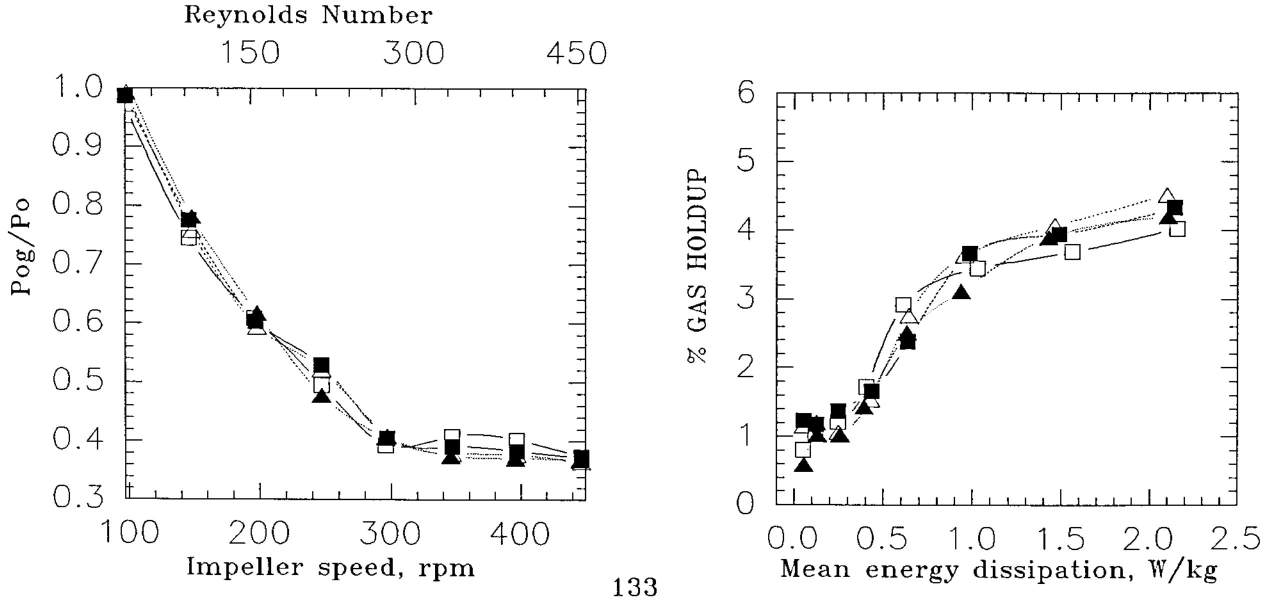

at the lowest impeller speed used (100 rpm). The heat transfer coefficient (see figure 6.6a) shows a distinct axial profile at all impeller speeds. At higher gas flow rates (0.4, 0.6 and 0.8 vvm), flooding occurs at the lowest impeller speed (100 rpm), and the heat transfer coefficient reflects this hydrodynamic condition by showing a marked reduction in its value near the impeller plane. The gas holdup data suggests that the entrainment of gas in the system is not high enough to affect the physical properties of the continuous medium.

For medium (0.8% CMC) and highly viscous (1.4% CMC) shear thinning fluids even a small air input rate leads to the formation of large, stable, equi-sized cavities behind the agitator blades. Increase in aeration rate do not change the cavity size significantly but increase both the rate and, to a lesser extent, the size at which bubbles break away from them. The power ratio curve in figure 6.6 e (0.8% CMC) and 6.7 e (1.4% CMC) reinforces the above theory in that it becomes independent of the gas flow rate. The cavity structure seems to be influenced by the impeller speed at all gas flow rates, at low impeller speed flooding still occurs, and further at a critical speed the cavity size becomes independent of the impeller speed. The gas holdup data too is independent of gas flow rate especially so for the 1.4% CMC (see figure 6.7e). Increase in aeration increases both the rate and, to a lesser extent, the size at which bubbles break away from cavities behind the impeller. At high aeration rates, the increased breakaway frequency and bubble size at breakaway leads to enhanced coalescence of bubbles, so that bigger and bigger ones break through the top surface. Therefore, though the increase in gas flow rate does not increase the gas holdup but the size and frequency of bubble break up at the fluid surface (especially at high air flow rate) caused severe mechanical vibrations in the vessel.

The flooded condition is reflected in heat transfer measurement at low impeller (100 rpm) speed for both 0.8% and 1.4% CMC. 0.8% CMC shows a distinct axial profile above the flooding loading transition, though probe 3 which is farthest from the impeller shows little variation with impeller speed and gas flow rates (see figures 6.6 a to d) suggesting that, due to highly shear thinning behaviour of this solution the velocity flow field would quantitatively be considerably reduced. Further due to high shear region around the impeller there are sharp differences in heat transfer coefficients values between probes 1 and 2 with both 0.8% and 1.4% CMC (see figures 6.6 a to d and 6.7 a to d).

6.3.1 Empirical correlation

The standard local heat transfer correlation using the dimensionless power factor for dispersed regime is shown in figure 6.8, which is,

for probe-1
$Nu = 0.50\ Pf^{2/9}\ Pr^{1/3}\ Vi^{0.14}$ (6.7)

for probe-2
$Nu = 0.27\ Pf^{2/9}\ Pr^{1/3}\ Vi^{0.14}$ (6.8)

and for probe-3
$Nu = 0.13\ Pf^{2/9}\ Pr^{1/3}\ Vi^{0.14}$ (6.9)

The value of the constant k shows a decrease with increasing axial distance from the impeller, which is consistent with similar trend observed with the Newtonian fluids.

The overall standard local heat transfer correlation is,
$Nu = 0.08\ Pf^{2/9}\ Pr^{1/3}\ Vi^{0.14}\ (X/D_T)^{-0.91}$ (6.10)

It is interesting to note that there is not much difference between the value of the constant for aerated and the unaerated correlations (equations 5.15 to 5.17). This is in contrast to the Newtonian case where aeration leads to substantial differences in the correlations when compared with the unaerated case. This then suggests that aeration has more influence on heat transfer in case of Newtonian fluid than the non-Newtonian fluid, this can be explained on the basis of totally different hydrodynamics. It may be inferred that this may be due to the cavity structure behind the impeller blade which is uniform and equisized in case of non-Newtonian fluid, specially high viscosity, leading to a uniform and gentle affect on heat transfer, whereas the cavity structure in Newtonian fluid varies widely with both impeller speed and gas flow rate which leads to a wide variation in heat transfer.

6.4 <u>Aerated Newtonian fluid - dual impeller system</u>

For aerated systems with dual Rushton impellers, it has been suggested by Nienow and Lilly [128] to consider the lower impeller to draw the gassed power that it would if operating alone at the gassing rate of interest and the upper impeller to draw the power that it would if

Fig 6.8: Heat transfer correlation for aerated non-Newtonian solutions with power factor using single Rushton impeller

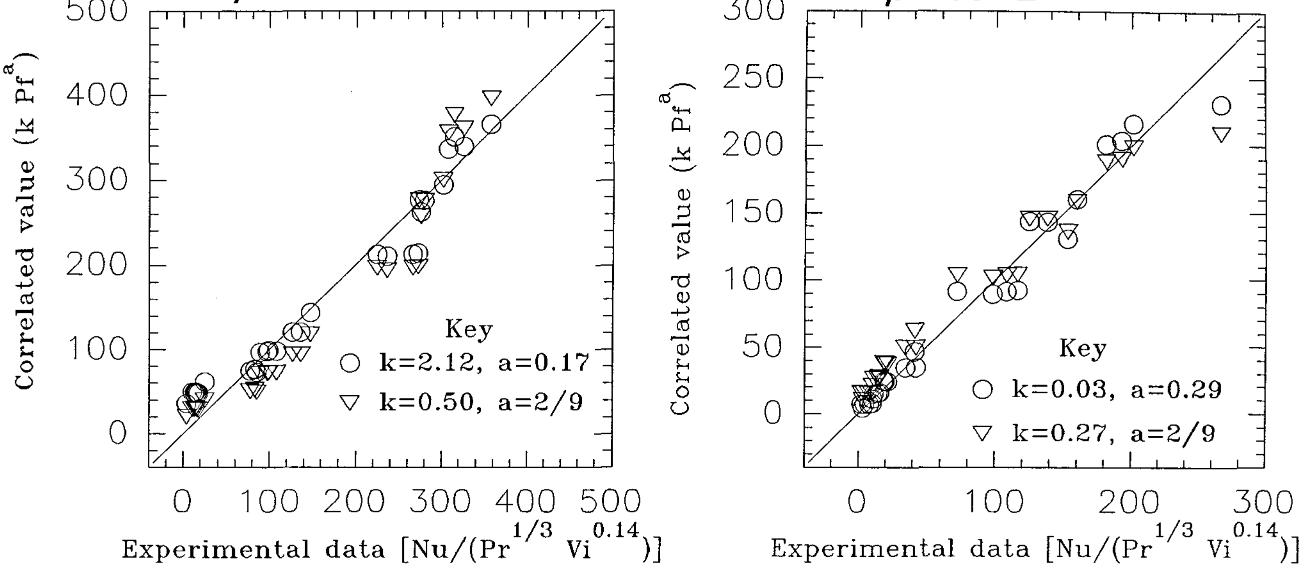

a) Local correlation for probe -1

b) Local correlation for probe -2

c) Local correlation for probe -3

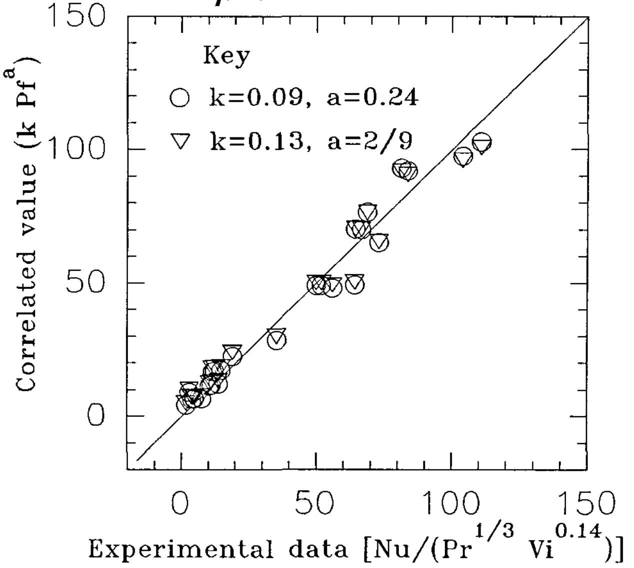

d) Overall local heat transfer coefficient correlation

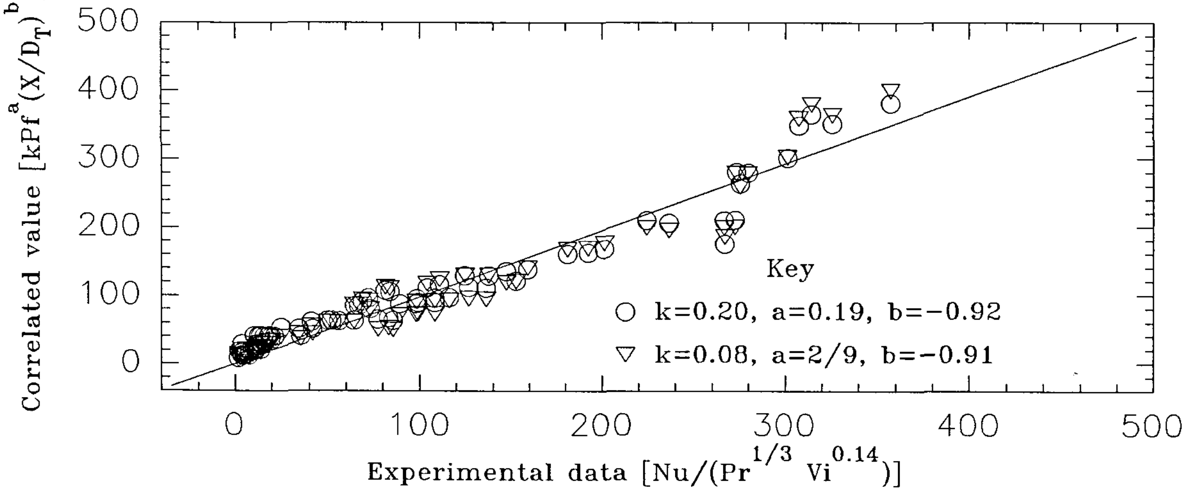

operating alone in a liquid equal to the density of the dispersion. The total power is then the sum of the two. However, they cautioned about the physical inadequacy of this approach for the impeller since it neglected the link with gas cavity structure.

For dual impeller system the flooding loading transition (FLT) is very different for each of the two impellers and is strongly dependent on their clearance. With the two impellers touching and at a constant aeration, the FLT occurs at a lower impeller speed than with a single impeller. Clearly, two impellers touching can be considered as a "deep single" impeller [131] with a greater pumping capacity. As the impellers separate, FLT for each impeller starts to deviate. For a clearance between 0.5D to 1.5D the lower impeller requires a higher speed to achieve FLT as compared to a single impeller. It is as though the unaerated upward discharge direction sucks (by upper impeller) the gas through the impeller and makes flooding easier. This reaches a maximum at a clearance of 1.5D (as in this case), when the full independent flow patterns exist, the lower FLT occurs at the same point as in the case of the single impeller. The upper impeller completes this transition at a considerably lower speed for all clearances. The small amount of dispersion achieved by the lower impeller, even when it is flooded, is sufficient to make dispersion by the upper easy. It is somewhat similar to the effect of a large ring sparger or of an impeller placed high above the sparger even without the lower one [135].

Thus impeller close to the sparger breaks up the sparged air for distribution and in the process it becomes more liable to be flooded first. This theory is supported by the heat transfer measurement for dual impeller glucose 3 solution such that at a low gas flow rate of 0.2 vvm and an impeller speed of 100 rpm the heat transfer coefficient measured by probe 1 (near the lower impeller plane) shows marked reduction, whereas in impeller plane two a clear axial profile exists (see figure 6.9 a). At a higher gas flow rate (0.4 and 0.6 vvm) both the impellers get flooded at the impeller speed of 100 rpm (see figure 6.11 b and c). Further at 0.6 vvm and 200 rpm probe 1 again indicates flooding at the lower impeller whereas the upper impeller is above flooding loading transition. In general, the upper impeller would draw considerably more power, at the same gas flow number, the two impellers would draw a higher proportion of the unaerated power than would a single impeller. Thus at very low impeller speeds, the gas passes through in a very similar manner to that found with a single Rushton impeller i.e. the impeller has no effect on the gas flow. The first sign of the impeller influencing bubble break-up is the formation of bubbling cavities. Bubbling cavities are indicated by relatively large discrete bubbles breaking away from the lower outer quarter of the blade. They leave with a swirling motion and the back of the blade is often completely covered in liquid. Hence the power number of the impeller under this condition should be greater than when large cavities are permanently attached to the back of the blade as shown in figure 6.9 d. The start

Fig 6.9: Local aerated heat transfer and mixing results for 2 impeller glucose-3 solution

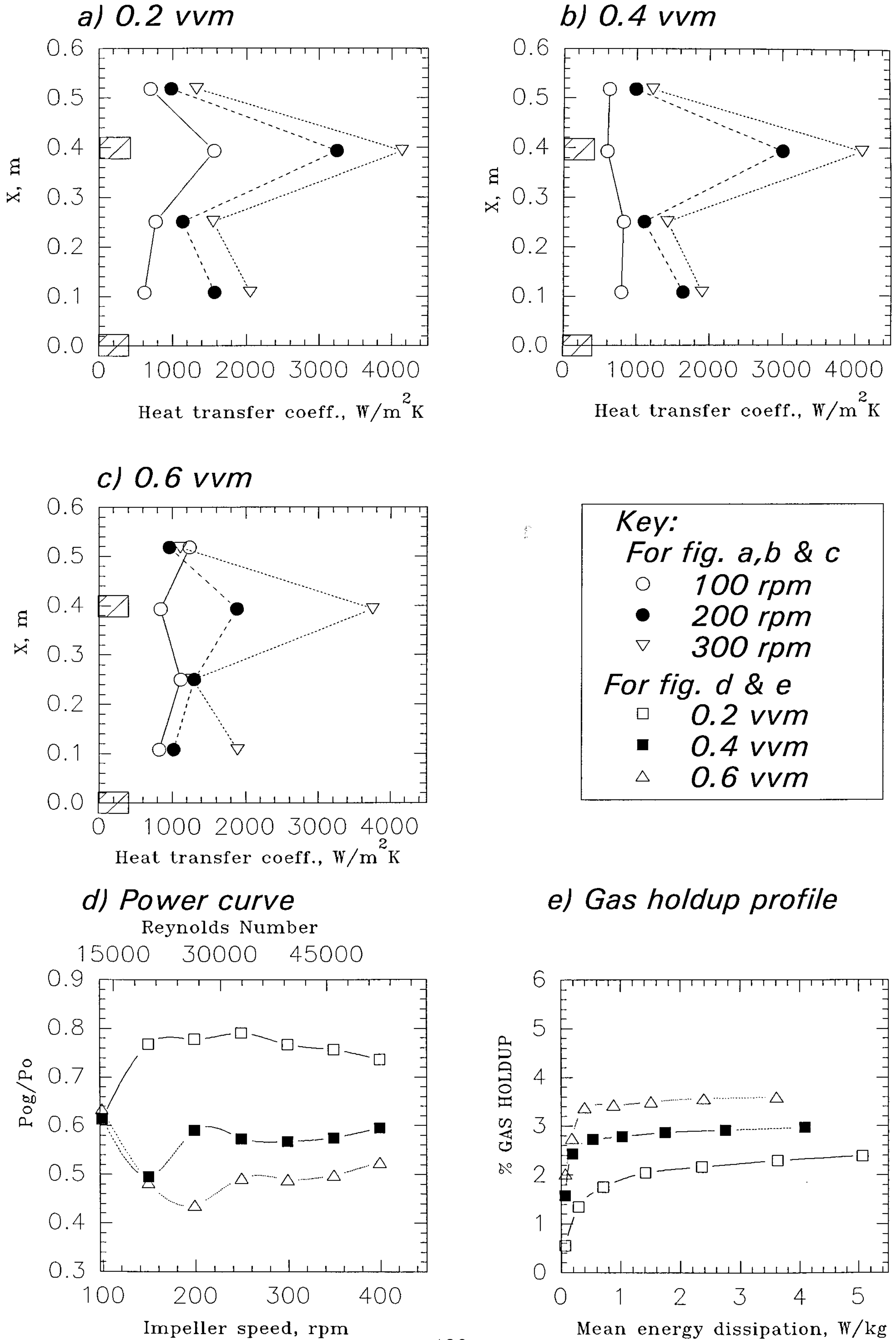

a) 0.2 vvm

b) 0.4 vvm

c) 0.6 vvm

d) Power curve

e) Gas holdup profile

of dispersion by bubbling cavities from the lower impeller enables the upper to be the first to achieve some effective local dispersion. The impeller speed at which this initial dispersion occurs increases rapidly with increasing gassing rate. Somewhat surprisingly, once the lower impeller effectively disperses the gas the normal figure-of-eight flow pattern associated with disc turbines does not appear [128].

Comparing dual with the single impeller system for probe 1 heat transfer coefficient value (see figure 6.3), confirms again that the lower impeller in dual impeller system floods easily as compared to single impeller system. Further, in dispersed condition in dual impeller system probe 1 shows heat transfer coefficient value almost similar to the corresponding value in single impeller system (see Appendix 5). The Probe 2 is influenced more by upper impeller as it is closer to it, therefore generally probe 2 heat transfer data for dual impeller system shows a higher value as compared to the single impeller system, this is because following the above discussion it is clear that the upper impeller draws more power as compared with a single impeller system.

Finally, in the qualitative assessment of the heat transfer data, it is also observed that the heat transfer coefficient values measured by probe 2 is consistently higher than the ones measured by probe 4. There could be two reasons for this, firstly, the position of probe 2 is slightly closer to the upper impeller than probe 4 and secondly, there might be some interaction between the two independent compartments around each impeller.

6.5 Aerated non-Newtonian fluid - dual impeller system

Figure 6.10 shows the heat transfer and power data for 0.28% CMC for dual impeller system. The lower impeller is the first to be flooded, this is again reflected in heat transfer measurement observed at air flow rate of 0.4 vvm at impeller speed of 200 rpm (see figure 6.10 b) and also at air flow rate of 0.6 vvm and impeller speeds of 200, 300 and 400 rpm (see figure 6.10 c). Like in Newtonian fluid the heat transfer coefficient reported by probe 2 is consistently higher than that reported by probe 4, especially so at higher impeller speeds which again supports the theory that there might be interaction between the two impeller flow fields.

In highly viscous pseudoplastic fluids such as 0.8% and 1.4% CMC , the hydrodynamics would be significantly different. The lower impeller, aerated from the sparger, forms cavities similar to that found in one impeller system. However, the cavity structure for the upper

Fig 6.10: Local aerated heat transfer and mixing results for 0.28 % CMC solution using dual Rushton impeller

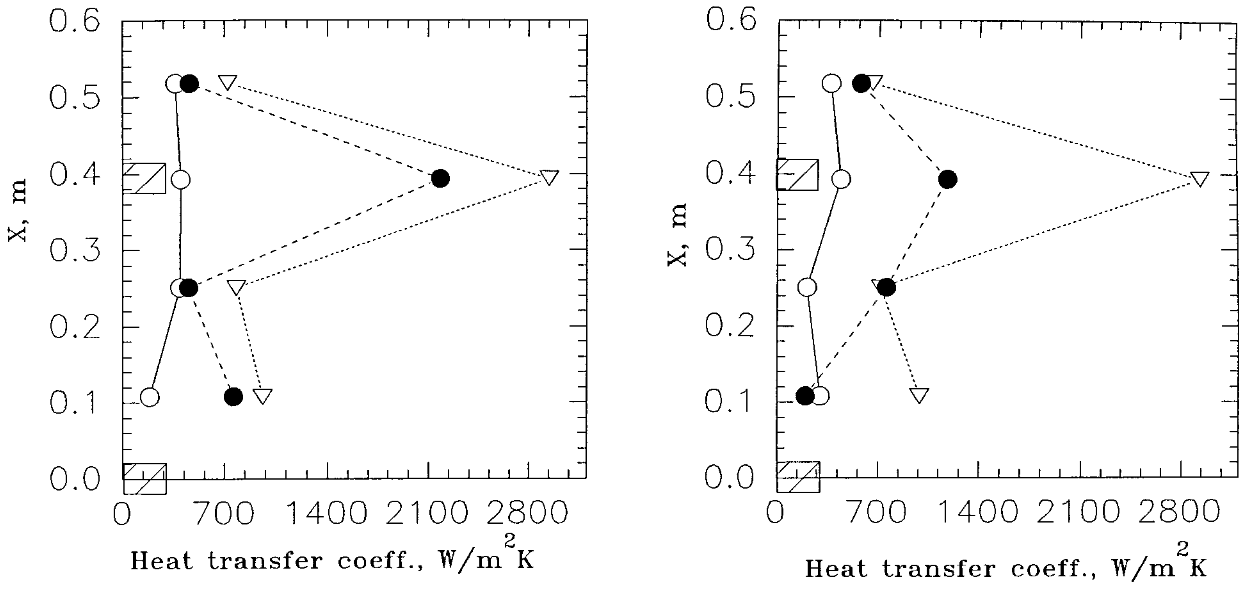

a) 0.2 vvm *b) 0.4 vvm*

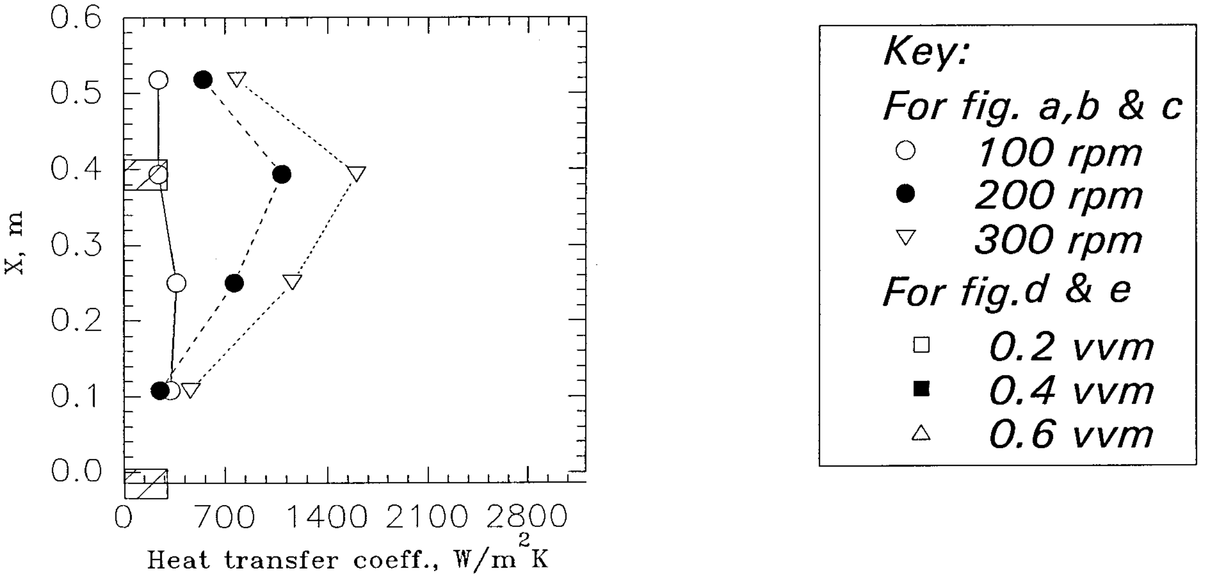

c) 0.6 vvm

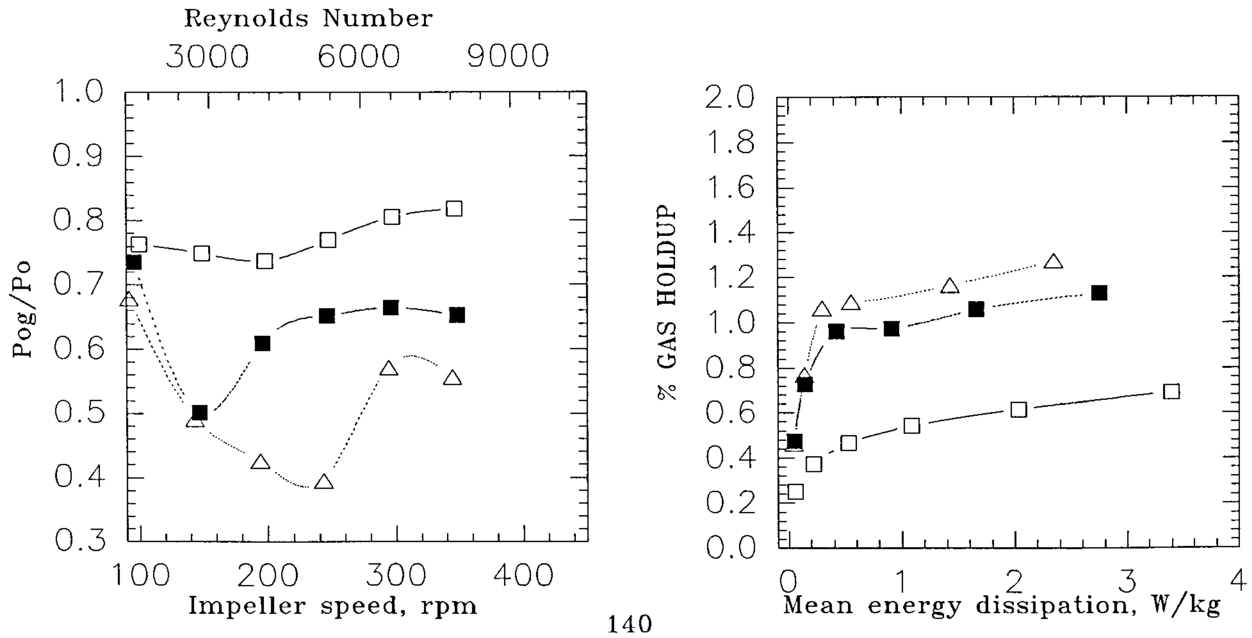

d) Power curve *e) Gas holdup profile*

Fig 6.11: Local aerated heat transfer and mixing results for 0.8 % CMC solution using dual Rushton impeller

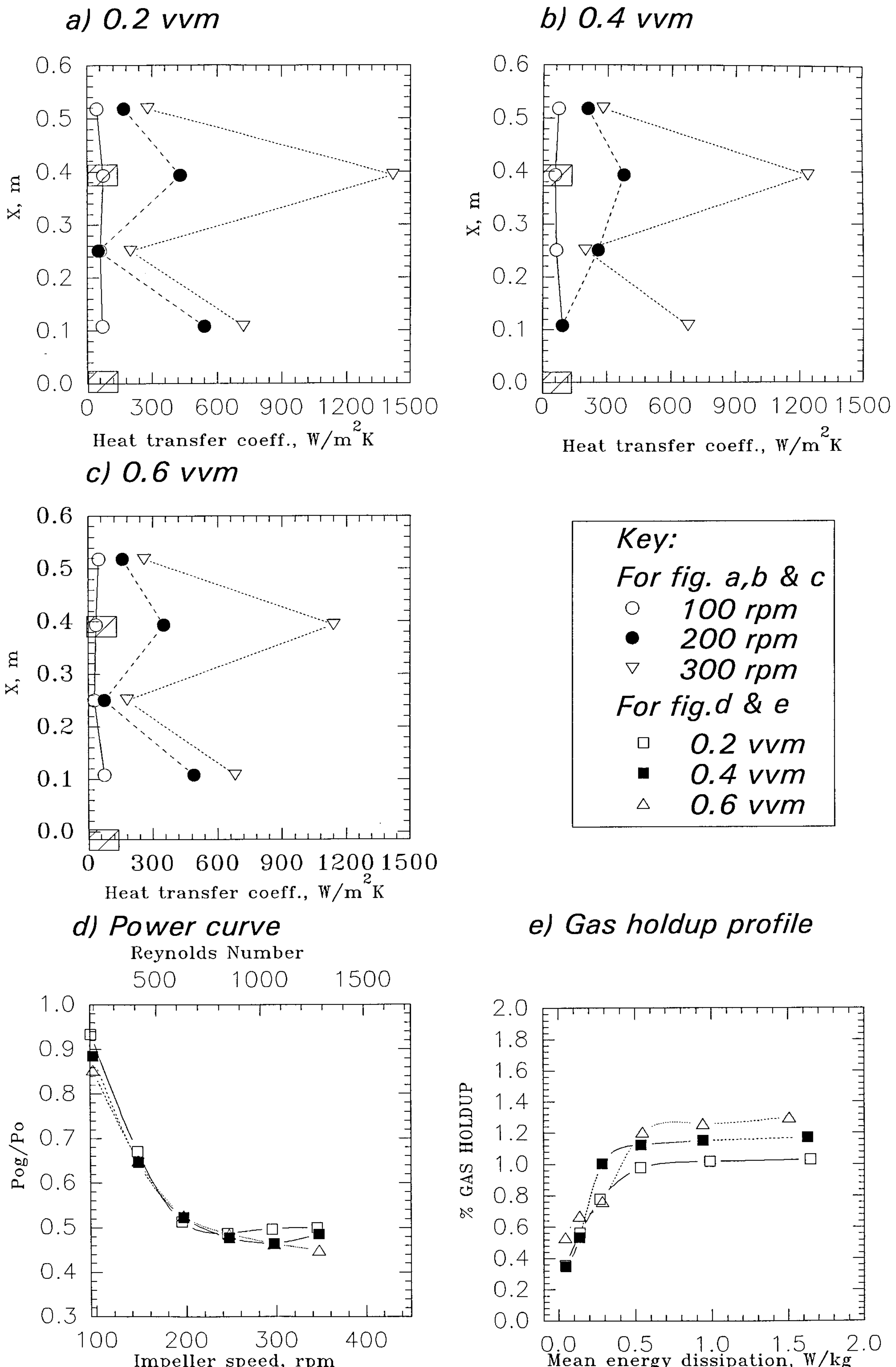

Fig 6.12: Local aerated heat transfer and mixing results for 1.4 % CMC solution using dual Rushton impeller

a) 0.2 vvm *b) 0.4 vvm*

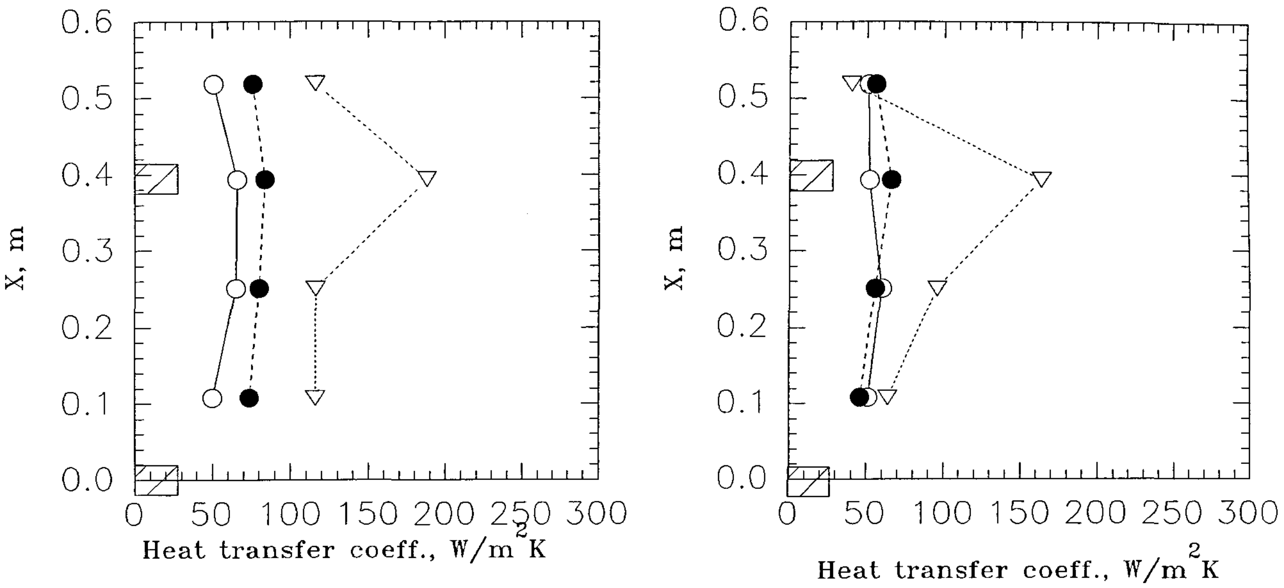

c) 0.6 vvm

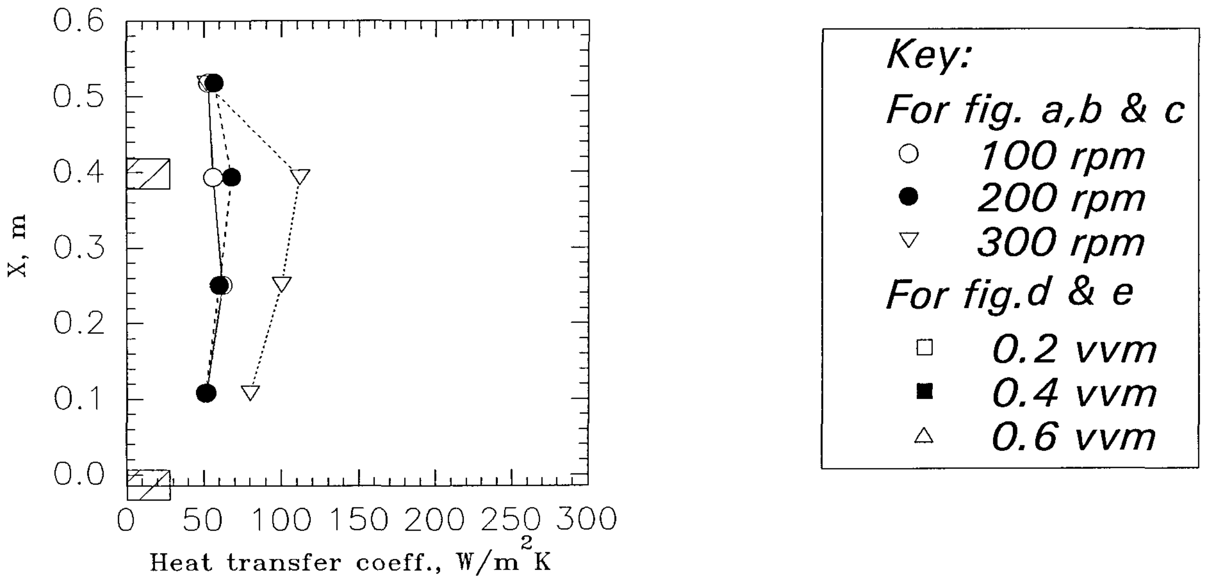

d) Power curve *e) Gas holdup profile*

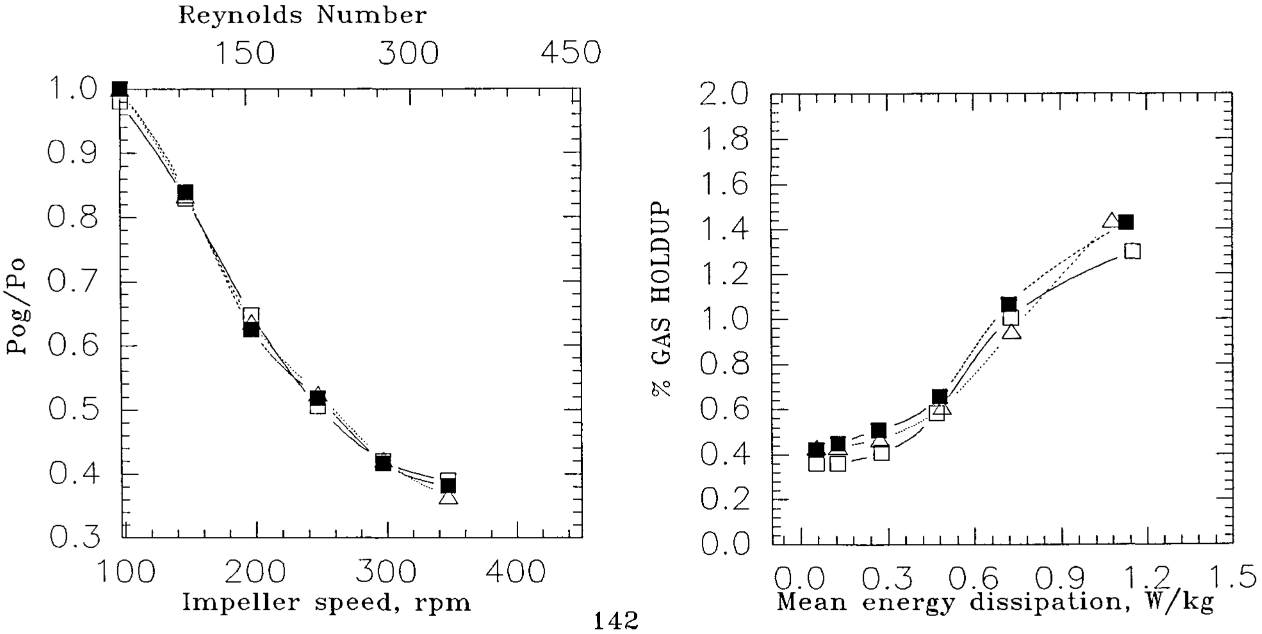

impeller is not described in the literature. On observation of the power ratio curve (see figures 6.11d and 6.12d) and gas hold up curve (see figures 6.1e and 6.12e) it becomes clear that the global mixing data for dual impeller system follow similar profile as in the case of single impeller system (see chapter 5). Therefore, the cavity structure for the upper impeller must be of a similar nature. However, there may be some difference in size of cavities formed because the heat transfer data show that flooding occurs first at the lower impeller (see figure 6.11 and 6.12). Further due to the highly shear thinning behaviour there is a high value of heat transfer coefficient in the impeller discharge stream (see figures 6.11 and 6.12).

CHAPTER 7

Heat transfer and mixing in real and simulated multiphase fermentation systems

Heat evolution during growth and metabolism is a universal characteristic of living organisms. By carrying out oxidation of glucose or a similar substrate in many steps the cells generate energy to perform three types of work; Chemical synthesis of simple and complex molecules (for both growth and turnover), transport of ionic and neutral substances into or out of the cell or its internal organelles, and the mechanical work required for cell division and motion. Most of the remaining energy is dissipated as heat, which must be removed in some fashion to keep the temperature in the physiologically suitable range (see chapter 2, section 2.7). Heat transfer in fermentation broths is complicated by the presence of the biomass which can not only make the broth shear thinning but also can modify the film heat transfer process itself. This chapter focuses on the impact of the third phase on this film heat transfer.

7.1 <u>*Introduction*</u>

Heat transfer is particularly important for large production scale vessels because an increase of the vessel size leads to a reduction of surface area to volume ratio due to the fact that the volume is proportional to D_T^3, and the cooling surface to D_T^2. Therefore in large production scale vessels heat transfer may be process limiting. Thus, it is particularly important for biochemical engineers to understand the heat transfer in such a multiphase system for efficient design of the heat transfer surface. Fermentation heat transfer studies are particularly difficult because both the heat evolved by the organism and the driving force for heat transfer are rather small; therefore highly sensitive and accurate probes, such as those used in this project, have to be employed. These probes have only recently become widely available.

7.2 Fermentation experiment

An introduction to the penicillin fermentation is given in chapter 2 (section 2.7). The Penicillin fermentation is highly susceptible to contamination because it is fairly slow and the mould is outgrown by contaminants such as yeast. The initial two fermentations at the pilot scale were contaminated and are not described further; however they provided valuable experience in aseptic culture handling, which was reflected in the success of subsequent fermentations.

7.2.1 Fermentation experiment - 1

For this fermentation, a defined medium was used whose major constituents were 25 g/l of glucose, 10 g/l of $(NH_4)_2SO_4$ and 7.5 g/l of KH_2PO_4. The air flow rate was initially 200 l/m but this was raised, first to 250 l/m at 25.5 hours and then to 300 l/m at 29 hours, in order to meet the oxygen demand (see figure 7.1). Similarly the agitator speed was increased over the same period over the range 250-350 rpm (see figure 7.1). The temperature setpoint for the fermentation was 26 ^{o}C (for optimum growth and Penicillin production) and this was maintained by the jacket cooling loop (see chapter 3, section 3.1); however, in this fermentation the jacket cooling loop was accidentally switched off for 3 hours and this allowed the temperature to rise above the setpoint (see figure 7.3d and e). Figure 7.2 shows the apparent viscosity and biomass profile, which shows a nearly exponential growth. The broth rheology was here characterised using a conventional Contraves rheometer but the particulate nature of mycelial suspensions poses particular problems to the use of such conventional viscometers, since the particle size can often be of a similar order of magnitude to that of the clearance between the rotating bob and the cylinder. For the following fermentation an impeller viscometer was used (see chapter 3, section 3.4).

The local heat transfer coefficient profile is presented in figure 7.3, which covers the period during which the cell growth passes from the exponential to the stationary phase. During the earlier part of the growth phase the heat transfer was, as for water, service-side (probe and jacket) controlled (refer to chapter 4). Furthermore, due to the low viscosity (and low biomass) the driving force and the heat flux were too low to be effectively measured by the probe. The data shown here are from 23 hours to about 29 hours, which falls within the late exponential growth phase when the biomass increases nearly exponentially (see figure 7.2) and the apparent viscosity also increases in the same manner. The local heat transfer data for the two heat flux probes (probe-1 and probe-3) shows a distinct axial profile, with the maximum value near the impeller plane (see figure 7.3a).

Fig 7.1: Aeration rate, speed and dissolved oxygen profile for fermentation-1

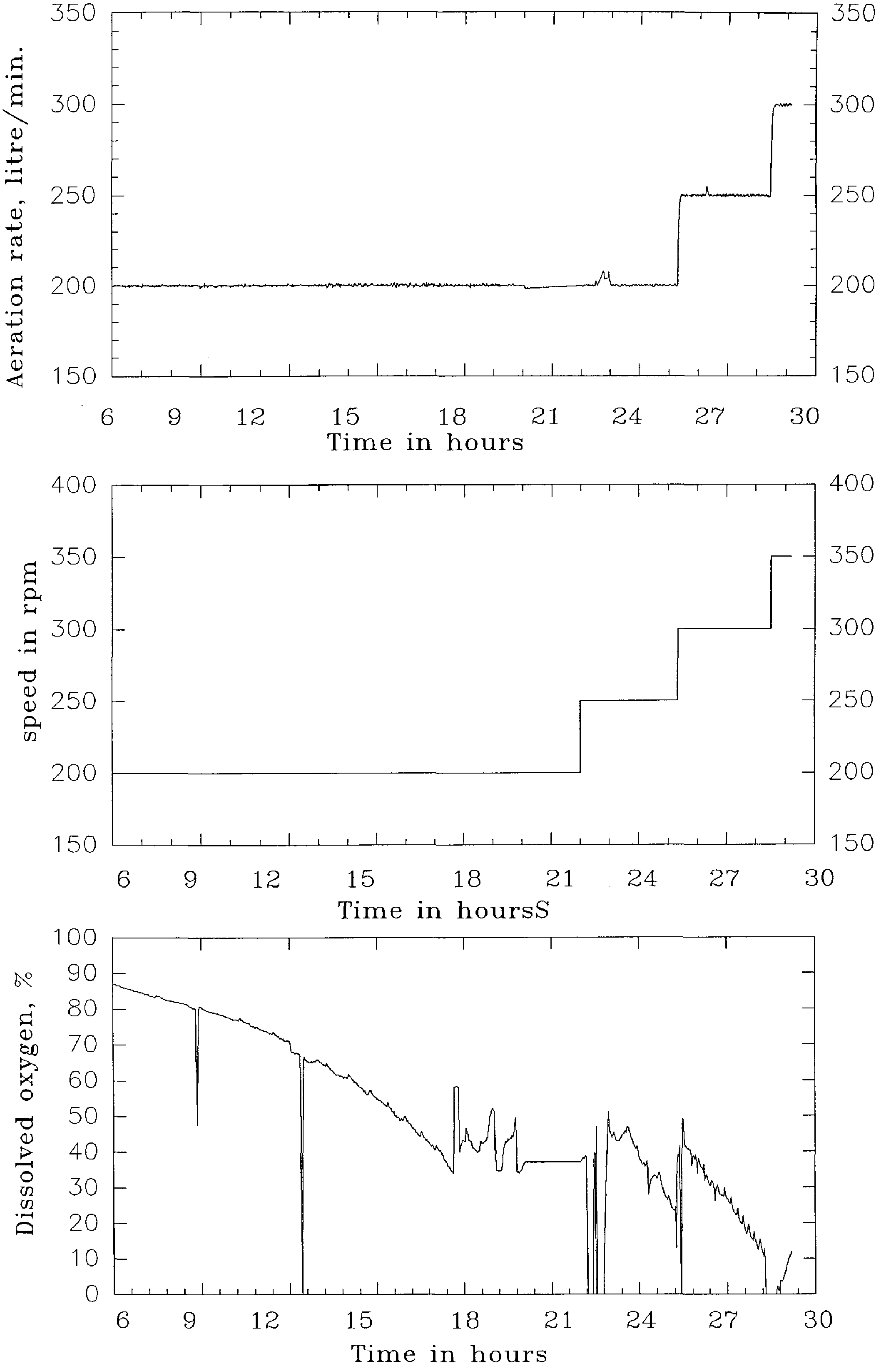

Fig. 7.2: Apparent viscosity and biomass profile for fermentation-1

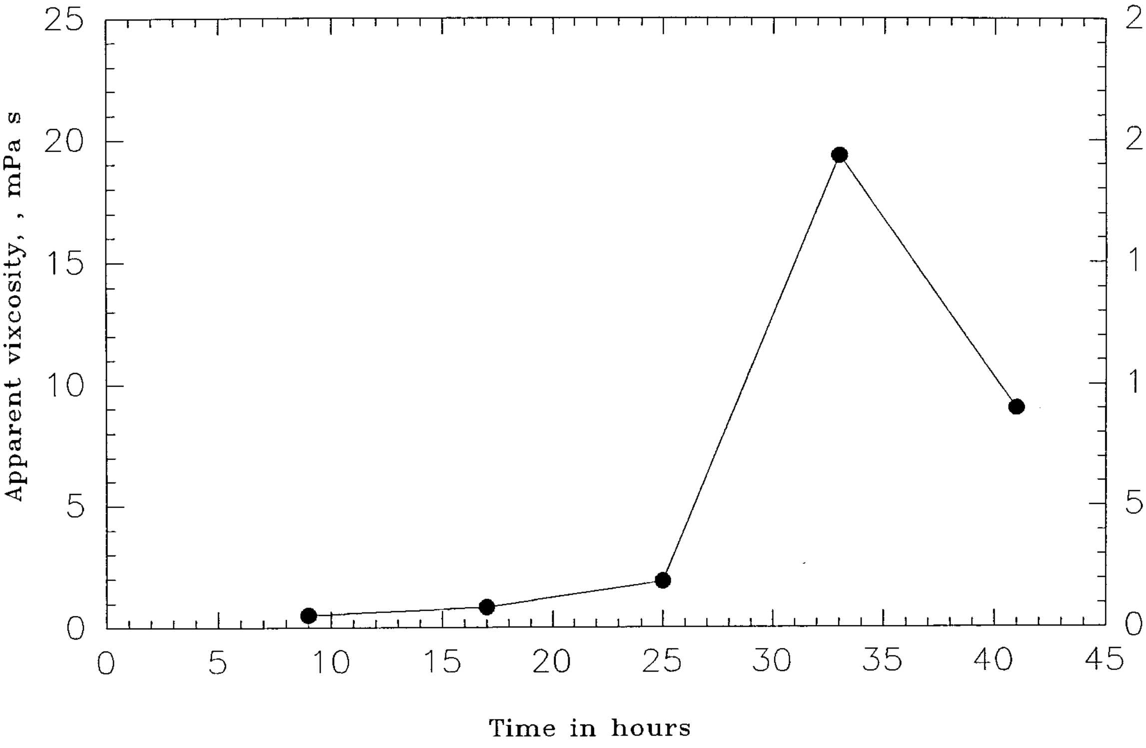

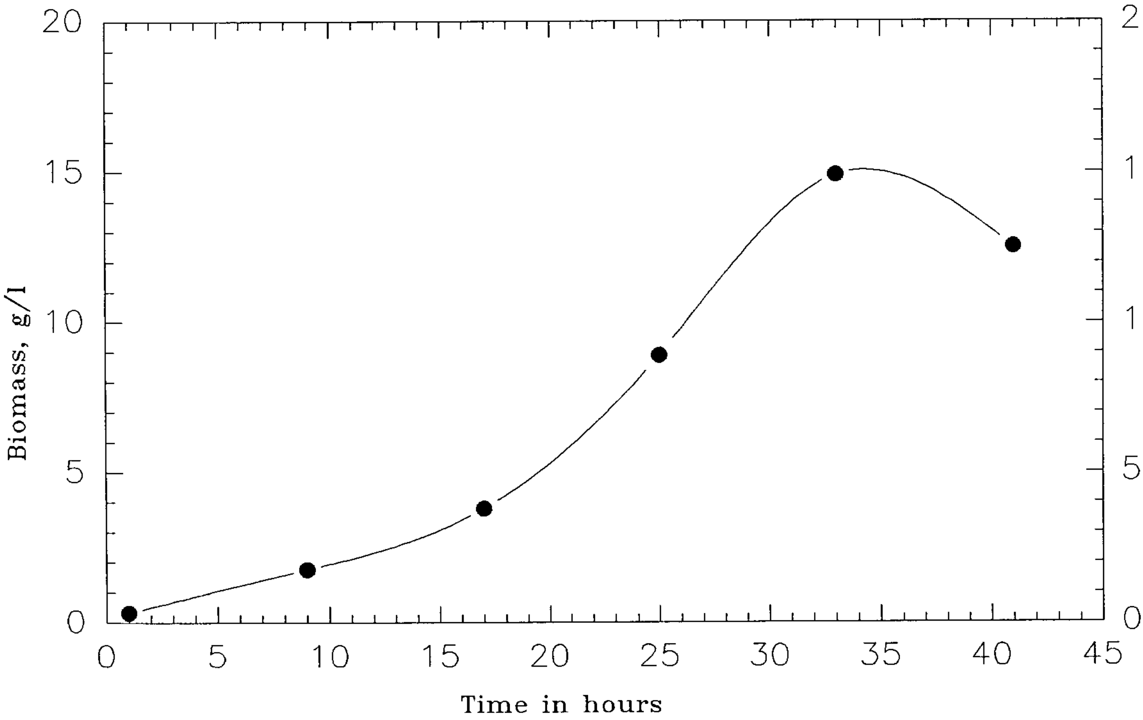

Fig.7.3: Local Heat Transfer Profile for Penicillin Ferm.-1

a) Local Heat Transfer Coefficient Profile

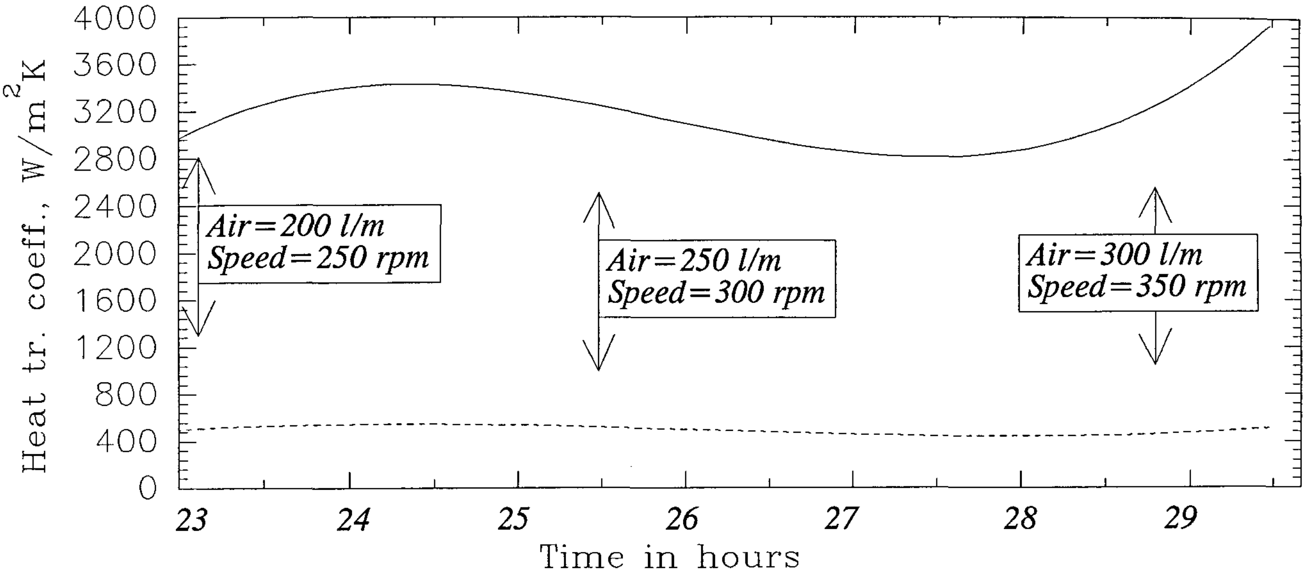

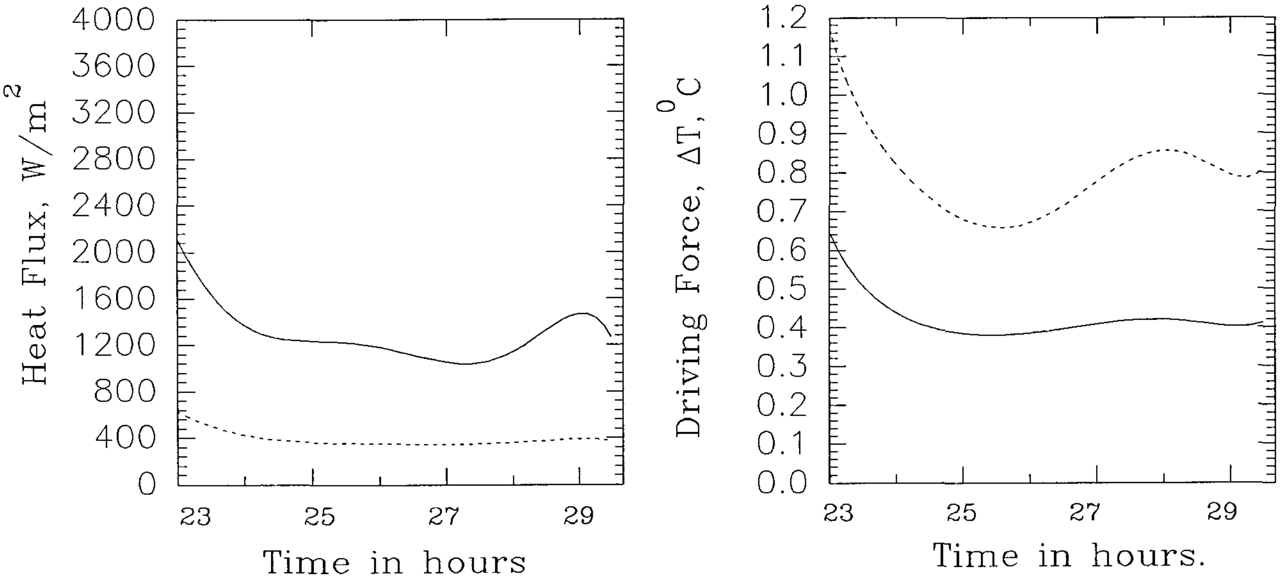
b) Local Heat Flux Profile

c) Driving Force Profile

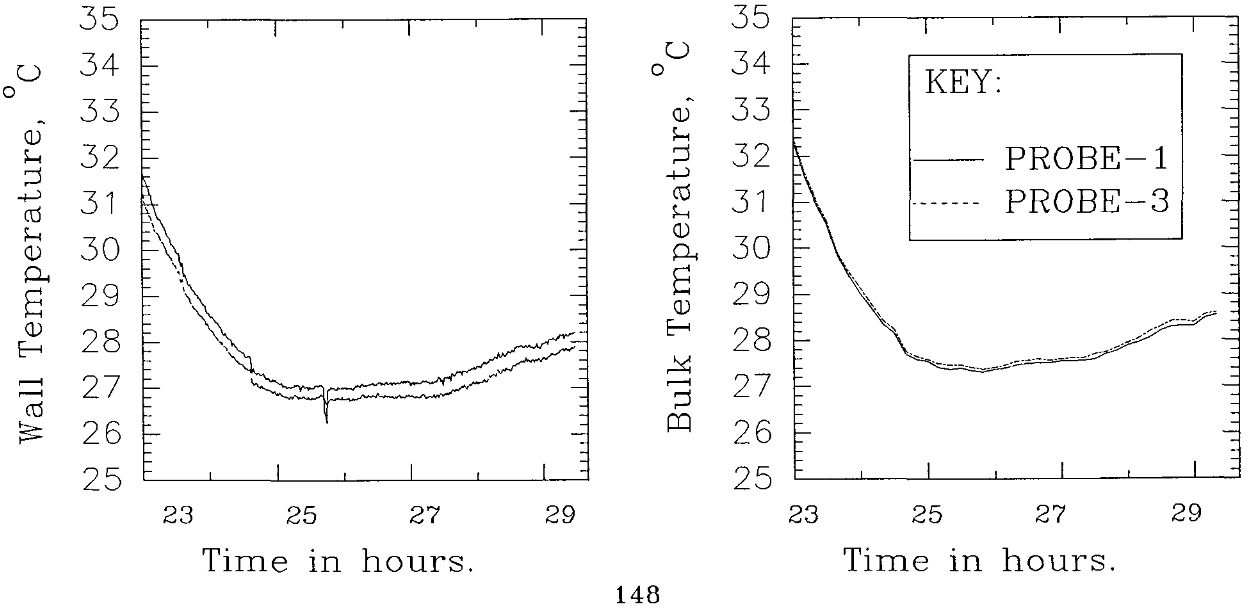
d) Local wall Temp. Profile

e) Local Bulk Temp. Profile

Given the usual type of correlation for heat transfer, an increase in apparent viscosity leads to a drop in Reynolds number and hence a drop in the heat transfer coefficient (the increase in Prandtl and its effect on heat transfer is less significant than that through the Reynolds number). However, this is not the case with this fermentation. Figure 7.2 shows that at 23 hours the biomass concentration is still low (7 g/l) but that, as the biomass and apparent viscosity increase, then (at an air flow rate of 200 l/m and an impeller speed of 250 rpm, see figure 7.3a) there is a general increase in heat transfer coefficient, specially noticeable near the impeller plane, as measured by probe 1. After about 25.5 hours the speed and airflow rate were increased to 300 rpm and 250 l/m respectively, following which the heat transfer coefficient initially declines (but only slightly) and then gradually increases, this being especially noticeable close to the impeller plane (probe-1). With further increases in impeller speed and gas flow rate to 350 rpm and 300 l/m respectively the increase in heat transfer coefficient is even more noticeable particularly in the plane close to that of the impeller, even though both biomass and apparent viscosity are still increasing rapidly at this stage.

The only explanation for such an enhancement of the film heat transfer coefficient is that the morphology of the fungi is modifying the thermal boundary layer. The effect of the biomass could be thought of as a brushing action due to the impact on the vessel wall. The magnitude of such an impact reduces with the distance above the impeller discharge stream and this explains the difference between the response of probe -1 (which shows a sharper increase in heat transfer coefficient) and that of probe-3. Furthermore, the increase in heat transfer coefficient is more noticeable towards the end of the exponential phase when there is a substantial presence (15g/l) of the biomass. Blakeborough et al [90] made a similar observation, using a more basic heat flux probe in an air lift fermenter, that at higher biomass concentrations the solid phase tends to brush the boundary layer thus enhancing the heat transfer.

Thus it emerges from the above discussion that the morphology significantly affects heat transfer. This means that the morphology, which in turn is dependent on the physiological state of the organism, must be clearly understood in order to interpret heat transfer results in mycelial fermentations.

7.2.2 Exploring relationship between heat transfer and morphology

The mycelial micro-organism *(Pencillium chrysogenum)* has varied morphological characteristics. The morphologies range between two extremes: individual dispersed filamentous mycelia and pellets. The dispersed form, typically branched, has hyphae up to several hundred microns long and 0.5-10 μm in diameter. Larger colonies, ie. pellets, vary in diameter from 100 μm to several centimetres across [135]. In industrial antibiotic fermentations the dispersed form is widely used, although it is probable that the culture contains a significant proportion of permanently aggregated mycelia (clumps, not true pellets). Mycelial entanglement can result in high apparent viscosities (several thousands mPas) and pseudoplastic like behaviour, even at relatively low biomass concentration [136]. The shear thinning behaviour can cause stagnant regions to form in the fermenter leading to poor heat transfer. Increasing agitation speed and power consumption can cause damage to the hyphae as they circulate through the region of high energy dissipation near the impeller.

Despite these problems little progress has been made in obtaining useful correlations between the rheological properties of the broth and the morphology and biomass concentration of filamentous microorganisms. This has been partly due to the inadequate methods of characterising mycelial morphology. Until recently analysis of mycelial morphology consisted of qualitative, subjective interpretation by an observer, or the use of a sample digitising table with its inherent operator dependence and lack of speed. Considering the problems of quantifying mycelial morphology it is not surprising that very few workers have looked for correlations between the morphology and biomass concentration of the mycelia and the resultant rheological properties of the fermentation broths. Roels et al [137] and Metz et al [138] both claimed that the rheological properties of the broth were dependent on the morphology of the micro-organism, particularly that of the dispersed form. Recently Kim and Yoo [139] also related the consistency index to the volume fraction of three different categories of dispersed mycelial morphology present within the broth. The only published attempt to correlate the rheological properties of mycelial broths to the structure of aggregates is that of Fatile [140] who concluded that mycelial broths show non-Newtonian behaviour described by the Power law, and the consistency and flow behaviour indices were related to the diameter of the mycelial aggregate.

More recently however, image analysis has been used, with rapid and automatic measurement of the morphological parameters of freely dispersed hyphae such as main hyphal length, total hyphal length and number of tips [141,142]. An image analysis method recently developed by Dr. C.R.Thomas' image analysis group in Birmingham characterises not only the freely dispersed form but also clumps, and is fast enough to measure enough mycelia to compensate for the inherently large variation within samples. Comprehensive characterisation of mycelial morphology was performed by fully automated image analysis on a Quantimet 570 image analyser (Leica Cambridge Ltd, Cambridge, U.K.) connected to a Polyvar optical microscope (Reichert Jung Opstiche Werke AG, Australia). Samples were prepared by mixing a few ml with an equal volume of fixative (13 ml of 40% formaldehyde, 5 ml glacial acetic acid and

200 ml 50% v/v ethanol), diluting 30 fold with 20% sucrose solution and staining with Lactophenol Cotton Blue [142].

The measurements of morphological features for the dispersed mycelia included: mean main hyphal length; mean total hyphal length; mean number of tips per mycelium; mean hyphal diameter; mean dimensionless length (main length/diameter); and mean hyphal growth unit (total length/number of tips). The mycelia present in the form of clumps could not be measured individually. The proportion of clumps by area was measured, and each clump was further characterised in terms of area, perimeter, "compactness", and external "roughness". The compactness was estimated as the ratio of the (projected) area of the hyphae in the clump to the (projected) convex area of that clump, the latter being the area after filling internal voids and concavities in the clump's external perimeter. The clump roughness was characterised using a circularity parameter $\{\text{Perimeter}^2 / (4\pi \text{ Area})\}$ [141]. From the work of Keith, Mohan and Thomas [135] it appears that the interaction of mycelial clumps and thus clump morphology can be crucial in determining filamentous fermentation broth rheology. The two morphological parameters found to be significant, clump compactness and roughness, are probably important in several respects. The roughness of the clumps may be expected to affect their interactions and possibly the flow between them. Increasing roughness should result in greater levels of interaction and more viscous broths. The compactness may affect clump distortion in flow, as well as the amount of occluded suspending medium not available for the dispersion of other mycelia. At sufficiently high biomass concentrations compactness may also affect broth viscosity by influencing changes in the packing of clumps during suspension flow.

Thus it is clear from the above argument that the morphology has a significant affect on the broth rheology. Since the morphology changes continually throughout the fermentation along with the biomass this makes the prediction of rheology difficult. Furthermore it is clear from chapters 5 and 6 that, for shear thinning fluids (such as mycelial broth), the rheology depends on the local shear. Thus the characterisation of rheology in such a system is extremely complex and without a significant development in this area the affect of broth rheology on heat transfer cannot be quantified. However, the local heat transfer results (see figure 7.3) suggest that the particulate nature of the mycelia has a greater influence than the increasing apparent viscosity. This again should depend on the morphological state of the mycelia.

Thus fermentation conditions therefore add an additional level of complexity to understanding and prediction of heat transfer in non-Newtonian fluids- and for the biochemical engineer it is an important objective to relate the effects on heat transfer to quantifiable morphological determinants exhibited by the fungal mycelium. The work of Packer and Thomas [142] now enables the latter to be quantified using methods based on image analysis. In fermentation experiment 1 the morphological data could not be obtained. The next fermentation (experiment 2) was then planned to include morphology measurement (in collaboration with Dr Thomas' group, mainly Mr K. G. Tucker). This fermentation was also designed to use one defined gas flow rate and impeller speed throughout the main growth phase during which heat transfer determinations were made.

7.3 Fermentation experiment - 2

The second fermentation was carried out using complex medium. The intention was to examine more closely the effect of the morphology on heat transfer coefficient, that is its effects on both boundary layer modification and on rheology. The impeller speed and the gas flow rate for the final stages of growth (where heat transfer was process-side controlled) of the fermentation were kept constant at 350 rpm and 300 l/m respectively, to eliminate any effects on heat transfer coefficient of changes in impeller speed and gas flow rate.

The initial seed vessel used was the 25 litre vessel (20 litre working volume). Figure 7.4a shows the engineering parameters during the 15 hours seed fermentation; even in this initial seeding stage the dissolved oxygen level started falling rapidly during the final stages, suggesting a healthy culture. This formed the inoculum for the next seed vessel (75 litre vessel, 60 litre working volume) the engineering parameters of which are shown in figure 7.4b. Here again the rapid drop of dissolved oxygen, even after increasing periodically the impeller speed and gas flow rate, assured a good biomass growth and a healthy fermentation. Finally figure 7.4 c shows the overall performance of the fermentation on the pilot scale with 400 litre volume of the broth.

Figure 7.5 shows the rheology results for the fermentation (as measured now by the impeller viscometer). The initial broth is a Newtonian fluid with a viscosity close to that of water but after about 14 hours, due to the presence of the biomass, the nature of the broth rheology changes, it becoming shear thinning (and looking like a particle suspension). The shear thinning nature is due to the progressive alignment of filamentous structures within the fluid at increasing shear (see chapter 2, section 2.5.2.1). With the increase in the biomass the shear thinning behaviour increases, and this is reflected in the power law index profile (see figure 7.5b) where the index decreases from 0.9 to about 0.6 with a very sharp initial transition. The minimum value of the power law index corresponds to the highest biomass, that is the end of the exponential growth phase. The consistency index profile is shown in figure 7.5a, which follows a similar profile to that of the biomass (see figure 7.6 a). The apparent viscosity

Fig 7.4: 25 litre, 75 litre and 800 litre process parameter profile

a) 25 litre seed fermentation process parameter profile

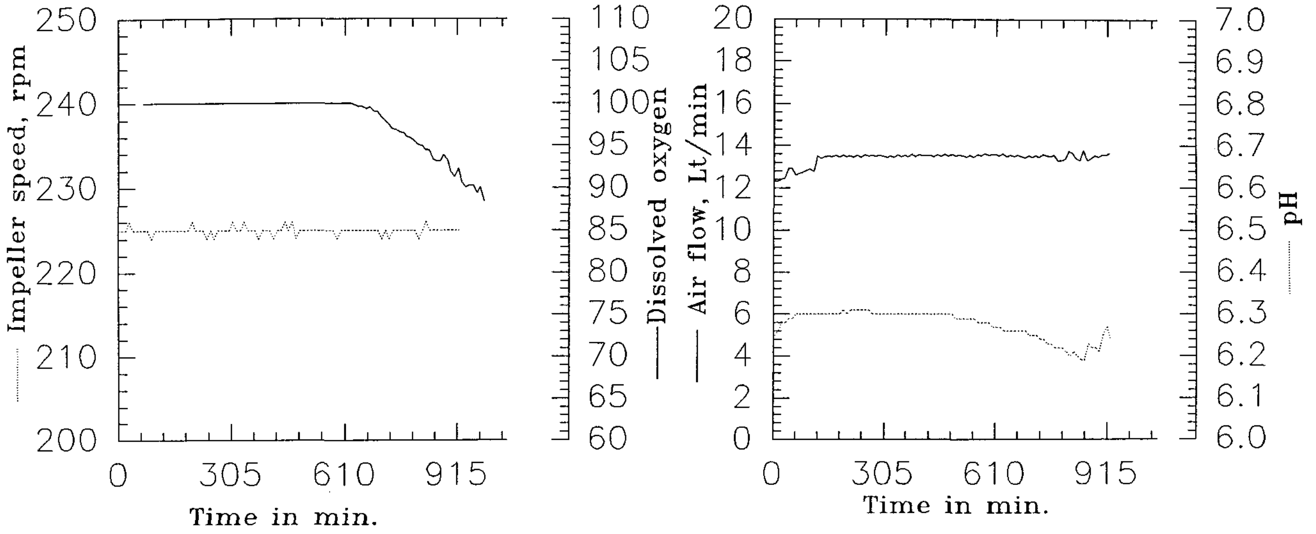

b) 75 litre seed fermentation process parameter profile

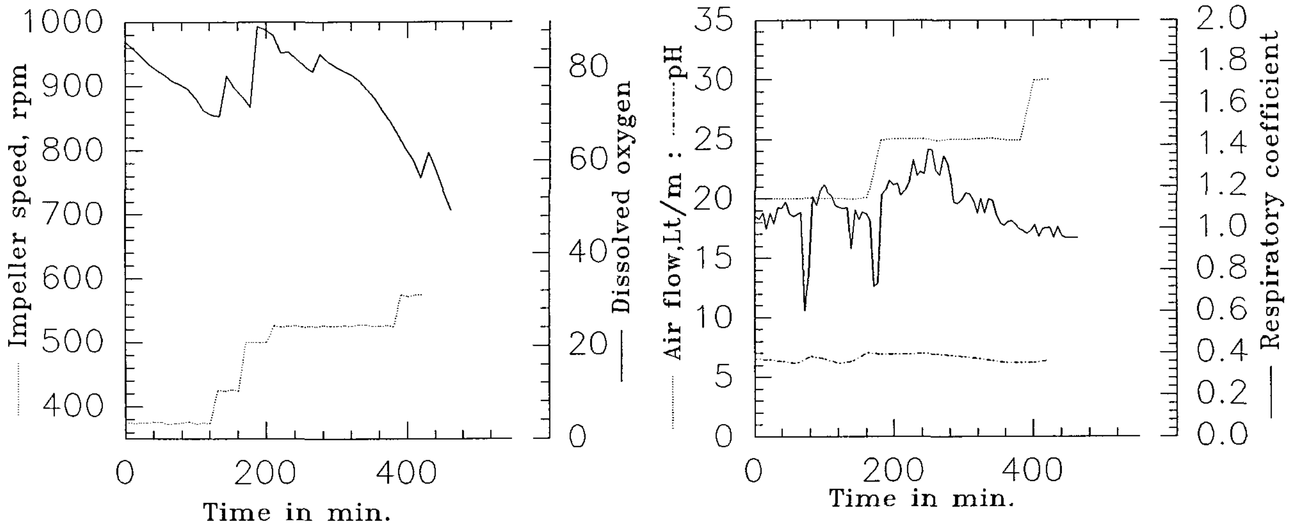

c) 800 litre fermentation process parameter profile

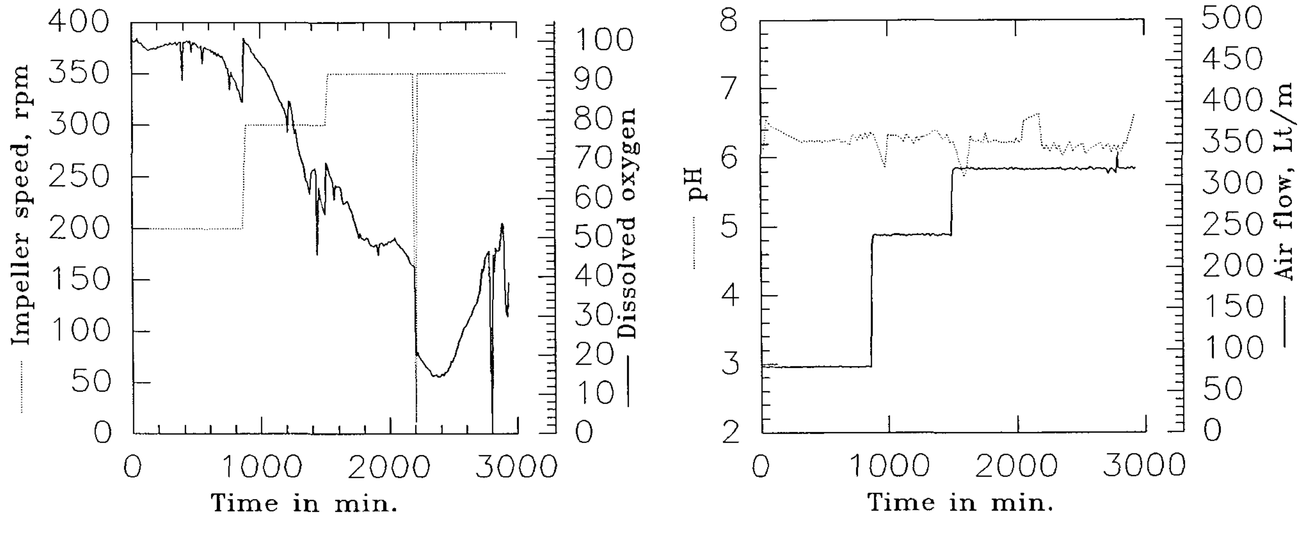

Fig 7.5: Rheological profile for Penicillin Fermentation 2

a) Consistancy index profile

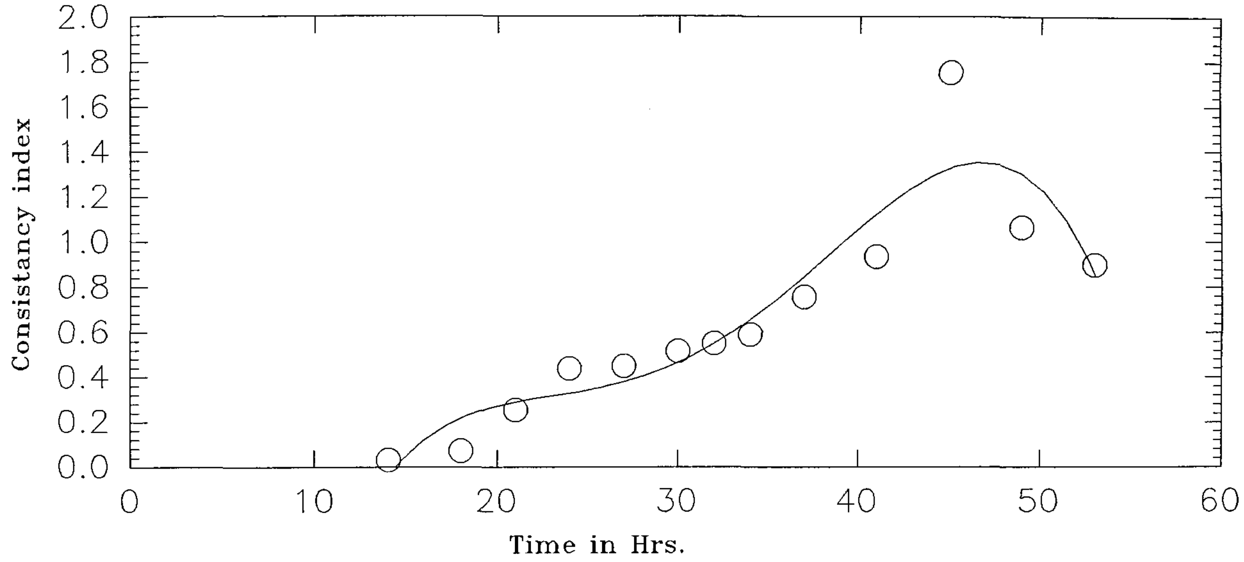

b) Power law index profile

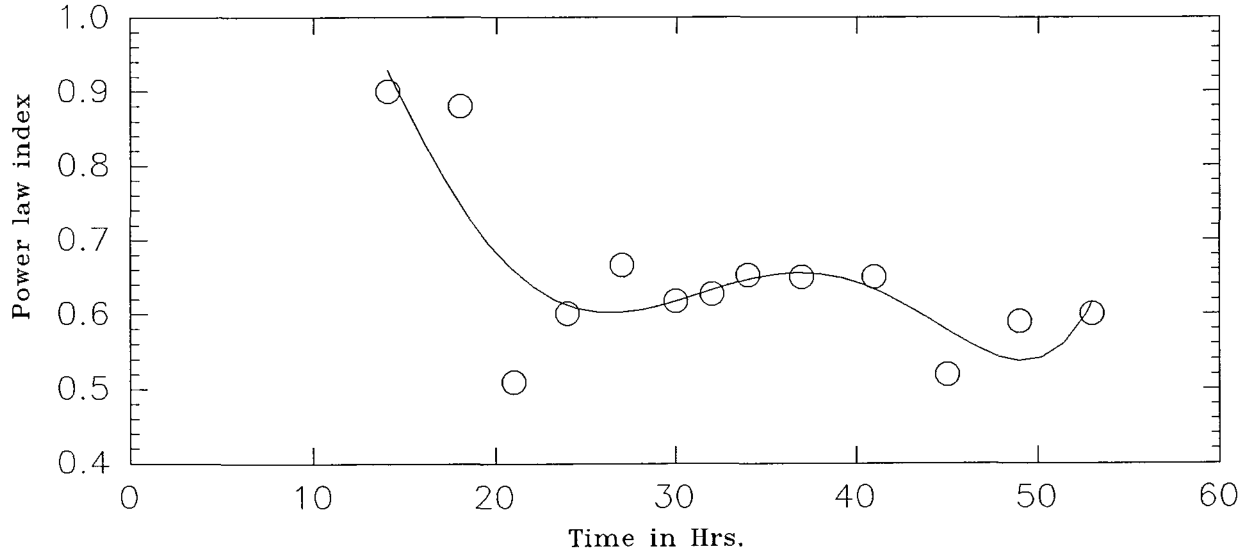

c) Apparent viscosity profile

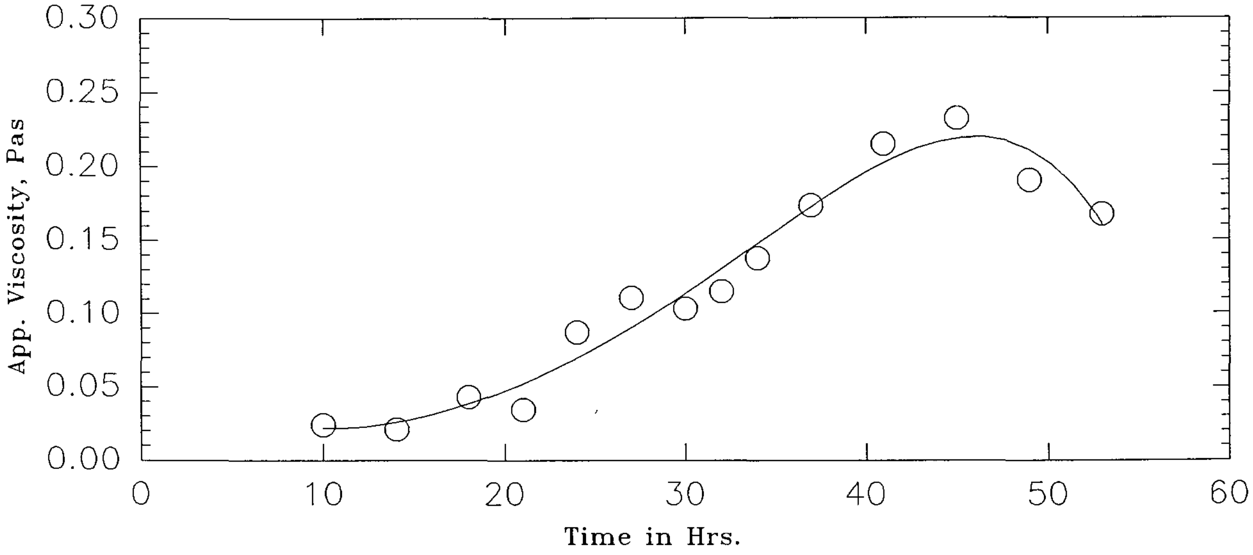

Fig. 7.6: Biomass, Rheology and Mixing profile for Penicillin Ferm.-2

a) Biomass Profile

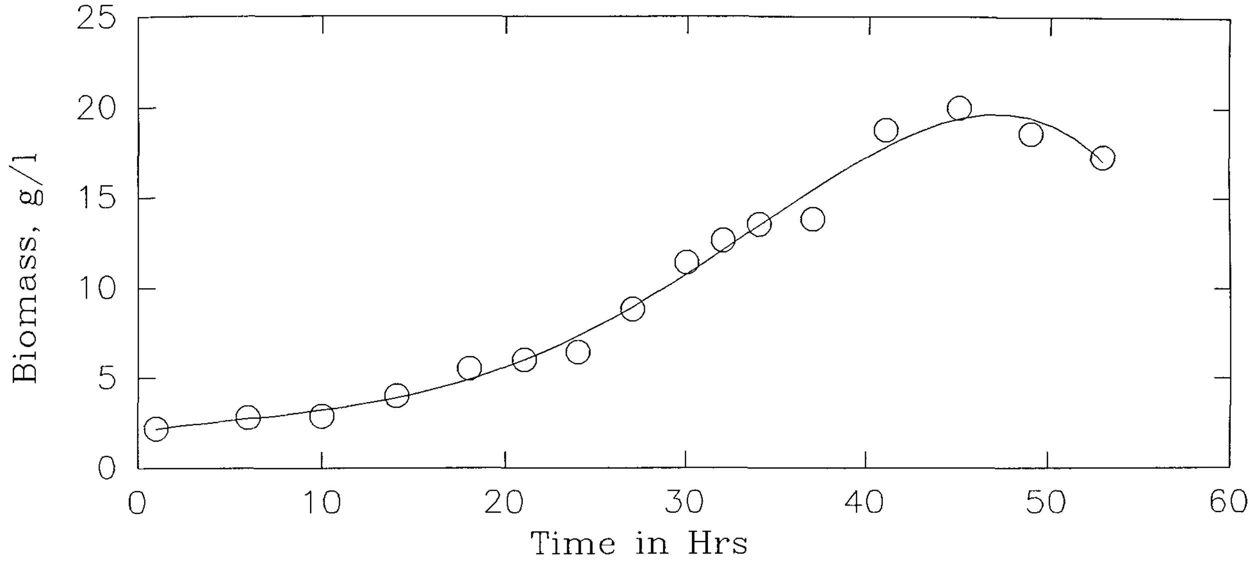

b) Apparent Viscosity and Reynolds number Profile

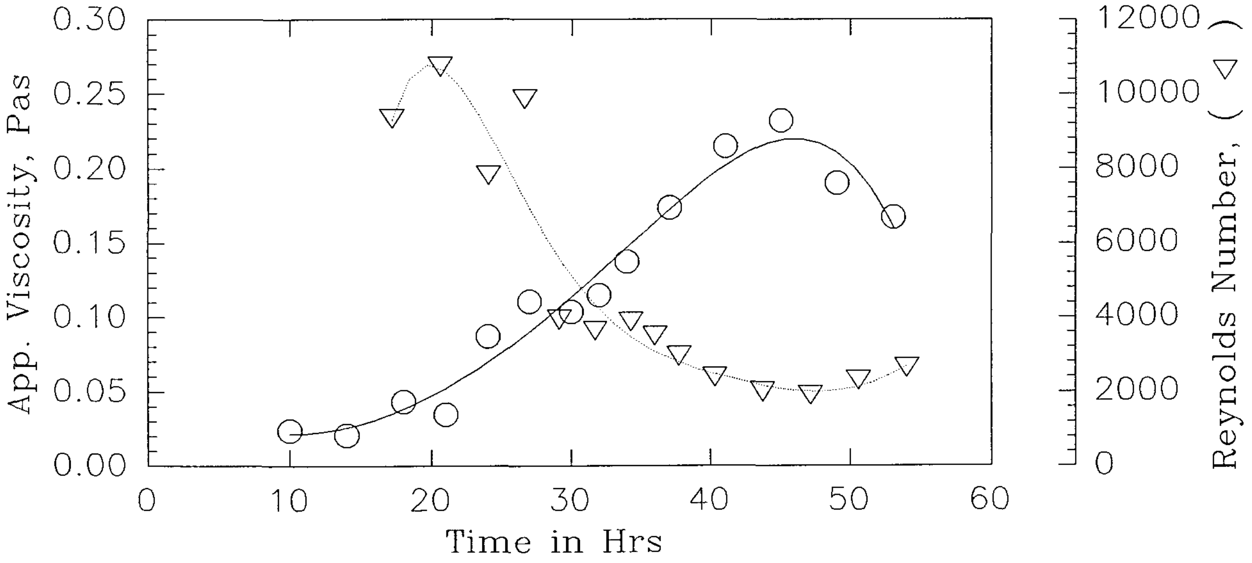

c) Power Draw and Power no. as measured by the St. Gauge

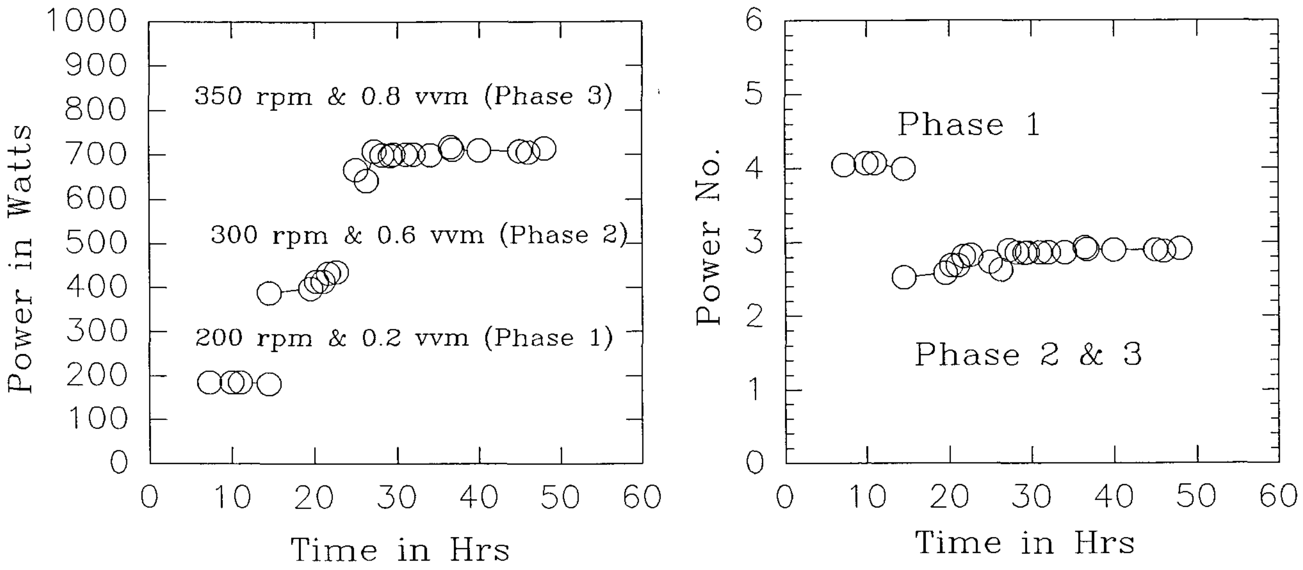

profile, assuming the power law model (see chapter 2, section 2.5.2.1), is shown in figure 7.5c, and this again follows a similar profile to the biomass.

Figure 7.6 b shows the Reynolds number profile which changes from the turbulent to transitional regimes. The power and the power number are shown in figure 7.6 c. During the initial phase of the fermentation (phase 1) the power draw is at a minimum and it then increases due to changes in the impeller speed and air flow, until a constant power draw is maintained throughout the main period of growth (24-48 hours).

Figure 7.7 shows the heat transfer profile for the second fermentation from 24 to 48 hours. The heat transfer data for the other two phases are again not shown as the viscosity was low and the controlling resistance was in the probe itself (see chapter 4). The figure shows that there is again a distinct axial variation, with the maximum value of heat transfer coefficient near the impeller plane and rapidly decreasing values away from it. Comparing the magnitude of the difference between probe positions 1 and 3 for fermentation 2 with that of fermentation 1, it is observed that this difference is much higher for the latter even at the same impeller speed and air flow rate, even though they have similar geometry, impeller speed and air flow rate. This difference could emerge from two related phenomena:

1) Differences in rheology - even at the same biomass level the rheology is different, this could be only due to the differences in the morphology. For instance a filamentous fermentation would have a higher apparent viscosity than a pelleted one at the same biomass. A high apparent viscosity would make the broth even more shear thinning, and this would then significantly reduce the velocity flow field near the vessel wall, leading to a low heat transfer coefficient. This reduction in the velocity flow field would also affect the brushing action of the third phase on the thermal boundary layer. Furthermore (as discussed below) the rheology also determines the resistances in the boundary layer.

2) Differences in morphology - The particulate nature of the mycelia depends on its morphology. The boundary layer modification depends on this particulate nature of the mycelia. The morphological parameters for the second fermentation are shown in figure 7.8. The clump roughness decreases initially and then remains constant, whereas the clump compactness increases during the fermentation (from 0.307 to 0.363). Both these morphological factors influence rheology as discussed in the preceding section.

A typical compactness factor of 0.2 suggests a filamentous form whereas a compactness factor of 1 suggests a solid lump. Therefore for this second fermentation the morphology was a mixture of free mycelia and mycelial clumps [135]. A quantitative comparison with the

Fig.7.7: Local Heat Transfer Profile for Penicillin Ferm.-2
Impeller speed = 350 : Air Flow = 0.8 vvm

a) Local Heat Transfer Coefficient Profile

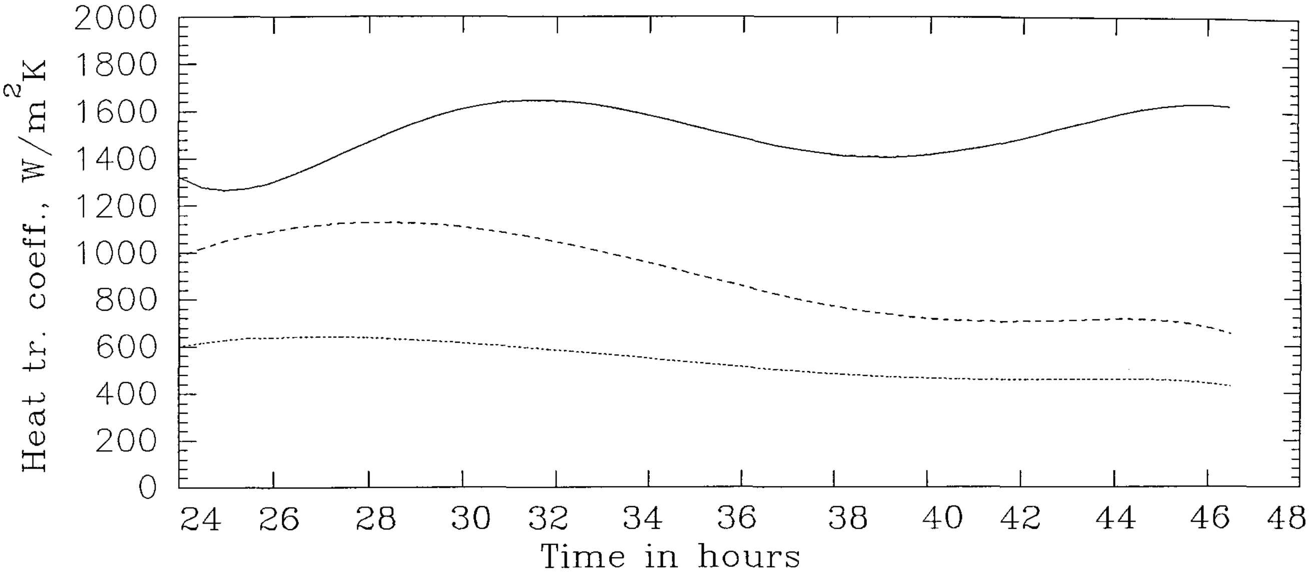

b) Local Heat Flux Profile *c) Driving Force Profile*

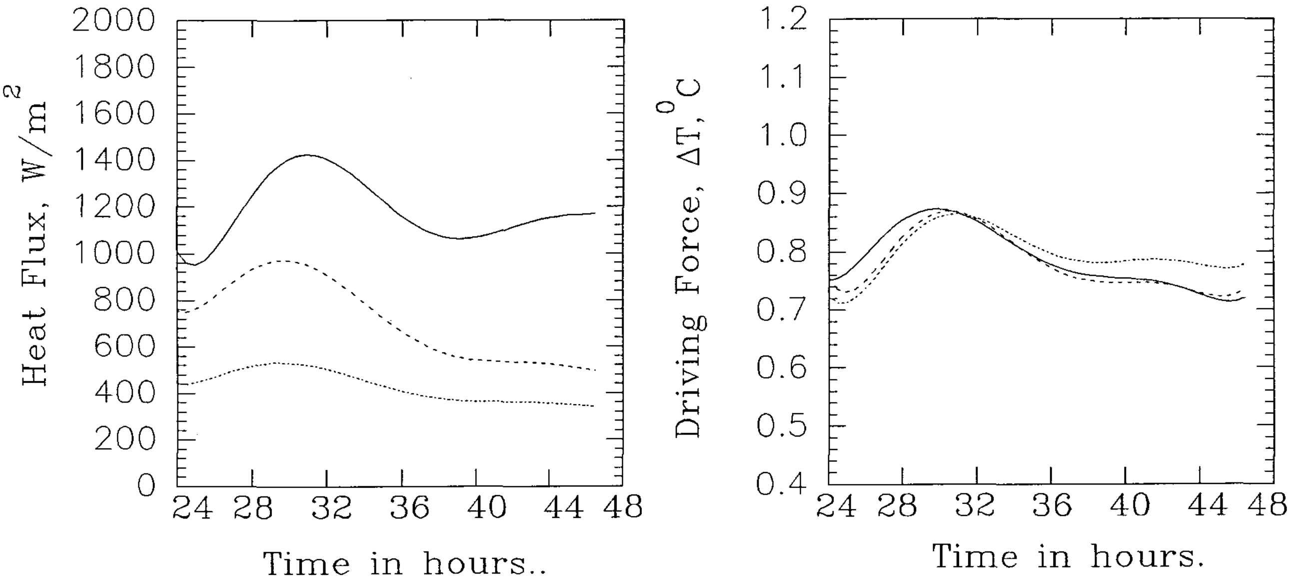

d) Local wall Temp. Profile *e) Local Bulk Temp. Profile*

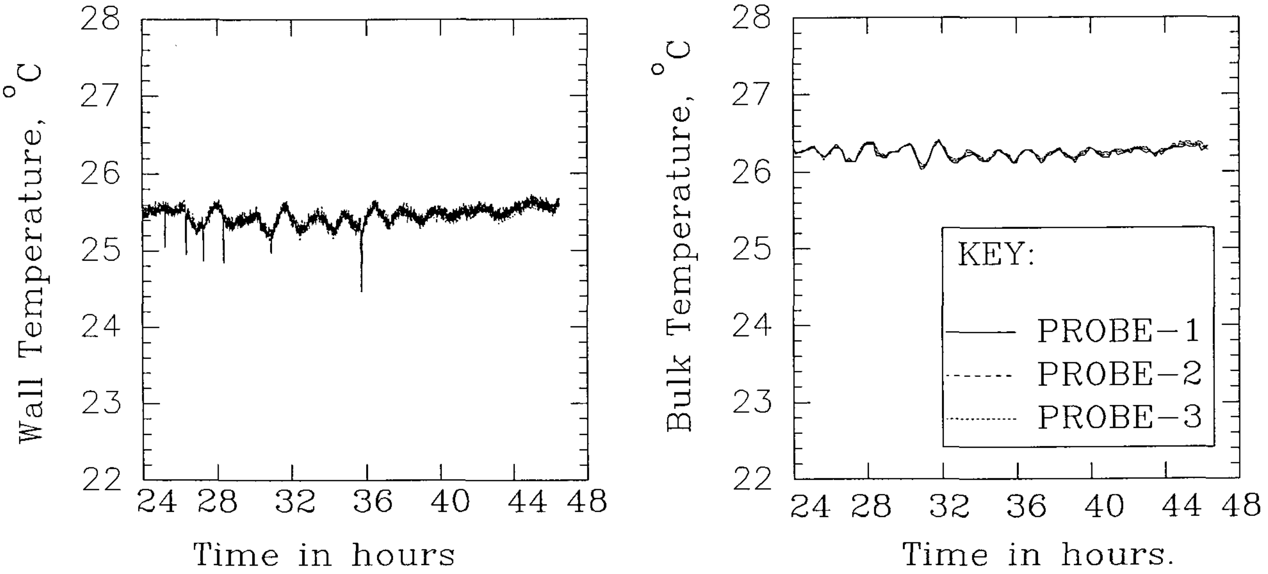

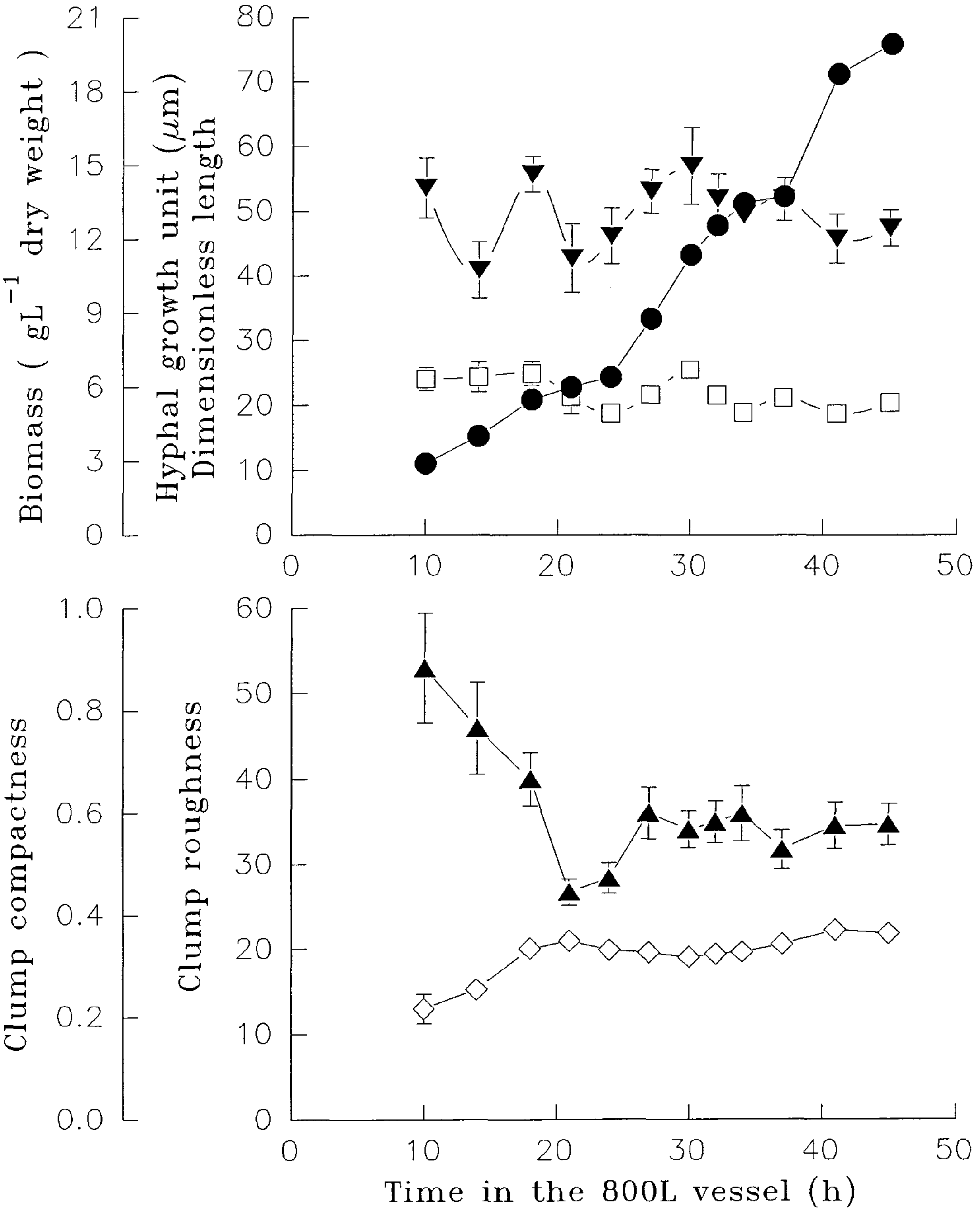

Figure 7.8: Variation in biomass concentration and some morphological variables during the time course of a 400L *P. chrysogenum* batch fermentation. The error bars show ± one standard error in the mean.

● Dry cell weight (gL^{-1})
▼ Hyphal growth unit (μm)
□ Dimensionless length
◇ Clump compactness
▲ Clump roughness

morphology of the earlier fermentation 1 is not possible as this aspect was not then examined. However, since the spore concentration in fermentation 1 was low and also the apparent viscosity was considerable lower than that of fermentation 2 (however, it must be noted that the two methods used for rheological characterisation are not comparable), a high concentration of clumps and more compact mycelia might be reasonably assumed (an almost pelleted fermentation). This was also backed by visual observation for fermentation 1, that the appearance was more like pelleted and the biomass was settling fast. In the case of a pelleted fermentation the apparent viscosity is low compared with a filamentous fermentation at the same biomass concentration, and this would lead to a higher heat transfer coefficient. This could be one reason why the heat transfer coefficient in fermentation 1 is higher.

Furthermore, the greater difference between probe position 1 and 3, for fermentation 1 and 2, (see figures 7.3a and 7.7a) could only be explained by the particulate nature of the mycelia. In the pelleted form, due to lower viscosity, there is a higher velocity flow field near the vessel wall and the brushing affect is higher than with the filamentous form.

Figure 7.7 d shows the change in wall temperature due to change in the cooling rate (as the cooling demand changes). A similar profile (as might be expected) is seen in the bulk temperature (see figure 7.7e). Figure 7.7b shows the modification of the heat flux, which again is a balance between the effects of morphology and rheology. From equations 4.9, 4.10 and 4.11 one can infer that the thermal boundary layer resistance (for laminar sublayer, buffer layer and turbulent layer) depends on the apparent viscosity of the broth. With an increase in the biomass the broth becomes more viscous leading to a greater overall thermal boundary layer resistance. However on the other hand the brushing action of the biomass may erode part of the boundary layer thus reducing its thickness and hence the boundary layer resistance; this affect should depend upon the magnitude of the impact by the biomass, which would be related to the axial distance from the impeller plane. Thus initially at 25 hours, due to the low apparent viscosity (87.1 mPas), the brushing effect of biomass (7.0 g/l) is more pronounced and probe 1 shows a much greater rise in heat flux than probes 2 and 3 (due to axial dependence). However, with further increase in the biomass, the rheology becomes more complex and viscous and overtakes the effect of the brushing action. This trend is specially noticeable at probe 2 and 3, these being away from the impeller in which case the magnitude of the surface effects of the mycelia would be lower. With further increase in biomass, probe 1 again shows signs of the dominance of the particulate nature, whereas at probe position 2 and 3 there is the dominance of the rheological factor.

To examine further the above phenomena, further heat transfer and power uptake experiments were conducted at the end of the exponential growth phase of the second fermentation. The apparent viscosity and the biomass level decreased rapidly after the exponential growth phase. Average physical properties were taken for heat transfer and power measurement. Figure 7.9 shows the power draw and power number profile for a range of impeller speeds and gas flow rates. The broth has a similar power law index to that of 0.28% CMC (for broth, n=0.6, for 0.28% CMC, n=0.63) but has a higher consistency index (for broth, K=0.898; for 0.28% CMC, K=0.25). Therefore the fermentation broth is not exactly modelled using this concentration of CMC. The difference in the gassed to ungassed power ratio profile of the broth (see figure 7.10) and that of 0.28% CMC (see figure 6.5, chapter 6) suggests that there might be differences in the size and shape of the cavity structure behind the impeller plane caused possibly by the presence of the third phase (biomass), and its effects on the coalescence properties of the bubbles.

Figure 7.11 shows the local axial unaerated and aerated heat transfer coefficient profile for a range of impeller speed and gas flow rates (note that probe -2 failed during the heat transfer experiment, hence only probe 1 and 3 data is available). Figure 7.11a shows a distinct axial variation in heat transfer coefficient. In order to study the effect of the particulate nature of the mycelia on heat transfer, the unaerated heat transfer coefficients for the mycelia and for 0.28% CMC can be compared. Although the apparent viscosity of the broth is higher (at least 2 folds) at all impeller speeds, as compared to 0.28% CMC, and therefore it would be expected that the heat transfer coefficient of the broth would be lower, in fact the opposite is true (comparing figure 7.11a and figure 5.6a). The same is true for aerated broth as well (comparing figure 7.11 b to d, and figure 6.5 a to d). Furthermore, this difference between corresponding heat transfer coefficient values for fermentation-2 and 0.28% CMC, is much higher for probe position 1 (at least 4 folds) which is close to the impeller than the probe position 3 (at least 2 folds).

In summary then, there is strong evidence that, the third phase (biomass) significantly contributes to heat transfer enhancement. It is also important to see that the heat transfer coefficient values for broth show little dependence on the impeller speed (except at the lowest impeller speed) and air flow rate, specially near the impeller plane.

Clearly, then the interacting effects in the three phase system, including, for example, bubble capture in the fibrous matrix, clumping and pelleting effects on rheological properties and the effects of mycelial morphology on surface brushing, are complex and beyond mechanistic modelling at this stage. It is necessary therefore to go back a step to a simpler defined system in which the solid properties at least, as well as the continuous suspension composition and

Power draw and Power number profile for ferm-2 (Single Rushton Impeller; D = 0.262 m)

Fig 7.9a : Power draw profile

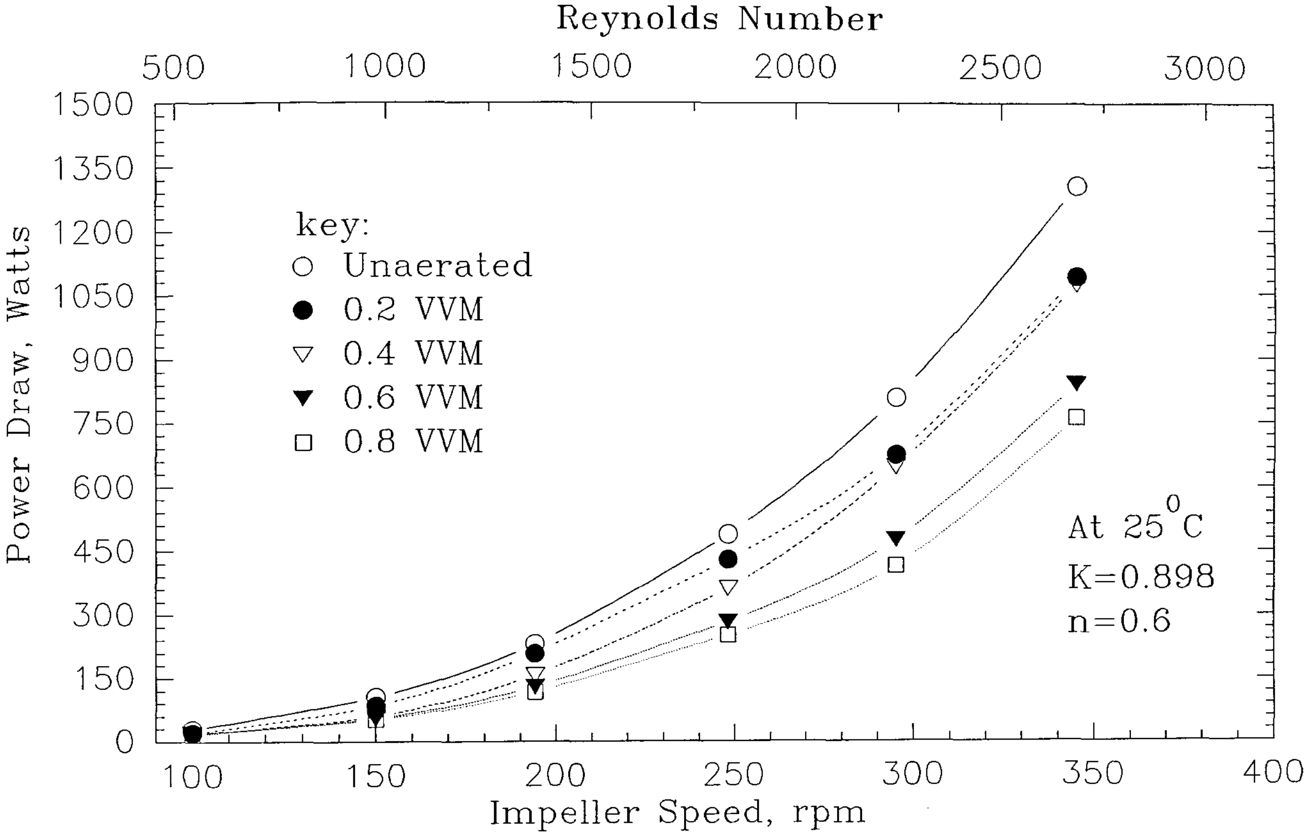

Fig 7.9b Power number profile

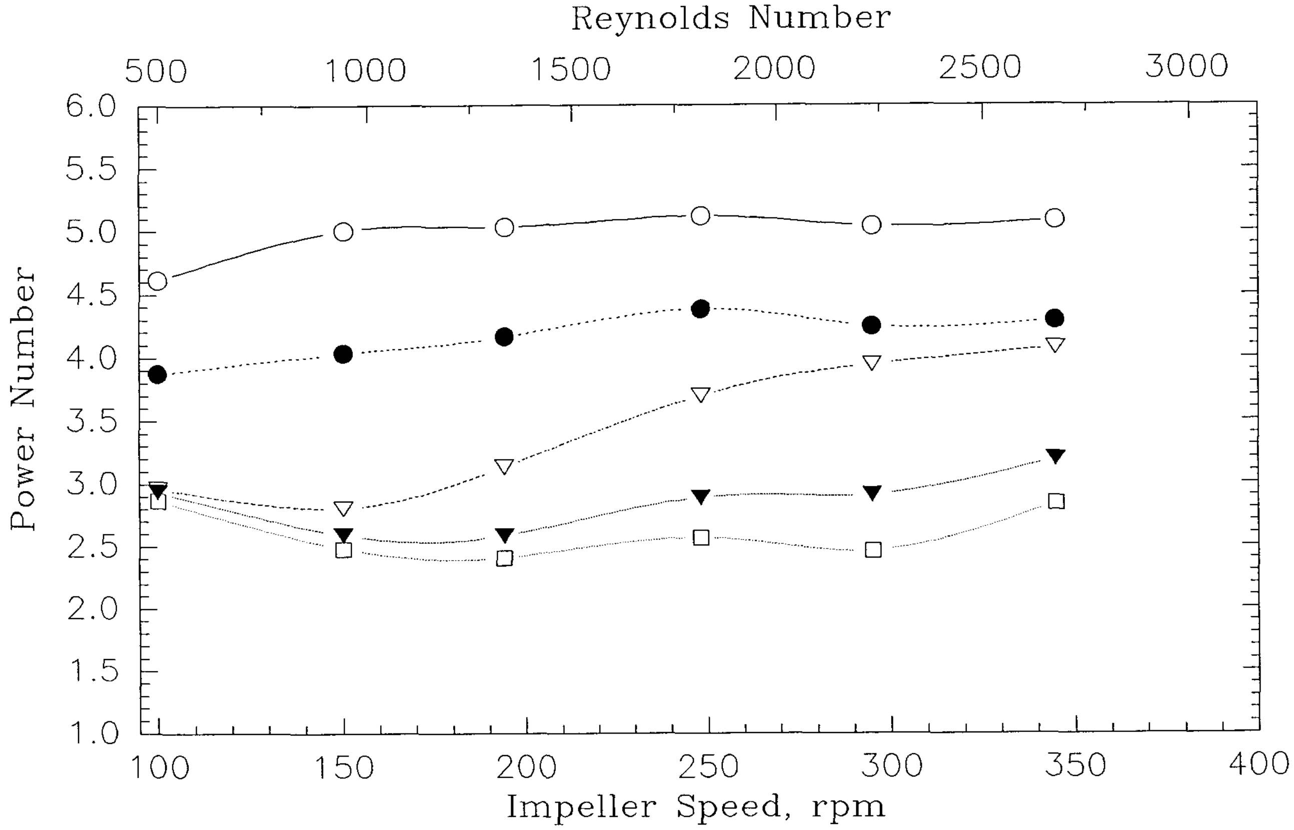

Fig 7.10: Power ratio profile for ferm-2
(single Rushton impeller)

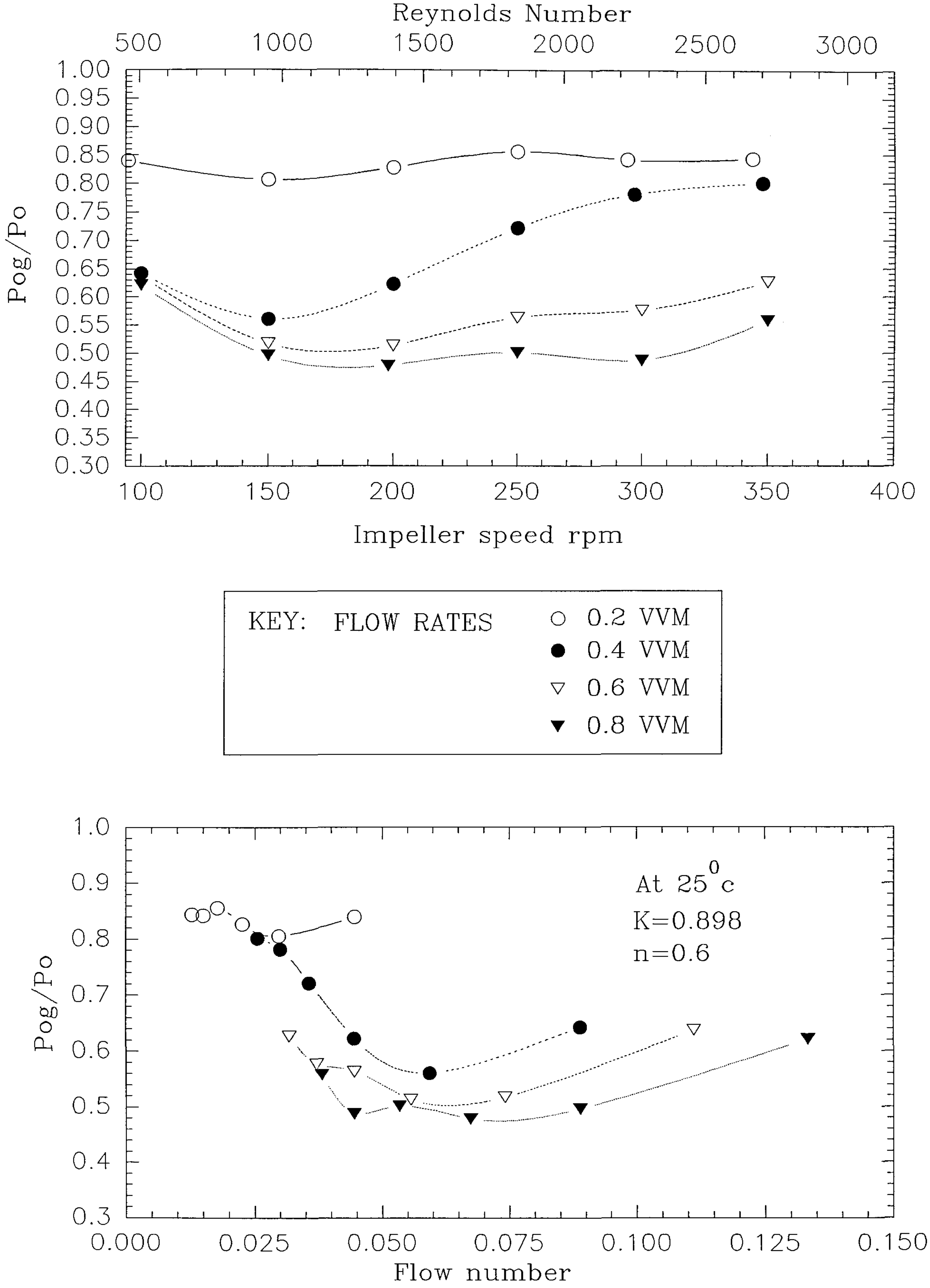

Fig 7.11: Local unearated and aerated heat transfer coefficient profile for fermentation-2

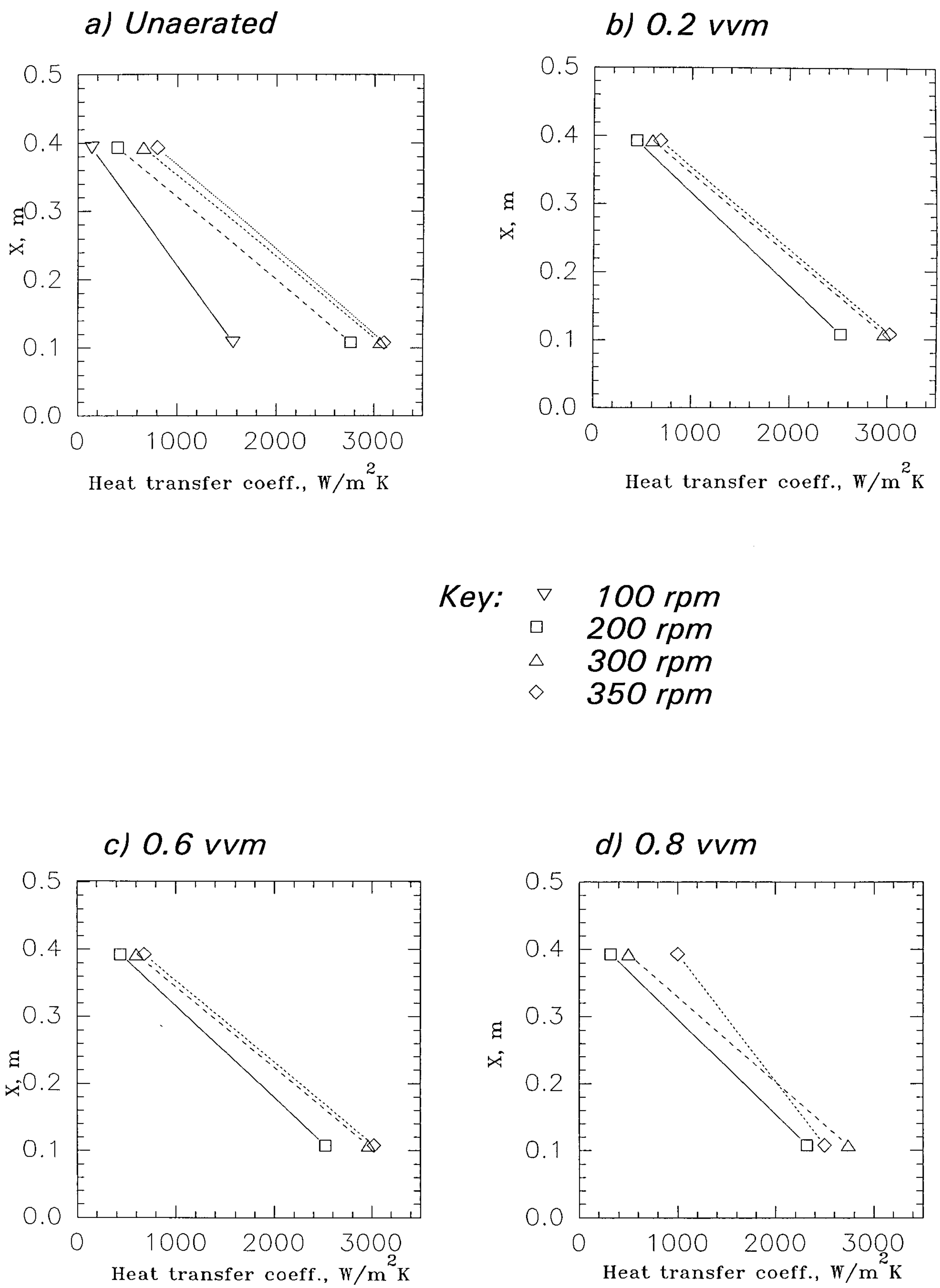

rheology, are defined. For, this purpose simulations of fermentation broth have been used and these are described next.

7.4 Simulating the mycelial broth

It is clear from the foregoing discussion that morphology of the mycelial broth is of paramount importance in deciding the heat transfer characteristic in a filamentous fermentation broth. Therefore, to simulate such a fluid (broth) for heat transfer purposes, the traditional model fluids such as CMC could give a misleading impression (as has been seen). Real multi-phase fermentations could be represented closely by suspending paper pulp fibres (simulating and having the same flow properties as a mycelial biomass) in a Newtonian solution (glucose) solutions.

In order to simulate mycelial suspensions, paper pulp fibres (supplied by ICI plc) were suspended in glucose -3 solution (46-48% glucose solution). Four concentrations of fibres were used (1 g/l, 2.5 g/l, 5 g/l and 10 g/l) . The length and diameter of the pulp fibres were found by microscopic examination to be approximately three times those of mycelial hyphae but the rheological behaviour is typical of that seen for fungal systems.

7.4.1 Local Unaerated Heat Transfer

All the local heat transfer experimental results for unaerated fluids (1g/l, 2.5 g/l Pulp, 5 g/l Pulp, and 10 g/l Pulp) for a range of impeller speeds (100, 200, 300 and 400) are shown in figures 7.12 - 7.15 (all the data are taken at a constant bulk temperature of 25 ± 2^{0}C). There exists a distinct axial variation for all concentrations of the pulp used, suggesting the importance of velocity flow field and the local hydrodynamics. The unaerated data for 1g/l pulp suspension (in glucose 3) shows a similar value to that of unaerated glucose 3 solution (see figures 7.12a and 5.3a). However, with the further addition of pulp fibres there are distinct differences from the glucose 3 solution heat transfer coefficient values, which will be examined below.

Equation 5.7 (validated in chapter 5) can be used to predict values for the heat transfer coefficient in unaerated Newtonian fluids, and therefore any difference between the measured and these predicted values can be said to be due to the presence of the solid phase, all other conditions being equal. The addition of 1 g/l of pulp to the Glucose solution does not change

Fig 7.12: Local unaerated heat transfer coefficient, power draw and power number profile for 1 g/l pulp solution

a) Local unaerated heat transfer coefficient profile

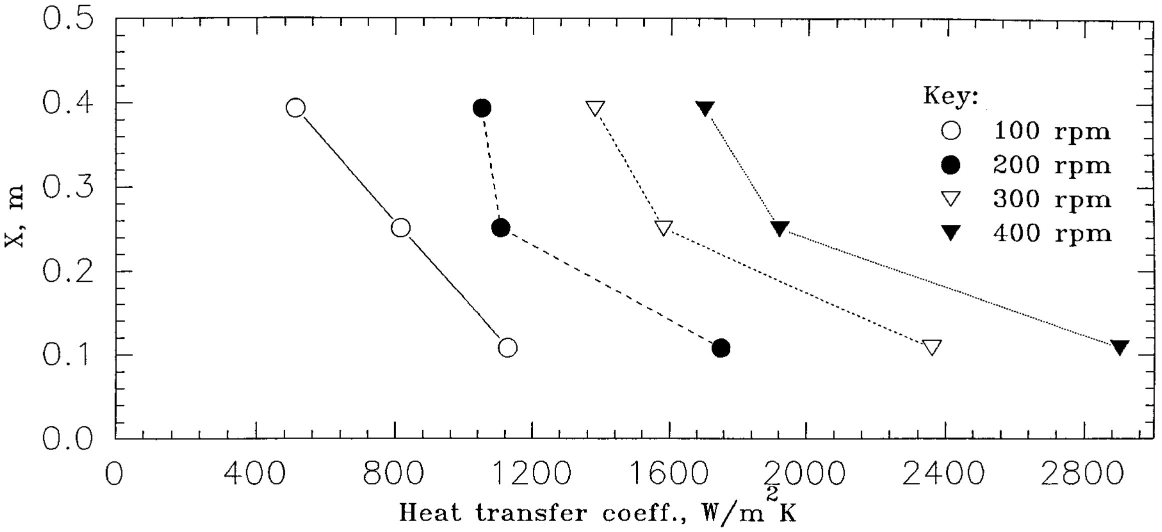

b) Power draw profile

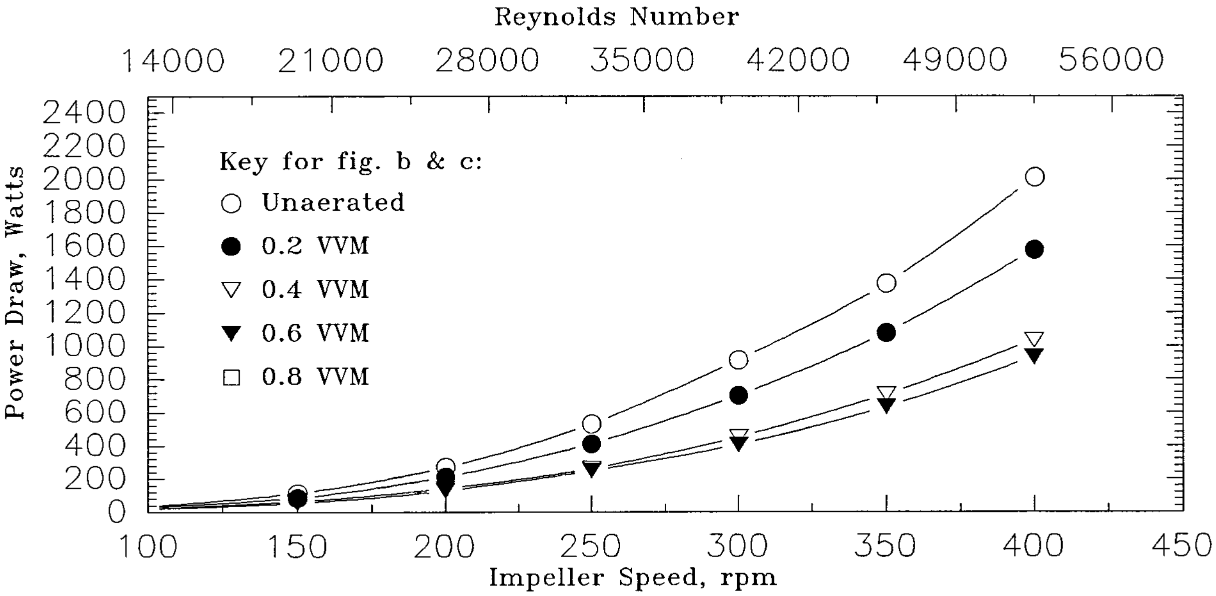

c) Power number profile

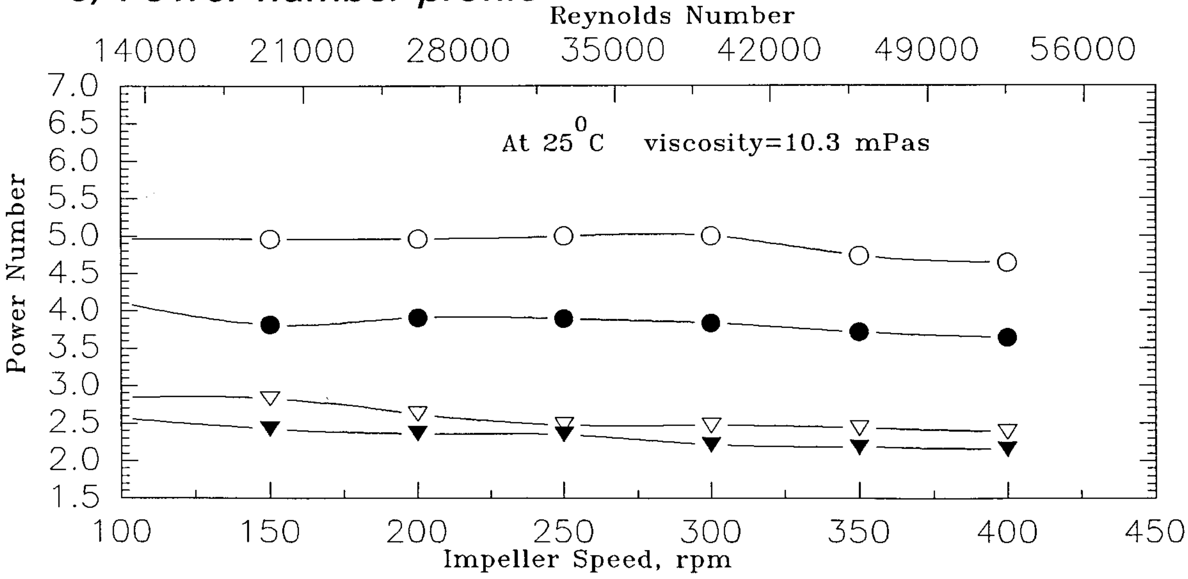

Fig 7.13: Local unaerated heat transfer coefficient, power draw and power number profile for 2.5 g/l pulp solution

a) Local unaerated heat transfer coefficient profile

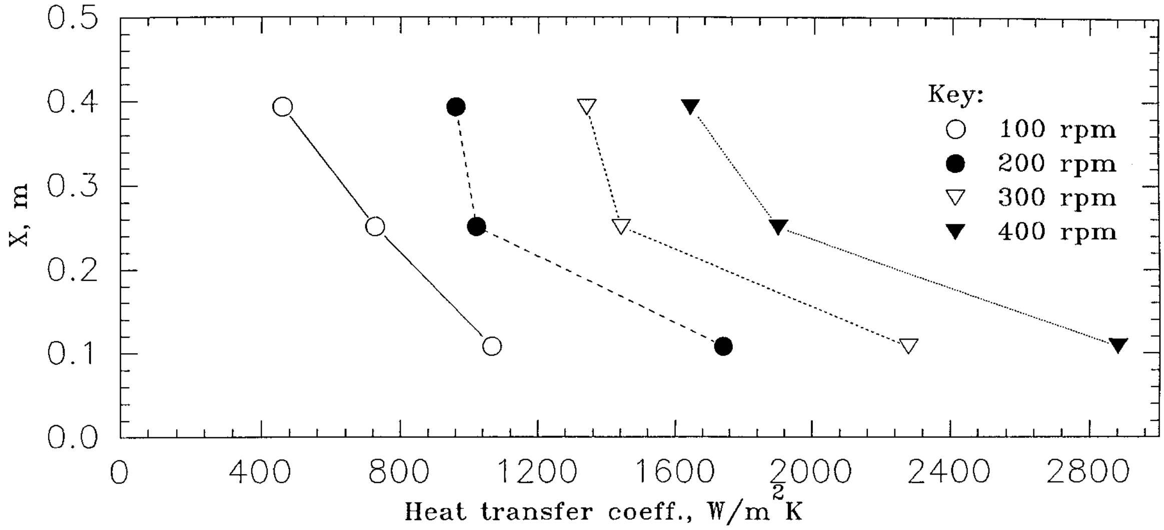

b) Power draw profile

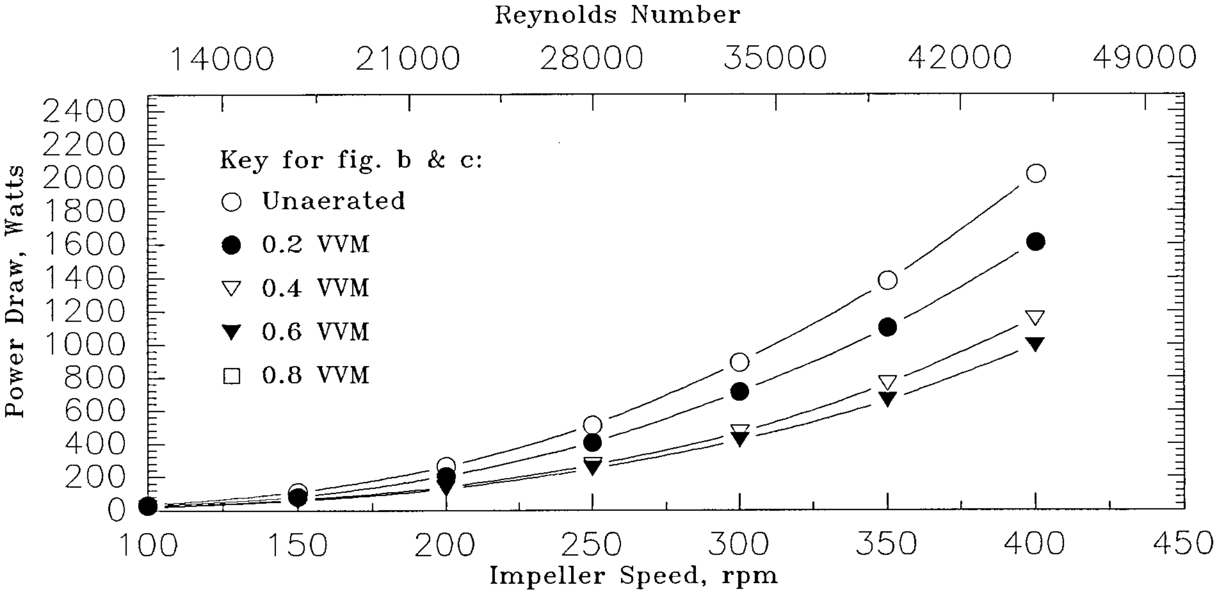

c) Power number profile

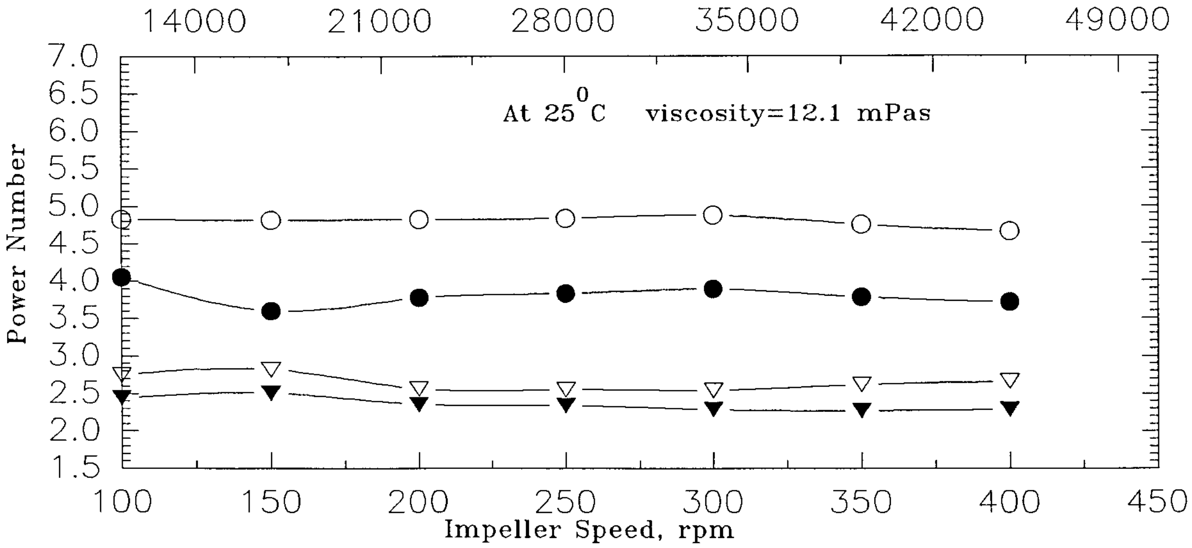

Fig 7.14: Local unaerated heat transfer coefficient, power draw and power number profile for 5g/l pulp solution

a) Local unaerated heat transfer coefficient profile

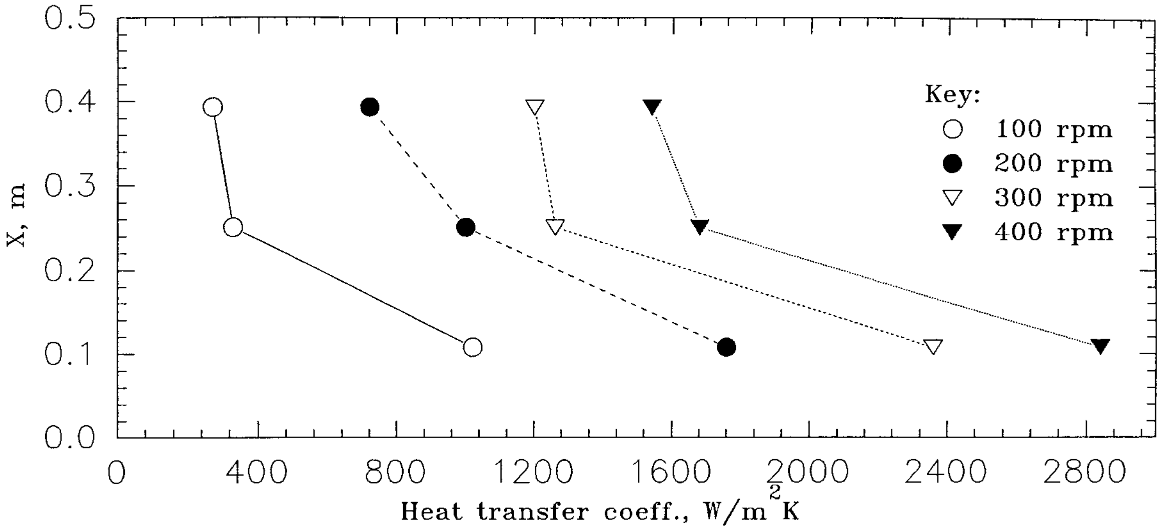

b) Power draw profile

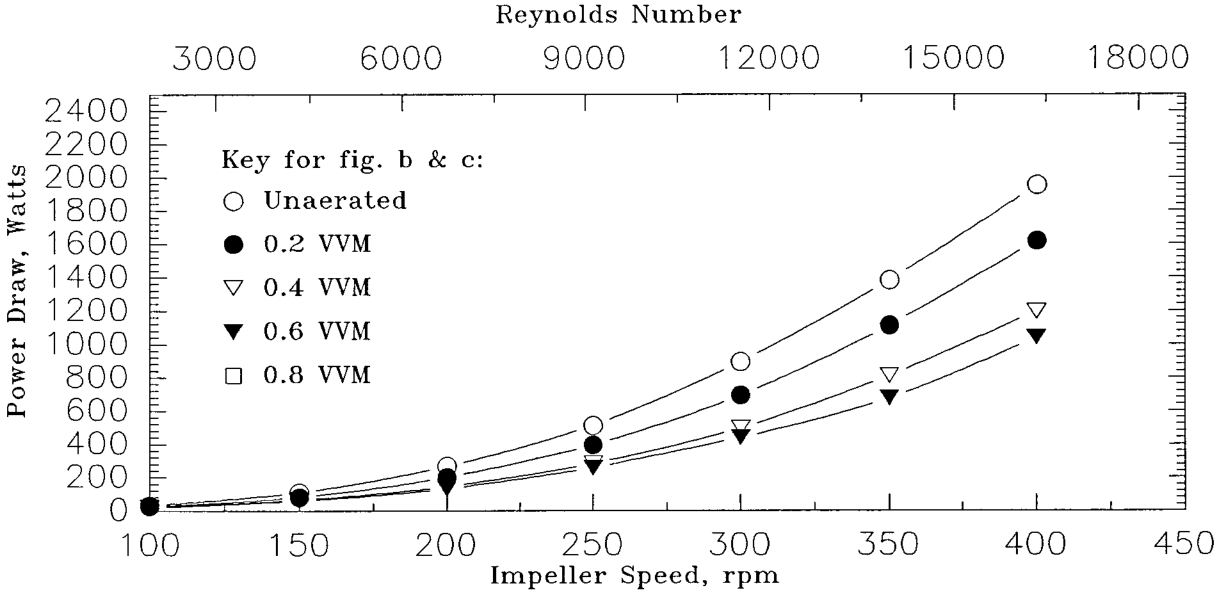

c) Power number profile

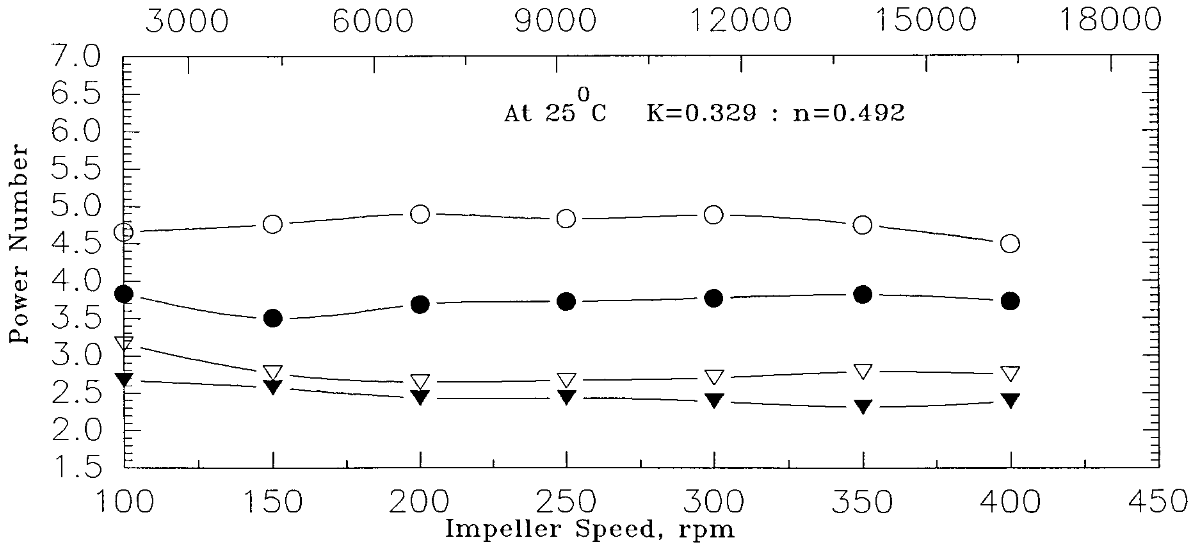

Fig 7.15: Local unaerated heat transfer coefficient, power draw and power number profile for 10g/l pulp solution

a) Local unaerated heat transfer coefficient profile

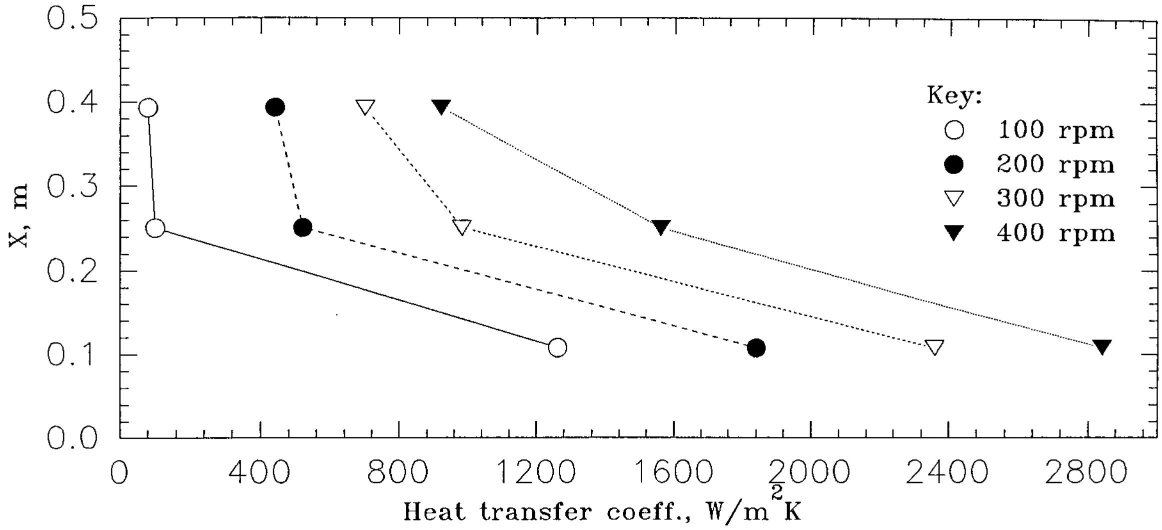

b) Power draw profile

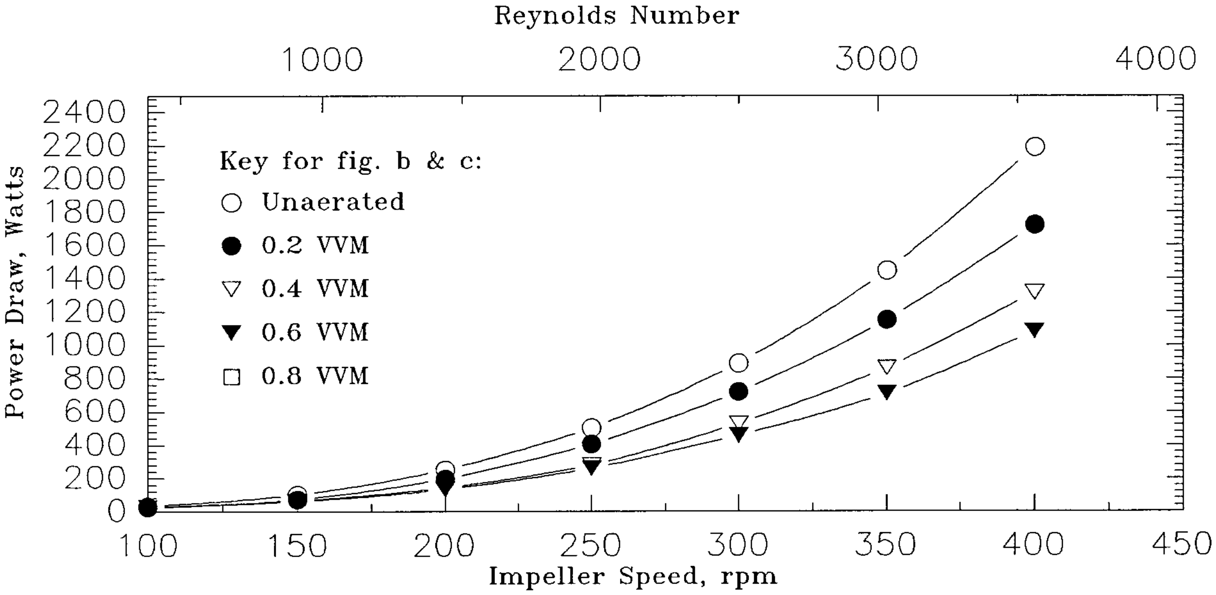

c) Power number profile

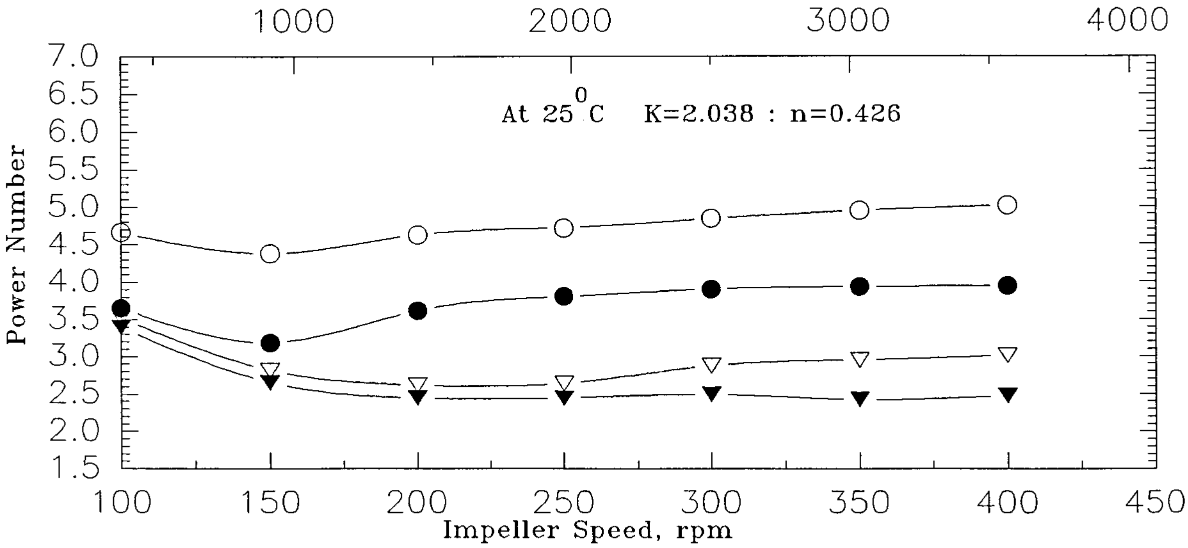

the viscosity (as measured by a Contraves viscometer) and the local heat transfer coefficient value varies insignificantly (see figure 7.16, the solid line is the empirical model whereas the symbols are the experimental data points).

Further addition up to 2.5 g/l of pulp increases the viscosity of the solution to 12.1 mPas with the fluid still exhibiting Newtonian character. The experimental heat transfer values (see figure 7.17) still compare well with the predicted local heat transfer value using equation 5.7 (chapter 5), and it could be said that at this stage there is no effect of the solid phase on heat transfer and the suspension is effectively acting as a homogenous fluid.

A suspension of 5 g/l of pulp in the Glucose solution significantly affects the fluid rheology. It becomes a shear thinning non-Newtonian fluid with values for K and n of 0.329 and 0.492 respectively (refer chapter 3, section 3.4). The methods used for rheological characterisation are those described in chapter 3 (section 3.4). At the lowest impeller speed (100 rpm) the heat transfer coefficients at positions 2 and 3 are very low (reduced now to only 40-45% of the clear solution values), due to the shear thinning behaviour of the fluid which leads to much reduced fluid motion away from the impeller plane (see figure 7.18). At all speeds the heat transfer coefficients near to the impeller plane are similar to those for the glucose solution alone even though the apparent viscosities of the pulp suspensions are considerably higher than that of the Glucose solution. At the other two positions the discrepancies from the glucose solution values become progressively smaller as the speed increases. The experimental values now exceed those predicted (now using the correlation for non-Newtonian fluids, equation 5.14, validated in chapter 5 using the measured rheological characteristics) at all positions, particularly at the plane of the impeller, where the apparent enhancement reaches 50-70%.

At a pulp concentration of 10 g/l in glucose solution, the fluid becomes very viscous and the values of K and n reach 2.038 and 0.426 respectively. At the lowest impeller speed the transfer coefficients at probes 2 and 3 show even lower values, as would be expected with the more extreme shear thinning behaviour of this fluid. However, near the plane of the impeller (probe-1) the coefficients at all speeds are still at or above the clear solution values even though the apparent viscosities now differ by more than an order of magnitude. The reductions from the clear solution values at the other two positions are significant at all speeds, as would be expected with what is a rather viscous fluid. Nonetheless the experimental values are in all cases, except at a speed of 100 rpm, well above those predicted from (equation 5.14). Figure 7.19 illustrates clearly that the divergence of measured from predicted values as speed increases is highly position dependent both in scale and trend.

Fig 7.16 : Comparison of unaerated experimental and predicted data for 1 g/ l pulp solution

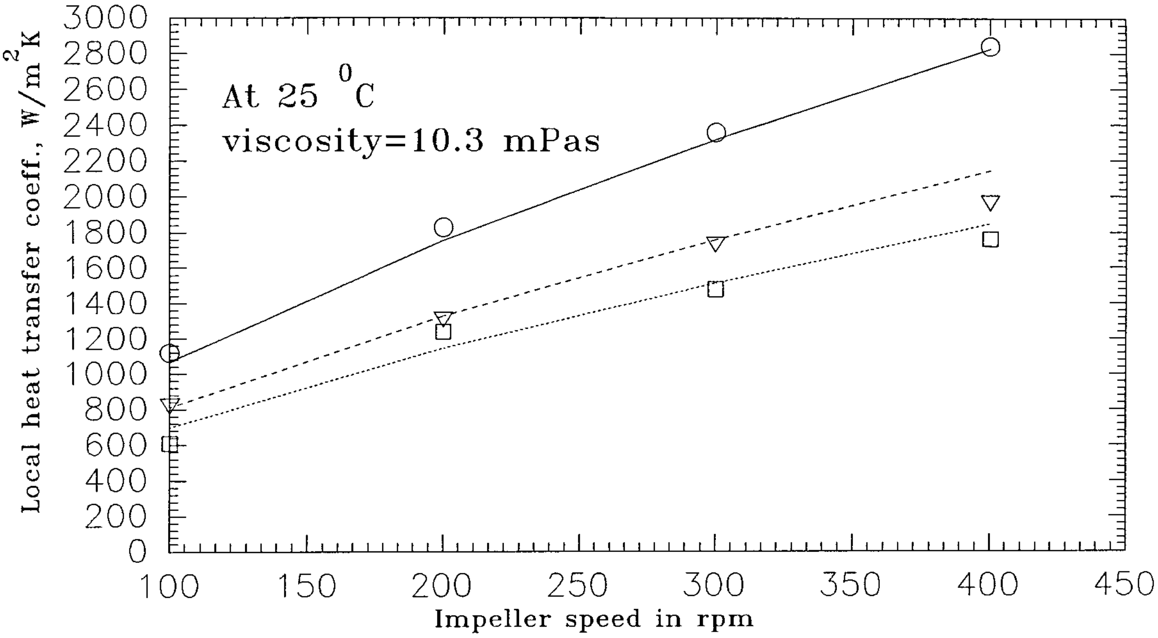

Key:	*Experimental values*	*Predicted values*
Probe 1	○	———
Probe 2	▽	- - - - -
Probe 3	□	··········

Fig 7.17 : Comparison of unaerated experimental and predicted data for 2.5 g/l pulp solution

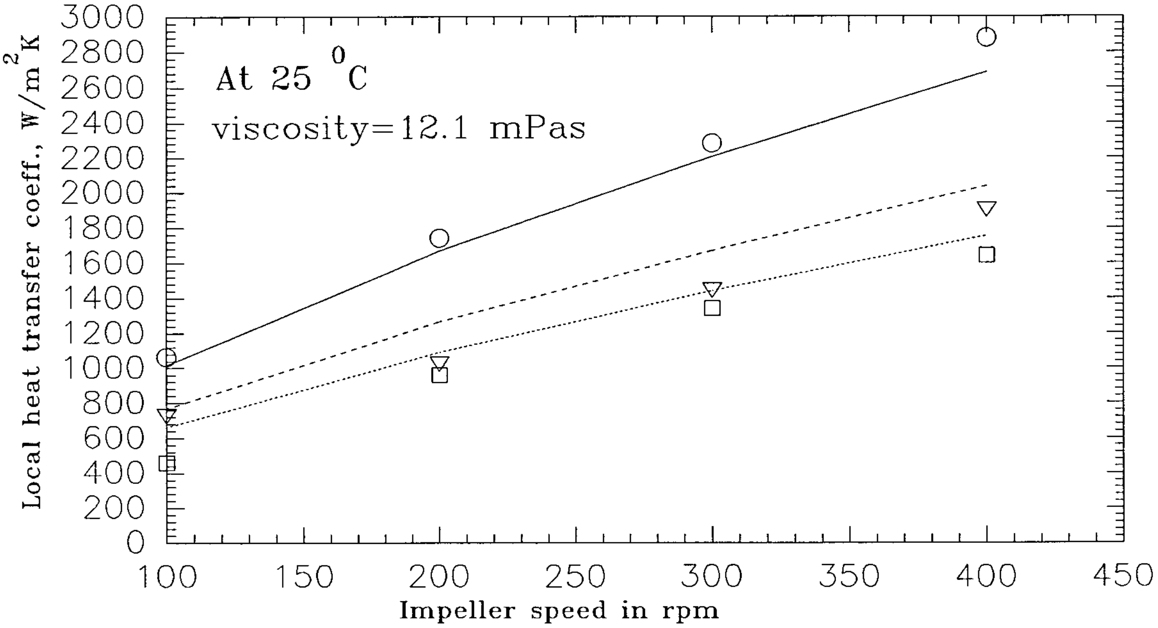

Fig 7.18 : Comparison of unaerated experimental and predicted data for 5 g/l pulp solution

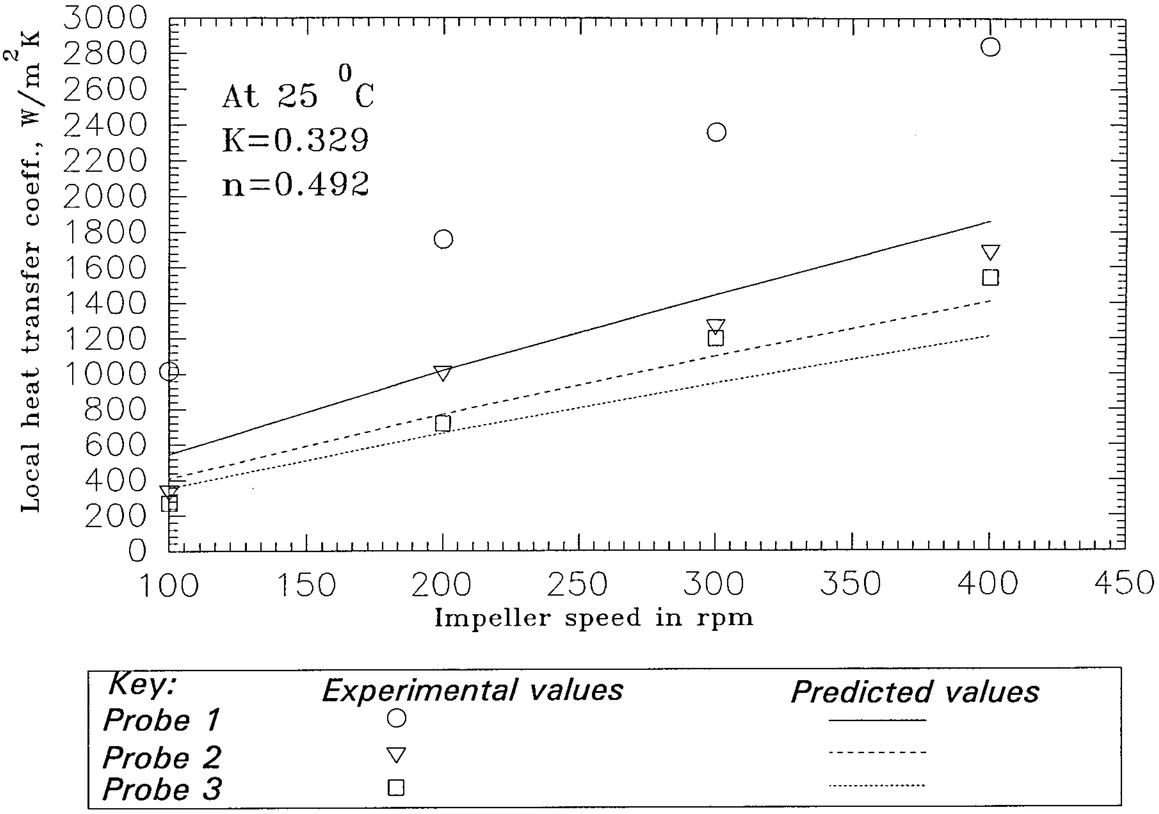

Fig 7.19 : Comparison of unaerated experimental and predicted data for 10 g/l pulp solution

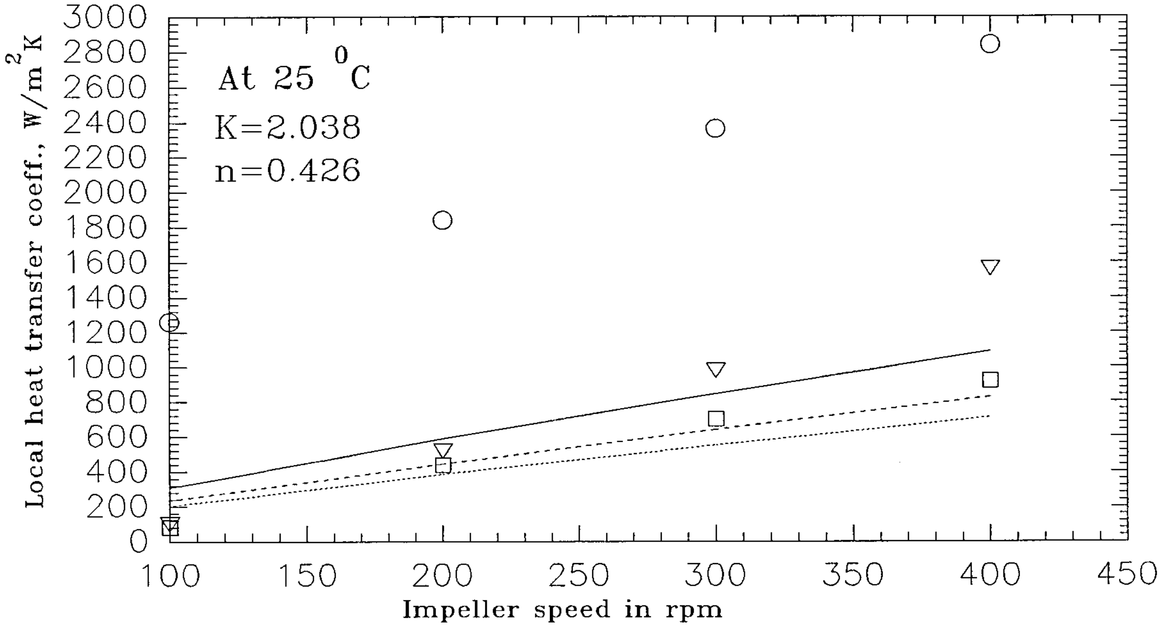

It can be clearly seen that the effect of suspended solids on the local heat transfer coefficients is highly position dependent. Near the plane of the impeller it may be surmised that the "brushing" effect of solids on the boundary layer counteracts any reduction in local flow velocity arising from the increase in apparent viscosity so that the heat transfer coefficient remains largely unchanged. Away from this plane the effect is attenuated and it may be suggested that this is because the solid actually needs to impinge normally to the wall to have a significant "brushing" effect and such impingement is reduced in shear thinning conditions away from the impeller plane.

The net result is that the prediction of heat transfer based on simple modification of the viscosity term in the Reynolds and Prandtl numbers become increasingly unreliable as the solid concentrations rise. In practice the modification that would be necessary would probably need to reflect a "shape factor" describing the morphology of the fungal mycelium. For example, compare the heat transfer coefficients for the unaerated 5 g/l pulp (K=0.329, n=0.492, see figure 7.14a) and the unaerated fermentation 2 (K=0.898, n=0.6, see figure 7.11a), the basis of comparison here is Reynolds number. The 5 g/l pulp has a much higher Reynolds number for the same impeller speed than has the fermentation broth. Therefore one would expect that the 5 g/l pulp heat transfer coefficient would be higher - however the opposite is true. Nonetheless the values for heat transfer coefficient obtained using 5 g/l pulp are much closer to those obtained in the fermentation broth than those using (the broadly similar rheologically) 0.28% CMC solution. Therefore, even though the suspension of fibres is a definite improvement over the traditional model fluid, still it is not a perfect model fluid mainly due to the difference in the morphology. Another important difference is that for all the pulp solutions there is a distinct influence of impeller speed on the heat transfer coefficient (though this effect is less than obtained in 0.28% CMC) ; however in the case of the real multi phase fermentation the effects of both impeller speed and air flow rate (above a critical value) are much less pronounced.

7.4.2 Local Aerated heat transfer

In real multiphase fermentations the presence of air adds another level of complexity. Figures 7.20 to 7.23 shows local aerated heat transfer coefficient and mixing results for 1 g/l, 2.5 g/l, 5g/l and 10g/l pulp solutions in glucose 3 respectively. Figure 7.21, for 1 g/l pulp suspension, shows that flooding also occurs at 100 rpm but at gas flow rates of 0.4 vvm and 0.6 vvm.

Beyond the flooding loading transition (FLT), the addition of pulp has analogous effects to those observed in the unaerated state. The heat transfer coefficients are essentially similar for

Fig 7.20: Local aerated heat transfer and mixing results for 1 g/l pulp solution

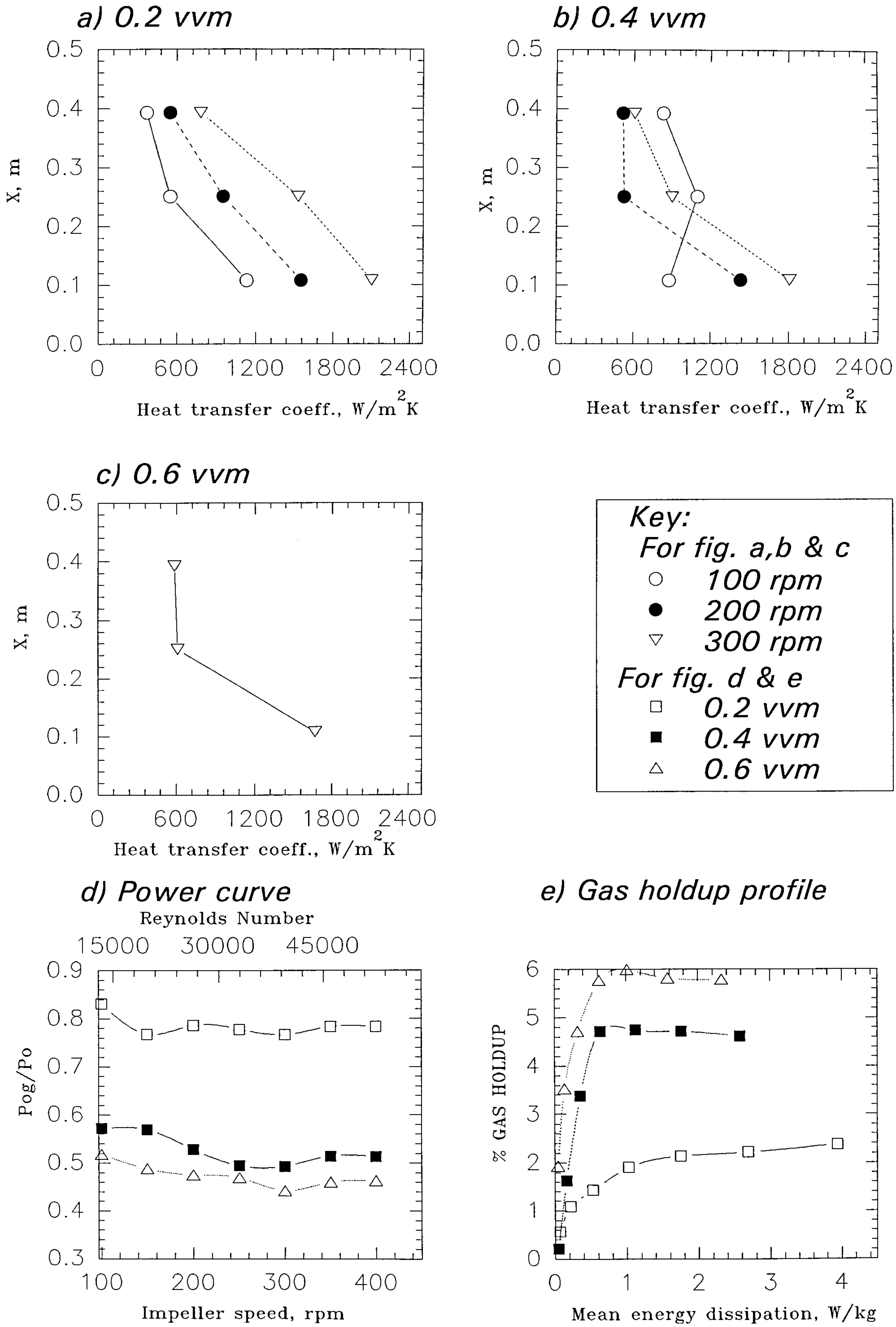

Fig 7.21: Local aerated heat transfer and mixing results for 2.5 g/l pulp solution

a) 0.2 vvm

b) 0.4 vvm

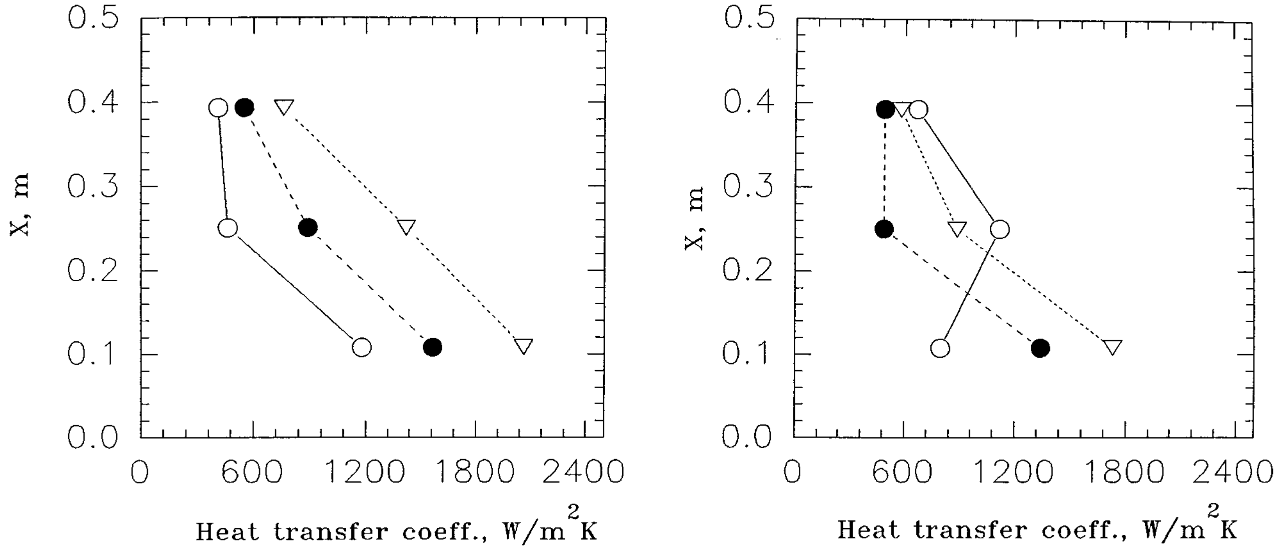

c) 0.6 vvm

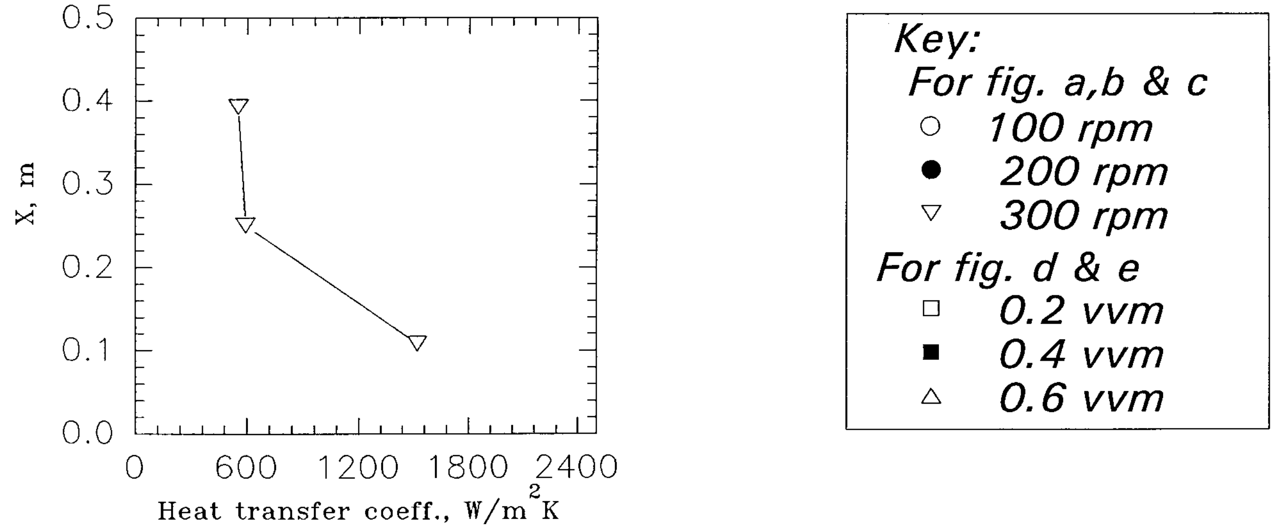

d) Power curve

e) Gas holdup profile

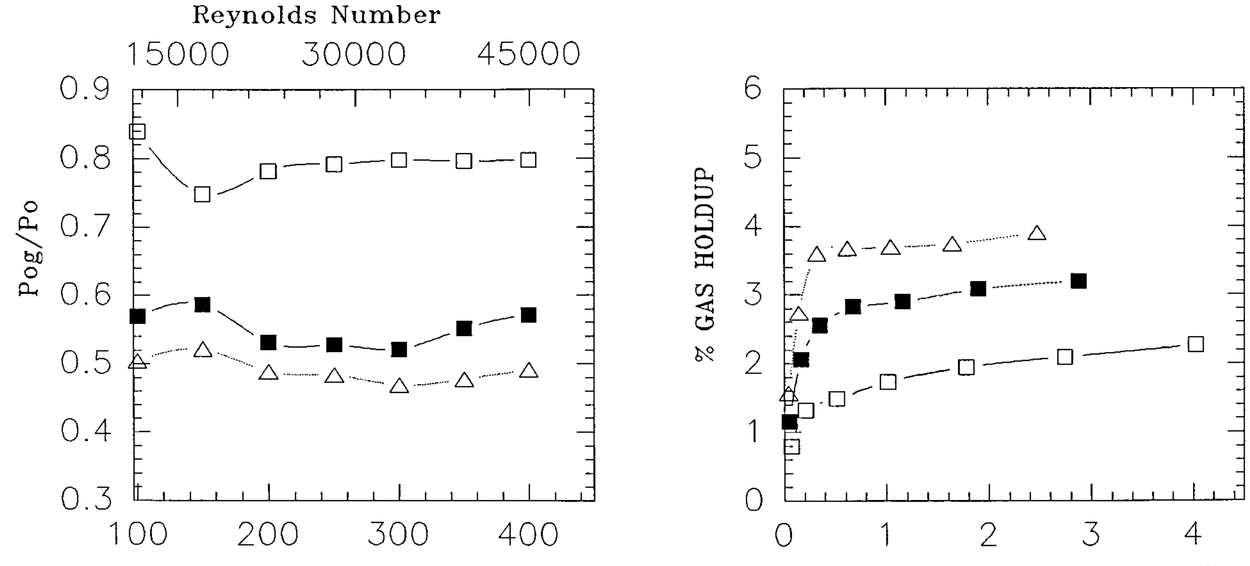

Fig 7.22: Local aerated heat transfer and mixing results for 5 g/l pulp solution

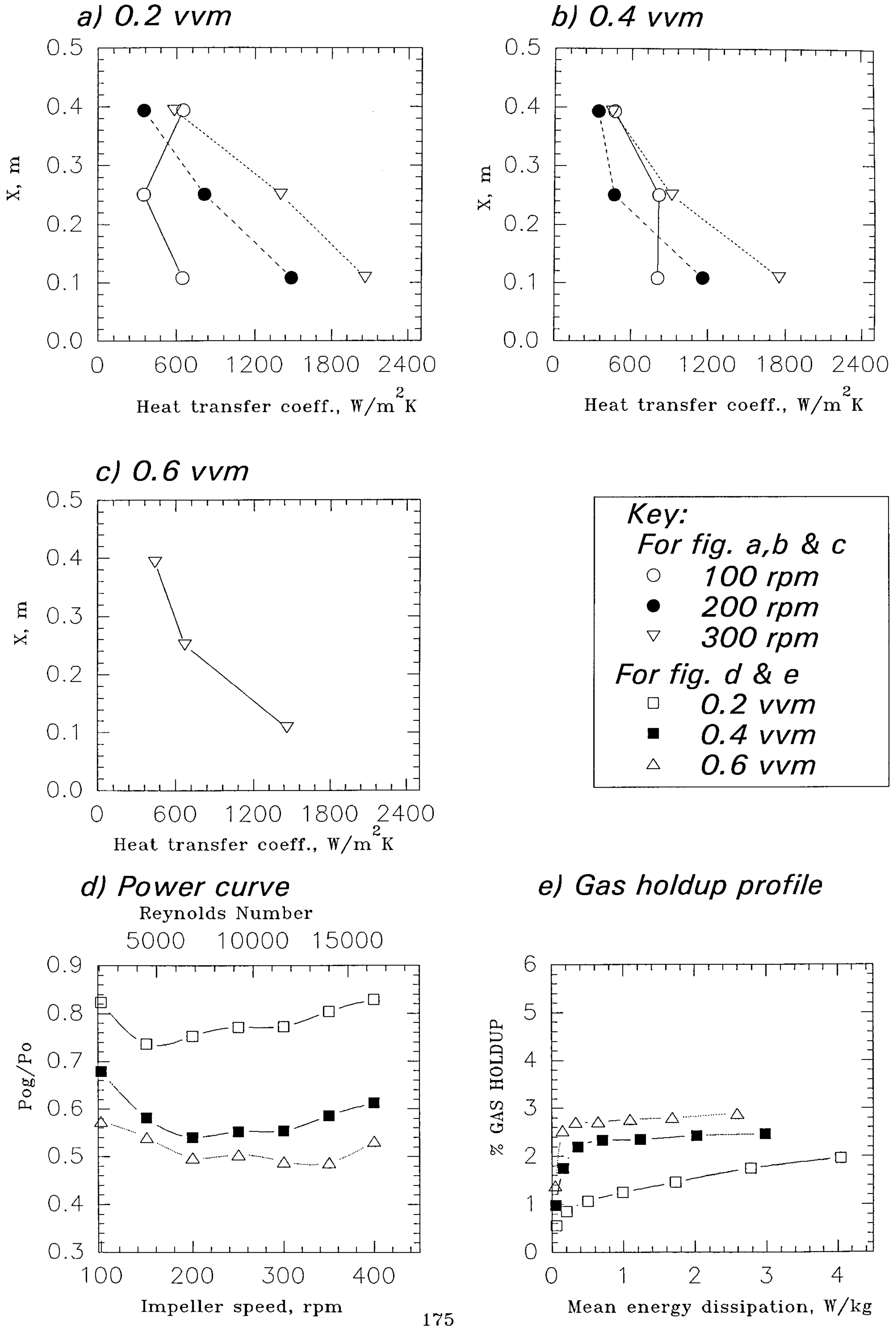

Fig 7.23: Local aerated heat transfer and mixing results for 10 g/l pulp solution

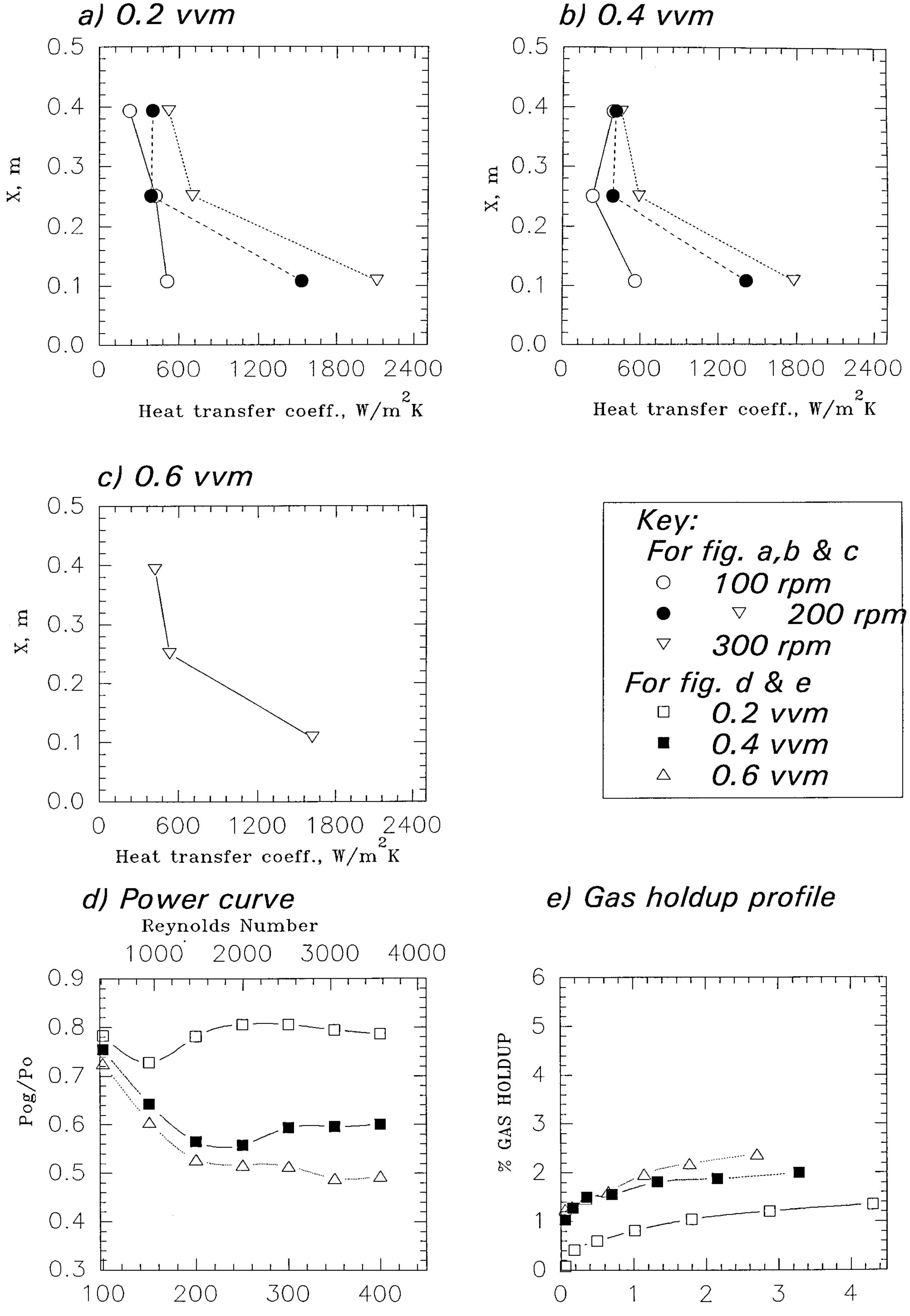

all pulp solutions (see figure 7.20 - 7.23) to those for glucose 3 (see figure 5.3) near to the impeller plane but at other positions there are significant reductions from those observed for aerated glucose conditions. The heat transfer coefficients measured in the fermentation 2 experiment are nonetheless higher than measured using any of the pulp suspensions under equivalent conditions, particularly near the impeller plane. They are also of course higher still than those measured using 0.28% CMC solution.

The power curve is characteristic for aerated broths of this type (see figures 7.20 to 7.23 d). The data shown for gas hold-up shows the substantial reductions in this parameter at all flow rates in the presence of solids, presumably through interference with the cavity formation process in trailing vortices and also through effects on bubble coalescence and therefore on their size distribution. This is however a complex situation that yet requires considerable more analysis for its full understanding.

The above results for the first time clearly demonstrate the significance of the third phase in the modification of heat transfer in real multiphase fermentations. Thus in any experimental simulation care must be taken to represent the solid matrix of a real mycelial fermentation. The traditional way of modelling a mycelial fermentation with carboxy-methylcellulose or carbopol should be approached with caution. The same degree of caution needs to be applied to any use of heat flux measurements as process indicators, since clearly such measurements are going to reflect both position and fluid rheology dependence.

Although this work has been completed using a defined paper pulp suspension, there are other factors which can lead to fungal morphologies differing from the continuous filamentous structure used here. The constitution of the medium, osmolarity, culture age etc., may all cause variations between fully developed pellet formation and dispersed mycelium - and the likelihood is that these may result in differing heat transfer performance. Therefore, though the present approach is a definite improvement for simulations of such fermentations, its limitations must be clearly recognised.

CHAPTER 8

Discussion and direction for future work

This project evolved in stages with the aim of understanding and exploring the fundamentals of heat transfer in agitated vessels to enable a better approach to equipment design. The modification of the heat flux probe allows an accurate measurement of heat flux and temperature even in fermentation conditions. There exists now a body of data for a range of fluids and operating conditions, and in the absence of quantitative description of local hydrodynamics a qualitative link between local heat transfer and global hydrodynamics is critically examined. Various correlations are proposed as well to aid the design calculations for similar geometry. Perhaps the most significant finding of this project is the confirmation that the third phase does actually modify the boundary layer, establishing a strong link between heat transfer and morphology.

The heat flux probe, which is at the heart of this study, was critically examined in the light of boundary layer fundamentals, and necessary modification was carried out to ensure accurate and reliable measurement. The use of the probe was validated using correlations in the literature. However, it could be improved further by reducing the resistances in the probe. The company (RdF inc.) is willing to explore alternative substitute materials of lower resistance to reduce the overall impedance of the probe. This development in the probe is specially desirable for low temperature driving force fermentation processes. Further, a comparison between modified and unmodified probe would be interesting as a means to ascertain the effect of discontinuity of the boundary layer in actual measurement.

The single phase heat transfer behaviour for Newtonian fluids show a distinct axial variation due to local axial variation in velocity flow field. A good qualitative link with the global hydrodynamics was achieved. However the lack of knowledge of the local hydrodynamics in such vessels forced an empirical approach. A number of correlations were arrived at for both local probe positions and one correlation incorporating the local axial velocity flow fields. The correlation with the power factor appears to be more representative of the local hydrodynamics than the Reynolds number correlation, this is specially suggested by the laser Doppler anemometry work.

The dual impeller Newtonian system shows a tendency towards compartmentalisation of the impeller primary loop. It would be interesting to explore the effect of varying the inter impeller spacing and to establish clearly this concept of compartmentalisation in heat transfer.

In non-Newtonian systems the shear thinning nature of the fluid implies that the rheology of the fluid varies with the applied shear, and that the shear varies inside the vessel (the maximum being in the impeller discharge stream). The global shear value (11.5N) assumed for all the correlations may not be most suitable, and further work needs to be done to map shear in such vessels.

For the dual impeller unaerated non-Newtonian system, the concept of compartmentalisation becomes invalid, mainly due to the shear thinning behaviour of the fluid. It seems likely that one secondary loop exists instead of two independent primary loops (as in the case of Newtonian fluid). This aspect needs further investigation and flow visualisation could be very helpful in understanding the bulk mixing and its effect on heat transfer.

Aeration introduces a new challenge in the understanding of heat transfer. In the literature there was utter confusion regarding the role of the second phase (gas) on the heat transfer, as a link with hydrodynamic behaviour was rarely (even qualitatively) made. It is clear from this work that the introduction of gas has two independent and opposing effects on heat transfer:

a) The formation of gas cavities behind the impeller blade, which changes with both impeller speed and the gas flow rate, leads to a drop in power number and hence in impeller power draw. The reduction in the impeller power draw then leads to a drop in the heat transfer coefficient.

b) The gas imparts kinetic energy into the system enhancing the total power and hence the heat transfer; however this increase is negligible at high impeller speeds due to a comparatively much higher impeller power draw.

Therefore, to account for both these effects, the total power (impeller and gas power) is used for the first time, in all the aerated correlations. In general (except at low impeller speeds), aeration leads to a drop in heat transfer coefficient as compared with the unaerated case.

The data for aerated Newtonian fluids (using a single impeller) show a greater scatter than that for the non-Newtonian fluids. This possibly could be qualitatively linked to the cavity structure behind the impeller blade. In Newtonian fluids the cavity structure changes both in size and shape with the impeller speed and gas flow rate and this then has a dynamic influence on the heat transfer; whereas for non-Newtonian fluids the cavities (specially for 0.8% and 1.4% CMC) are uniform in shape and size as the operating parameters change and thus having a uniform and predictable affect on the heat transfer.

In the dual impeller aerated system the lower impeller floods at a lower impeller speed than the upper impeller and this is reflected in the heat transfer coefficient measurement. However, understanding of the heat transfer is limited by the knowledge of hydrodynamics in dual impeller system and requires further research.

Heat transfer in fermentation broth is particularly complicated by the presence of the mycelial biomass (the third phase). The presence of biomass not only make the broth shear thinning but can actually modify the film heat transfer coefficient. This work examines, for the first time, the role of the mycelial morphology on heat transfer in a stirred bioreactor.

The morphology influences both the bulk rheology and the particulate action on the thermal boundary layer at the heat transfer surface. The enhancement of apparent viscosity leads to a drop in the heat transfer coefficient, whereas the "brushing action" of the mycelia on the boundary layer leads to its enhancement. This effect is position dependent; near the impeller plane the brushing action dominates and there is almost a constant heat transfer coefficient at varying impeller speed (except at the lowest impeller speed, where due to the shear nature of the fluid the movement and hence the brushing action is minimum near the vessel wall). For axial positions away from the impeller of this effect is much more limited.

The heat transfer coefficient value near the impeller plane is almost independent of the impeller speed, suggesting that there is a limit to which the thermal boundary layer could be modified. This concept requires further research to develop a model for boundary layer modification by the mycelial biomass. Parallels could be drawn with scraped surface heat exchangers.

It is also clear that heat transfer simulation of a fermentation using traditional model fluids such as CMC is not valid. Furthermore, even the simulation with suspended fibres has limitations. The affect of morphology on the boundary layer and on the rheology, and the effect of rheology on the thermal boundary layer and local hydrodynamics, is the complex to be understood clearly.

The further research could include the following steps:

1) Quantification of the local hydrodynamics using optical techniques and computational fluid dynamics. It is clear from this work that a clear understanding of local hydrodynamics is of paramount importance for a fundamental understanding of heat transfer. Optical techniques such as laser Doppler anemometry could be used to obtain data near the vessel wall and then relate it to the global parameters such as global power or impeller tip speed. This could then be modelled for a range of geometries using the computational fluid dynamics. However, the optical technique is not suitable for opaque system such as a real multiphase fermentation. Further, the computational technique could work for single phase systems but has inherent problems in modelling two phase systems and even more so in three phase systems.

2) Mapping of the shear inside the vessel for shear thinning fluids. In this project a global shear value of 11.5N was assumed for all shear thinning fluids. Recent work suggests that shear rate varies from as high as 90N to 11N inside the vessel, this is particularly important for heat transfer measurements as near the vessel wall due to the wall drag force the shear would be totally different which will also vary axially.

3) Quantifying relationship between morphology and rheology. The effect of morphology on the rheology has to be clearly understood in order to quantify its effect on the heat transfer.

5) Deriving a fundamental model for boundary layer modification by the mycelial biomass. It is clear from this work that the morphology of the mycelia modifies the boundary layer. There are three zones in a thermal boundary layer; the laminar sublayer, the buffer zone and the turbulent layer. In my opinion the laminar sublayer is difficult to modify as it is very thin and

almost static, whereas the turbulent and the buffer zone could be modified by the particulate nature of the mycelia. This concept certainly needs further research to establish any basic model.

The clear understanding of the above stages will enable the fundamental understanding of heat transfer in a complex multiphase fermentation. However attempts were made during this project to explore the possibility of a better optical technique (than laser Doppler anemometry) for quantifying the local hydrodynamics, which is discussed in the following section.

A note on the collaboration with the Technical University of Munich

In this project a collaboration was sought with the University of Munich, under the Anglo-German collaboration programme, for the understanding of the hydrodynamics in mechanically agitated vessels. I spent one month to carry out experimental work in two visits. In Munich a novel optical technique using double pulse ruby laser was developed to facilitate optical studies of spray droplets from a nozzle providing information on spray geometry and velocity distributions. Their experiments involved the dispersion of liquid droplets in air, whereas this project involved the dispersion of air in liquid. Therefore the first step was to validate this technique in liquid-air system.

During the first visit the usefulness of the technique was assessed specially for hydrodynamic studies. The technique was found to be very useful and powerful specially for gas bubble velocity and distribution. After training and initial induction the second visit was planned. The aim of the second visit was to validate the equipment and the experimental set-up with predictions based on literature correlations for bubble size and rise velocity. The bubble column was constructed with three sizes of nozzles, and then correct optical arrangement was ensured with bubble column as the object of study. The double pulse ruby laser was used to make holograms. The first shot (single pulse) gave information about the size and shape of the bubble whereas the second shot (double pulse) records a change in position and by knowing the time interval between pulses the rise velocity of the bubbles were calculated.

The optical arrangement is such that the incident beam passing through the object (bubble column) has the same path length as the reference beam, which is from the same source (ruby laser) being split by the beam splitter. The incident and the reference beam meet at the holographic plate causing interference. Once the holographic plate is exposed by the laser, the plate is developed by a simple technique. After development the image is reconstructed using a continuos He-Ne laser at the same angle as the reference beam. The image is then processed using a digital image processing system. The data obtained from the monitor is then measured and photographed.

The data for the bubble column agreed with the prediction in the literature, and thus the equipment was validated for the hydrodynamic study. The next phase of the collaboration (which is now, being followed by different research member) aims to carry out the hydrodynamic studies in stirred vessel. This data could then be used to derive appropriate model using computational fluid dynamics.

APPENDIX - 1

A) Dimensions of the vessel and the inserts are shown in figure A1.1 .

B) A comparison is made between the Standard Rushton turbine and the one used in the present work. The diameter of the impeller is 0.262 m .

Characteristic Ratio's	Standard Rushton	Presently used impeller
D/D_T	0.33	0.33
w/D	0.20	0.20
L/D	0.25	0.25
D_d / D	0.75	0.676

There is a significant deviation in the final characteristic ratio. Therefore the present impeller cannot be treated strictly as a Standard Rushton turbine. The power number of this impeller was found to be close to 6.0, by testing in a 0.56 m diameter mixing vessel with a reliable strain gauge.

Figure A 1.1 The 800L Vessel Dimensions

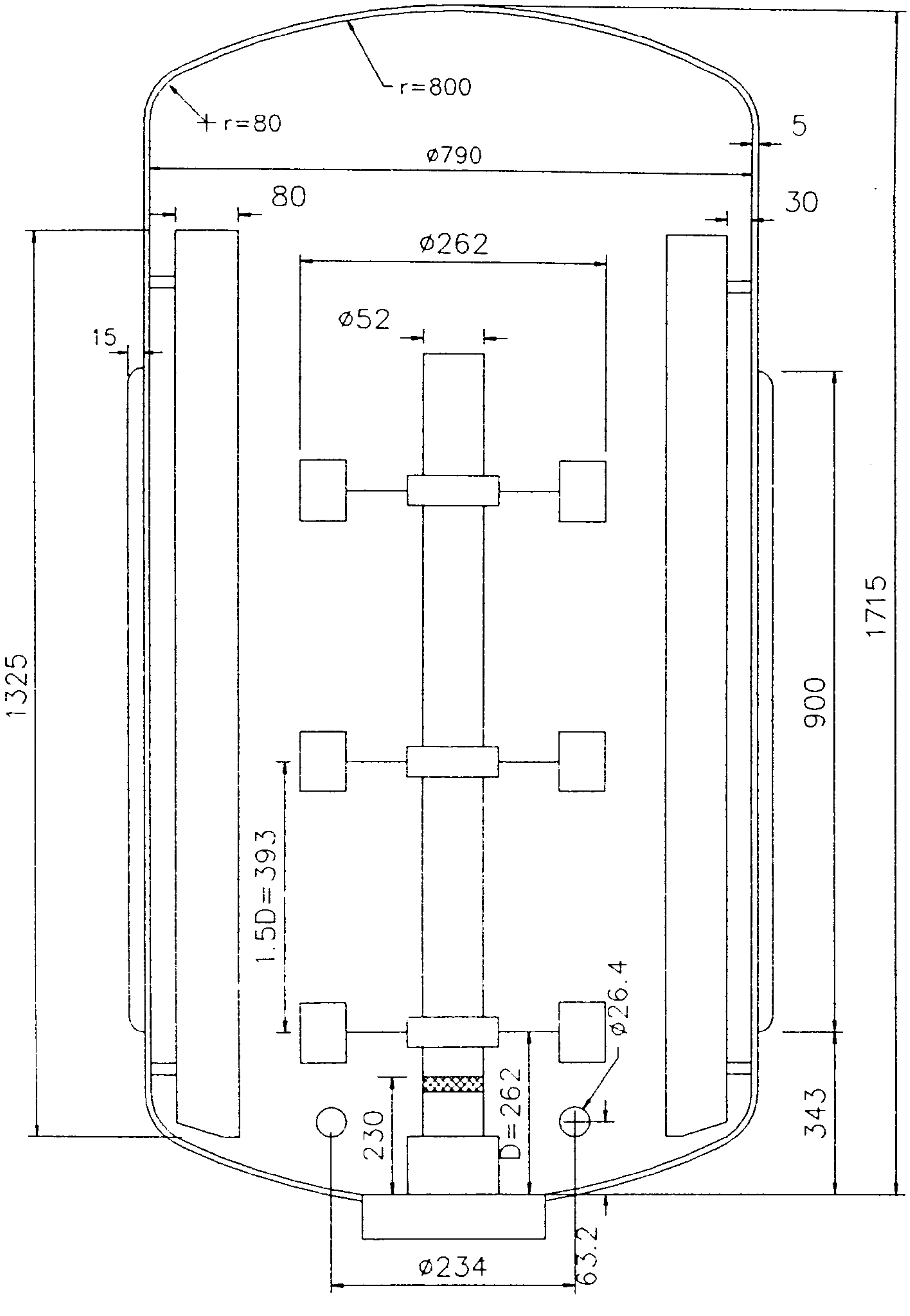

D=impeller diameter

All dimensions in mm

A2.1: Variation of viscosity with temperature for Glucose (measured)

a) Glucose-1

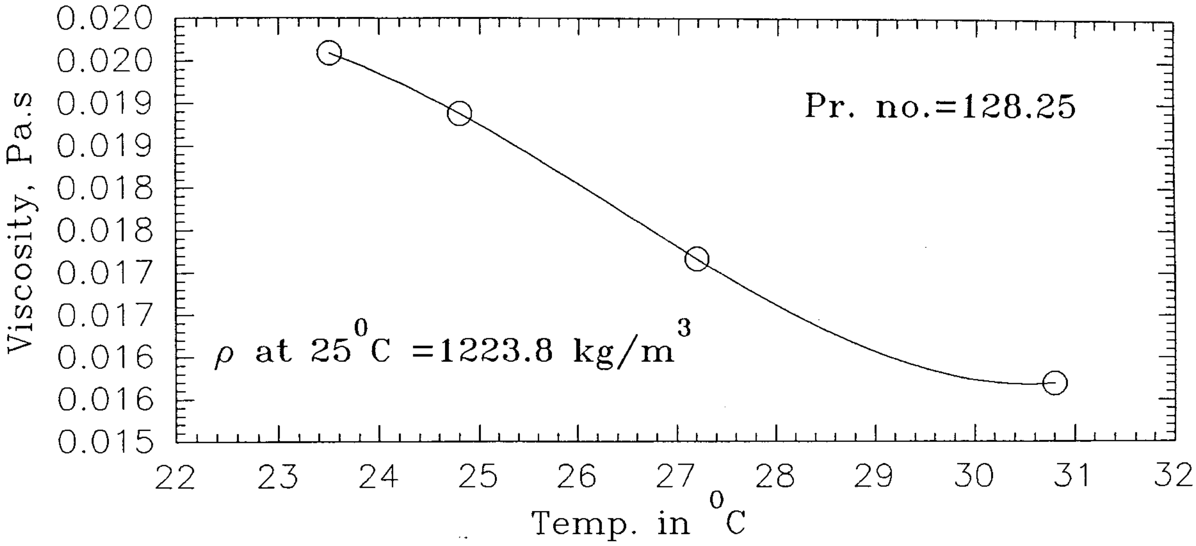

b) Glucose-2

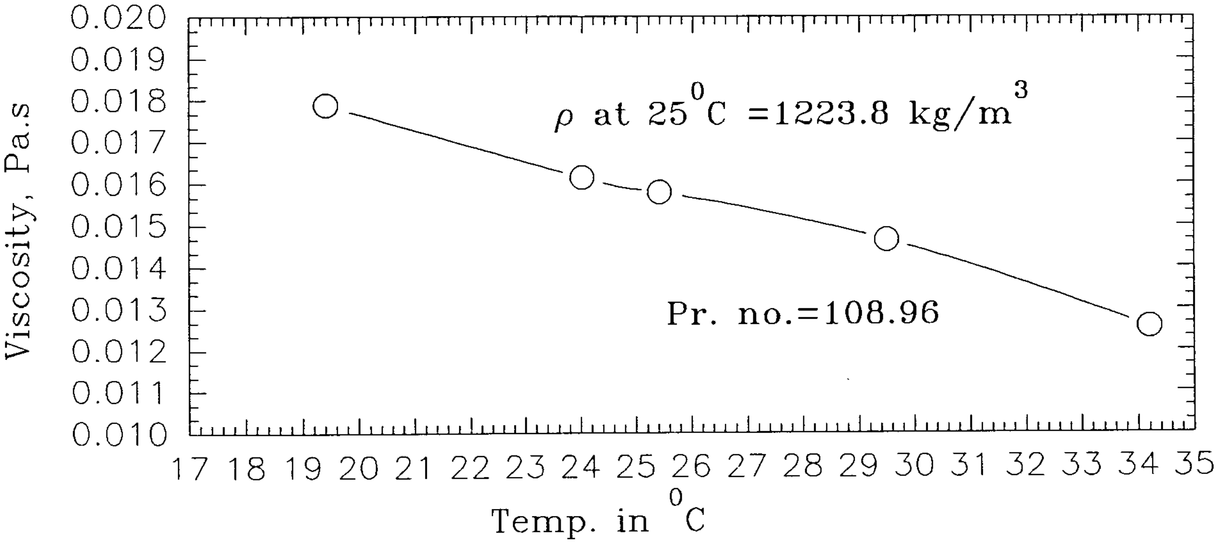

c) Glucose-3

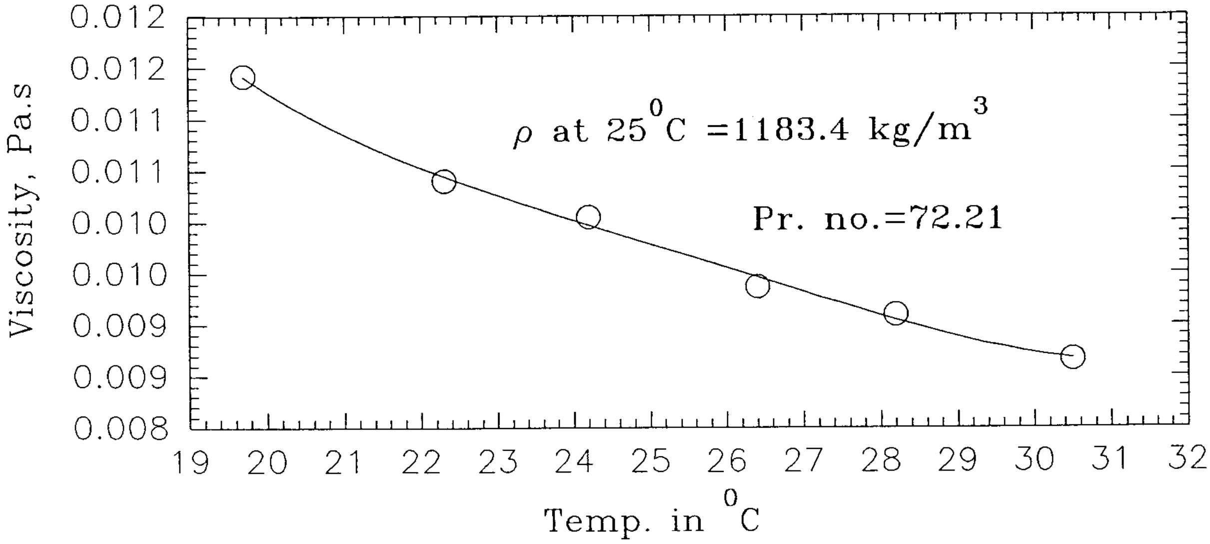

A2.2: Thermal and physical properties of Glucose

a) Relationship between thermal conductivity and % dry wt

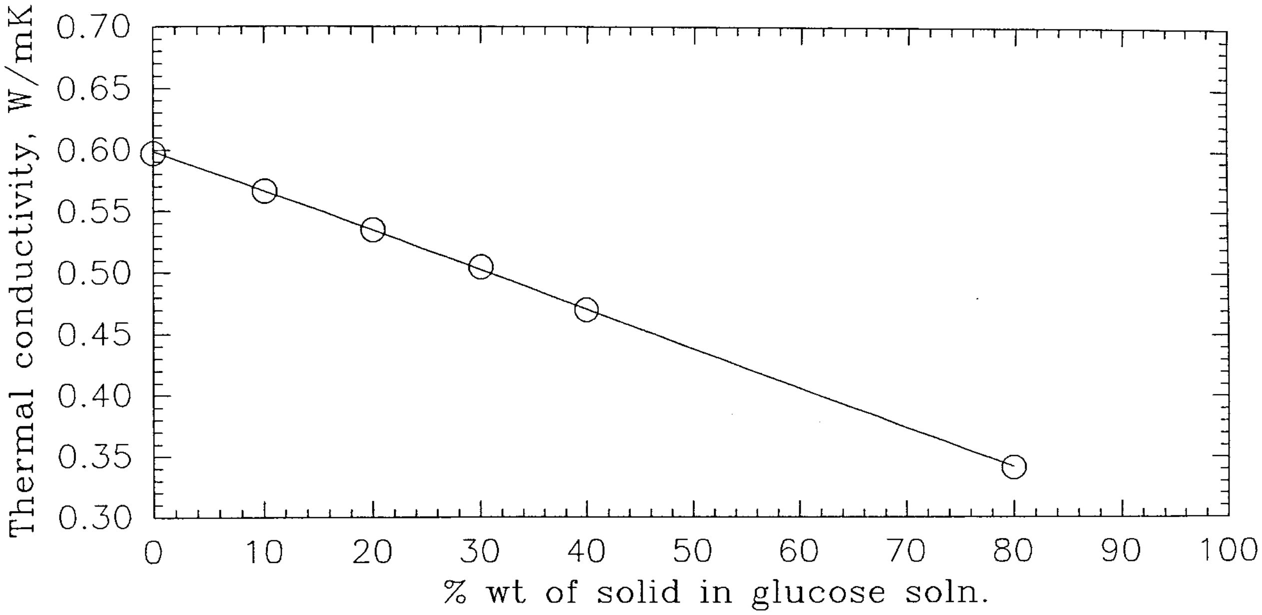

b) Relationship between viscosity and % dry wt

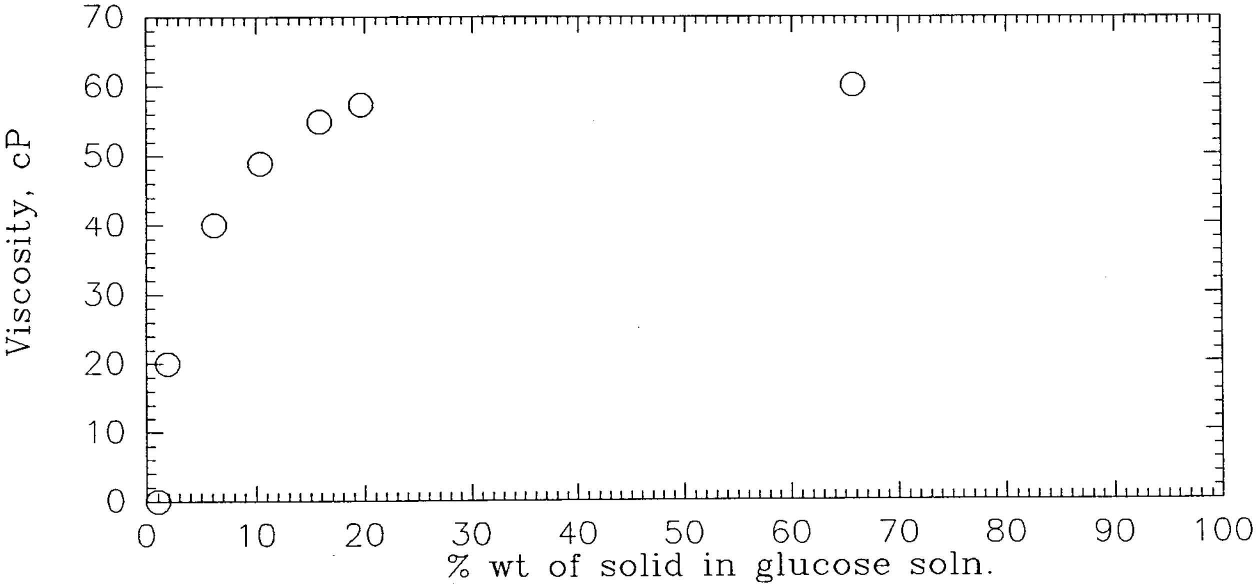

c) Relationship between Specific heat (C_p) and % dry wt.

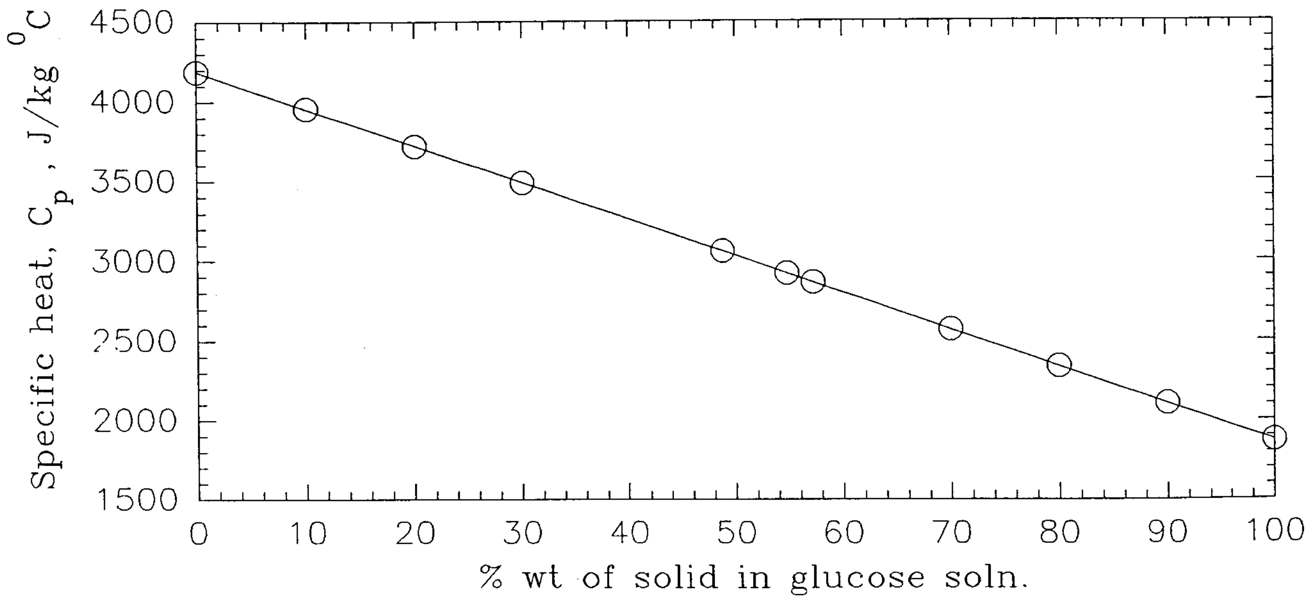

APPENDIX-3

Physical properties of CMC

1) Values of K and n at varying temperature for 0.28% CMC

Temperature, °C	K	n
19	0.32	0.61
22	0.30	0.61
25	0.25	0.63
28	0.22	0.65
31.5	0.17	0.67
39.5	0.15	0.69
41.5	0.13	0.70
46.5	0.11	0.72

3) Values of K and n at varying temperature for 0.8% CMC

Temperature, °C	K	n
20	3.33	0.47
24.8	2.81	0.49
28.5	2.44	0.51
32	1.97	0.54
42.5	0.91	0.63

3) Values of K and n at varying temperature for 1.4% CMC

Temperature, °C	K	n
24.8	21.15	0.34
28	19.71	0.35
34.4	12.84	0.41
41	9.44	0.46

The values of thermal conductivity and c_p were assumed to be that of water (0.6 W/mK and 4,200 J/kg °C respectively). The density was also very close to that of water (1000 kg/m^3).

APPENDIX - 4

A) Programme for Signal Processing (for the heat flux probe)

The data is processed by a Sigma Plot 4 scientific graph system by simple computer programs. Each column of the spread sheet contains the data of one probe which is then systematically processed by the program.

a) Each heat flux probe is supplied with temperature multiplication graph. This graph compensates for the change in thermal conductivity of the probe with temperature. A common equation was found from these graph for all the probes,

$$MF = 1.01118-0.000759066\ T$$

Where MF is the multiplication factor and T is the wall temperature of the probe in degree centigrade.

The signal as received and displayed by the computer is in "mV". Let this output be "X" mV.

i) Note the temperature of the wall and work out the multiplication factor from the above equation.

ii) Sensitivity of the heat flux probe 1 at 21 $^{\circ}$C = 3.4394316 $\mu V/(W/m^2)$
Convert "X" into μV, and then the μV signal into engineering unit =1000X /3.4394316 W/m^2. .

iii) The heat flux probe has a double sided adhesive tape of Scotch high temperature Acrylic (ref no. 966) manufactured by 3M. The thermal conductivity of the tape is 0.24234 W/m K and a thickness of 0.051 mm. An allowance must be given for this resistance in correcting the wall temperature, which is :

$$TC = T + HQ\ (x/K) = T + HQ\ (0.00021)$$

where HQ is the heat flux in W/m . In case of cooling HQ becomes negative and the factor is then subtracted.

iv) The temperature at the boundary of the probe and the fluid is calculated by compensating for the probe impedance (in between the thermocouple and the surface). This temperature is then used with the bulk temperature to obtain the driving force.

Finally the heat transfer coefficient is obtained by dividing the measured heat flux with this driving force. The driving force is:

ΔT = Corrected probe surface temperature - bulk temperature

The following transform was written for processing:

Step 1
MF1=1.01118-0.000759066*HT1;(Multiplication factor for probe 1)
MF2=1.01118-0.000759066*HT2;(Multiplication factor for probe 2)
where HT1 and HT2 are the wall temperatures of probe 1 and 2 respectively

Step 2
HQ1=HF1*MF1/0.0034394316; (Heat flux in W/m^2 for probe 1)
HQ2=HF2*MF2/0.0034140717; (Heat flux in W/m^2 for probe 2)
where HF1 and HF2 are the heat flux signals from probe 1 and 3 respectively

Step 3
TC1=HT1+HQ1*R; (Compensation for resistance between the thermocouple and the fluid boundary, for probe 1)

TC2=HT2+HQ2*R; (Compensation for probe 2)

Step 4
HC1=HQ1/(TC1-TK1); (Heat transfer coefficient for probe 1)

HC2=HQ2/(TC2-TK2); (Heat transfer coefficient for probe 2)

B) Strain gauge
a) The signal from the strain gauge (ST) is in millivolts which needs conversion into engineering units to obtain torque, T,

T= ST * CF ; CF is calibration factor in Nm/mV

b) Power drawn by the impeller

P = 2 *π* N *T ; where N is the impeller speed in rps

C) Turbine flow meter

After being calibrated by the company it was also calibrated after installation. It was found that the calibration supplied by the company was applicable. According to which ;

Average pulse per liter = 368.714

therefore 1 lt/sec = 368.714 Hz

1 lt/min = 368.714/60 = 6.1452333 Hz

1 {(lt/lt) *10 m }*{(min/min)*1/60 sec} = 6.1452333 Hz

1 m /s = 368.714 * 10 Hz

therefore 1 Hz = 2.71212 * 10 m /s

Volumetric flow rate for 1 Hz is equal to 2.71212 *10 m /s

The signal registered in the SETCON is in kHz. Therefore the final calibration factor is ,

1kHz = 0.00271212 m /s

Table A5.1 Local heat transfer and power data for Glucose-1 - one impeller system

Speed rpm	Air flow vvm	Probe-1 W/m²K	Probe-2 W/m²K	Probe-3 W/m²K	Reynolds no.	Impeller Power W	Gas Power W
100	unaerated	770	650	300	7001	32	
200	unaerated	1230	940	650	14679	276	
300	unaerated	1580	1130	940	22206	915	
400	unaerated	1830	1480	1040	29733	2046	
100	0.2	950	350	360	7001	25.5	13.1
200	0.2	1065	590	390	14679	214.8	13.1
300	0.2	1440	1260	575	22206	700.2	13.1
100	0.4	740	920	530	7001	17.6	26.1
200	0.4	1070	380	380	14679	144.9	26.1
300	0.4	1250	615	440	22206	454.5	26.1
100	0.6	535	980	690	7001	16.8	39.2
200	0.6	1125	450	418	14679	129	39.2
300	0.6	1220	440	470	22206	415.8	39.2

Table A5.2 Local heat transfer and power data for Glucose-2 - one impeller system

Speed rpm	Air flow vvm	Probe-1 W/m²K	Probe-2 W/m²K	Probe-3 W/m²K	Reynolds no.	Power W	Gas Power W
100	unaerated	910	740	460	8264	28.9	
200	unaerated	1460	1060	890	17136	265.7	
300	unaerated	1940	1480	1240	25835	891.1	
400	unaerated	2200	1700	1340	34533	1989.1	
100	0.2	970	345	500	8264	25.5	12.8
200	0.2	1300	860	500	17136	203.3	12.8
300	0.2	1740	1340	710	25835	720.9	12.8
100	0.4	760	1040	695	8264	16.6	25.6
200	0.4	1240	422	480	17136	140.6	25.6
300	0.4	1520	720	560	25835	490.7	25.6
100	0.6	650	1020	870	8264	16.3	38.4
200	0.6	1340	542	515	17136	130.2	38.4
300	0.6	1420	545	510	25835	431.5	38.4

Table A5.3 <u>Local heat transfer and power data for Glucose-3 - one impeller system</u>

Speed rpm	Air flow vvm	Probe-1 W/m^2K	Probe-2 W/m^2K	Probe-3 W/m^2K	Reynolds no.	Power W	Gas Power W
100	unaerated	1120	820	610	13018	39.9	
200	unaerated	1830	1310	1240	26036	277.2	
300	unaerated	2360	1730	1480	39054	922.6	
400	unaerated	2840	1960	1760	52073	2028.1	
100	0.2	1210	550	410	13018	28.1	12.6
200	0.2	1600	990	600	26036	211.2	12.6
300	0.2	2120	1520	960	39054	696.6	12.6
100	0.4	920	1140	830	13018	19.5	25.3
200	0.4	1460	520	530	26036	141.6	25.3
300	0.4	1785	1030	670	39054	453.6	25.3
100	0.6	780	1220	980	13018	17.7	37.9
200	0.6	1500	620	590	26036	128.4	37.9
300	0.6	1690	670	605	39054	403.2	37.9

Table A 5.4 Local heat transfer and power data for glucose-3 solution - dual Rushton impeller

Speed rpm	Air flow vvm	Probe-1 W/m^2K	Probe-2 W/m^2K	Probe-3 W/m^2K	Probe-4 W/m^2K	Re no.	Imp. Power W	Gas Power W
100	unaerated	1060	780	2300	700	13018	63.3	
200	unaerated	1700	1280	3360	1120	26036	510.5	
300	unaerated	2280	1550	4450	1350	39054	1722.3	
400	unaerated	2750	2100	5600	1720	52073	3854.6	
100	0.2	620	770	1560	700	13018	38.8	24.7
200	0.2	1570	1140	3240	980	26036	397	24.7
300	0.2	2050	1550	4140	1325	39054	1321	24.7
100	0.4	800	830	600	630	13018	38.9	49.5
200	0.4	1640	1110	3000	990	26036	301.5	49.5
300	0.4	1900	1430	4100	1220	39054	977.8	49.5
100	0.6	820	1120	840	1240	13018	40.1	74.2
200	0.6	1020	1300	1880	960	26036	222.7	74.2
300	0.6	1890	1280	3750	1110	39054	843.2	74.2

Table A5.5 Local heat transfer and power data for 0.28 % CMC - one impeller

Speed rpm	Air flow vvm	Probe-1 W/m²K	Probe-2 W/m²K	Probe-3 W/m²K	Reynolds no.	Impeller Power W	Gas Power W
100	unaerated	365	120	90	1340.3	23	
200	unaerated	610	230	140	3459.6	199.9	
300	unaerated	750	430	160	6024.4	744.9	
400	unaerated	845	700	180	8960.4	1729.9	
100	0.2	415	116	100	1340.3	18.5	10.7
200	0.2	560	180	125	3459.6	125.2	10.7
300	0.2	700	370	160	6024.4	566.4	10.7
400	0.2	790	590	245	8960.4	1456.4	10.7
100	0.4	220	400	190	1340.3	16.8	21.3
200	0.4	590	245	140	3459.6	104.4	21.3
300	0.4	650	320	155	6024.4	375.6	21.3
400	0.4	695	445	230	8960.4	1146.6	21.3
100	0.6	230	560	130	1340.3	16.6	32
200	0.6	665	270	130	3459.6	104	32
300	0.6	635	290	150	6024.4	367.2	32
400	0.6	720	425	180	8960.4	926.9	32
100	0.8	200	425	170	1340.3	17.5	42.7
200	0.8	680	290	160	3459.6	97.1	42.7
300	0.8	640	355	170	6024.4	347.9	42.7
400	0.8	680	400	185	8960.4	866.9	42.7

Table A 5.6 Local heat transfer and power data for 0.8 % CMC - one impeller

Speed rpm	Air flow vvm	Probe-1 W/m²K	Probe-2 W/m²K	Probe-3 W/m²K	Reynolds no.	Impeller Power W	Gas Power W
100	unaerated	156	48	55	183.8	17	
200	unaerated	415	140	50	506.8	150.5	
300	unaerated	540	200	103	938.2	569	
400	unaerated	770	260	120	1445.3	1478.5	
100	0.2	102	70	55	183.8	13.6	10.7
200	0.2	530	70	65	506.8	75.5	10.7
300	0.2	500	120	65	938.2	228	10.7
400	0.2	715	220	100	1445.3	533.5	10.7
100	0.4	56	64	58	183.8	13.6	21.3
200	0.4	480	88	70	506.8	75.5	21.3
300	0.4	550	110	70	938.2	228	21.3
400	0.4	665	180	100	1445.3	533.5	21.3
100	0.6	60	106	76	183.8	13.4	32
200	0.6	480	90	80	506.8	77.5	32
300	0.6	530	100	80	938.2	235.8	32
100	0.8	60	105	77	183.8	13.5	42.7
200	0.8	480	90	80	506.8	71.9	42.7
300	0.8	580	100	80	938.2	222.1	42.7

Table A5.7 Local heat transfer and power data for 1.4% CMC - one impeller

Speed rpm	Air flow vvm	Probe-1 W/m²K	Probe-2 W/m²K	Probe-3 W/m²K	Reynolds no.	Impeller Power W	Gas Power W
100	unaerated	24	36	34	35.4	20.9	
200	unaerated	136	31	50	116.3	161.9	
300	unaerated	230	70	25	231	622.7	
400	unaerated	390	40	20	376.6	1557	
100	0.2	32	46	28	35.4	20.4	10.7
200	0.2	44	38	22	116.3	98.5	10.7
300	0.2	192	84	42	231	245.1	10.7
400	0.2	246	102	30	376.6	626	10.7
100	0.4	48	70	56	35.4	21.2	21.3
200	0.4	44	48	52	116.3	99.1	21.3
300	0.4	172	84	42	376.6	254.6	21.3
100	0.6	40	68	52	35.4	22	32
200	0.6	50	56	52	116.3	99	32
300	0.6	140	22	50	376.6	256.7	32
100	0.8	38	64	38	35.4	21.8	42.7
200	0.8	68	85	80	116.3	102.9	42.7
300	0.8	112	48	54	376.6	253.2	42.7

Table 5.8 Local heat transfer and power data for 0.28 % CMC - dual Rushton impeller

Speed rpm	Air flow vvm	Probe-1 W/m^2K	Probe-2 W/m^2K	Probe-3 W/m^2K	Probe-4 W/m^2K	Reynolds no.	Impeller Power W	Gas Power W
100	unaerated	410	170	1320	240	1340.3	33.65	
200	unaerated	610	485	2310	480	3459.6	412.25	
300	unaerated	1180	840	3240	820	6024.4	1344.9	
100	0.2	185	395	400	360	1340.3	31.92	20.9
200	0.2	760	455	2180	460	3459.6	294.96	20.9
300	0.2	960	780	2940	720	6024.4	1139.96	20.9
100	0.4	300	210	440	370	1340.3	27.22	41.8
200	0.4	200	760	1180	580	3459.6	236.56	41.8
300	0.4	990	720	2940	660	6024.4	931.39	41.8
100	0.6	320	360	240	240	1340.3	25.10	62.7
200	0.6	250	760	1090	550	3459.6	165.14	62.7
300	0.6	460	1160	1600	780	6024.4	801.13	62.7

Table 5.8 Local heat transfer and power data for 0.8 % CMC - dual Rushton impeller

Speed rpm	**Air flow vvm**	**Probe-1 W/m²K**	**Probe-2 W/m²K**	**Probe-3 W/m²K**	**Probe-4 W/m²K**	**Reynolds no.**	**Impeller Power W**	**Gas Power W**
100	unaerated	145	125	180	80	183.8	26.28	
200	unaerated	360	260	1380	255	506.8	294.1	
300	unaerated	520	325	2920	360	938.2	1116.59	
100	0.2	70	60	75	45	183.8	24.55	20.9
200	0.2	540	50	430	170	506.8	150.88	20.9
300	0.2	720	200	1420	280	938.2	554.26	20.9
100	0.4	94	64	59	72	183.8	24.7	41.8
200	0.4	95	260	380	210	506.8	158.5	41.8
300	0.4	680	200	1240	280	938.2	529.12	41.8
100	0.6	75	28	36	48	183.8	23.89	62.7
200	0.6	490	75	350	160	506.8	159.6	62.7
300	0.6	680	180	1140	260	938.2	528.22	62.7

Table 5.9 Local heat transfer and power data for 1.4% CMC - dual Rushton impeller

Speed rpm	Air flow vvm	Probe-1 W/m²K	Probe-2 W/m²K	Probe-3 W/m²K	Probe-4 W/m²K	Reynolds no.	Impeller Power W	Gas Power W
100	unaerated	28	48	16	44	35.4	30.67	
200	unaerated	88	32	96	68	116.3	238.67	
300	unaerated	350	280	540	170	231	970.66	
100	0.2	50	65	66	51	35.4	30.08	20.9
200	0.2	74	80	84	76	116.3	154.52	20.9
300	0.2	116	116	188	116	231	408.13	20.9
100	0.4	51	60	52	51	35.4	30.67	41.8
200	0.4	46	56	66	56	116.3	149.13	41.8
300	0.4	64	96	164	40	376.6	404.52	41.8
100	0.6	52	62	56	53	35.4	30.67	62.7
200	0.6	51	60	68	57	116.3	152.13	62.7
300	0.6	80	100	112	52	376.6	409.93	62.7

Table 6.1 **Local heat transfer profile for fermentation-2**

Speed rpm	Air flow vvm	Probe-1 W/m²K	Probe-2 W/m²K	Probe-3 W/m²K	Reynolds no.	Impeller Power W	Gas Power W
100	unaerated	1560	---	140	454.6	28.9	
200	unaerated	2760	---	400	1199.6	230	
300	unaerated	3060	----	660	2067.1	809.4	
350	unaerated	3130	----	800	2573.7	1305.8	
200	0.2	2520	---	440	1199.6	208.6	10.7
300	0.2	2960	---	600	2067.1	674.8	10.7
350	0.2	3020	---	680	2573.7	1092.9	10.7
200	0.6	2360	---	360	1199.6	129.3	32.0
300	0.6	2800	---	560	2067.1	476.1	32.0
350	0.6	3000	---	600	2573.7	840.6	32.0
200	0.8	2320	---	320	1199.6	116.8	42.7
300	0.8	2740	---	500	2067.1	415	42.7
350	0.8	2500	1000	600	2573.7	760.8	42.7

Table 6.2 **Local heat transfer profile for 1g/l pulp solution**

Speed rpm	Air flow vvm	Probe-1 W/m²K	Probe-2 W/m²K	Probe-3 W/m²K	Reynolds no.	Impeller Power W	Gas Power W
100	unaerated	1125	815	510	12882	31.6	
200	unaerated	1750	1105	1050	26289	268.8	
300	unaerated	2360	1580	1380	39434	913.6	
400	unaerated	2900	1920	1700	52578	2010.1	
100	0.2	1130	550	370	12882	27.9	10.7
200	0.2	1550	950	550	26289	211.5	10.7
300	0.2	2100	1530	780	39434	700.2	10.7
100	0.4	880	1100	835	12882	19.2	21.3
200	0.4	1430	530	520	26289	142	21.3
300	0.4	1805	905	610	39434	450.9	21.3
300	0.6	1670	610	585	39434	404.1	32

Table 6.3 **Local heat transfer profile for 2.5 g/l pulp solution**

Speed rpm	Air flow vvm	Probe-1 W/m^2K	Probe-2 W/m^2K	Probe-3 W/m^2K	Reynolds no.	Impeller Power W	Gas Power W
100	unaerated	1065	725	460	11214	32.7	
200	unaerated	1740	1020	960	22428	261.6	
300	unaerated	2280	1440	1340	33641	891.1	
400	unaerated	2880	1900	1640	44855	2016.1	
100	0.2	1180	465	410	11214	27.5	10.7
200	0.2	1565	890	550	22428	204.6	10.7
300	0.2	2060	1420	760	33641	711	10.7
100	0.4	800	1120	670	11214	18.6	21.3
200	0.4	1340	490	490	22428	138.9	21.3
300	0.4	1730	890	580	33641	464.4	21.3
300	0.6	1520	590	550	33641	417.6	32.0

Table 6.4 Local heat transfer profile for 5 g/l pulp solution

Speed rpm	Air flow vvm	Probe-1 W/m²K	Probe-2 W/m²K	Probe-3 W/m²K	Reynolds no.	Impeller Power W	Gas Power W
100	unaerated	1020	330	270	1941	31.6	
200	unaerated	1760	1000	720	5522	265.8	
300	unaerated	2360	1260	1200	10179	893.3	
400	unaerated	2840	1680	1540	15708	1950	
100	0.2	645	350	650	1941	26	10.7
200	0.2	1485	810	350	5522	200.1	10.7
300	0.2	2060	1400	580	10179	690.3	10.7
100	0.4	810	820	470	1941	21.5	21.3
200	0.4	1160	470	340	5522	143.7	21.3
300	0.4	1750	920	450	10179	495	21.3
300	0.6	1460	670	440	10179	437	32.0

Table 6.5 Local heat transfer profile for 10 g/l pulp solution

Speed rpm	Air flow vvm	Probe-1 W/m^2K	Probe-2 W/m^2K	Probe-3 W/m^2K	Reynolds no.	Impeller Power W	Gas Power W
100	unaerated	1260	100	80	383	31.8	
200	unaerated	1840	520	440	1142	252.6	
300	unaerated	2360	980	700	2162	891.1	
400	unaerated	2840	1560	920	3401	2187.1	
100	0.2	510	420	225	383	24.9	10.7
200	0.2	1530	390	400	1142	197.4	10.7
300	0.2	2110	700	520	2162	718.2	10.7
100	0.4	560	230	390	383	24	21.3
200	0.4	1410	390	410	1142	142.8	21.3
300	0.4	1775	590	450	2162	529.2	21.3
300	0.6	1620	530	420	2162	458.1	32.0

APPENDIX - 7

When the sampling if from a parent distribution that is normal, the statistic *t* has a sampling distribution known as Student's t-distribution. In this case the signal was randomly picked as explained in chapter 4.

This distribution resembles the standard normal distribution, but it is more spread out and less peaked than the standard normal distribution, and consequently has a bigger variance.

In general, the 95% confidence interval based on a sample size of say 10, is

$$[X_m - 2.262 * (s/(10)^{0.5}),\ X_m + 2.262 * (s/(10)^{0.5})]$$

where X_m is the mean, and s is the standard deviation.

This is because 2.262 is the upper 2.5% point (that is, 97.5 percentile) of the Student's *t*-distribution with 10-1=9 degrees of freedom. This technique is described in details by Anderson and Sclove [143].

REFERENCES

1. Chilton, T.H., Drew, T.B., and Jebens, R.H., Heat Transfer Coefficients in Agitated Vessels, Ind.Eng.Chem, Vol. 36, pp. 510-516, 1944.

2. Seider, E.N., and Tate, G.E., Heat Transfer and Pressure Drop of Liquids in Tubes, Ind. Eng. Chem., Vol. 28, No. 12, pp. 1429-1435, 1936.

3. Kraussold, H., Der Wärmeübergang in Rührgefäben (German), Chem.-Ing-Tech., Vol. 23, No. 8, pp. 177-183, 1951.

4. Uhl, V.W., Heat Transfer to Viscous Materials in Jacketed Agitated, Chem. Eng. Prog. Sym. Ser., N . 17, Vol.51 , pp. 93-108, 1955.

5. Brooks, G., and Su, G.J., Heat Transfer in Agitated Kettles, Chem. Eng. Prog Vol. 55, No. 10, pp. 54-57, 1959.

6. Wilson, E.E., Basis for Rational Design of Heat Transfer Apparatus, Trans. Am. Soc. Mech. Engrs., pp. 47-53, 1915.

7. Khartabil, H.F., Christensen, R.N. and Richards, D.E., A modified Wilson plot technique for determining heat transfer correlations, Second U.K. Conference on Heat Transfer, Volume II, Sessions 4A-6C, pp. 1331-1357, 1988.

8. Cumming, G.H. , and West, A.S., Heat Transfer Data for Kettles with Jackets and Coils, Ind. Eng. Chem., Vol. 42, pp. 2303-2313, 1950.

9. Ackley, E.J., Film Coefficients of Heat Transfer For Agitated Process Vessels, Chem. Eng., Vol. 69, pp. 133-140, 1960.

10. Nagata, S.,Nishikawa, M.,Takimoto,T.,Kida, F., and Kayama,T., Turbulent Heat Transfer from the Wall of a Jacketed Tank, Heat Transfer - Japan Research, Vol. 1, No. 1, pp 66-74, 1972.

11. Brown, R.W.,Scott,R. and Toyne,C., An Investigation of Heat Transfer in Agitated Jacketed Cast Iron Vessels, Trans. Inst. Chem. Eng., Vol. 25, pp.181-190 1947.

12. Edwards M.F., Shamlou,P.A. and Wang,H.Z., Heat transfer in Agitated Vessels, IChem.E. symp. series., No. 64., F1-F13, 1981.

13. Strek, F., Heat Transfer in Liquid Mixers-Study of a Turbine Agitator with six flat

blades, Int. Chem. Eng., Vol. 3, No. 4, pp. 533-556, 1963.

14. Chapman, F.S., Dallenbach, H. and Holland,F.A., Heat Transfer in Baffled, Jacketed, Agitated Vessels, Trans Inst. Chem. Engrs., Vol. 42, pp. T398-T406, 1964.

15. Richards, J.W.: Power Input to Fermentators and Similar Vessels, Brit. Chem Eng., Vol 8, No. 3, pp. 158-163, 1963.

16. Yamamoto, K., Hydrodynamic study in agitated vessels, PhD Thesis, Kyoto Univ., Kyoto, 1961.

17. Zlokarnik, M., Heat Transfer to the Wall of a Stirred Tank on Cooling and Heating in the Range of $10^o<Re<10^5$, Chem - Ing - Tech., Vol. 41, No.22, pp. 1195-1202, 1969.

18. Nagata,S.,Nishikawa,M.,Kayama,T. and Nakajima,M., Heat Transfer to Cooling Coil Acting as Rotating Impeller in Highly Viscous Liquids, J. Chem. Eng. Japan, Vol. 5, No. 2, pp. 187-192, 1972.

19. Aske, H., Beek, W.J., Van Berkel, F.C., and Graauw,J.De., The Local Heat Transfer at the Wall of a Large Vessel Agitated by Turbine Impellers, Chem. Eng. Sci., Vol. 22, pp. 135-146, 1967.

20. Balakrishna, M and Murthy, M.S., Heat Transfer Studies in Agitated Vessels Chem. Eng. Sci., Vol. 35 , pp. 1486-1494 , 1980 .

21. Bourne,J.R.,Dossenbach,O.,and Post.T., Local and Average Mass and Heat Transfer due to Turbine Impellers, 5th European Conf. on Mixing, Wurzburg, West Germany, Ed. Stanbury J., pp.199-207, 10-12 June, 1985.

22. Man,K.L.,Edwards,M.F.,Polley,G.T., A Study of Local Heat Transfer Coefficients in Agitated Vessels, Inst of Chem Eng Symp Ser, No. 89, pp 193-207, 1984.

23. Chilton ,T.H. and Colburn,A.P., Mass Transfer (Absorption) Coefficients, Ind. Eng. Chem., Vol.26, No.11, pp. 1183-1187, 1934.

24. Mizushina,T., The Electrochemical Method in Transport Phenomena, Advances in Heat Transfer , Vol.7., pp 87-161, Academic Press, 1971.

25. Smith,R., Application of electrochemical techniques for mass transfer studies, Ph.D Thesis, Univ of Bradford , Bradford, U.K, 1975.

26. Fasano,J.B., Brodkey,R.S. and Haam,S.J., Local Wall Heat Transfer Coefficients using Surface Calorimeters, 7th European Congress on Mixing, Ed. Bruxelmane, M. and

Froment,G., Brugge, Belgium, Vol 2, pp 497-505, 18-20 Sep., 1991.

27. Nagata, S., Mem. Fac. Eng. Kyoto University., 21, 260, 1959.

28. Strek, F.,Masiuk,S.,Gawor,G. and Jagiello,R., Heat Transfer in Mixers for liquids (Studies of Propeller Agitators), Int. Chem. Eng., Vol.5, No.4, pp 695-710, 1965.

29. Schlichting, H., Boundary Layer Theory, 6th Edn., McGraw Hill, New York, 1960.

30. Holman,J.B., Heat Transfer ,6th. Int. Student Edn., McGraw Hill, NewYork, 1986.

31. Kolbel, H., Siemens,W., Maas, R. and Müller, K., Wärmeübergang an Blasensaulen (German), Chem. Ing. Tech., Vol. 30, pp. 400-408, 1958.

32. Kast,W., Untersuchungen zum Wärmeübergang in Blasensäulen (German), Chem. Ing. Tech., Vol. 35, pp. 785-794, 1963.

33. Kast,W., Analyse Des Wärmeübergangs in Blasensaulen, Int. J. Heat Mass Transfer, Vol. 5, pp. 329-336, 1962.

34. Fair,F.R.,Lambright,A.J. and Andersen,J.W., Heat Transfer and Gas Holdup in a Sparged Contactor, Ind.Eng.Chem.Process Des. Develop., Vol. 1, pp. 226-238, 1962.

35. Konestova,V.V., Int. J. Heat Mass Transfer, 9, pp. 1103-1109 , 1966.

36. Lehrer,L.H., Gas Agitation of Liquids, Ind. Eng. Chem. Process Des. Develop., Vol. 7, pp. 226-232, 1968.

37. Rao, K.B. and Murti, P.S, Heat Transfer in Mechanically Agitated Gas-Liquid System, Ind. Eng. Chem. Proc. Des. Dev., Vol.12, No. 2, pp. 190-197, 1973.

38. Dunlop, I.R., and Rushton, J.H., Heat-Transfer Coefficients in Liquid Mixing Using Vertical-Tube Baffles, Chem. Eng. Prog. Sym. Ser., Vol. 49, No 5, pp137-151, 1953.

39. Strek, F. and Karcz, J., A Local Heat Transfer for Mechanically Stirred Gas-Liquid Systems, 6th. European Conference on Mixing, Pavia, Italy, Ed. Baldi, G and Cucchetti, P., pp. 375-380, 24-26 May, 1988.

40. Man, K.L., A Study of Local Heat-Transfer Coefficients in Mechanically Agitated Gas-Liquid Vessels, 5th. European Conference on Mixing, Wurzburg, West Germany, Organised by VDI-GVC, pp. 221-231, 10-12 June, 1985.

41. Karcz,J. and Strek,F., Heat Transfer in Mechanically Stirred Gis-Liquid System, 7th

European Congress on Mixing, Ed. Bruxelmane,M. and Froment,G. Brugge, Belgium, Vol 1, pp 251-259, 18-20 Sep., 1991.

42. De Maerteleire,E., Heat Transfer in Turbine Agitated Gas-Liquid Dispersions, International Symposium on Mixing , European Federation of Chemical Engineering, Mons, Belgium, pp. XC7-XC35, 21-24 Feb. 1978.

43. Calderbank,P.H. and Moo-Young,M.B., The Prediction of power consumption in the Agitation of Non-Newtonian Fluids, Trans Instn. Chem. Engrs., Vol 37, pp 26-33, 1959.

44. Sano, Y.K. and Yamo, L.S., Chem. Eng. Res. Des., Vol. 23, pp. 245-263, 1969.

45. Hrunby, M., Relationship Between the Dissipation of Mechanical Energy and Heat Transfer in Agitated Vessels, Int. Chem. Eng., Vol. 7, No. 1, pp. 86-90, 1967.

46. de Guzman, J.Anales Real Soc. Esban. Fis Quim (Madrid), No. 11, pp. 353-361,1913.

47. Andrade, E.N., The Viscosity of Liquids, Nature, Vol. 125, No. 3148, pp. 12-13, 1930.

48. Erying, H.J., Chem. Phys. , Vol 4, pp. 205-211, 1936.

49. Krishnan,R.M. and Pandya S.B., Heat Transfer to Non Newtonian Fluids in Jacketed Agitated Vessels, Indian Chem Engineer, Trans 43, April 1966.

50. Metzner, A.B., Vaughn, R.D. and Houghton, G.L., Heat Transfer to Non Newtonian Fluids, A.I.Ch.E. Journal, Vol. 3, No. 1, pp. 92-100, 1957.

51. Pigford, R.L., Nonisothermal Flow and Heat Transfer Inside Vertical Tubes, Chemical Engineering Progress Symposium Series, pp. 79-92, 1955.

52. Sandall, O.C. and Patel. K.G., Heat Transfer to Non-Newtonian Pseudoplastic Fluids in Agitated Vessels, Ind. Eng. Chem. Process Design and Development, Vol 9, No. 1, pp. 139-143, 1970.

53. Carreau, P. , Charest, G. and Corneille, J.L., Heat Transfer to Agitated Non-Newtonian Fluids, The Can. Journal of Chem. Eng., pp. 3-8, February, 1966

54. Foresti, R. and Liu, T., Agitation of Non-Newtonian Liquids, Industrial and Engineering Chemistry, Vol. 7, No. 7, pp. 860-864, 1959.

55. Metzner, A.B. and Otto, R.E., Agitation of Non-Newtonian Fluids, A.I.Ch.E. Journal, Vol. 3, No. 1, pp. 3-10, 1957.

56. Suryanarayanan, S., Mujawar, B.A. and RajaRao, M., Heat Transfer to Pseudoplastic Fluids in an Agitated Vessel, Ind Eng Chem Process Des Dev, Vol. 15, No. 4, pp. 564-569, 1976.

57. Kai, W. and Shengyao, Y., Heat Transfer and Power Consumption of Non-Newtonian Fluids in Agitated Vessels, Chem Eng Sci, Vol. 44, No. 1, pp. 33-40, 1989.

58. Mohan, P., Emery, A.N. and Al-Hassan, T., Heat transfer to Newtonian mechanically agitated vessels , accepted for publication in Experimental Fluid Sciences.

59. Heinlein, H,W and Sandall, O.C, Low Reynolds Number Heat Transfer to Non-Newtonian Fluids in Anchor-Agitated Vessels, Ind.Eng.Chem.Process Des. Develop., Vol. 11, No. 4, pp. 490-495, 1972.

60. Skelland, A.H.P. and Dimmick, G.R., Heat Transfer between Coils and Non-Newtonian Fluids with Propeller Ind. Eng. Chem. Process Design and Development, Vol. 8, No. 2, pp. 267-274, 1969.

61. Uhl, V.W. and Voznick, H.P., Chem. Eng. Progr., Vol. 56, pp. 72-78, 1960.

62. Shamlou, P.A. and Edwards, M.F., Heat Transfer to Viscous Newtonian and Non-Newtonian Fluids for Helical Ribbon Mixers, Chem. Eng. Science, Vol. 4 pp.41, No. 8, 1957-1967, 1986.

63. Shamlou, A.P. and Edwards, M.F., Chem. Eng. Sci., Vol. 40, pp. 1773-1781, 1983.

64. Shamlou, A., Ph.D thesis, University of Bradford, U.K., 1981.

65. Calderbank, P.H., The Inter-Dispersion of Immiscible Fluid Phases, British Chemical Engineering, pp. 267-274, September, 1956.

66. Oyama, Y. and Endoh, K., Chem. Eng. (Japan), Vol. 10, No. 2, pp. 42-47, 1955.

67. Michel, B.J. and Miller, S.A., Power Requirement of Gas-Liquid Agitated Systems, A.I.Ch.E. Journal, Vol. 8, No. 2, pp. 262-266, 1962.

68. Nishikawa, F., Masters Thesis, University of Pennsylvania, U.S.A., 1965.

69. Taguchi, H. and Miyamoto, S., Power Requirement in Non-Newtonian Fermentation Broth, Biotechnology and Bioengineering, Vol. VIII, pp. 43-54, 1966.

70. Blakebrough, N. and Sambamurthy, K., Performance of Turbine Impellers in Sparger-

Aerated Fermentation Vessels, J. Appl. Chem., Vol. 14, October, 1964.

71. Bruijn, W., Riet, K. and Smith, M., Power Consumption with Aerated Rushton Turbines, Trans. Instn. Chm. Engrs, Vol. 52, pp. 88-104, 1974.

72. Bolliger, D.H., Assessing Heat Transfer in Process-Vessel Jackets, Chem. Eng., Vol. 89, pp. 95-100, Sept. 20, 1982.

73. Uhl,V.W. and Gray,J.B., Mixing : Theory and Practice, Vol.1, Academic Press, New York, 1966.

74. Perry, J.H., Chemical Engineers Handbook, pp. 10-14, McGraw-Hill, New York, 1966.

75. Kern, D.Q., Process Heat Transfer, pp.103-120, McGraw-Hill, New York, 1950.

76. Markovitz,R.E., Picking the Best Vessel Jacket, Chem. Eng., pp. 156-162, Nov.15, 1971.

77. Penney,W.R. and Koopman,R.N., Prediction of Net Removal Capabilities for Agitated Vessels (and Pumped-Through Heat Exchanger), AIChE. Symp. Ser., Vol. 68, No. 118, pp. 62-73, 1972.

78. Wilkinson, W.L., Non Newtonian Fluids, Volume 1, Fluid Mechanics, Mixing and Heat Transfer, Pergamon Press, 1960.

79. Whorlow, R.W., Rheological Techniques, John Wiley and Sons, 1980.

80. Metzner, A.B. and Taylor, J.S., A.I.Ch.E. J., Vol. 6, No. 1, pp. 109-116, 1960.

81. Wichterle, K. and Wein, O., Int. Chem. Eng., Vol. 21, No. 1, pp.116-123, 1981.

82. Solomon, J., Nienow, A.W. and Pace, G.W., Proc. 6th Int. Fermentation, Canada, 1980, in Adv. in Biotechnology, Pergamon Press, Vol. 1, pp. 503-509, 1981.

83. Unwin, W.C., Proc. Roy. Soc., A31, pp. 54-61, 1880.

84. Rushton, J.H., Costich, E.W. and Everett, M.J., Chem. Eng. Prog., Vol. 46, pp. 467-475, 1950.

85. Metzner, A.B., Feehs, R.H., Ramos, H.L., Otto, R.E. and Tuthill, J.D., A.I.Ch.E. J, Vol. 7, No. 1, pp. 3-9, 1961.

86. Nienow, A.W., Hudcova, V., Haozhung, W and Huoxing, L., Chem. Eng. Sci., Vol. 42, pp. 375, 1987.

87. Tucker, K.G. , Mohan, P. and Thomas C.R., The influence of mycelial morphology on the rheology of filamentous fermentation broths, to be published.

88. Laufhûtte, H.D. and Mersmann, A, Local Energy Dissipation in Agitated Turbulent Fluids and its Significance for the Design of Stirring Equipment, Chem. Eng. Technol., Vol. 10, pp. 56-63, 1987.

89. Bailey and Ollis, Fundamentals of Biochemical Engineering, 2nd edition, 1984.

90 Blakebrough, N., McManamey, W.J. and Tart, K. R., Heat Transfer to Fermentation Systems in an Air-Lift Fermenter, Trans IChemE, Vol. 56, pp. 1978.

91. Blakebrough, N., McManamey, W.J. and Walker, G., Heat Transfer to Fermentation Systems in an Air-Lift Fermenter (Part II), Chem Eng Res Des, Vol. 61, pp. 264-266, July, 1983.

92. Calam, C.T. and Ismail, B.A.K., Investigation of factors in the optimization of penicillin production, J. Appl. Chem. Biotechnol., Vol. 30, pp. 249-262, 1980.

93. Queener, S.W. and Swartz, R.W. , Penicillins: biosynthesis and semisynthetic, Economic Microbiology, editor-A.H.Rose,Vol. 3, Academic press, New York, pp. 35-123, 1979.

94. Smith, G.M., Calam, C.T., Variation in inocula and their influence on the productivity of antibiotic fermentations, Biotechnol. letters, Vol. 2, pp. 261-266, 1980.

95. G.C.Paul, PhD Thesis, University of Birmingham, 1992.

96. Hosler,P. and Johnson, M.J., Penicillin from chemically defined media, Ind. Eng. Chem., Vol. 45, pp. 871-874, 1953.

97. Pirt, S.J. and Righelato, R.C., Effect of growth rate on the synthesis of penicillin by *Penicillium chrysogenum* in batch and chemostat cultures, Appl. Microbiol., Vol. 15, pp.1234-1250, 1967.

98. Pan, S.C., Bonanno, S. and Wagman, G.H., Efficient utilisation of fatty oils energy source in penicillin fermentation, Appl. Microbiol., Vol. 7, pp. 176-180, 1959.

99. Jarvis, F.G. and Johnson, M.J., The mineral utilisation of Penicillium chrysogenum Q176, J. Bacteriol., Vol. 59, pp. 51-60, 1950.

100. Pan, S.C., Hepler, L and Elander, R.P., Control of pH and Carbohydrate addition in the penicillin fermentation, Dev. Ind. Microbiol., Vol. 13, pp. 103-112, 1972.

101. Calam, C.T., Driver, N. and Bowers, R.H., Studies in the production, respiration and growth of *Penicillium chrysogenum* in submerged culture, in relation to agitation and oxygen transfer, J. Appl. Chem., Vol. 1, pp. 209-216, 1961.

102. McCann, E.P. and Calam, C.T., The metabolism of *Penicillium chrysogenum* and the production of penicillin using a high yielding strain at different temperature, J. Appl. Chem. Biotechnol., Vol. 22, pp. 1201-1208, 1972.

103. Pirt, S.J. and Callow, D.S., Continuous flow culture of the filamentous mold *Penicillium chrysogenum* and the control of its morphology, Nature, Vol. 184, pp. 307-310, 1959.

104. Hockenhull, D.J.D., Antibiotics, Biochemistry of Industrial Microorganisms, editors-Rainbow, C and Rose, A.M., Academic press, New York, pp. 227-299, 1963.

105. Varder, F. and Lilly, M.D., Effect of cycling dissolved oxygen concentration on product formation in penicillin fermentations, Eu. J. Appl. Microbiol. Biotechnol., Vol. 14, pp. 203-211, 1982.

106. König, B, Seewald, C. and Schügrel, K., Process engineering investigation of penicillin production, Eu. J. Appl. Microbiol. Biotechnol., Vol. 12, pp. 205-211, 1981.

107. Smith, J.J., Lilly, M.D. and Fox, R.I., The effect of agitation on the morphology and penicillin production of *Penicillium chrysogenum* , Biotechnol. Bioeng., Vol. 35, pp. 1011-1023, 1990.

108. Righelato, R.C., Trinci, A.P.J., Pirt, S.J. and Peat, A., The influence of maintanance energy and growth rate on the metabolic activity, morphology and conidation of *Penicillium chrysogenum*, J. Gen. Microbiol., Vol 50, pp. 399-412, 1968.

109. Placek, J., Ujcova, E., Musilkova, M., Selchert, L. and Fencl, Z, The role of mechanical shear and cultivation on the behaviour of molds, 1st Microbiol. Czech. Akad. Sci., Prague, 1981.

110. Pace, G.W., Rheology of mycelial fermentation broths in fungal biotechnology, editors-Berry,J.E., Smith,D.R. and Kristiansen, B., Academic press, London, 1980.

111. Harnby, N., Edwards, M.F. and Nienow, A.W., Mixing in the process industries, Butterworths, London, 1985.

112. Charles, M., Technical aspects of the rheological properties of microbial cultures, Advances in Biochem. Eng., Vol. 8, pp. 1-7, 1978.

113. Bongenaar, J.J.M., Kossen, N.W.F., Metz, B. and Meijboom, F.N., A method for characterising the rheological properties of viscous fermentation broths, Biotech. and Bioeng., Vol. 15, pp. 201-209, 1973.

114. Baker, M.R., The Development and application of a biological modelling fluid for mycelial fermentation, PhD thesis, The University of Birmingham, 1987.

115. McFarlane, C., PhD. thesis, The University of Birmingham, 1991.

116. Kreith, F., Principles of heat transfer , 3rd. edition, Harper and Row publishers, 1976.

117. Hansen, M., Velocity distribution in the boundary layer of a submerged plate, NACATM 585, 1930.

118. von Karmen, T., The analogy between fluid friction and heat transfer, Trans. ASME, Vol. 61, pp. 705-711, 1939.

119. Murray, D.B. and Fitzpatric, J.A., Local heat transfer coefficients for a tube array using a micro-foil heat flow sensor, Second UK national conference on heat transfer, Vol. II, pp. 1635-1647, University of Strathclyde, Glasgow, Sept. 14-16, 1988.

120. Van der Molen K. and Van Maanen, H.R.E., Laser-Doppler measurements of the turbulent flow in stirred vessels to establish scaling rules, Chem. Eng. Sci., Vol. 22, pp. 1161-1167, 1978.

121. Dyster, K.N., Koutsakos, E, Jaworski, Z. and Nienow A.W., An LDA study of the radial discharge velocities generated by a Rushton turbine: Newtonian Fluids, Re≥5, Trans. IChemE, Vol. 71, part A, pp. 11-23, January, 1993.

122. Solomon, J., Nienow, A.W., Elson, T.P. and Pace, G.W., Cavern sizes in agitated fluids with a yield stress, Chem. Eng. Comm., Vol. 11, pp. 143-147, 1981.

123. Wichterle, K., Zak, L. and Mitschka, P., Shear stress on the walls of agitated vessels, Chem. Eng. Commun., Vol. 32, pp. 289-305, 1985.

124. Strek, F and Karcz, J, Experimental determination of the optimal geometry of baffles for heat transfer in an agitated vessel, Chem. Eng. Process, Vol. 29, pp. 165-172, 1991.

125. Voncken, R.M., Symposium on Mixing, paper 10.4, A.I.Ch.E.-I.C.E. Joint Meeting, London 1965.

126. Koutsakos, E., Nienow, A.W. and Dyster K.N., Laser anemometry study of shear thinning fluids agitated by a Rushton turbine, IChemE symp. series no.121, pp. 51-73, 1990.

127. Nienow, A.W., Wisdom, D.J., Solomon, J., Machon, V., Vlcek, J., Chem. Eng. Commun., Vol. 19, pp. 273-279, 1983.

128. Nienow, A.W. and Lilly, M.D., The power drawn by multiple impellers in sparged, agitated vessels, Biotech. and Bioeng., Vol. 21, pp. 2341-2345, 1979.

129. Bates, R.L., Fondy, P.L. and Fenic, J.G., Impeller characteristics and power, Mixing, Vol. 1, Editor Uhl, V. and Gray, J.B., Academic press, pp. 112-176, 1966.

130. Kuboi, R. and Nienow, A.W., The power drawn by dual impeller systems under gassed and ungassed conditions, 4th European conference on mixing, pp. 247-261, April 27-29, 1982.

131. Hudcova, V., Machon, V. and Nienow, A.W., Gas-liquid dispersion with dual Rushton turbine impellers, Biotech. and Bioeng., Vol. 34, pp. 617-628, 1989.

132. Edney, H.G.S. and Edwards, M.F., Trans.IChemE, Vol. 54, pp. 160-166, 1976.

133. De. Martelaere, E., Chem. Eng. Sci., Vol. 33, pp. 1107-1114, 1978.

134. Shah, Y.T., Kelkar, B.G., Godbole, S.P. and Deckwer, W.D., Design parameters estimation for bubble column reactors, AIChE Journal, Vol. 28, No. 3, pp. 353-379, May 1982.

135. Tucker, K.G., Mohan, P. and Thomas C.R. , Bioreactor and Bioprocess fluid dynamics, 3rd International conference, Cambridge, Sept., 1993 (Accepted).

136. Tucker, K.G. and Thomas, C.R., Effect of Biomass concentration and morphology on the rheological parameter of *Penicillium Chrysogenum* fermentation broths, Tans.IChemE, Vol. 71, part C, June 1993.

137. Roels, J.A., van der Berg, J. and Voncken, R.M., Biotech. Bioeng., Vol. 16, pp. 181-

208, 1974.

138. Metz, B., Kossen, N.W.F. and van Suijdam, J.C., Adv. Biochem. Eng., Vol. 11, pp. 103-156, 1979.

139. Kim, E.Y. and Yoo, Y.J., Biotech. Bioeng., Vol. 26, pp. 285-295, 1984.

140. Fatile, I.A., Appl. Microbiol. Biotechnol., Vol. 21, pp. 60-64, 1974.

141. Tucker, K.G., Kelly, T. , Delgrazia., P. and Thomas, C.R., Biotechnol. Progress, Vol. 8, pp. 353-359, 1993.

142. Packer, H.L. and Thomas C.R., Biotech. Bioeng., Vol. 35, pp. 870-881, 1990.

143. Anderson, T.W. and Sclove, S.L., The statistical analysis of data, 2nd edition, The scientific press, U.S.A. .

NOMENCLATURE

a	Dimensionless exponent of Reynolds number
A_1	Heat transfer area above the impeller plane : m^2
A_2	Heat transfer area below the impeller plane : m^2
A_f	Cross-sectional flow area inside the jacket : m^2
A_H	heat transfer area : m^2
A_t	constant : dimensionless
b	Dimensionless exponent of Prandtl number
c	Dimensionless exponent of Viscosity ratio
C	impeller height : m
C_L	clearance between impeller tip and the vessel wall : m
Cs	clearance between turns of coil : m
c_p	specific heat of the fluid : J/kg K
D	impeller diameter : m
D_c	coil helix diameter : m
d_c	diameter of coil tubing : m
D_T	vessel diameter : m
D_e	equivalent diameter , 4 x (flow area) / (wetted perimeter) : m
E	activation energy of a viscous solution : J/mol
f	fanning friction factor , dimensionless
F	proportionality constant
G_s	superficial gas velocity base on the cross section of the sparger : m/s
g	accelaration due to gravity : 9.8 m/s
h_c	coil heat transfer coefficient (Process side) : W/m^2K
h_j	Jacket heat transfer coeficient (Process side) : W/m^2K
H	dispersion height : m
H_A	height of impeller from the base : m
H_L	height of liquid : m
H_B	depth of impeller from surface : m
h_1	heat transfer coefficient for transfer across the layer above the impeller plane : W/m^2K
h_2	heat transfer coefficient for transfer across the layer below the impeller plane : W/m^2K
h_o	film heat transfer coeficient on service side (for coil subscript "c" and for jacket subscript "j") : W/m^2K

H_C	height of coil : m
H'	height of heat transfer surface: m
H_w	height of the vessel : m
i	number of impellers
J	width of the baffle : m
k	dimensionless constant (for coil subscript C or for jacket subscript j)
K_w	fluid consistency at the wall : dimensionless
K	fluid consistency at the bulk : dimensionless
K_T	Thermal conductivity : W/m K
l	latent heat : J/kg
L	length of impeller blade : m
L_1,L_2	lengths of the plates above and below the impeller plane : m.
M	impeller torque : Nm
m_s	mass flow rate of the condensate : kg/s
N_o	rotational speed of impeller : rev/min
N	rotational speed of impeller : rev/s
N_{cd}	complete dispersion speed : rev/s
N_F	impeller speed at flooding : rev/s
n_p	number of impeller blades
n_b	number of baffles
n	power law index
P	power dissipated in mixing vessel : W
P_g	gassed power : W
p	pitch of the impeller : m
q	latent heat of steam condensate : W
q_{lost}	heat lost : W
Q	turbine discharge flow rate : m^3/s
Q_g	volumetric gas flow rate : m^3/s
Q_{BL}	flow rate of liquid inside the thermal boundary layers : m^3/s
Q_h	effective heat transfer : W
R	radius of the vessel : m
r_d	fouling factor
T_w	vessel wall temperature : K
T_b	bulk temperature : K
T_B	temperature of the fluid inside the boundary layer : K
t	time : s
t_v	thickness of the vessel : m
u	main stream velocity : m/s

U	overall heat transfer coefficient : W/m^{2}K
V_r	radial velocity of the jet near the wall : m/s
V	volume of the vessel : m^3
V_L	liquid volume in the vessel : m^3
V_s	superficial gas velocity based on empty cross sectional area : m/s
V_t	tangential velocity of mixing liquid near surface of wall : m/s
V_n	velocity of the fluid leaving the nozzle : m/s
w_p	mass flow rate of fluid leaving nozzle : kg/s
w	width of the impeller blade : m
W_b	width of the baffle : m
x	axial distance measured from the centre of impeller plane : m

Greek Symbols:

ε	power consumed per unit mass = $P/ [(\pi/4)\, D_T^2 H_L \rho]$: W/kg
ε_g	power per unit mass dissipated by the gas : W/kg
ρ	density : kg/m^3
μ	viscosity at bulk temperature : (N.s)/m^2 or Pa.s
μ_a	apparent viscosity at bulk temperature: (N.s)/m^2 or Pa.s
μ_w	viscosity at temp. of heat transfer surface:(N.s)/m^{2}or Pa.s
θ	angle of impeller blade : rad
σ	surface tension of process liquid : kg/sec^2
ν	kinematic viscosity , μ/ρ : m^2/s
τ	shear stress : N/m^2
$\dot{\gamma}$	shear stress : s^{-1}
ϕ	gas holdup : m

Dimensionless Numbers:

Fr	Froude Number $= V_s^2 /g\, D_T$ or $N^2 D/g$
Nu_c	Nusselt number for coils $= h_c D_T/K_T$ or $h_c d_c /K_T$
Nu_j	Nusselt number for jackets $= h_j D_T /K_T$
N_P	Dimensionless power number = $P / N^3 D^5 \rho$
Re	Reynolds number $= \rho N D^2/\mu$
Re*	Modified Reynolds number $= \rho N(D+V_s)^2 /\mu$

Re_g	Generalised Reynolds number = $D^2N\rho/\mu_a$
Pr	Prandtl number = $c_p\ \mu/K_T$
Pr_g	Generalised Prandtl number = $c_p\mu_a/K_T$
Vi	Viscosity ratio $=\mu/\mu_w$
We	Weber no. = $\dfrac{D^3N^2\rho}{\sigma}$